UNIVERSITY OF CALIFORNIA

RIVERSIDE

Computational Insights into Materials and Interfaces for Capacitive Energy Storage

A Dissertation submitted in partial satisfaction
of the requirements for the degree of

Doctor of Philosophy

in

Chemistry

by

Cheng Zhan

June 2018

Dissertation Committee:
Dr. De-en Jiang, Chairperson
Dr. Gregory Beran
Dr. Ludwig Bartels

Copyright by
Cheng Zhan
June 2018

The Dissertation of Cheng Zhan is approved:

_____

_____

_____

Committee Chairperson

University of California, Riverside

COPYRIGHT ACKNOWLEDGEMENT

The text and figures in Chapter 1, Chapter 2 and Chapter 10, in part or full, are a reprint of the material as it appears in *Adv. Sci*., 4, 170059 (2017). The coauthor (Dr. De-en Jiang) listed in that publication directed and supervised the research that forms the basis of this chapter.

The text and figures in Chapter 3, in part or full, are a reprint of the material as it appears in *J. Phys. Chem. C*, 119, 22297–22303 (2015). The coauthor (Dr. De-en Jiang) listed in that publication directed and supervised the research that forms the basis of this chapter.

The text and figures in Chapter 4, in part or full, are a reprint of the material as it appears in *Phys. Chem. Chem. Phys*., 18, 4668-4674 (2016). The coauthor (Dr. De-en Jiang) listed in that publication directed and supervised the research that forms the basis of this chapter.

The text and figures in Chapter 5, in part or full, are a reprint of the material as it appears in *J. Phys. Chem. Lett.*, 7, 789−794 (2016). The coauthor (Dr. De-en Jiang) listed in that publication directed and supervised the research that forms the basis of this chapter.

The text and figures in Chapter 6, in part or full, are a reprint of the material as it appears in *Carbon*, 116, 278-285 (2017). The coauthor (Dr. De-en Jiang) listed in that publication directed and supervised the research that forms the basis of this chapter.

The text and figures in Chapter 7, in part or full, are a reprint of the material as it appears in *ACS Energy Letters*, 1, 1241-1246 (2016). The coauthor (Dr. De-en Jiang) listed in that publication directed and supervised the research that forms the basis of this chapter.

The text and figures in Chapter 8, in part or full, are a reprint of the material as it appears in *J. Phys. Condens. Matter*, 28, 464004 (2016). The coauthor (Dr. De-en Jiang) listed in that publication directed and supervised the research that forms the basis of this chapter.

The text and figures in Chapter 9, in part or full, are a reprint of the material as it appears in *J. Phys. Chem. Lett.*, 2018, 9, 1223–1228 (2018). The coauthor (Dr. De-en Jiang) listed in that publication directed and supervised the research that forms the basis of this chapter.

DEDICATION

First of all, I would like to thank my research advisor Prof. De-en Jiang for his helpful and patient guidance and support during my 4 years PhD career. I also would like to thank my committee members, Dr. Gregory Beran and Dr. Ludwig Bartels for their helpful comments in my qualify exam, which helped me a lot in my further research work and this dissertation.

Then, I would like to thank my research collaborators in FIRST-EFRC: Prof. Jianzhong Wu in UCR-CEE for his helpful discussion and significant suggestions in our collaborative research project, Prof. Peter Cummings in Vanderbilt University, Dr. Paul R. C. Kent in ORNL, Dr. Sheng Dai in ORNL and Prof. Yury Gogotsi in Drexel University for their helpful discussion and important comments to my scientific publication. In addition, I would like to than another important collaborator in Lawrence Livermore National Laboratory, Dr. Brandon C. Wood and Dr. Tuan Anh Pham, who offered me a very precious summer intern opportunity supported by CCMS program in LLNL. This great experience significantly benefit my research career.

Finally, I would like to appreciate my group colleagues, especially Dr. Ziqi Tian, Dr. Qing Tang and Dr. Bo Li, for their help in solving many technical problems in my research. I also want to appreciate my parents for their strong support to my academic dream.

ABSTRACT OF THE DISSERTATION

Computational Insights into Materials and Interfaces for Capacitive Energy Storage

by

Cheng Zhan

Doctor of Philosophy, Graduate Program in Chemistry

University of California, Riverside, June 2018

Dr. De-en Jiang, Chairperson

Supercapacitors, such as electric double-layer capacitors (EDLCs) and pseudocapacitors, are becoming increasingly important in the field of electrical energy storage. Theoretical study of energy storage in EDLCs focuses on solving for the electric double-layer structure in different electrode geometries and electrolyte components, which can be achieved by molecular simulations such as classical molecular dynamics (MD), classical density functional theory (classical DFT), and Monte-Carlo (MC) methods. In recent years, combining first-principles and classical simulation to investigate the carbon-based EDLCs has become increasingly popular due to the importance of quantum capacitance in graphene-like 2D systems. More recently, the development of joint density functional theory (JDFT) enables self-consistent electronic-structure calculation for an electrode being solvated by an electrolyte. In contrast with the large amount of theoretical and computational effort on EDLCs, theoretical understanding of pseudocapacitance is very limited. In this dissertation project, we first study the carbon-based EDLCs and focus on several important aspects of EDLCs including quantum capacitance, nitrogen doping,

dielectric screening, and edge effect. Then, based on our physical understanding on EDLCs, we designed novel 2D boron supercapacitors, which exhibit promising capacitive performance comparing with conventional carbon electrodes. Finally, we also introduced how to study pseudocapactive mechanism through first principle calculation with solvation model technique. Two typical pseudocapacitor systems are investigated: RuO_2(110) and $Ti_3C_2T_x$ (T=O,OH) in H_2SO_4 electrolyte. Based on our study, the relation between EDL and redox behavior were revealed. We summarize and conclude with an outlook for the future of materials design and discovery for capacitive energy storage.

Table of contents

Chapter 1. Introduction 1
1.1 Basics of capacitive energy storage 1
1.2 Operating mechanism of electric double-layer capacitors 1
1.2.1 The Helmholtz model of an electric double layer 1
1.2.2 The Gouy-Chapman model and beyond 2
1.3 An estimate of how many ions need to be separated when charging an EDLC 4
1.4 Recent experimental advances in EDLCs 5
1.5 Experimental techniques for characterizing EDL 6
1.6 Important issues in capacitive energy storage 8
1.6.1 Classical vs. quantum capacitance 8
1.6.2 Pore size, surface area, pore geometry 9
1.6.3 Electrolytes 10
1.6.4 Defects and functional groups on carbon 11
1.6.5 EDLC vs. pseudocapacitor 12
References 12

Chapter 2. Simulation methods used in supercapacitor modeling 17
2.1 Classical methods to simulate EDLCs 17
2.1.1 Coarse-grained classical density functional theory 17
2.1.2 Atomistic classical molecular dynamics 19
2.1.3 Constant voltage Grand Canonical Monte Carlo 21
2.2 Ab initio simulations of the electrochemical interfaces 22
2.2.1 Effective screening medium (ESM) 23
2.2.2 Joint density functional theory (JDFT) 24
2.2.2.1 Theoretical framework 24
2.2.2.2 Implicit solvation and linear polarizable continuum model 24

2.2.2.3 Electrochemical simulation by JDFT and corresponding technical details 25

References 26

Chapter 3. Quantum Effects on the Capacitance of Graphene-based Electrodes 33

3.1 Introduction 33

3.2 Computational methods 34

3.3 Results and discussion 37

3.3.1 Quantum capacitance of single-layer and multi-layer graphenes 37

3.3.2 Total capacitance for an aqueous electrolyte next to a single-layer graphene 39

3.3.3 Total capacitance for an ionic-liquid electrolyte next to a single-layer graphene 40

3.3.4 Total capacitance as a function of the number of graphene layers 41

3.3.5 Comparison of integral capacitance from -0.6 V to 0.6 V 43

3.3.6 Relevance to realistic carbon electrodes 46

3.4 Summary and conclusions 47

References 48

Chapter 4. Enhancing Graphene Capacitance by Nitrogen: Effects of Doping Configuration and Concentration 52

4.1 Introduction 52

4.2 Computational methods 53

4.3 Results and discussion 58

4.3.1 Quantum capacitance of different N-doping configurations at low concentration 58

4.3.2 Quantum capacitance of graphitic N-doped graphene at different doping levels 60

4.3.3 Quantum capacitance of pyridinic N-doped graphene at different doping levels 61

4.3.4 Quantum capacitance of pyrrolic N-doped graphene 62

4.3.5 EDL capacitance of N-doped graphene in 1M NaCl aqueous electrolyte 64

4.3.6 Total integral and differential capacitance of N-doped graphene in 1M NaCl electrolyte 66

4.3.7 Relevance to real N-doped carbon electrodes 69

4.4 Summary and Conclusions 70

References 71

Chapter 5. Contribution of Dielectric Screening to the Total Capacitance of Few-Layer Graphene Electrodes 76

5.1 Introduction 76

5.2 Method 77

5.2.1 Electronic structure calculation of solvated electrodes 77

5.2.2 Charging simulation and Fermi level shift 78

5.3 Results and discussion 80

5.3.1 Differential capacitance and total capacitance of FLG and Pt electrodes 80

5.3.2 Quantum capacitance of FLG separated from total capacitance 80

5.3.3 Dielectric screening effect in FLG 82

5.3.4 Contribution of dielectric screening and “three contribution” model 84

5.4 Summary and conclusion 86

References 87

Supporting Information 91

Chapter 6. Computational insight into the capacitive performance of graphene edge planes 94

6.1 Introduction 94

6.2 Methods 95

6.2.1 Joint density functional theory 95

6.2.2 Classical molecular dynamics (CMD) simulations 98

6.3 Results and discussion 99

6.3.1 Electronic chemical potential (μ_e) shift and potential at the point of zero charge (ψ_{PZC}) for the graphene edge plane 99

6.3.2 Charge-potential curve of graphene edges in contact with an implicit solvation model 100

6.3.3 Electrostatic potential drop inside the electrode 102

6.3.4 Potential drop and capacitance contribution for graphene edge 102

6.3.5 Classical molecular dynamics (CMD) study on the armchair and zigzag edge 104

6.3.6 Combining JDFT and CMD results 107

6.4 Summary and conclusions 109

References 110

Supporting Information 116

Chapter 7. Boron Supercapacitors 121

7.1 Introduction 121

7.2 Model and Method 122

7.3 Results and Discussion 124

7.3.1 Cohesive energy, electronic structure and PZC of boron sheets 124

7.3.2 Charging behavior and capacitive performance of 2D boron sheets 126

7.3.3 Potentiality and challenges of 2D boron supercapacitor 132

7.4 Summary and conclusion 132

References 133

Supporting Information 138

Chapter 8. Understanding the pseudocapacitance of RuO_2 from joint density functional theory 141

8.1 Introduction 141

8.2 Methods 143

8.3 Results and Discussion 146

8.3.1 Potential of zero charge on RuO_2(110) 146

8.3.2 Influence of surface hydrogen adsorption on EDL capacitance 147

8.3.3 Comparison of EDL energy and H adsorption energy 149

8.3.4 Capacitive behavior on RuO_2(110) 150

8.3.5 Adsorption structure of hydrogen on RuO_2(110) and its influence on pseudocapacitance 152

8.4 Summary and conclusions 155

References 156

Supporting Information 162

Chapter 9. Understanding the MXene Pseudocapacitance 166

9.1 Introduction 166

9.2 Method and model 168

9.2.1 Electronic structure calculation of solvated system via implicit solvation model 168

9.2.2 Voltage-dependent Gibbs Free Energy in Redox Reaction 169

9.3 Results and Discussion 172

9.3.1 Influence of H coverage on the point of zero charge (PZC) of MXene 172

9.3.2 Gibbs free energy, ensemble-averaged H coverage, and surface charge 172

9.3.3 Comparison with the experimental capacitances 175

9.3.4 Electronic structure and charge distribution 176

9.3.5 Analysis of oxidation state of Ti 178

9.4 Summary and Conclusion 179

References 180

Supporting Information 184

Chapter 10 Summary and future work on capacitive energy storage and solid/liquid interfacial model 188

10.1 Summary 188

10.2 Challenges and future works 190

References 191

List of Tables

Table 4-1 Integral capacitance of N-doped graphene 68

Table 6-1 Electronic chemical potential and PZC of graphene edges 100

Table 6-2 Quantum and non-quantum contribution in graphene edges 103

Table 6-3 Solvent accessible surface area (SASA) relative to that of the basal plane 109

Table 7-1 Hole density ($\boldsymbol{\eta}$), calculated cohesive energy (Eb), and potential at the point of zero charge (PZC) of the six boron sheets 125

Table S8-1 Bond information of RuO_2 164

List of Figures

Figure 1-1 Capacitive mechanism of EDLCs 5

Figure 1-2 The length and time scales of different simulation and experimental techniques 8

Figure 1-3 Definition of quantum capacitance 9

Figure 3-1 Quantum capacitance of FLG 39

Figure 3-2 Charging curve and differential capacitance of single layer graphene in 1M NaF aqueous electrolyte 40

Figure 3-3 Charging curve and differential capacitance of single layer graphene in ionic liquid electrolyte 41

Figure 3-4 Charging curve and differential capacitance of FLG in 1M NaF aqueous electrolyte 43

Figure 3-5 Charging curve and differential capacitance of FLG in ionic liquid electrolyte 43

Figure 3-6 Capacitance change with layer number 45

Figure 3-7 Contribution of C_Q and C_{EDL} 46

Figure 4-1 CMD simulation and different nitrogen configuration 57

Figure 4-2 Quantum capacitance of N-doped graphene 59

Figure 4-3 DOS of N-doped graphene 60

Figure 4-4 Quantum capacitance of graphitic N-doped graphene 61

Figure 4-5 Quantum capacitance of pyridinic N-doped graphene 62

Figure 4-6 Quantum capacitance of pyrrolic N-doped graphene 63

Figure 4-7 DOS of pyrrolic N-doped graphene 64

Figure 4-8 EDL capacitance of N-doped graphene 66

Figure 4-9 Total differential capacitance of N-doped graphene 68

Figure 5-1 Schematic of a charged few layer graphene in contact with an implicit electrolyte on both sides 78

Figure 5-2 Definition of potential drop during charging process 79

Figure 5-3 Differential and integral capacitance of FLG 81

Figure 5-4 Quantum capacitance of FLG 82

Figure 5-5 Electrostatic potential drop in charged electrodes 86
Figure 5-6 Potential drop contribution in FLG 86
Figure S5-1 Fluid charge response 91
Figure S5-2 Excess charge distribution in FLG 92
Figure S5-3 Electrostatic potential drop in different solvation 93
Figure 6-1 Structure of armchair and zigzag edges 97
Figure 6-2 Charging-potential plot of graphene edges 101
Figure 6-3 Electrostatic potential drop in electrodes 104
Figure 6-4 EDL capacitance of graphene edges from CMD 106
Figure 6-5 Ion density profiles 107
Figure 6-6 Potential drop contribution 109
Figure S6-1 CMD snapshots 116
Figure S6-2 Structures of armchair edges with different thickness 116
Figure S6-3 Structures of zigzag edges with different thickness 117
Figure S6-4 DOS of armchair edges 118
Figure S6-5 DOS of zigzag edges 119
Figure S6-6 Excess charge distribution in electrodes 120
Figure 7-1 Structure of 2D boron sheets 125
Figure 7-2 Total DOS of 2D boron sheets 126
Figure 7-3 Electrode and electrolyte charge distribution 129
Figure 7-4 Charge-potential plot 130
Figure 7-5 Differential capacitance of 2D boron sheets 131
Figure 7-6 Integral capacitance of 2D boron sheets and graphene 131
Figure S7-1 Solvation model test on charging simulation 139
Figure S7-2 Quantum capacitance of 2D boron sheets 140
Figure 8-1 Structure of RuO_2 (110) 145
Figure 8-2 Scheme of capacitive behavior simulation 146
Figure 8-3 EDL capacitance of RuO_2 (110) 148

Figure 8-4 DOS of RuO_2 (110) 149
Figure 8-5 EDL energy and hydrogen adsorption energy 151
Figure 8-6 Charging curve and differential capacitance 152
Figure 8-7 H adsorption structures on RuO_2 (110) 155
Figure S8-1 DOS of H atom in RuO_2-3H 162
Figure S8-2 Crystal structure of RuO_2 163
Figure S8-3 Specific capacitance of RuO_2 165
Figure 9-1 Structure of $Ti_3C_2T_x$ 169
Figure 9-2 Gibbs free energy at different electrode potential 174
Figure 9-3 H coverage and surface net charge at different potential 174
Figure 9-4 Differential capacitance 176
Figure 9-5 DOS of charged $Ti_3C_2T_x$ 177
Figure 9-6 Planar charge distribution 178
Figure S9-1 Structure of $Ti_3C_2T_x$ with different H coverage 184
Figure S9-2 Linear fit of E(x) and PZC 185
Figure S9-3 Gaussian function g(x) 186
Figure S9-4 H coverage distribution at different electrode potentials 186
Figure S9-5 DFT-optimized lattice parameter 187
Figure S9-6 Bader charge and valance change of Ti 187

Chapter 1. Introduction

1.1 Basics of capacitive energy storage

The wide adoption of renewable energy, in the form of solar and wind energy, combined with the electrification of transportation and the proliferation of mobile devices are all driving the need for efficient, cost-effective electric energy storage devices in sizes ranging from hand-held to grid-based. The most commonly used energy storage devices are batteries and supercapacitors. A battery stores energy by bulk redox/intercalation reactions, while a supercapacitor stores energy through surface ion-adsorption or surface redox/intercalation reactions. A battery has high energy density but low power density, while a supercapacitor boasts of high power density due to the fast surface physical and chemical processes.[1] The global supercapacitor market was $1.2B in 2014 and by some estimates will grow over 20% per year to more than $7B in 2023.[2] There are two main types of supercapacitors: electric double-layer capacitors (EDLCs) store electrical energy through formation of electric double layer at the electrode/electrolyte interface, while pseudocapacitors store electrical energy by reversible surface redox reaction or ion intercalation. EDLCs, pseudocapacitors, and batteries exhibit distinctly different electrochemical behavior in cyclic voltammetry (CV).[3]

1.2 Operating mechanism of electric double-layer capacitors

1.2.1 The Helmholtz model of an electric double layer

In EDLCs, electrical energy is stored by the formation of an EDL through the counter ion adsorption at the electrode surface. The concept of the EDL originated from the interfacial double layer model in classical surface physical chemistry, first proposed by

Hermann von Helmholtz in 1853.[4] Thus, it is also known as the "Helmholtz Layer", formed by the co-ion exclusion and counter-ion adsorption. According to the Helmholtz model, the differential capacitance of an EDL can be computed by:

$$C = \frac{\varepsilon_r \varepsilon_0 A}{d} \ , \qquad 1\text{-}1$$

where A is the area of the electrode, ε_r is the dielectric constant of the electrolyte solvent, ε_0 is vacuum permittivity, and d is the thickness of the Helmholtz layer. Note that this is independent of applied voltage or properties of the electrolyte other than the solvent dielectric constant.

We can use Eq.1-1 to estimate the areal capacitance ($C_d = C/A$) for a planar electrode. Generally speaking, the value of d in aqueous electrolytes is several angstroms. Here we assume d=0.3 nm, the value of ε_r should be about 6 instead of 80 for water in a high electric field.[5] Thus, C_d is about 18 μF/cm^2, in good agreement with the average reported values for aqueous electrolyte EDLCs (~15 μF/cm^2).[6] Ionic liquids (IL) usually have a dielectric constant about 10, but their sizes tend to be larger, so we estimate their C_d to be about 10 μF/cm^2, very close to experimental measurement of ~11 μF/cm^2.[6]

1.2.2 The Gouy-Chapman model and beyond

Between 1910 and 1913, Gouy and Chapman derived, independently, an improved model for differential capacitance, which exhibits dependence on electrode voltage and ionic concentration. The "Gouy-Chapman" (GC) model introduced the diffuse layer, which describes the ion charge distribution as a function of distance to the electrode surface, and the Maxwell–Boltzmann statistics to account for the thermal effect. In 1924, Stern proposed combining the Helmholtz model with the Gouy-Chapman model to describe the

electrode/electrolyte interface: a subset of the ions with finite size absorb on surface to form the "Stern Layer", while others form the Gouy-Chapman diffuse layer. This model is known as the "Gouy-Chapman-Stern" (GCS) model.[7] The GCS model gives a more general description of the electrode/electrolyte interfacial behavior, but is highly simplified. For example, the diffusive ions in the GCS model are treated as point charges. Thus, important ionic features that influence capacitance, such as radii and valences, are ignored. A more rigorous model is necessary, especially for systems utilizing an ionic liquid electrolyte where the diffuse layer and ion steric effect have large influence on the charge capacitive behavior.

In 2007, Kornyshev proposed a model to describe the interfacial capacitance of the metal/ionic liquid system by solving the "Poisson-Fermi" equation, which treats the electrolyte by a mean-field lattice-gas model.[8] They derived an analytical expression for the differential capacitance:

$$C = C_0 \cdot \frac{\cosh(\frac{u_0}{2})}{1+2\gamma sinh^2(\frac{u_0}{2})} \cdot \sqrt{\frac{2\gamma sinh^2(\frac{u_0}{2})}{\ln(1+2\gamma sinh^2(\frac{u_0}{2}))}} \quad , \qquad 1\text{-}2$$

where γ is reduced concentration of ions, C_0 is the linear Gouy-Chapman capacitance defined by $C_0 = \epsilon/4\pi L_D$, L_D is the Debye length, and u_0 is surface electric potential in reduced unit. They found that when the concentration changes from high to low, the differential capacitance curve changes from the "bell" shape to the "Bactrian-camel" shape , due to the competition between Stern layer and diffuse layer, which cannot be captured by the traditional GCS model. This analytical method provides a clear physical picture for the interfacial capacitive behavior. Moreover, this theory has been improved recently by

adding the short-range correlation for the ionic liquid electrolyte.[9] Independently, Bazant *et al.* derived the same analytical solution (Eq. 2) from solving a modified Poisson-Nernst-Planck (MPNP) equation to describe the ion transport during dynamic charging at large bias voltage.[10, 11]

1.3 An estimate of how many ions need to be separated when charging an EDLC

An EDLC consists of two symmetric porous electrodes sandwiching a separator, with the electrolyte stored mainly inside the pore volumes of the electrodes (for a commercial device, volume contribution from the separator is negligible). When charged up, the ions separate and form two separate EDLs at the two opposite electrodes (Figure 1-1). A typical organic-electrolyte, activated-carbon-electrode EDLC has a specific capacitance of about 100 F/g based on the weight of carbon. Suppose 1 g of carbon for the positive electrode is charged to 1.5 V, while 1g of carbon for the negative electrode is charged to -1.5 V. This leads to a surface charge of +150 C on the positive electrode and -150 C on the negative electrode. The typical pore volume of activated carbon is 0.90 cm^3/g and a typical concentration of an organic electrolyte is 1 M of tetraethylammonium tetrafluoborate ($TEABF_4$) in acetonitrile or propylene carbonate. Hence the total numbers of available ions in this EDLC are 170 C of cations and 170 C of anions. In other words, ion separation is essentially complete when the EDLC is fully charged: all anions move to the positive electrode, while all cations move to the negative electrode. The typical thickness of an EDLC electrode is about 200 μm coated on two sides of a current collector (such as Al foil), so the typical length of ions traveled during cycling of an EDLC should

be about 100 μm. Thickness of a typical separator is about 40 μm, so we have neglected it in this simple estimate.

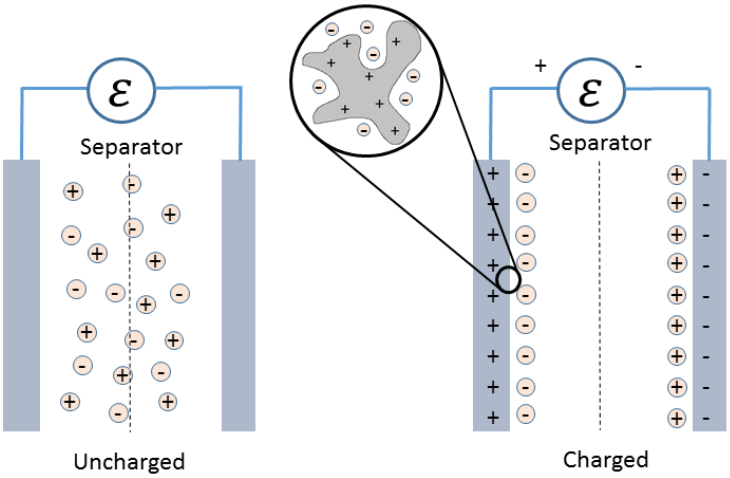


Figure 1-1. Schematic of an EDLC consists of two planar electrodes in an electrochemical cell.

1.4 Recent experimental advances in EDLCs

The most widely used electrode materials for EDLCs are porous carbon-based materials,[12, 13] such as activated graphene oxide,[14] activated carbons (AC),[15] carbide-derived carbons (CDC),[16-18] carbon nanotubes (CNT),[19-21] onion-like carbons (OLC)[22, 23] and graphene.[24, 25] The gravimetric capacitance of these carbon materials is sensitive to their structure, especially the porosity and specific surface area (SSA). The pore size can also greatly affect the ion partitioning and packing inside the pores, which causes a large change in capacitance. The relationship between the pore size and the capacitance of ionic liquids has been investigated experimentally by Simon and Gogotsi.[26-28] This important work reveals the pore size-dependent capacitance and suggests that the capacitance maximum can be achieved by optimally matching the pore size and ion size. Carbon nanotubes (CNT) have been reported for use in novel EDLCs electrode materials.[29, 30] The

reported capacitance of single-wall carbon nanotube (SWCNT) is 180 F/g (or ~14 $\mu F/cm^2$) with an aqueous electrolyte,[20] and the SSA is estimated to be 1315 m^2/g.[31] Onion-like carbons have also been reported as promising EDLC electrode materials exhibiting very large power density at discharging rate of up to 200 V/s.[22, 32] Moreover, graphene's unique electronic structure has large influence on the charge capacitive behavior.[15, 24]

1.5 Experimental techniques for characterizing EDL

Characterizing the EDL with various experimental techniques is important in both revealing the underlying physics and validating the theoretical predictions and simulations. Within the Fluid Interface Reaction Structure and Transport (FIRST) Energy Frontier Research Center (EFRC), funded by the U.S. Department of Energy,[33] computational/theoretical modeling methods are combined with complementary experimental characterization tools that probe similar spatial and/or temporal scales, as shown in Figure 1-2. Among the experimental methods, Quasi-Elastic Neutron Scattering (QENS) is an effective technique to study microscopic dynamics on the time scale of pico-seconds to nano-seconds for spatially constrained diffusion and long-range translational diffusion of ions inside porous carbons.[34, 35] Another important tool to probe the solid/liquid interfacial structure on a flat substrate is X-ray reflectivity, which can provide the structural change of the electrolyte at the interface with sub-angstrom resolution and under applied potential.[36-38]

Electrochemical Strain Microscopy has been developed within the FIRST Center to explore dynamic electrochemical processes, such as voltage-controlled ion transport, intercalation and local electrochemical reactivity at the nanometer and meso scales. In

particular, for the intercalation process, Electrochemical Strain Microscopy can clearly measure ion dynamics and electrode structure changes, such as expansion and distortion.[39-42] Nuclear Magnetic Resonance (NMR)[43, 44] could measure the structure of ion sorption and configuration in supercapacitor electrodes. In addition, it is also able to provide the picture of ion dynamics in supercapacitor.[45] Scanning Probe Microscopy (SPM) can directly measure the structure of EDL through the AFM tip that approaches the surface. By measuring the force during the surface scanning, one can obtain the exact structure of EDL, such as the oscillating ion distribution.[39, 46-48] Other experimental probes, not shown in Figure 1-2, useful for characterizing EDLs include Sum Frequency Generation (SFG)[49] and Second Harmonic Generation (SHG)[50], which can provide the structural information of carbon at interface, such as molecular vibration and bond stretching. Infrared Spectroscopy (IRS) and Scanning Transmission Electron Microscope (STEM) are also used to solve for and visualize the structure at interfaces without measuring dynamic information.

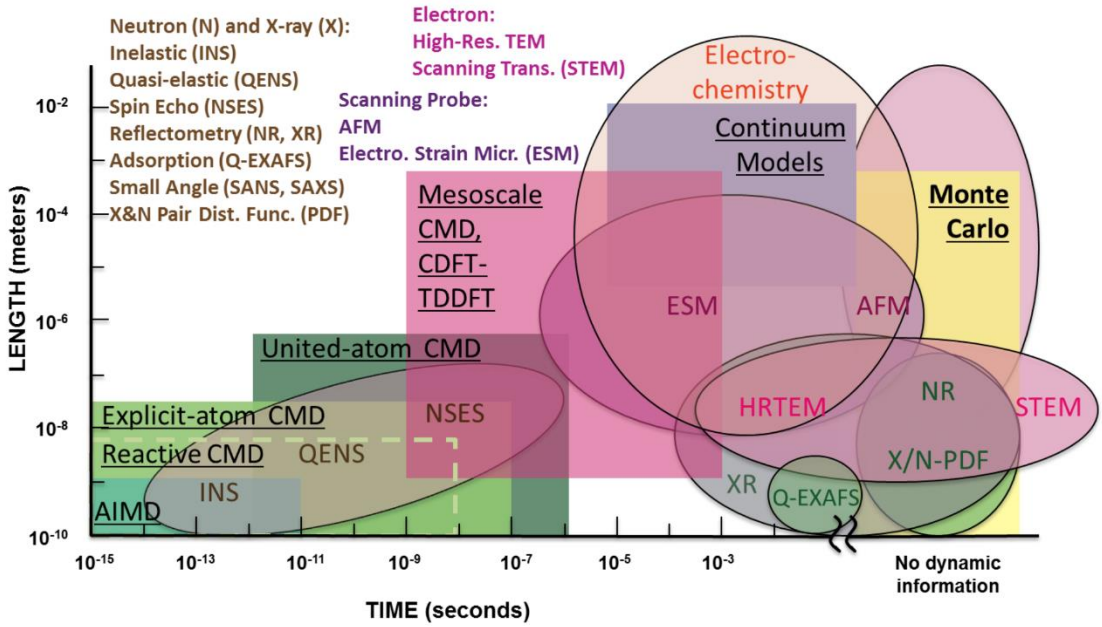


Figure 1-2. The length and time scales of different simulation and experimental techniques.

1.6 Important issues in capacitive energy storage

For capacitors, the most urgent issue is to improve their energy density (generally speaking, the energy density of supercapacitor is below 10 Wh kg^{-1}, while battery could possess the energy density over 100 Wh kg^{-1}) so that they can better compete with batteries.[1] To design materials and interfaces for EDLCs with higher energy density requires a deeper understanding of the factors and contributions affecting the total capacitance of an EDLC.

1.6.1 Classical vs. quantum capacitance

From conventional EDL theory, the capacitance of EDLCs stems from the adsorption of counter-ion at the charged electrode surface. This electrolyte response induced capacitance can be obtained from classical thermodynamics and electrostatics.[8, 51] Thus, we refer to it as "classical capacitance", which is not explicitly dependent on the

electronic state of electrodes. The macroscopic electrode potential is related to the electron chemical potential μ_e. For an ideal metal electrode, which has extremely large electronic density of states (DOS), adding or removing few electrons does not cause a significant shift in μ_e (Figure 1-3a). Thus, the macroscopic electrode potential change is dominated by the surface potential drop of the EDL. However, a small electronic DOS at the Fermi level could result in an additional significant potential drop when adding or removing the same amount of electrons from the electrode (Figure 1-3b). This capacitance due to the electronic structure of the electrode being a poor metal is called quantum capacitance (C_Q), which is especially important for graphene. Different from C_Q, the capacitance caused by electrolyte response and EDL formation is defined as EDL capacitance (C_{EDL}), which is not explicitly dependent on the electronic property of electrode.

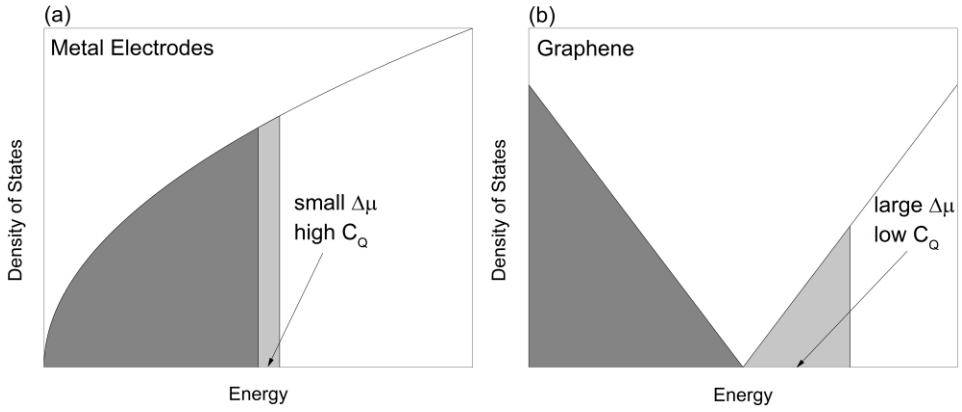


Figure 1-3. Different electrode-charging behaviors: (a) metal and (b) graphene electrodes. With the same amount of excess charge, graphene could exhibit significantly larger shift in the Fermi level ($\Delta\mu$) than a typical metal.

1.6.2 Pore size, surface area, pore geometry

Experimental studies have shown that optimal pore size is related to ion size and can result in a maximum in the capacitance.[26, 27] Theoretical calculations and molecular

simulations also verified this phenomenon and predicted that capacitance oscillates with pore size for ionic liquids inside an ideal slit pore.[51, 52] However, treating a porous carbon as a single slit pore is problematic because pore size is not uniform in a real porous carbon, which can exhibit complex features such as a broad distribution and/or a bimodal distribution. These complexities make such systems difficult to model. In particular, ion accessibility and selectivity in a distribution of nanopores could have a significant impact on the macroscopic capacitance.

Specific surface area (SSA) and pore geometry are also important factors in determining EDLC performance. For a flat single layer graphene in contact with electrolyte on both sides, the theoretical SSA is about 2630 m^2/g. However, in porous carbon, the SSA is strongly related to the pore geometry. In particular, the curvature is important in porous carbons dominated by micropores.[53] Numerical simulation of the Poisson-Boltzmann (PB) equation has shown that the capacitance of a cylindrical or spherical electrode is radius (R_0)-dependent when R_0 is small; for large R_0, the capacitance approaches that of a planar electrode.[54] However, an electrode composed of real porous carbon is not in an ideal geometry such as planar, cylindrical or spherical. Thus, the pore size, SSA and pore geometry are coupled together.

1.6.3 Electrolytes

The capacitance can be effectively modified by changing the ion size, valence, and concentration in the electrolyte, which calls for guidance from simulations. For ionic liquids, the cation and anion are usually different in size. As a result, the charging behavior on the two electrodes become asymmetric, as is observed experimentally.[55] Moreover,

solvent is also very important to the energy density of supercapacitor since, for example, it dictates the electrochemical window. Organic solvents offer electrochemical windows up to 3V. Aqueous electrolytes usually have higher capacitance than ionic liquid, but suffer from narrow voltage window of about 1.2V. In addition, the capacitance depends on the scan rate and a promising EDLC is also expected to have large capacitance at fast charging/discharging rate. This requires fast ion transport in response to the electrode charge. The time-dependent charging behavior can in principle be simulated by molecular dynamics (MD) or solving the Poisson-Nernst-Planck (PNP) equation, but difference of many orders of magnitude exists between the simulated time scale (on the order of ns to μs) and the experimental scan rate (seconds).[10, 11, 56] A multiscale approach is needed to bridge the gap.

1.6.4 Defects and functional groups on carbon

Introducing surface defects (both physical and topological defects) could change the surface structure, atomic bonding and SSA, hence the EDL structure and capacitance.[57] Simulations need to take into account changes on both the electrode's electronic structure and the EDL structure.[58] Functionalization is another effective way to modify the graphene electrode and improve the capacitive performance. The mechanism of how functional group influences capacitance can be more complicated than surface defect effect due to the possible redox reaction caused by functional groups. When the functional group is introduced on a graphene electrode, the electronic structure change is likely to cause the C_Q to change, and the interaction between functional group and electrolyte could influence

the EDL structure and C_{EDL}. Some oxygen or nitrogen contained groups have redox reactivity that can make the capacitive mechanism change from EDL to pseudocapacitive.

1.6.5 EDLC vs. pseudocapacitor

The methods to model EDLCs have been well developed. However, currently there is no appropriate method for modeling pseudocapacitance due to the complexity of interfacial redox processes. During the charging process of a pseudocapacitor, the pseudocapacitance can be affected by many factors, such as the diffusing behavior of reactant species, EDL at interface, and surface redox kinetics. These issues are difficult to be self-consistently captured in the same model. So developing a feasible model to capture the pseudocapacitance is urgently needed.

References

(1) Simon, P.; Gogotsi, Y. Materials for electrochemical capacitors. *Nat. Mater.* **2008**, 7, 845-854

(2) Supercapacitor Market to Reach $7.4B by 2023. *https://epsnews.com/2016/01/13/supercapacitor-market-to-reach-7-4b-by-2023/*

(3) Lukatskaya, M. R.; Dunn, B.; Gogotsi, Y. Multidimensional materials and device architectures for future hybrid energy storage. *Nat. Commun.* **2016**, 7, 12647

(4) Helmholtz, H. Ueber einige Gesetze der Vertheilung elektrischer Ströme in körperlichen Leitern mit Anwendung auf die thierisch-elektrischen Versuche. *Ann. Phys. Chem.* **1853**, 89, 211–233

(5) Yeh, I. C.; Berkowitz, M. L. Dielectric constant of water at high electric fields: Molecular dynamics study. *J. Chem. Phys.* **1999**, 110, 7935-7942

(6) Nanjundiah, C.; McDevitt, S. F.; Koch, V. R. Differential capacitance measurements in solvent-free ionic liquids at Hg and C interfaces. *J. Electrochem. Soc.* **1997**, 144, 3392-3397

(7) Stern, O. Z. Stern layer. *Electrochem* **1924**, 30, 508

(8) Kornyshev, A. A. Double-Layer in Ionic Liquids: Paradigm Change? *J. Phys. Chem. B* **2007**, 111, 5545-5557

(9) Goodwin, Z. A.; Feng, G.; Kornyshev, A. A. Mean-Field Theory of Electrical Double Layer In Ionic Liquids with Account of Short-Range Correlations. *Electrochim. Acta* **2016**, 225, 190-197

(10) Kilic, M. S.; Bazant, M. Z.; Ajdari, A. Steric effects in the dynamics of electrolytes at large applied voltages. II. Modified Poisson-Nernst-Planck equations. *Phys. Rev. E* **2007**, 75, 021503

(11) Kilic, M. S.; Bazant, M. Z.; Ajdari, A. Steric effects in the dynamics of electrolytes at large applied voltages. I. Double-layer charging. *Phys. Rev. E* **2007**, 75, 021502

(12) Zhang, L. L.; Zhao, X. S. Carbon-based materials as supercapacitor electrodes. *Chem. Soc. Rev.* **2009**, 38, 2520-2531

(13) Zhai, Y. P.; Dou, Y. Q.; Zhao, D. Y.; Fulvio, P. F.; Mayes, R. T.; Dai, S. Carbon materials for chemical capacitive energy storage. *Adv. Mater.* **2011**, 23, 4828-4850

(14) Wang, D. W.; Li, F.; Liu, M.; Lu, G. Q.; Cheng, H. M. 3D aperiodic hierarchical porous graphitic carbon material for high-rate electrochemical capacitive energy storage. *Angew. Chem., Int. Ed.* **2008**, 47, 373-376

(15) Zhu, Y. W.; Murali, S.; Stoller, M. D.; Ganesh, K. J.; Cai, W. W.; Ferreira, P. J.; Pirkle, A.; Wallace, R. M.; Cychosz, K. A.; Thommes, M., et al. Carbon-Based Supercapacitors Produced by Activation of Graphene. *Science* **2011**, 332, 1537-1541

(16) Chmiola, J.; Largeot, C.; Taberna, P. L.; Simon, P.; Gogotsi, Y. Monolithic Carbide-Derived Carbon Films for Micro-Supercapacitors. *Science* **2010**, 328, 480-483

(17) Gogotsi, Y.; Nikitin, A.; Ye, H. H.; Zhou, W.; Fischer, J. E.; Yi, B.; Foley, H. C.; Barsoum, M. W. Nanoporous carbide-derived carbon with tunable pore size. *Nat. Mater.* **2003**, 2, 591-594

(18) Dash, R.; Chmiola, J.; Yushin, G.; Gogotsi, Y.; Laudisio, G.; Singer, J.; Fischer, J.; Kucheyev, S. Titanium carbide derived nanoporous carbon for energy-related applications. *Carbon* **2006**, 44, 2489-2497

(19) Hu, S.; Rajamani, R.; Yu, X. Flexible solid-state paper based carbon nanotube supercapacitor. *Appl. Phys. Lett.* **2012**, 100, 104103

(20) An, K. H.; Kim, W. S.; Park, Y. S.; Moon, J. M.; Bae, D. J.; Lim, S. C.; Lee, Y. S.; Lee, Y. H. Electrochemical properties of high-power supercapacitors using single-walled carbon nanotube electrodes. *Adv. Funct. Mater.* **2001**, 11, 387-392

(21) Yu, C. J.; Masarapu, C.; Rong, J. P.; Wei, B. Q.; Jiang, H. Q. Stretchable Supercapacitors Based on Buckled Single-Walled Carbon Nanotube Macrofilms. *Adv. Mater.* **2009**, 21, 4793-4797

(22) Pech, D.; Brunet, M.; Durou, H.; Huang, P. H.; Mochalin, V.; Gogotsi, Y.; Taberna, P. L.; Simon, P. Ultrahigh-power micrometre-sized supercapacitors based on onion-like carbon. *Nat. Nanotechnol.* **2010**, 5, 651-654

(23) Portet, C.; Yushin, G.; Gogotsi, Y. Electrochemical performance of carbon onions, nanodiamonds, carbon black and multiwalled nanotubes in electrical double layer capacitors. *Carbon* **2007**, 45, 2511-2518

(24) Stoller, M. D.; Park, S. J.; Zhu, Y. W.; An, J. H.; Ruoff, R. S. Graphene-based ultracapacitors. *Nano Lett.* **2008**, 8, 3498-3502

(25) Liu, C. G.; Yu, Z. N.; Neff, D.; Zhamu, A.; Jang, B. Z. Graphene-Based Supercapacitor with an Ultrahigh Energy Density. *Nano Lett.* **2010**, 10, 4863-4868

(26) Chmiola, J.; Yushin, G.; Gogotsi, Y.; Portet, C.; Simon, P.; Taberna, P. L. Anomalous increase in carbon capacitance at pore sizes less than 1 nanometer. *Science* **2006**, 313, 1760-1763

(27) Largeot, C.; Portet, C.; Chmiola, J.; Taberna, P. L.; Gogotsi, Y.; Simon, P. Relation between the ion size and pore size for an electric double-layer capacitor. *J. Am. Chem. Soc.* **2008**, 130, 2730-2731

(28) Chmiola, J.; Largeot, C.; Taberna, P. L.; Simon, P.; Gogotsi, Y. Desolvation of ions in subnanometer pores and its effect on capacitance and double-layer theory. *Angew. Chem., Int. Ed.* **2008**, 47, 3392-3395

(29) Collins, P. G.; Bradley, K.; Ishigami, M.; Zettl, A. Extreme oxygen sensitivity of electronic properties of carbon nanotubes. *Science* **2000**, 287, 1801-1804

(30) Baughman, R. H.; Zakhidov, A. A.; de Heer, W. A. Carbon nanotubes - the route toward applications. *Science* **2002**, 297, 787-792

(31) Peigney, A.; Laurent, C.; Flahaut, E.; Bacsa, R. R.; Rousset, A. Specific surface area of carbon nanotubes and bundles of carbon nanotubes. *Carbon* **2001**, 39, 507-514

(32) Gao, Y.; Zhou, Y. S.; Qian, M.; He, X. N.; Redepenning, J.; Goodman, P.; Li, H. M.; Jiang, L.; Lu, Y. F. Chemical activation of carbon nano-onions for high-rate supercapacitor electrodes. *Carbon* **2013**, 51, 52-58

(33) *http://web.ornl.gov/sci/first/index.shtml*

(34) Chathoth, S. M.; Mamontov, E.; Kolesnikov, A. I.; Gogotsi, Y.; Wesolowski, D. J. Quasielastic neutron scattering study of water confined in carbon nanopores. *EPL (Europhys. Lett.)* **2011**, 95, 56001

(35) Osti, N. C.; Cote, A.; Mamontov, E.; Ramirez-Cuesta, A.; Wesolowski, D. J.; Diallo, S. O. Characteristic features of water dynamics in restricted geometries investigated with quasi-elastic neutron scattering. *Chem. Phys.* **2016**, 465, 1-8

(36) Fears, T. M.; Doucet, M.; Browning, J. F.; Baldwin, J. K. S.; Winiarz, J. G.; Kaiser, H.; Taub, H.; Sacci, R. L.; Veith, G. M. Evaluating the solid electrolyte interphase formed on silicon electrodes: a comparison of ex situ X-ray photoelectron spectroscopy and in situ neutron reflectometry. *Phys. Chem. Chem. Phys.* **2016**, 18, 13927-13940

(37) Li, S.; Banuelos, J. L.; Guo, J.; Anovitz, L.; Rother, G.; Shaw, R. W.; Hillesheim, P. C.; Dai, S.; Baker, G. A.; Cummings, P. T. Alkyl Chain Length and Temperature Effects on Structural Properties of Pyrrolidinium-Based Ionic Liquids: A Combined Atomistic Simulation and Small-Angle X-ray Scattering Study. *J. Phys. Chem. Lett.* **2012**, 3, 125-130

(38) Lin, Z. F.; Rozier, P.; Duployer, B.; Taberna, P. L.; Anasori, B.; Gogotsi, Y.; Simon, P. Electrochemical and In-situ X-ray Diffraction Studies of $Ti_3C_2T_x$ MXene in Ionic Liquid Electrolyte. *Electrochem. Commun.* **2016**, 72, 50-53

(39) Black, J. M.; Feng, G.; Fulvio, P. F.; Hillesheim, P. C.; Dai, S.; Gogotsi, Y.; Cummings, P. T.; Kalinin, S. V.; Balke, N. Strain-Based In Situ Study of Anion and Cation Insertion into Porous Carbon Electrodes with Different Pore Sizes. *Adv. Energy Mater.* **2014**, 4, 1300683

(40) Black, J. M.; Okatan, M. B.; Feng, G.; Cummings, P. T.; Kalinin, S. V.; Balke, N. Topological defects in electric double layers of ionic liquids at carbon interfaces. *Nano Energy* **2015**, 15, 737-745

(41) Black, J. M.; Walters, D.; Labuda, A.; Feng, G.; Hillesheim, P. C.; Dai, S.; Cummings, P. T.; Kalinin, S. V.; Proksch, R.; Balke, N. Bias-Dependent Molecular-Level Structure of Electrical Double Layer in Ionic Liquid on Graphite. *Nano Lett.* **2013**, 13, 5954-5960

(42) Black, J. M.; Zhu, M. Y.; Zhang, P. F.; Unocic, R. R.; Guo, D. Q.; Okatan, M. B.; Dai, S.; Cummings, P. T.; Kalinin, S. V.; Feng, G., et al. Fundamental aspects of electric double layer force-distance measurements at liquid-solid interfaces using atomic force microscopy. *Sci. Rep.* **2016**, 6,

(43) Deschamps, M.; Gilbert, E.; Azais, P.; Raymundo-Pinero, E.; Ammar, M. R.; Simon, P.; Massiot, D.; Beguin, F. Exploring electrolyte organization in supercapacitor electrodes with solid-state NMR. *Nat. Mater.* **2013**, 12, 351-358

(44) Blanc, F.; Leskes, M.; Grey, C. P. In Situ Solid-State NMR Spectroscopy of Electrochemical Cells: Batteries, Supercapacitors, and Fuel Cells. *Acc. Chem. Res.* **2013**, 46, 1952-1963

(45) Forse, A. C.; Griffin, J. M.; Merlet, C.; Carretero-Gonzalez, J.; Raji, A. R. O.; Trease, N. M.; Grey, C. P. Direct observation of ion dynamics in supercapacitor electrodes using in situ diffusion NMR spectroscopy. *Nat. Energy* **2017**, 2, 16216

(46) Chung, D. W.; Balke, N.; Kalinin, S. V.; Garcia, R. E. Virtual Electrochemical Strain Microscopy of Polycrystalline LiCoO2 Films. *J. Electrochem. Soc.* **2011**, 158, A1083-A1089

(47) Jesse, S.; Balke, N.; Eliseev, E.; Tselev, A.; Dudney, N. J.; Morozovska, A. N.; Kalinin, S. V. Direct Mapping of Ionic Transport in a Si Anode on the Nanoscale: Time Domain Electrochemical Strain Spectroscopy Study. *Acs Nano* **2011**, 5, 9682-9695

(48) Morozovska, A. N.; Eliseev, E. A.; Balke, N.; Kalinin, S. V. Local probing of ionic diffusion by electrochemical strain microscopy: Spatial resolution and signal formation mechanisms. *J. Appl. Phys.* **2010**, 108, 053712

(49) Achtyl, J. L.; Vlassiouk, I. V.; Dai, S.; Geiger, F. Interactions of Organic Solvents at Graphene/alpha-Al2O3 and Graphene Oxide/alpha-Al2O3 Interfaces Studied by Sum Frequency Generation. *J. Phys. Chem. C* **2014**, 118, 17745-17755

(50) Achtyl, J. L.; Vlassiouk, I. V.; Surwade, S. P.; Fulvio, P. F.; Dai, S.; Geiger, F. M. Interaction of Magnesium Ions with Pristine Single-Layer and Defected Graphene/Water Interfaces Studied by Second Harmonic Generation. *J. Phys. Chem. B* **2014**, 118, 7739-7749

(51) Jiang, D. E.; Jin, Z. H.; Wu, J. Z. Oscillation of Capacitance inside Nanopores. *Nano Lett.* **2011**, 11, 5373-5377

(52) Feng, G.; Cummings, P. T. Supercapacitor Capacitance Exhibits Oscillatory Behavior as a Function of Nanopore Size. *J. Phys. Chem. Lett.* **2011**, 2, 2859-2864

(53) Lian, C.; Jiang, D. E.; Liu, H. L.; Wu, J. Z. A Generic Model for Electric Double Layers in Porous Electrodes. *J. Phys. Chem. C* **2016**, 120, 8704-8710

(54) Wang, H. N.; Pilon, L. Accurate Simulations of Electric Double Layer Capacitance of Ultramicroelectrodes. *J. Phys. Chem. C* **2011**, 115, 16711-16719

(55) Van Aken, K. L.; Beidaghi, M.; Gogotsi, Y. Formulation of Ionic-Liquid Electrolyte To Expand the Voltage Window of Supercapacitors. *Angew. Chem., Int. Ed.* **2015**, 54, 4806-4809

(56) He, Y. D.; Qiao, R.; Vatamanu, J.; Borodin, O.; Bedrov, D.; Huang, J. S.; Sumpter, B. G. Importance of Ion Packing on the Dynamics of Ionic Liquids during Micropore Charging. *J. Phys. Chem. Lett.* **2016**, 7, 36-42

(57) Chen, J. F.; Han, Y. L.; Kong, X. H.; Deng, X. Z.; Park, H. J.; Guo, Y. L.; Jin, S.; Qi, Z. K.; Lee, Z.; Qiao, Z. H., et al. The Origin of Improved Electrical Double-Layer Capacitance by Inclusion of Topological Defects and Dopants in Graphene for Supercapacitors. *Angew. Chem. Int. Edit.* **2016**, 55, 13822-13827

(58) Pak, A. J.; Paek, E.; Hwang, G. S. Tailoring the performance of graphene-based supercapacitors using topological defects: A theoretical assessment. *Carbon* **2014**, 68, 734-741

Chapter 2. Simulation methods used in supercapacitor modeling

2.1 Classical molecular methods to simulate EDLCs

In this section, we briefly review the most commonly used classical molecular simulation methods to simulate EDL and EDLCs. These include classical density functional theory (CDFT), classical molecular dynamics (CMD), and grand canonical Monte Carlo (GCMC). In both CDFT and GCMC, coarse-grained models are commonly used for the electrolyte, while in CMD all-atom models are usually employed.

2.1.1 Coarse-grained classical density functional theory

CDFT is a powerful method to simulate the equilibrium properties of complex liquids and soft materials. Both primitive and non-primitive coarse-grained models are employed to represent the ionic species, impurities, and solvent molecules in the electrolyte solution.[1] The model system consists of charged hard spheres for ionic species and a hard-sphere dimer for solvent molecules. CDFT was used to simulate the EDL structure and capacitance for the electrolyte solution in various pore geometries.[2-6] The details of the CDFT calculations have been published before.[7-10] The density profiles of cations, anions, impurities, and the solvent segments inside the pore can be obtained by minimization of the grand potential, given the number densities of ions and solvent molecules in the bulk, system temperature, pore size, pore geometry, and the surface electrical potential. To illustrate, we may consider an electrolyte system containing spherical cations and anions and solvent molecules represented by two tangentially connected spheres of opposite charge. The grand potential is given by[11]

$$\beta\Omega[\rho_M(R),\{\rho_a(r)\}] = \beta F[\rho_M(R),\{\rho_a(r)\}] + \int[\beta\Psi_M(R) - \beta\mu_M]\rho_M(R)dR + \sum_a \int[\beta\Psi_a(r) - \beta\mu_a]\rho_a(r)dr \quad , \qquad 2\text{-}1$$

where $\beta^{-1} = k_B T$, $R \equiv R(r_{\delta+}, r_{\delta-})$ represents two coordinates specifying the positions of two segments in each solvent molecule, μ_α is the chemical potential of an ionic species, μ_M is the chemical potential of the solvent, $\Psi_a(r)$ stands for the external potential for ions, and $\Psi_M(R)$ is the summation of the external potential for a solvent molecule. *F* is the total intrinsic Helmholtz energy

$$\beta F = \int[\ln \rho_M(R) - 1]\rho_M(R)dR + \beta \int V_b(R)\rho_M(R)dR + \sum_a \int[\ln \rho_a(r) - 1]\rho_a(r)dr + \beta F^{ex} \quad , \qquad 2\text{-}2$$

where V_b stands for the bonding potential of the solvent molecule and $F^{ex}$is the excess contribution due to intermolecular interactions. The detailed expression for each contribution and the numerical details can be found from a previous study.[1] The mean electrostatic potential can be obtained from the density distributions of the ions by using the Poisson equation. The surface charge density *Q* is obtained from the condition of overall charge neutrality. The differential capacitance C_d of the EDLs can be calculated as a derivative of the surface charge density *Q* with respect to the surface potential.

Time-dependent density functional theory (TDDFT) is an extension of the classical DFT to describe dynamic or time-dependent processes based on the assumption of local thermodynamic equilibrium.[12-14] For ion diffusion in an electrolyte solution near electrodes, TDDFT asserts that the time evolution for the local density profiles of ionic species, $\rho_i(r,t)$, follows the generalized diffusion equation

$$\frac{\partial \rho_i(r,t)}{\partial t} = \nabla \cdot \{D_i \rho_i(r,t) \nabla[\beta \mu_i(r,t) + \beta V_i(r)]\} \ , \qquad 2\text{-}3$$

where D_i stands for the self-diffusivity of ion i, $\mu_i(r,t)$ is the local chemical potential and could be obtained by a derivative of the intrinsic Helmholtz energy F with respect to the density, and $V_i(r)$ denotes the external potential arising from the electrodes. With TDDFT, one could examine the ion dynamics inside the nanopores.

2.1.2 Atomistic classical molecular dynamics

Atomistic molecular dynamics (MD) simulations have been broadly and effectively employed to investigate the structure of EDL and capacitance of EDLCs. The key for MD simulation to accurately capture the fundamental aspects of EDLCs relies on the model used for the electrode/electrolyte interface. When simulating the charged electrodes, currently there are two methodologies that have been developed: the constant charge method and the constant potential method. In the constant charge method, a partial charge (of equal value) is assigned to each atom on the electrode surface. The potential associated with each value of surface charging is calculated by solving Poisson's equation. Given its simplicity of implementation, the constant charge method has been widely adopted by researchers to simulate electrodes with simplified geometries, such as graphene basal planes,[15-19] carbon onions,[20] carbon nanotubes[21, 22] and slit pores.[23, 24] These studies provide insights into the charging mechanism of EDLCs, and the results match well with the experimental results in both capacitance and interfacial structures.[25]

The constant charge method neglects possible fluctuations and inhomogeneities in surface charges induced by electrolytes. The constant potential method overcomes this drawback and constrains a constant potential drop between the two electrodes by

redistributing the surface charge over the course of simulation. The charges on the electrode atoms fluctuate in order to satisfy the condition of minimizing the electrostatic energy of the system.[26-28] Researchers have compared these two different methods when simulating supercapacitors. Merlet and co-workers modeled a supercapacitor based on 1-butyl-3-methylimidazolium hexafluorophosphate (BMIM-PF6) and carbon electrodes, and found that both methods showed quite similar ionic density profiles at low potential drop for the planar surface.[29] Wang et al. modeled the $LiClO_4$-acetonitrile/graphite EDLCs and drew a similar conclusion.[30] However, in both studies, the structural difference becomes significant when the potential difference is high (over 5 V).[31] The constant potential method is computationally slower than the constant charge method,[29, 32, 33] but it allows MD simulations to explore more complex and inhomogeneous electrode systems, such as rough surfaces,[34-36] activated carbon[37] and amorphous CDCs,[38-40] where the constant-charge method is not really applicable.

Accurate force fields for the electrolyte are also necessary for MD simulations of EDLCs. Many force fields have been developed for RTILs, including coarse grained,[41-43] united-atom,[44-46] all-atom[47, 48] and polarizable force fields.[49-52] Coarse-grained force fields simplify the whole molecule into a few or even one bead, and are hence useful in reducing computational cost to capture long-time dynamic[39] and interfacial properties.[43, 44] But their lack of atomic details for the electrolyte molecule may limit the degree of agreement that can be achieved with experiments.[53] All-atom force fields provide a richer representation of the electrostatic interactions and molecule configurations in the EDL. However, the non-polarizable all-atom force fields for ionic liquids usually overestimate the ion-ion

interactions, resulting in smaller diffusion coefficients and higher viscosities compared with experimental results. Scaling partial charges has been considered as an effective way to compensate the polarization effect and recover diffusion coefficients and electrical conductivity.[54-58] Another solution is to use a polarizable force field. The inclusion of electronic polarizability has been shown to not only improve dynamic properties, but also reproduce local ion structures,[50, 59] but at an order of magnitude higher computational cost.[60]

2.1.3 Constant voltage Grand Canonical Monte Carlo

Kiyohara et al. developed a constant voltage GCMC to simulate an EDLC system with planar electrodes and coarse-grained ions.[61, 62] The Monte Carlo steps include ion insertion, deletion, migration and exchange in the electrolyte as well as charge balance and exchange among electrodes. Given the electrode setup, the bulk electrolyte activity, and the applied potential, many millions of MC steps are performed to reach the equilibrium. Then EDL structure, surface charge, and capacitance can be derived, similar to the process from the CDFT method. The oscillatory behavior in the capacitance of an ionic liquid electrolyte in a slit nanopore shown by CDFT and CMD simulations was successfully reproduced by constant voltage GCMC.[63, 64] Unlike the available CDFT method which is limited to simulate EDLC in one dimension (hence can treat only one pore size in a single simulation), the GCMC method is three-dimensional and can simulate a multiple-sized and more realistic porous electrode.

2.2 *Ab initio* simulations of the electrochemical interfaces

The role of electrode chemistry in EDLCs is important when the electrode is not an ideal metal or hard wall boundary. Generally speaking, the influence of electrode chemistry can be considered from two perspectives: "contact layer" effect and "quantum capacitance" effect. The former one comes from the electron-solvent repulsion at charged interface and could influence the structure and screening potential of electric double layer, as reported by Ando et al through *ab initio* MD,[65] while the latter one cause the additional electrode potential drop and decrease the total capacitance. In this review, we mainly focus on the quantum capacitance effect. The simplest way to capture the electrode chemistry in carbon-based electrodes is considering the quantum capacitance (C_Q), which has been briefly introduced in 1.6.1. One can compute C_{tot} by combining C_{EDL} from classical simulation with C_Q from electronic structure. The total electrode potential drop is calculated through summing up the potential drop contribution of C_Q and C_{EDL} at the same surface charge density.[18, 66] Methods have also been developed to capture the polarization effect (the electrostatic interaction between electrode and electrolyte) self-consistently at the electronic-structure level. Here, the electronic chemical potential shift $\Delta\mu_e$ is treated as the electrode potential drop and has contributions from band filling/emptying in the electrode and ionic screening in the electrolyte. Currently, there are two methods that can capture the electronic structure of the electrode in contact with the EDL: the effective screening medium (ESM) and joint density functional theory (JDFT).

2.2.1 Effective screening medium (ESM)

The original idea of ESM was proposed by Otani *et al*. to achieve first-principles calculation of charged surfaces and interfaces taking into account ionic screening.[67] In the ESM method an infinite dielectric medium was inserted at the boundary of the periodic cell that can ideally screen all the excessive charge in the periodic cell through setting a mirror charge at the dielectric boundary.[68] The position and dielectric constant of the ESM are adjustable, which can influence the electrostatic potential of the whole system. The total energy functional includes the electrostatic interaction between the electronic system and the ESM; the electrostatic potential is obtained by solving the Poisson equation. ESM can capture the polarization effect on the electrode from ionic screening of electrolyte. The thickness of the vacuum slab between the screening medium and the electrode is known, so the vacuum part can be regarded as a dielectric capacitor with $\epsilon_r = 1$ and $C_{vac} = \epsilon A/d$. Here, A is the surface area and d is the vacuum slab thickness. By subtracting the contribution of the vacuum slab from $\Delta\mu_e$, one can obtain the potential drop due to the electrode and then compute C_Q. However, there are still several limitations in ESM: first, the mirror charge in ESM cannot be used to describe the EDL in the electrolyte because the thermal behavior and ion diffusion are not included in the Poisson equation; second, the liquid response to the electrode charge cannot be captured in ESM. Thus, ESM is more applicable to study the electrode capacitive behavior.

2.2.2 Joint density functional theory (JDFT)

2.2.2.1 Theoretical framework

The concept of Joint Density Functional Theory (JDFT) was originally proposed by Arias, aimed at solving the solid/liquid interface self-consistently.[69] The philosophy of JDFT is treating the solute by electronic DFT and solvent by classical DFT. By minimizing the total free energy, one can obtain the equilibrium state of the solute/solvent system. The free energy functional in JDFT formalism can be written as:[70]

$$A_{JDFT}[n, \{N_\alpha\}, V(r)] = A_{HK}[n] + A_{lq}[\{N_\alpha\}] + \Delta A[n, \{N_\alpha\}, V(r)] \,. \quad 2\text{-}4$$

A_{HK} is the electronic energy functional from Hohenberg-Kohn Theorems and A_{lq} is the classical density functional of the liquid free energy.[70] ΔA is the coupling energy related to the interaction between solute (the electrode) and solvent (the liquid).

2.2.2.2 Implicit solvation and linear polarizable continuum model

Besides classical DFT, the solvation effect and the electrolyte response can be more easily described by implicit solvation with linear response approximation. For example, the total free energy functional of an electronic system solvated in the linear polarizable continuum model (Linear PCM) can be written as:[71]

$$A[n(r), \phi(r)] = A_{TXC}[n(r)] \; + \int d^3r \{\phi(r)[n(r) - N(r, \{Z_I, R_I\})] - \frac{\epsilon(r)}{8\pi}|\nabla\phi(r)|^2 - \frac{\epsilon_b \kappa^2(r)}{8\pi}[\phi(r)]^2\} \,. \quad 2\text{-}5$$

A_{TXC} is the single particle Kohn-Sham kinetic energy plus exchange-correlation energy. The second term on the right-hand side is the electrostatic energy of electron and nuclei in electrostatic field. The last two terms correspond to the energy of electric field in the

dielectric medium and the energy contributed by electrolyte ions described by the Debye-Hückel theory. In this equation, $n(r)$ is the electron density of the explicit system, $N(r,\{Z_I,R_I\})$ is the nuclei density and ϕ(r) is the total electrostatic potential including Hartree potential and solvation contribution. The local dielectric constant $\epsilon(r)$ and inverse Debye length $\kappa(r)$ are determined from the local solvent density, cavity function, bulk dielectric constant (ϵ_b) and the inverse Debye screening length in the bulk fluid (κ_b).[72] The equilibrium state of the solute/solvent system is given by minimizing the total free energy functional with respect to $n(r)$ and $\phi(r)$.[71] Advanced solvation models have been developed for JDFT, including non-local effects,[73] nonlinear dielectric response,[74] spherically averaged liquid susceptibility *ansatz* (SaLSA), and charge-asymmetric nonlocally determined local-electric (CANDLE) solvation model.[75, 76] SaLSA and CANDLE could capture the nonlocal dielectric response of polar solvent.[77]

2.2.2.3 Electrochemical simulation by JDFT and corresponding technical details

In a two-electrode electrochemical cell, the electrode potential $\mathcal{E}$ (the voltage) of the working electrode is defined by the energy required to move one electron from the working electrode (electronic chemical potential at μ^R) to the reference electrode (electronic chemical potential at μ^W): so $\mathcal{E} = \mu^R - \mu^W$ per the fundamental charge. If we choose zero potential as reference, then $\mathcal{E} = -\mu$. When the electrode in the simulation is neutral, the calculated μ is related to the potential of zero charge (PZC). By plotting the calculated PZC and experimental PZC of different metal surfaces, one can extrapolate the potential of standard hydrogen electrode (SHE).

The procedures of charge-potential curve simulation via JDFT are: (1) Build a slab model with the vacuum thickness larger than 10 Å to avoid inter-layer interaction; (2) Optimize the electrode structure (ionic and lattice optimization) via general electronic DFT code; (3) Specify a solvation model (Linear PCM, Non-linear PCM, SalSA, CANDLE etc.) and parameters (concentration, ion type, solvent etc.), then import the optimized electrode structure and run JDFT calculation. The calculated Fermi level is treated as the potential of zero charge and the zero potential reference $\mathcal{E} = -\mu$; (4) Transfer the target surface charge density or gravimetric charge density to unit cell charge, then redo the electronic structure calculation under the same solvation condition with target electrode charges; (5) By calculating the voltage $\mathcal{E}$ at various charge *Q*, one can plot the *Q*- $\mathcal{E}$ curve and calculate the capacitance by differentiating the curve. The parameters (both for electronic structure part and solvation part) used in our simulation are in the "method" section in each chapter, which can help readers to learn the JDFT code and reproduce my computation.

References

(1) Henderson, D.; Jiang, D. E.; Jin, Z. H.; Wu, J. Z. Application of Density Functional Theory To Study the Double Layer of an Electrolyte with an Explicit Dimer Model for the Solvent. *J. Phys. Chem. B* **2012**, 116, 11356-11361

(2) Evans, R. Nature of the Liquid-Vapor Interface and Other Topics in the Statistical-Mechanics of Nonuniform, Classical Fluids. *Adv. Phys.* **1979**, 28, 143-200

(3) Evans, R.; Oettel, M.; Roth, R.; Kahl, G. New developments in classical density functional theory. *J. Phys.: Condens. Matter* **2016**, 28, 240401

(4) Haghmoradi, A.; Wang, L.; Chapman, W. G. A density functional theory for colloids with two multiple bonding associating sites. *J. Phys.: Condens. Matter* **2016**, 28, 244009

(5) Wu, J. Z.; Li, Z. D. Density-functional theory for complex fluids. *Annu. Rev. Phys. Chem.* **2007**, 58, 85-112

(6) Lian, C.; Chen, X. Q.; Zhao, S. L.; Lv, W. J.; Han, X.; Wang, H. L.; Liu, H. L. Substrate Effect on the Phase Behavior of Polymer Brushes with Lattice Density Functional Theory. *Macromol. Theor. Simul.* **2014**, 23, 575-582

(7) Jiang, D. E.; Wu, J. Z. Microscopic Insights into the Electrochemical Behavior of Nonaqueous Electrolytes in Electric Double-Layer Capacitors. *J. Phys. Chem. Lett.* **2013**, 4, 1260-1267

(8) Jiang, D. E.; Jin, Z. H.; Henderson, D.; Wu, J. Z. Solvent Effect on the Pore-Size Dependence of an Organic Electrolyte Supercapacitor. *J. Phys. Chem. Lett.* **2012**, 3, 1727-1731

(9) Lian, C.; Liu, K.; Van Aken, K.; Gogotsi, Y.; Wesolowski, D.; Liu, H. L.; Jiang, D. E.; Wu, J. Z. Enhancing the Capacitive Performance of Electric Double-Layer Capacitors with Ionic Liquid Mixtures. *ACS Energy Lett.* **2016**, 1, 21-26

(10) Lian, C.; Jiang, D. E.; Liu, H. L.; Wu, J. Z. A Generic Model for Electric Double Layers in Porous Electrodes. *J. Phys. Chem. C* **2016**, 120, 8704-8710

(11) Jiang, D. E.; Wu, J. Z. Unusual effects of solvent polarity on capacitance for organic electrolytes in a nanoporous electrode. *Nanoscale* **2014**, 6, 5545-5550

(12) Archer, A. J. Dynamical density functional theory for molecular and colloidal fluids: A microscopic approach to fluid mechanics. *J. Chem. Phys.* **2009**, 130, 014509

(13) Zhao, S. L.; Wu, J. Z. Self-consistent equations governing the dynamics of nonequilibrium colloidal systems. *J. Chem. Phys.* **2011**, 134, 054514

(14) Lian, C.; Wang, L.; Chen, X. Q.; Han, X.; Zhao, S. L.; Liu, H. L.; Hu, Y. Modeling Swelling Behavior of Thermoresponsive Polymer Brush with Lattice Density Functional Theory. *Langmuir* **2014**, 30, 4040-4048

(15) Li, S.; Feng, G.; Cummings, P. T. Interfaces of dicationic ionic liquids and graphene: a molecular dynamics simulation study. *J. Phys.: Condens. Matter* **2014**, 26, 284106

(16) Black, J. M.; Walters, D.; Labuda, A.; Feng, G.; Hillesheim, P. C.; Dai, S.; Cummings, P. T.; Kalinin, S. V.; Proksch, R.; Balke, N. Bias-Dependent Molecular-Level Structure of Electrical Double Layer in Ionic Liquid on Graphite. *Nano Lett.* **2013**, 13, 5954-5960

(17) Uysal, A.; Zhou, H.; Feng, G.; Lee, S. S.; Li, S.; Fenter, P.; Cummings, P. T.; Fulvio, P. F.; Dai, S.; McDonough, J. K., et al. Structural Origins of Potential Dependent Hysteresis at the Electrified Graphene/Ionic Liquid Interface. *J. Phys. Chem. C* **2014**, 118, 569-574

(18) Paek, E.; Pak, A. J.; Hwang, G. S. A Computational Study of the Interfacial Structure and Capacitance of Graphene in [BMIM][PF6] Ionic Liquid. *J. Electrochem. Soc.* **2013**, 160, A1-A10

(19) Liu, X. H.; Wang, Y. Y.; Li, S.; Yan, T. Y. Effects of anion on the electric double layer of imidazolium-based ionic liquids on graphite electrode by molecular dynamics simulation. *Electrochim. Acta* **2015**, 184, 164-170

(20) Li, S.; Van Aken, K. L.; McDonough, J. K.; Feng, G.; Gogotsi, Y.; Cummings, P. T. The Electrical Double Layer of Dicationic Ionic Liquids at Onion-like Carbon Surface. *J. Phys. Chem. C* **2014**, 118, 3901-3909

(21) Feng, G.; Li, S.; Atchison, J. S.; Presser, V.; Cummings, P. T. Molecular Insights into Carbon Nanotube Supercapacitors: Capacitance Independent of Voltage and Temperature. *J. Phys. Chem. C* **2013**, 117, 9178-9186

(22) Paek, E.; Pak, A. J.; Hwang, G. S. Curvature Effects on the Interfacial Capacitance of Carbon Nanotubes in an Ionic Liquid. *J. Phys. Chem. C* **2013**, 117, 23539-23546

(23) Feng, G.; Qiao, R.; Huang, J. S.; Sumpter, B. G.; Meunier, V. Ion Distribution in Electrified Micropores and Its Role in the Anomalous Enhancement of Capacitance. *Acs Nano* **2010**, 4, 2382-2390

(24) Feng, G.; Cummings, P. T. Supercapacitor Capacitance Exhibits Oscillatory Behavior as a Function of Nanopore Size. *J. Phys. Chem. Lett.* **2011**, 2, 2859-2864

(25) Banuelos, J. L.; Feng, G.; Fulvio, P. F.; Li, S.; Rother, G.; Dai, S.; Cummings, P. T.; Wesolowski, D. J. Densification of Ionic Liquid Molecules within a Hierarchical Nanoporous Carbon Structure Revealed by Small-Angle Scattering and Molecular Dynamics Simulation. *Chem. Mater.* **2014**, 26, 1144-1153

(26) Siepmann, J. I.; Sprik, M. Influence of Surface-Topology and Electrostatic Potential on Water Electrode Systems. *J. Chem. Phys.* **1995**, 102, 511-524

(27) Reed, S. K.; Lanning, O. J.; Madden, P. A. Electrochemical interface between an ionic liquid and a model metallic electrode. *J. Chem. Phys.* **2007**, 126, 084704

(28) Pastewka, L.; Jarvi, T. T.; Mayrhofer, L.; Moseler, M. Charge-transfer model for carbonaceous electrodes in polar environments. *Phys. Rev. B* **2011**, 83, 165418

(29) Merlet, C.; Pean, C.; Rotenberg, B.; Madden, P. A.; Simon, P.; Salanne, M. Simulating supercapacitors: can we model electrodes as constant charge surfaces? *J Phys. Chem. Lett.* **2013**, 4, 264-268

(30) Wang, Z. X.; Yang, Y.; Olmsted, D. L.; Asta, M.; Laird, B. B. Evaluation of the constant potential method in simulating electric double-layer capacitors. *J. Chem. Phys.* **2014**, 141, 184102

(31) Haskins, J. B.; Lawson, J. W. Evaluation of molecular dynamics simulation methods for ionic liquid electric double layers. *J. Chem. Phys.* **2016**, 144, 184707

(32) Vatamanu, J.; Borodin, O.; Smith, G. D. Molecular Simulations of the Electric Double Layer Structure, Differential Capacitance, and Charging Kinetics for N-Methyl-N-propylpyrrolidinium Bis(fluorosulfonyl)imide at Graphite Electrodes. *J. Phys. Chem. B* **2011**, 115, 3073-3084

(33) Merlet, C.; Limmer, D. T.; Salanne, M.; Van Roij, R.; Madden, P. A.; Chandler, D.; Rotenberg, B. The Electric Double Layer Has a Life of Its Own. *J. Phys. Chem. C* **2014**, 118, 18291-18298

(34) Vatamanu, J.; Vatamanu, M.; Bedrov, D. Non-Faradaic Energy Storage by Room Temperature Ionic Liquids in Nanoporous Electrodes. *Acs Nano* **2015**, 9, 5999-6017

(35) Vatamanu, J.; Vatamanu, M.; Borodin, O.; Bedrov, D. A comparative study of room temperature ionic liquids and their organic solvent mixtures near charged electrodes. *J. Phys.: Condens. Matter* **2016**, 28, 464002

(36) Bedrov, D.; Vatamanu, J.; Hu, Z. Z. Ionic liquids at charged surfaces: Insight from molecular simulations. *J. Non-Cryst. Solids.* **2015**, 407, 339-348

(37) Rajput, N. N.; Monk, J.; Hung, F. R. Ionic Liquids Confined in a Realistic Activated Carbon Model: A Molecular Simulation Study. *J. Phys. Chem. C* **2014**, 118, 1540-1553

(38) Merlet, C.; Pean, C.; Rotenberg, B.; Madden, P. A.; Daffos, B.; Taberna, P. L.; Simon, P.; Salanne, M. Highly confined ions store charge more efficiently in supercapacitors. *Nat. Commun.* **2013**, 4, 2701

(39) Pean, C.; Merlet, C.; Rotenberg, B.; Madden, P. A.; Taberna, P. L.; Daffos, B.; Salanne, M.; Simon, P. On the Dynamics of Charging in Nanoporous Carbon-Based Supercapacitors. *Acs Nano* **2014**, 8, 1576-1583

(40) Merlet, C.; Rotenberg, B.; Madden, P. A.; Taberna, P. L.; Simon, P.; Gogotsi, Y.; Salanne, M. On the molecular origin of supercapacitance in nanoporous carbon electrodes. *Nat. Mater.* **2012**, 11, 306-310

(41) Wang, Y. T.; Izvekov, S.; Yan, T. Y.; Voth, G. A. Multiscale coarse-graining of ionic liquids. *J. Phys. Chem. B* **2006**, 110, 3564-3575

(42) Bhargava, B. L.; Balasubramanian, S.; Klein, M. L. Modelling room temperature ionic liquids. *Chem. Commun.* **2008**, 29, 3339-3351

(43) Merlet, C.; Salanne, M.; Rotenberg, B.; Madden, P. A. Imidazolium Ionic Liquid Interfaces with Vapor and Graphite: Interfacial Tension and Capacitance from Coarse-Grained Molecular Simulations. *J. Phys. Chem. C* **2011**, 115, 16613-16618

(44) Liu, Z. P.; Wu, X. P.; Wang, W. C. A novel united-atom force field for imidazolium-based ionic liquids. *Phys. Chem. Chem. Phys.* **2006**, 8, 1096-1104

(45) Micaelo, N. M.; Baptista, A. M.; Soares, C. M. Parametrization of 1-butyl-3-methylimidazolium hexafluorophosphate/nitrate ionic liquid for the GROMOS force field. *J. Phys. Chem. B* **2006**, 110, 14444-14451

(46) Vatamanu, J.; Borodin, O.; Smith, G. D. Molecular Insights into the Potential and Temperature Dependences of the Differential Capacitance of a Room-Temperature Ionic Liquid at Graphite Electrodes. *J. Am. Chem. Soc.* **2010**, 132, 14825-14833

(47) Liu, Z. P.; Huang, S. P.; Wang, W. C. A refined force field for molecular simulation of imidazolium-based ionic liquids. *J. Phys. Chem. B* **2004**, 108, 12978-12989

(48) Lopes, J. N. C.; Padua, A. A. H. CL&P: A generic and systematic force field for ionic liquids modeling. *Theor. Chem. Acc.* **2012**, 131, 1129

(49) Yan, T. Y.; Burnham, C. J.; Del Popolo, M. G.; Voth, G. A. Molecular dynamics simulation of ionic liquids: The effect of electronic polarizability. *J. Phys. Chem. B* **2004**, 108, 11877-11881

(50) Borodin, O. Polarizable Force Field Development and Molecular Dynamics Simulations of Ionic Liquids. *J. Phys. Chem. B* **2009**, 113, 11463-11478

(51) Schroder, C.; Steinhauser, O. Simulating polarizable molecular ionic liquids with Drude oscillators. *J. Chem. Phys.* **2010**, 133, 154511

(52) Son, C. Y.; McDaniel, J. G.; Schmidt, J. R.; Cui, Q.; Yethiraj, A. First-Principles United Atom Force Field for the Ionic Liquid BMIM+BF4-: An Alternative to Charge Scaling. *J. Phys. Chem. B* **2016**, 120, 3560-3568

(53) Vatamanu, J.; Bedrov, D. Capacitive Energy Storage: Current and Future Challenges. *J. Phys. Chem. Lett.* **2015**, 6, 3594-3609

(54) Leontyev, I.; Stuchebrukhov, A. Accounting for electronic polarization in non-polarizable force fields. *Phys. Chem. Chem. Phys.* **2011**, 13, 2613-2626

(55) Chaban, V. Polarizability versus mobility: atomistic force field for ionic liquids. *Phys. Chem. Chem. Phys.* **2011**, 13, 16055-16062

(56) Chaban, V. V.; Voroshylova, I. V.; Kalugin, O. N. A new force field model for the simulation of transport properties of imidazolium-based ionic liquids. *Phys. Chem. Chem. Phys.* **2011**, 13, 7910-7920

(57) Schroder, C. Comparing reduced partial charge models with polarizable simulations of ionic liquids. *Phys. Chem. Chem. Phys.* **2012**, 14, 3089-3102

(58) Zhang, Y.; Maginn, E. J. A Simple AIMD Approach to Derive Atomic Charges for Condensed Phase Simulation of Ionic Liquids. *J. Phys. Chem. B* **2012**, 116, 10036-10048

(59) Choi, E.; McDaniel, J. G.; Schmidt, J. R.; Yethiraj, A. First-Principles, Physically Motivated Force Field for the Ionic Liquid [BMIM][BF4]. *J. Phys. Chem. Lett.* **2014**, 5, 2670-2674

(60) Salanne, M. Simulations of room temperature ionic liquids: from polarizable to coarse-grained force fields. *Phys. Chem. Chem. Phys.* **2015**, 17, 14270-14279

(61) Kiyohara, K.; Asaka, K. Monte Carlo simulation of electrolytes in the constant voltage ensemble. *J. Chem. Phys.* **2007**, 126, 214704

(62) Kiyohara, K.; Asaka, K. Monte Carlo simulation of porous electrodes in the constant voltage ensemble. *J. Phys. Chem. C* **2007**, 111, 15903-15909

(63) Varanasi, S. R.; Bhatia, S. K. Capacitance Optimization in Nanoscale Electrochemical Supercapacitors. *J. Phys. Chem. C* **2015**, 119, 17573-17584

(64) Varanasi, S. R.; Farmahini, A. H.; Bhatia, S. K. Complementary Effects of Pore Accessibility and Decoordination on the Capacitance of Nanoporous Carbon Electrochemical Supercapacitors. *J. Phys. Chem. C* **2015**, 119, 28809-28818

(65) Ando, Y.; Gohda, Y.; Tsuneyuki, S. Ab initio molecular dynamics study of the Helmholtz layer formed on solid-liquid interfaces and its capacitance. *Chem. Phys. Lett.* **2013**, 556, 9-12

(66) Zhan, C.; Neal, J.; Wu, J. Z.; Jiang, D. E. Quantum Effects on the Capacitance of Graphene-Based Electrodes. *J. Phys. Chem. C* **2015**, 119, 22297–22303

(67) Otani, M.; Sugino, O. First-principles calculations of charged surfaces and interfaces: A plane-wave nonrepeated slab approach. *Phys. Rev. B* **2006**, 73, 115407

(68) Radin, M. D.; Ogitsu, T.; Biener, J.; Otani, M.; Wood, B. C. Capacitive charge storage at an electrified interface investigated via direct first-principles simulations. *Phys. Rev. B* **2015**, 91, 125415

(69) Petrosyan, S. A.; Rigos, A. A.; Arias, T. A. Joint Density-Functional Theory: Ab initio study of Cr_2O_3 Surface Chemistry in Solution. *J. Phys. Chem. B* **2005**, 109, 15436-15444

(70) Petrosyan, S. A.; Briere, J. F.; Roundy, D.; Arias, T. A. Joint Density-Functional Theory for Electronic Structure of Solvated Systems. *Phys. Rev. B* **2007**, 75, 205105

(71) Letchworth-Weaver, K.; Arias, T. A. Joint Density Functional Theory of the Electrode-electrolyte Interface: Application to Fixed Electrode Potentials, Interfacial Capacitances, and Potentials of Zero Charge. *Phys. Rev. B* **2012**, 86, 075140

(72) Fattebert, J. L.; Gygi, F. Density functional theory for efficient ab initio molecular dynamics simulations in solution. *J. Comput. Chem.* **2002**, 23, 662-666

(73) Kornyshev, A. A.; Sutmann, G. Nonlocal nonlinear static dielectric response of polar liquids. *J. Electroanal. Chem.* **1998**, 450, 143-156

(74) Gunceler, D.; Letchworth-Weaver, K.; Sundararaman, R.; Schwarz, K. A.; Arias, T. A. The Importance of Nonlinear Fluid Response in Joint Density-Functional Theory Studies of Battery Systems. *Modell. Simul. Mater. Sci. Eng.* **2013**, 21, 074005

(75) Sundararaman, R.; Goddard, W. A. The Charge-Asymmetric Nonlocally Determined Local-Electric (CANDLE) Solvation Model. *J. Chem. Phys.* **2015**, 142, 064107

(76) Sundararaman, R.; Schwarz, K. A.; Letchworth-Weaver, K.; Arias, T. A. Spicing up continuum solvation models with SaLSA: The spherically averaged liquid susceptibility ansatz. *J. Chem. Phys.* **2015**, 142, 054102

(77) Sundararaman, R.; Schwarz, K. Evaluating computational models of the electrode-electrolyte interface: challenges and strategies for improvement. *arXiv preprint arXiv:1612.00931* **2016**

Chapter 3. Quantum Effects on the Capacitance of Graphene-based Electrodes

3.1 Introduction

Electric double-layer capacitors (EDLCs) are a type of supercapacitors that have high power density and long cycle life. Unlike rechargeable batteries, EDLCs store electric energy at solid-electrolyte interfaces by applying a bias voltage.[1] The specific capacitance of an EDLC is on the order of hundreds of Farads per gram, much greater than that of a conventional dielectric capacitor.[2] In recent years, graphene has been found to be a potential electrode for EDLCs.[3] Unlike traditional electrodes such as metals, graphene electrodes are unique two-dimensional materials with a quantum capacitance (QC).[4] This quantum effect arises from the limited electronic density of states at the Fermi level: when the graphene electrode is charged, electrons begin to occupy higher-energy states, leading to quantum capacitance.

In an EDLC of graphene and electrolyte, the total capacitance reflects the overall effect of quantum and electric double-layer (EDL) capacitances (Eq. 3-1). Quantum capacitance (C_Q) depends on the material's electronic structure, while EDL capacitance (C_{EDL}) depends on the electrode-electrolyte interfacial structure.[5, 6]

$$\frac{1}{C_{total}} = \frac{1}{C_Q} + \frac{1}{C_{EDL}} \qquad 3\text{-}1$$

For a metal electrode, quantum capacitance is extremely high due to the large electronic density of states at the Fermi level. As a result, its contribution to the total capacitance is negligible given the inverse-sum relationship in Eq. 3-1, and the experimentally measured capacitance of a metal electrode hence corresponds to the EDL capacitance. For a 2D-

material such as graphene, quantum capacitance and EDL capacitance are on the same order of magnitude, thereby greatly influencing the total capacitance.

According to recent experiments[7, 8] the quantum capacitance dominates the total capacitance for single-layer graphene in both ionic liquid and aqueous electrolytes. The new discovery raises an important question about the contribution of the quantum capacitance in the diverse carbon materials used in EDLCs. For example, commercial EDLCs use activated carbons as electrodes. How important the quantum capacitance is for those carbon materials remains unclear. As a first step to address this question, we consider variation of quantum capacitance with the graphene thickness. High-resolution transmission electron miscopy (TEM) images of porous carbons show that their walls consist of a few layers of stacked graphene.[9] In this paper, we investigate the quantum capacitance and their contribution in the total capacitance at the graphene/electrolyte interface as a function of the graphene layers for both the ionic-liquid and aqueous electrolytes.

3.2 Computational Methods

Quantum capacitance is computed with the electronic density functional theory within an implicit solvation model as implemented in the JDFTx software.[10, 11] Periodic boundary conditions (that is, the supercell model) were used to describe the interface: single layer graphene was modeled as a lateral 2.460×2.460 Å^2 rhombus sheet with a unit-cell length of 2.460 Å, close to the experimental value of 2.461 Å; the vacuum or electrolyte layer above the graphene electrode was modeled as a 20-Å slab along the z-direction. Generalized gradient approximation in the form of Perdew-Burke-Ernzerhof (GGA-PBE)

functional is applied to describe the exchange-correlation energy.[12] Ultra-soft pseudopotential is used to describe the interaction between the nuclei and the electrons;[13] the electron wavefunctions are described by a plane-wave basis set with a kinetic energy cutoff of 20 hartree. 24×24×1 k-point mesh is used to sample the Brillouin Zone. The linear polarizable continuum model (PCM)[10] is coupled with an implicit solvent model to fill the vacuum layer to study the influence of the electrolyte on the quantum capacitance.

Quantum capacitance is defined as $C_Q = \frac{dQ}{d\varphi}$, where Q is the excessive charge on the graphene electrode, and φ is external potential. Q can be expressed by an integral term related to the electronic density of state (DOS) and the Fermi-Dirac distribution function $f(E)$. When the chemical potential of electrons is shifted by applying an electrical potential, φ/e, the graphene charge is

$$Q = e\int_{-\infty}^{+\infty} D(E)[f(E) - f(E-\varphi)]dE, \qquad 3\text{-}2$$

where E is the relative potential to the Fermi level. By differentiating Q with respect to φ, one obtains C_Q:

$$C_Q = \frac{dQ}{d\varphi} = \frac{e^2}{4kT}\int_{-\infty}^{+\infty} D(E)sech^2\left[\frac{E-\varphi}{2kT}\right]dE \qquad 3\text{-}3$$

By obtaining DOS from the electronic DFT calculations, we can readily calculate the quantum capacitance from Eq. 3-3.[14] Here we should note that our quantum capacitance calculation is based on Fix-Band-Approximation[8, 15], which means that the band structure and density of states in the system is not affected by the electron occupation. Recently published paper has improved the quantum capacitance modeling by introducing the relaxed band structure in a charged system, which gave a more accurate and deeper

understanding on quantum capacitance.[16] When calculated few layers graphene system, we also doing the calculation without screening effect in inner graphene layers. Recent paper reported that few layers graphene can completely screen the electric field when the layer number go up to four.[17] Thus, our model will overestimate the quantum capacitance in few layers graphene. Although our quantum capacitance modeling is not perfect, we can still see its influence on total capacitance due to its low value at Fermi Level. Since quantum capacitance go up rapidly and can be very large, calculation with or without screening effect can both give similar total capacitance.

Classical density functional theory is used to obtain EDL capacitance for graphene in contact with an ionic liquid or aqueous electrolyte. The details of the CDFT calculations have been published before.[18-23] Briefly, we obtain the EDL differential capacitances by computing the surface charge densities at various surface potentials. The ionic liquid is modeled as a mixture of charged hard spheres of single valence and equal size (0.425 nm in diameter) at a molar volume of 154 cm^3/mol at 298 K. The model system mimics that of a typical ionic liquid such as 1-ethyl-3-methylimidazolium tetrafluoroborate [emim][BF_4]. An aqueous NaF electrolyte of 1 M in 298 K is modeled as charged hard spheres of 0.116 nm and 0.119 nm in diameter for the cations and anions, respectively. The Stern layer capacitance is calculated using the bulk dielectric constant ($\varepsilon = 6$) of NaF due to the compact layer formed at the surface observed in the density profile. Compared with classical molecular dynamics,[24-28] an alternative approach to obtain EDL capacitance, classical DFT is much more efficient. With both quantum capacitance and EDL

capacitance calculated from electronic and classical DFT, respectively, we then compute the total capacitance.

We establish the total capacitance as a function of applied voltage (φ_a) by combining C_Q and C_{EDL} as described in Hwang's work.[14, 29] We calculated quantum capacitance as a function of $\varphi_{QC} = (E - E_{Fermi})/e$ and EDL capacitance as a function of $\varphi_{EDL} = \varphi - \varphi_{PZC}$. The applied voltage is the sum of partial voltage in QC and EDL, thus we have $\varphi_a = \varphi_{QC} + \varphi_{EDL}$. C_Q amd C_{EDL} are both voltage-dependent, but they share the same interfacial charge. Thus, we can obtain the relationship between surface charge density with applied voltage by summing up the φ_{QC} and φ_{EDL} at the same surface charge density from quantum and EDL charge curve, as shown in Figure 3-2(c) and Figure 3-3(c).

3.3 Results and discussion

3.3.1 Quantum capacitance of single-layer and multi-layer graphenes

Figure 3-1a shows the quantum capacitance of a graphene electrode of different thickness next to the vacuum. One can see that the quantum capacitance exhibits a "V" shape near the Fermi level with the slope increasing proportionally to the number of layers. The thickness effect can be expected from the definition of quantum capacitance in Eq. 3-3.[14] As the number of layers increases, the total electronic DOS per unit area of the electrode surface increases proportionally. The non-zero quantum capacitance at the Fermi level can be interpreted by the thermal broadening function in Equation 3-3, consistent with the experimental observation.[15]

To examine the effect of an electrolyte on the quantum capacitance, we computed the quantum capacitance for a 1.0 M NaF aqueous electrolyte. The theoretical results

(Figure 3-1b) indicate that the presence of an electrolyte only slightly affects the quantum capacitance of a graphene electrode with few layers. The electrolyte effect is negligible for the single-layer graphene. In our calculation of the quantum capacitance using JDFT, the total Hamiltonian and free energy functional have included the implicit solvation part via an exact dielectric function and the Debye screening effect.[10] In the free-energy functional, all terms including the fluid part are electron density dependent. An electrolyte affects the quantum capacitance by shifting the Dirac point; however, the shift is small for a single-layer graphene as found previously.[30] In addition, both experimental observation[15, 31] and *ab initio* molecular dynamics simulation[32] have shown that the quantum capacitance of a single-layer graphene is insensitive to the presence of an electrolyte.

Direct measurements of quantum capacitance of a graphene electrode have been reported recently. Tao et al. measured quantum capacitance of single layer graphene in an ionic liquid electrolyte,[15] and obtained a value of about $6.7\mu F/cm^2$ at the Fermi level. Wang et al. obtained quantum capacitance by capacitance bridge technique in a vacuum[31] and found a value of about $0.8\ \mu F/cm^2$ at the Fermi level in vacuum. Our calculated quantum capacitance is about $1.3\ \mu F/cm^2$, close to Wang's result. Tao et al. explained their abnormally high quantum capacitance at the Fermi level in terms of the charge impurity effect induced by electrolyte during measurement.[15]

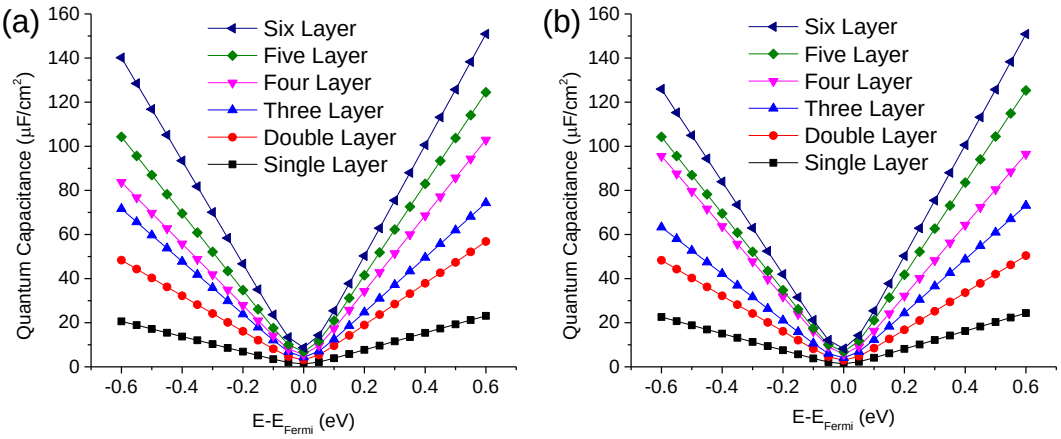


Figure 3-1. FBA based quantum capacitance of a graphene electrode with different numbers of graphene layers in (a) vacuum; (b) a 1.0-M NaF aqueous electrolyte.

3.3.2 Total capacitance for an aqueous electrolyte next to a single-layer graphene

It is computationally challenging to directly model the total capacitance of an electrode/electrolyte interface, as one has to simultaneously model both the electronic response in the electrode and the mobile-ion response in the electrolyte. Although JDFT[10, 11] can in principle solve this problem, the classical DFT part in the JDFT approach is still under development. We instead employed a more practical and commonly used approach,[8, 14, 29] by simulating quantum capacitance and electric double layer capacitance separately and then combining them together to obtain total capacitance.

Figure 3-2(b) presents the calculated total capacitance of single-layer graphene in a 1M aqueous electrolyte solution. One can see that the total capacitance is mostly dominated by quantum capacitance near the potential of zero charge (PZC) Here the PZC is 0 V in classical DFT simulation. Especially, from -0.1 to 0.1 V, the total capacitance is nearly equal to quantum capacitance in Figure 3-2(a). As the absolute potential increases,

the EDL capacitance becomes more significant. At |φ|=0.6 V, quantum capacitance is similar to EDL capacitance and the total capacitance is about half of the EDL capacitance. Thus, in single-layer graphene, the quantum capacitance always plays an important role. Qualitatively, our calculated total capacitance of single-layer graphene is in good agreement with recent experimental results,[8, 33] which also show a V-shaped capacitance-potential curve.

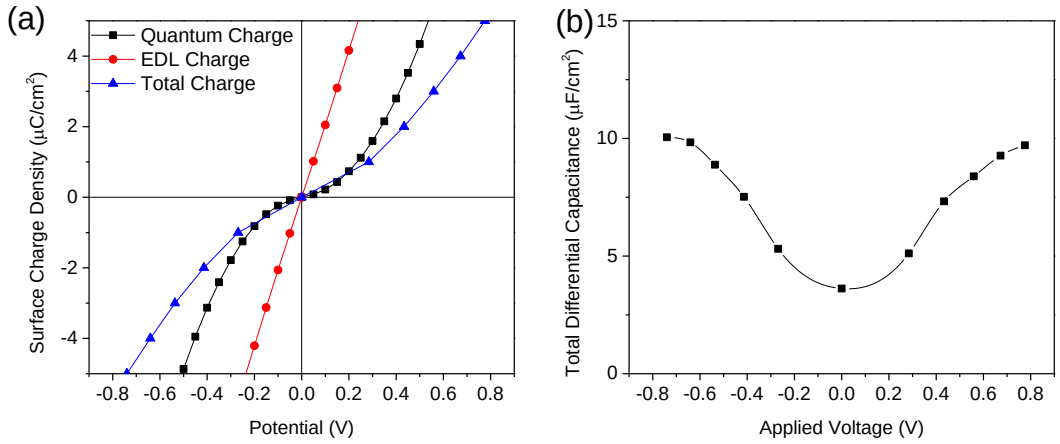


Figure 3-2. (a) Charging curve corresponds to C_Q, C_{EDL} and $C_{tot.}$ (b) Total differential capacitance of single layer graphene in 1M NaF.

3.3.3 Total capacitance for an ionic-liquid electrolyte next to a single-layer graphene

As shown by our earlier studies, classical DFT is a powerful tool for studying the EDL capacitance in ionic liquids.[34-36] The calculated total capacitance of the interface between a single-layer graphene electrode and an ionic-liquid electrolyte is plotted in Figure 3-3(b) by combining the quantum capacitance from electronic DFT and the EDL capacitance from classical DFT prediction. One can see that the EDL capacitance shows a

"bell" shape, which is related to ionic concentration and has been predicted by analytical theories,[37] classical DFT calculations,[34] and molecular dynamics simulations.[38, 39] The calculated total capacitance shows a V-shaped capacitance-potential curve, which matches the experimental measurement in ionic liquid very well.[7] Around the PZC (within +/- 0.4 eV), quantum capacitance also dominates the total capacitance in ionic liquid. But at higher voltages ($|\varphi-\varphi_{PZC}|$=0.6 V), the EDL capacitance tends to approach total capacitance and becomes more important, although quantum capacitance still has a significant contribution.

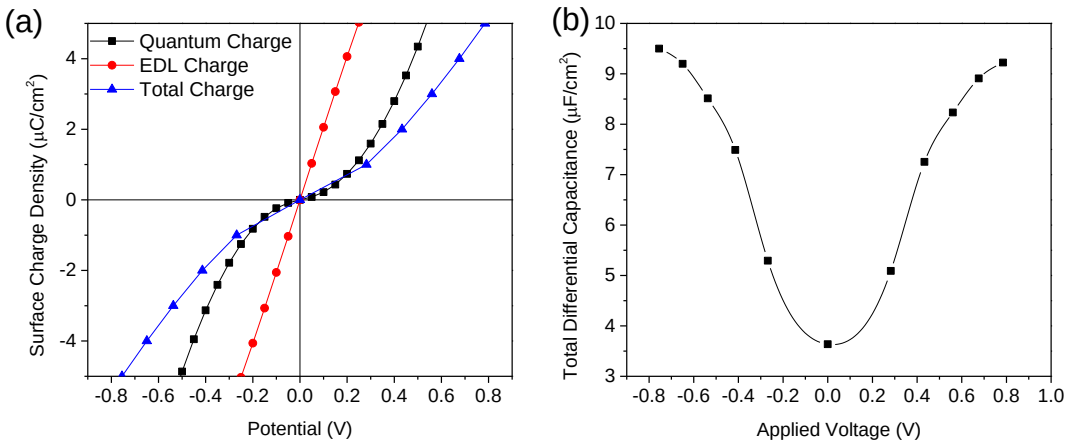


Figure 3-3. (a) Charging curve corresponds to C_Q, C_{EDL} and $C_{tot.}$ (b) Total differential capacitance of single layer graphene in ionic liquid.

3.3.4 Total capacitance as a function of the number of graphene layers.

The results above show that quantum capacitance is very important for the single-layer graphene electrode both in aqueous and ionic-liquid electrolytes. However, as the number of graphene layers increases, the quantum capacitance rises significantly (Figure 3-1) and thus it would be interesting to see how the corresponding total capacitance changes. Figure 3-4(b) shows the total capacitance of few-layer graphene electrodes in an

aqueous electrolyte solution. The capacitance increases significantly from a single-layer to a double-layer graphene. As the number of layers further increases, however, the capacitance increase becomes smaller and the V shape of the total capacitance profile tends to converge beyond around four layers. In addition, the V shape near the PZC becomes narrower due to the diminishing contribution of the quantum capacitance.

The layer effect in an ionic liquid is plotted in Figure 3-5(b). Unlike the V shape capacitance-potential curve obtained from the aqueous electrolyte, the total capacitance in the ionic liquid changes from a "bell shape" to a "camel shape" as the number of graphene layers increased. This change is due to the bell-shaped EDL capacitance in an ionic liquid and the diminishing contribution of the quantum capacitance for electrodes with a large number of graphene layers. For the single-layer graphene, the capacitance is dominated by the quantum capacitance, so its total capacitance is V-shaped. As the number of graphene layers increases, the total capacitance is still dominated by the quantum capacitance near the PZC, but away from the PZC (for example, more than 0.4 eV away), the total capacitance is dominated by the bell-shaped EDL capacitance. Consequently, the overall potential dependence shows a camel shape. The total-capacitance profile tends to converge beyond four layers of graphene.

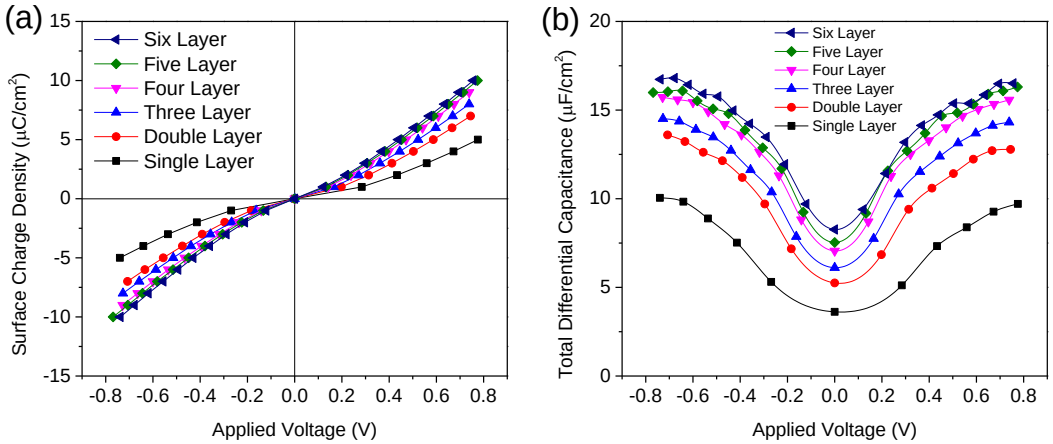


Figure 3-4. (a) The relationship between surface charge and potential drop in few layers graphene. (b) Calculated total capacitance as a function of the layer number in few layers graphene in 1M NaF aqueous electrolyte.

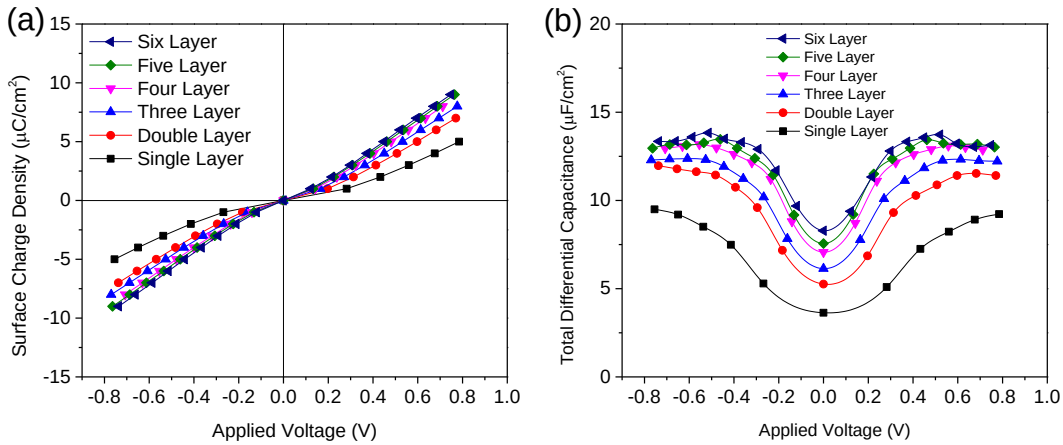


Figure 3-5. (a) The relationship between surface charge and potential drop in few layers graphene. (b) Calculated total capacitance as a function of the layer number in few layers graphene in ionic liquid.

3.3.5 Comparison of integral capacitance from -0.6 V to 0.6 V

In practical operations, a supercapacitor typically consists of two symmetric carbon electrodes that are charged up to the electrochemical window of the electrolyte: 1.2 V for aqueous electrolytes and 2.5 to 3.0 V for ionic liquids. It would be more informative to

compare the integral capacitance at an experimentally reasonable voltage range sufficiently away from the PZC and evaluate the influence of the quantum capacitance. Toward that end, we chose -0.6 to 0.6 V for the sweep range of electrode voltage, and the results for both aqueous and ionic liquid electrolytes are plotted in Figure 3-6(a). In both cases, the capacitance almost levels off beyond four layers of graphene. Our results agree well with a recent experiment for the ionic-liquid/graphene interface, which shows that total capacitance is limited by quantum capacitance when the number of graphene layers (N) is less than four and by EDL capacitance for $N > 4$.[7]

We have further analyzed the relative contribution of quantum capacitance and EDL capacitance in total differential capacitance for the case of the six-layer graphene at different surface potential. Figure 3-7 shows that, away from the PZC, the total capacitance is dominated by EDL capacitance although quantum capacitance is comparable to EDL capacitance at PZC. Due to the inverse-sum relationship in Eq. 3-1, when the quantum capacitance is much greater than the EDL capacitance, its contribution to the total capacitance becomes negligible and the EDL capacitance dominates the total capacitance. In addition, from partial voltage analysis on C_Q and C_{EDL}, we can also see that as the applied voltage go up, the partial voltage on C_Q becomes less dominative. When the total applied voltage is 0.2 V, the partial voltage contribution of C_Q is 0.11 V which is more than half of the total. When the applied voltage go up to 0.6 V, the voltage contribution of C_Q is 0.24 V and its corresponding C_Q is quite large. Thus, the total capacitance is dominated by EDL capacitance.

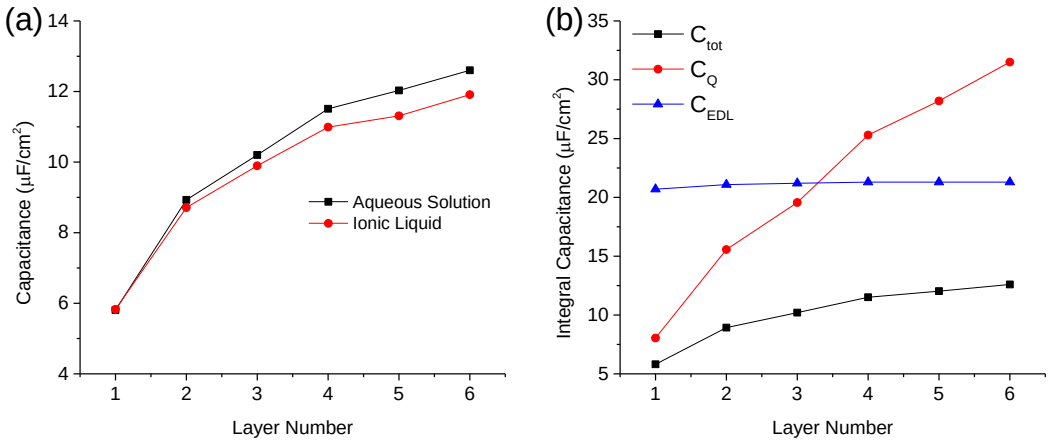


Figure 3-6. (a) Integral capacitance of a graphene electrode from -0.6 V to 0.6 V applied voltage as a function of the number of graphene layers in both aqueous and ionic liquid electrolytes. (b) Capacitance contribution in few layer graphene in aqueous electrolyte, corresponding to integral quantum, EDL and total capacitance at same surface charge density.

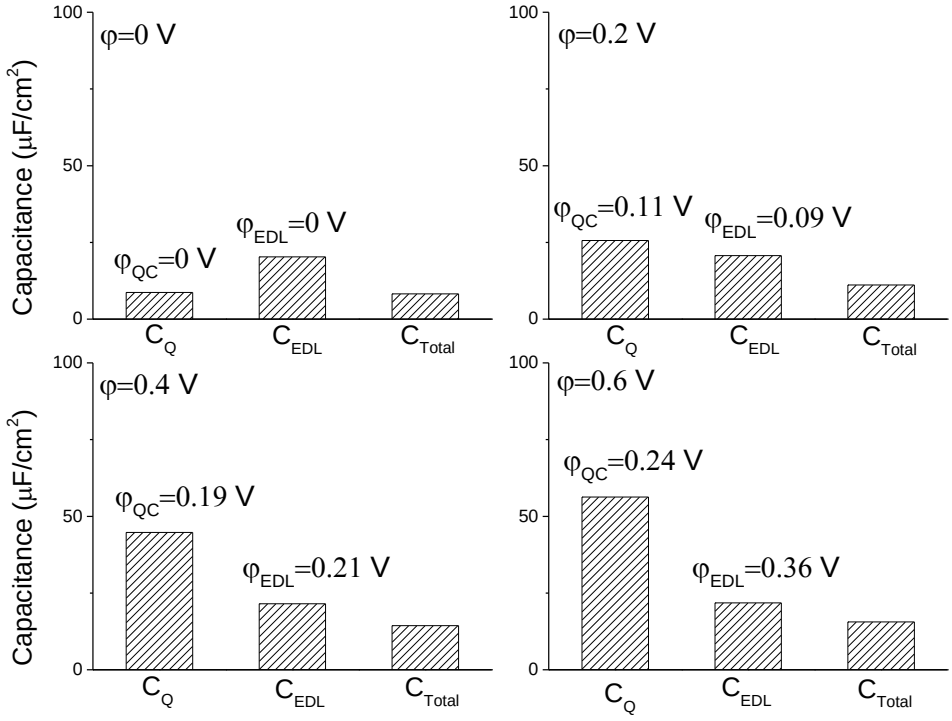


Figure 3-7. Relative contributions of quantum and EDL capacitances to the total differential capacitance of a six-layer graphene electrode at different voltage.

3.3.6 Relevance to realistic carbon electrodes

Activated carbon represents the most widely used electrode material for EDLCs; recent developments use other carbons such as carbide-derived carbons, onion-like carbons, and mesoporous carbons.[40, 41] High-resolution TEM images indicate that all these carbons consist of stacked graphene layers at the pore walls.[9, 42] In other words, the electrode surfaces are typically made of a few layers of graphene. Our work suggests that,

for these realistic carbons and away from the PZC, the quantum capacitance is probably insignificant for the performance of EDLC devices if the carbon pore-wall thickness is above three. In addition, our partial voltage analysis shows that even when the layer number go up to six and total capacitance is converged due to large quantum capacitance, C_Q can still consume about 1/3 applied voltage. This energy cost on electrode will induce a big waste! Thus, increasing conductivity (or quantum capacitance) is also a promising way to increase energy storage and efficiency.

3.4 Summary and conclusions

We have studied the quantum capacitance and the total capacitance of graphene electrodes as a function of the number of graphene layers for both aqueous and ionic-liquid electrolytes. The quantum capacitances were predicted from electronic density functional theory based on Fix-Band-Approximation with an implicit solvation model and the electric-double layer (EDL) capacitances were from classical density functional theory. For both aqueous and ionic-liquid electrolytes, quantum capacitance plays a dominant role in the total capacitance of a single-layer graphene electrode. The overall potential-dependent profile of total capacitance increases with the number of graphene layers but the extent diminishes quickly. When the number of layers reaches four, the total capacitance tends to converge and the EDL capacitance dominates at voltages sufficiently different from the potential of zero charge. Our work here shows that, for supercapacitors with realistic carbon electrodes, the capacitance performance depends on the pore-wall thickness.

References:

(1) Zhang, L. L.; Zhao, X. S. Carbon-based materials as supercapacitor electrodes. *Chem. Soc. Rev.* **2009**, 38, 2520-2531

(2) Wang, Y.; Shi, Z. Q.; Huang, Y.; Ma, Y. F.; Wang, C. Y.; Chen, M. M.; Chen, Y. S. Supercapacitor devices based on graphene materials. *J. Phys. Chem. C* **2009**, 113, 13103-13107

(3) Zhai, Y. P.; Dou, Y. Q.; Zhao, D. Y.; Fulvio, P. F.; Mayes, R. T.; Dai, S. Carbon materials for chemical capacitive energy storage. *Adv. Mater.* **2011**, 23, 4828-4850

(4) Kott, T. M.; Hu, B. H.; Brown, S. H.; Kane, B. E. Valley-Degenerate Two-Dimensional Electrons in the Lowest Landau Level. *Phys. Rev. B* **2014**, 89, 041107

(5) Uysal, A.; Zhou, H.; Feng, G.; Lee, S. S.; Li, S.; Cummings, P. T.; Fulvio, P. F.; Dai, S.; McDonough, J. K.; Gogotsi, Y., et al. Interfacial Ionic 'Liquids': Connecting Static and Dynamic Structures. *J. Phys.: Condens. Matter* **2015**, 27, 032101

(6) Chialvo, A. A.; Vlcek, L.; Cummings, P. T. Surface Strain Effects on the Water-Graphene Interfacial and Confinement Behavior. *J. Phys. Chem. C* **2014**, 118, 19701-19711

(7) Uesugi, E.; Goto, H.; Eguchi, R.; Fujiwara, A.; Kubozono, Y. Electric double-layer capacitance between an ionic liquid and few-layer graphene. *Sci. Rep.* **2013**, 3, 1595

(8) Stoller, M. D.; Magnuson, C. W.; Zhu, Y. W.; Murali, S.; Suk, J. W.; Piner, R.; Ruoff, R. S. Interfacial capacitance of single layer graphene. *Energ Environ. Sci.* **2011**, 4, 4685-4689

(9) Harris, P. J. F.; Liu, Z.; Suenaga, K. Imaging the Structure of Activated Carbon Using Aberration Corrected TEM. *J. Phys.: Conf. Ser.* **2010**, 241, 012050

(10) Letchworth-Weaver, K.; Arias, T. A. Joint density functional theory of the electrode-electrolyte interface: application to fixed electrode potentials, interfacial capacitances, and potentials of zero charge. *Phys. Rev. B* **2012**, 86, 075140

(11) Petrosyan, S. A.; Rigos, A. A.; Arias, T. A. Joint Density-Functional Theory: Ab initio Study of Cr_2O_3 Surface Chemistry in Solution. *J. Phys. Chem. B* **2005**, 109, 15436-15444

(12) Perdew, J. P.; Burke, K.; Ernzerhof, M. Generalized Gradient Approximation Made Simple. *Phys. Rev. Lett.* **1996**, 77, 3865-3868

(13) Garrity, K. F.; Bennett, J. W.; Rabe, K. M.; Vanderbilt, D. Pseudopotentials for High-throughput DFT Calculations. *Comput. Mater. Sci.* **2014**, 81, 446-452

(14) Paek, E.; Pak, A. J.; Hwang, G. S. A computational study of the interfacial structure and capacitance of graphene in [BMIM][PF_6] ionic liquid. *J. Electrochem. Soc.* **2013**, 160, A1-A10

(15) Xia, J. L.; Chen, F.; Li, J. H.; Tao, N. J. Measurement of the quantum capacitance of graphene. *Nat. Nanotechnol.* **2009**, 4, 505-509

(16) Radin, M. D.; Ogitsu, T.; Biener, J.; Otani, M.; Wood, B. C. Capacitive Charge Storage at an Electrified Interface Investigated via Direct First-Principles Simulations. *Phys. Rev. B* **2015**, 91, 125415

(17) Wood, B. C.; Ogitsu, T.; Otani, M.; Biener, J. First-Principles-Inspired Design Strategies for Graphene-Based Supercapacitor Electrodes. *J Phys Chem C* **2014**, 118, 4-15

(18) Yu, Y. X.; Wu, J.; Gao, G. H. Density-Functional Theory of Spherical Electric Double Layers and Zeta Potentials of Colloidal Particles in Restricted-Primitive-Model Electrolyte Solutions. *J. Chem. Phys.* **2004**, 120, 7223-7233

(19) Tang, Y.; Wu, J. A Density-Functional Theory for Bulk and Inhomogeneous Lennard-Jones Fluids from the Energy Route. *J. Chem. Phys.* **2003**, 119, 7388-7397

(20) Yu, Y. X.; Wu, J. Z. Density Functional Theory for Inhomogeneous Mixtures of Polymeric Fluids. *J. Chem. Phys.* **2002**, 117, 2368-2376

(21) Jiang, J.; Cao, D. P.; Jiang, D. E.; Wu, J. Z. Kinetic Charging Inversion in Ionic Liquid Electric Double Layers. *J. Phys. Chem. Lett.* **2014**, 5, 2195-2200

(22) Jiang, D. E.; Wu, J. Z. Microscopic Insights into the Electrochemical Behavior of Nonaqueous Electrolytes in Electric Double-Layer Capacitors. *J. Phys. Chem. Lett.* **2013**, 4, 1260-1267

(23) Jiang, D. E.; Jin, Z. H.; Henderson, D.; Wu, J. Z. Solvent Effect on the Pore-Size Dependence of an Organic Electrolyte Supercapacitor. *J. Phys. Chem. Lett.* **2012**, 3, 1727-1731

(24) Vatamanu, J.; Borodin, O.; Smith, G. D. Molecular Insights into the Potential and Temperature Dependences of the Differential Capacitance of a Room-Temperature Ionic Liquid at Graphite Electrodes. *J. Am. Chem. Soc.* **2010**, 132, 14825-14833

(25) Vatamanu, J.; Borodin, O.; Smith, G. D. Molecular Simulations of the Electric Double Layer Structure, Differential Capacitance, and Charging Kinetics for N-Methyl-N-

propylpyrrolidinium Bis(fluorosulfonyl)imide at Graphite Electrodes. *J. Phys. Chem. B* **2011**, 115, 3073-3084

(26) Xing, L. D.; Vatamanu, J.; Borodin, O.; Bedrov, D. On the Atomistic Nature of Capacitance Enhancement Generated by Ionic Liquid Electrolyte Confined in Subnanometer Pores. *J. Phys. Chem. Lett.* **2013**, 4, 132-140

(27) Vatamanu, J.; Cao, L. L.; Borodin, O.; Bedrov, D.; Smith, G. D. On the Influence of Surface Topography on the Electric Double Layer Structure and Differential Capacitance of Graphite/Ionic Liquid Interfaces. *J. Phys. Chem. Lett.* **2011**, 2, 2267-2272

(28) Feng, G.; Cummings, P. T. Supercapacitor Capacitance Exhibits Oscillatory Behavior as a Function of Nanopore Size. *J. Phys. Chem. Lett.* **2011**, 2, 2859-2864

(29) Pak, A. J.; Paekw, E.; Hwang, G. S. Relative contributions of quantum and double layer capacitance to the supercapacitor performance of carbon nanotubes in an ionic liquid. *Phys. Chem. Chem. Phys.* **2013**, 15, 19741-19747

(30) Sun, S.; Qi, Y.; Zhang, T. Y. Dissecting Graphene Capacitance in Electrochemical Cell. *Electrochim. Acta* **2015**, 163, 296-302

(31) Wang, L.; Chen, X.; Zhu, W.; Wang, Y.; Zhu, C.; Wu, Z.; Han, Y.; Zhang, M.; Li, W.; He, Y., et al. Detection of resonant impurities in graphene by quantum capacitance measurement. *Phys. Rev. B* **2014**, 89, 075410

(32) Paek, E.; Pak, A. J.; Hwang, G. S. On the Influence of Polarization Effects in Predicting the Interfacial Structure and Capacitance of Graphene-like Electrodes in Ionic Liquids. *J. Chem. Phys.* **2015**, 142, 024701

(33) Ji, H.; Zhao, X.; Qiao, Z.; Jung, J.; Zhu, Y.; Lu, Y.; Zhang, L. L.; MacDonald, A. H.; Ruoff, R. S. Capacitance of carbon-based electrical double-layer capacitors. *Nat. Commun.* **2014**, 5, 3317

(34) Jiang, D. E.; Meng, D.; Wu, J. Density Functional Theory for Differential Capacitance of Planar Electric Double Layers in Ionic Liquids. *Chem. Phys. Lett.* **2011**, 504, 153-158

(35) Wu, J. Z.; Jiang, T.; Jiang, D. E.; Jin, Z. H.; Henderson, D. A Classical Density Functional Theory for Interfacial Layering of Ionic Liquids. *Soft Matter* **2011**, 7, 11222-11231

(36) Jiang, D. E.; Jin, Z. H.; Wu, J. Z. Oscillation of Capacitance inside Nanopores. *Nano Lett.* **2011**, 11, 5373-5377

(37) Kornyshev, A. A. Double-Layer in Ionic Liquids: Paradigm Change? *J. Phys. Chem. B* **2007**, 111, 5545-5557

(38) Feng, G.; Jiang, D. E.; Cummings, P. T. Curvature Effect on the Capacitance of Electric Double Layers at Ionic Liquid/Onion-Like Carbon Interfaces. *J. Chem. Theory Comput.* **2012**, 8, 1058-1063

(39) Feng, G.; Zhang, J. S.; Qiao, R. Microstructure and Capacitance of the Electrical Double Layers at the Interface of Ionic Liquids and Planar Electrodes. *J. Phys. Chem. C* **2009**, 113, 4549-4559

(40) Zhang, C. F.; Hatzell, K. B.; Boota, M.; Dyatkin, B.; Beidaghi, M.; Long, D. H.; Qiao, W. M.; Kumbur, E. C.; Gogotsi, Y. Highly Porous Carbon Spheres for Electrochemical Capacitors and Capacitive Flowable Suspension Electrodes. *Carbon* **2014**, 77, 155-164

(41) Dyatkin, B.; Gogotsi, Y. Effects of Structural Disorder and Surface Chemistry on Electric Conductivity and Capacitance of Porous Carbon Electrodes. *Faraday Discuss.* **2014**, 172, 139-162

(42) Cao, M. S.; Song, W. L.; Hou, Z. L.; Wen, B.; Yuan, J. The Effects of Temperature and Frequency on the Dielectric Properties, Electromagnetic Interference Shielding and Microwave-Absorption of Short Carbon Fiber/Silica Composites. *Carbon* **2010**, 48, 788-796

Chapter 4. Enhancing graphene capacitance by nitrogen: effects of doping configuration and concentration

4.1 Introduction

Electric double-layer capacitors (EDLCs), also called supercapacitors, store electric energy physically at the electrode-electrolyte interface by the formation of electric double layer under a bias voltage.[1] The specific capacitance of an EDLC can be much greater than that of a conventional dielectric capacitor.[2] In recent years, carbon nanomaterials such as carbide-derived carbons and graphene have become popular as supercapacitor electrode materials due to their combination of good conductivity and high specific surface area.[2-9] Graphene, unlike a traditional metal electrode, has a different capacitive performance due to its quantum capacitance,[10-12] which is caused by its limited density of states (DOS) near the Fermi level.

In graphene supercapacitor, total capacitance C_{total} reflects the overall effect of quantum capacitance C_Q and the electric double-layer (EDL) capacitance C_{EDL} and can be estimated by

$$\frac{1}{C_{total}} = \frac{1}{C_Q} + \frac{1}{C_{EDL}} \qquad 4\text{-}1$$

if one ignores the polarization effect of solvent on the electronic structure of electrode surface.[13] Under this assumption, one can treat quantum and EDL capacitance separately to study the total capacitance.[8, 14, 15] The contribution of quantum capacitance to the total capacitance is negligible when the electrode is metal such as Pt which has extremely large DOS near the Fermi level. However, in graphene and graphene-like 2D systems, quantum capacitance is significant because it is comparable to the EDL capacitance.

A consequence of the theoretical relationship of quantum, EDL, and total capacitances in Eq. 4-1 is that $C_{total} < \min(C_Q, C_{EDL})$, suggesting that in cases where the quantum capacitance is less than the EDL capacitance, the total capacitance may be increased by increasing quantum capacitance. To alter the DOS and thus change the quantum capacitance, the most common and widely used way is doping. Nitrogen-doped graphene has been studied for many years and shows a higher capacitance than pristine graphene and porous carbon.[16-24] Ruoff et al. attributed this capacitance enhancement to quantum capacitance increase,[16] but Choi explained the capacitance increase by the higher binding energy between pyridinic group and cation.[18] So this topic is still controversial due to the complex structure of N-doped graphene and the experimental difficulty of accurate measurement of the quantum capacitance.

In this paper, we aim to elucidate the role of N-doping in graphene capacitance. To simplify the complex structure, we separately study the three most common configurations in N-doped graphene: graphitic, pyridinic, and pyrrolic. In N-doped carbons, these three configurations can be distinguished by X-ray Photoelectron Spectroscopy (XPS) of N 1s binding energy,[25] as experimentally observed.[26] Here we focus on a single-layer graphene sheet to elucidate the influence of N-doping on quantum capacitance and EDL capacitance.

4.2 Computational methods

Quantum capacitance is calculated by the electronic density functional theory (DFT) with implicit solvation model through the JDFTx code.[27, 28] N-doped graphene is modeled by a two-dimensional sheet with periodic boundary conditions; the lateral supercell is built up with repeating unit cells of graphene of a 2.46 Å lattice parameter,

close to the experimental value of 2.461 Å in pristine graphene. The thickness of the vacuum slab is 20 Å above graphene sheet along the z direction and filled with an implicit electrolyte (that is, a dielectric continuum). The generalized gradient approximation in the form of Perdew-Burke-Emzerhof functional is applied to describe the exchange-correlation effect.[29] Ultra-soft pseudopotential is used to describe the interaction between nuclei and valence electrons.[30] The optimization of ionic position is accomplished by the BFGS algorithm at fixed lattice constant with 20 hartree cutoff energy for the planewave bases, 6×6×1 k-point mesh to sample the Brillouin Zone, and 10^{-6} hartree tolerance in total energy for convergence. For accurate calculation of the density of states D(E) near the Fermi level, a 40 hartree cutoff energy and a 48×48×1 k-point mesh are used. From D(E), we can readily calculate the quantum capacitance from

$$C_Q = \frac{dQ}{d\varphi} = \frac{e^2}{4kT}\int_{-\infty}^{+\infty} D(E)sech^2\left[\frac{E+\varphi}{2kT}\right]dE \qquad 4\text{-}2$$

where Q is the excessive charge on the electrode and φ is external potential. See Ref. 14 for details about how we compute C_Q.

Classical Molecular Dynamics (CMD) simulations were performed to obtain EDL capacitance based on the same nitrogen-doped configurations as those used in calculating quantum capacitance. As illustrated in Fig. 1a, the simulated channel system consists of a slab of 1.0 M NaCl aqueous solution enclosed between two electrodes. The separation between the two electrodes was set to 5.0 nm to ensure a bulk-like behavior of the electrolyte in the channel center. The SPC/E model was used for the water molecules;[31] the Lennard-Jones (LJ) parameters for Na^+ and Cl^- were taken from the work of Smith *et al*.[32] All atoms in the electrode were described by a polymer consistent force field (PCFF)[33, 34]

and were fixed in space during the simulation. The electrode-electrolyte interaction included the Coulombic contribution (accounted for from the electrostatic interaction between atomic charges) and the van der Waals (vDW) contribution (accounted for from the LJ potentials). The LJ parameters for the vdW interaction between an electrode atom (type i with LJ parameters σ_{ii} and ϵ_{ii}) and an electrolyte atom (type j with LJ parameters σ_{jj} and ϵ_{jj}) were obtained by using Lorentz-Berthelot rules: $\sigma_{ij} = \frac{1}{2}(\sigma_{ii} + \sigma_{jj})$ and $\epsilon_{ij} = \left(\epsilon_{ii}\epsilon_{jj}\right)^{1/2}$.

The simulations were performed in the NVT ensemble using the MD package GROMACS.[35] Since the system has a slab geometry, the slab-PME method[36] was used here to compute the electrostatic interaction. The dimension vertical to the electrode was set to be 5 times the electrode separation to guarantee that the accuracy of the electrostatic force calculation is comparable to that of the two-dimensional Ewald method.[37] Each simulation was initiated at 800 K for 2 ns, followed by 9 ns of equilibrating at 298 K, with temperature controlled by Berendsen thermostat. Another 15 ns of production run was performed for analysis. The time step of 2 fs was applied and the atomic positions were saved every 4 ps. Our past experience showed that 2-fs time step is sufficient enough to yield stable dynamics for the aqueous systems. Herein, we indeed found that 2-fs time step afforded stable dynamics and stable electrostatic potential profiles in the water/graphene system.[38, 39] In addition, to ensure statistical accuracy, each simulation was repeated 3 times with different initial configurations (electrode configurations shown in Fig. 4-1b-d).

Different electrical potentials were created by varying the surface charge densities of the electrode. The excess charges were evenly distributed to each atom. The final partial

charge of each atom is comprised of the excess charge and the partial charge from force field. MD calculation setup is similar to previous work. [40]

We establish the total capacitance as a function of applied voltage (φ_a) by combining C_Q and C_{EDL} as described in literature.[14] First, we calculated the charging curves (Q vs.φ) for both quantum and EDL capacitances separately: quantum capacitance as a function of $\varphi_{QC} = (E - E_{Fermi})/e$ and EDL capacitance as a function of $\varphi_{EDL} = \varphi - \varphi_{PZC}$. Then, we used the interfacial charge Q to connect the two capacitances by obtaining the corresponding potential drops φ_{EDL} and φ_{QC} from EDL and quantum capacitances, respectively, at the same surface charge. So the total applied potential drop $\varphi_a = \varphi_{EDL} + \varphi_{QC}$ and total capacitance is therefore $C_{tot} = Q/\varphi_a$. By varying Q, the charging curve for the total capacitance is obtained.[41]

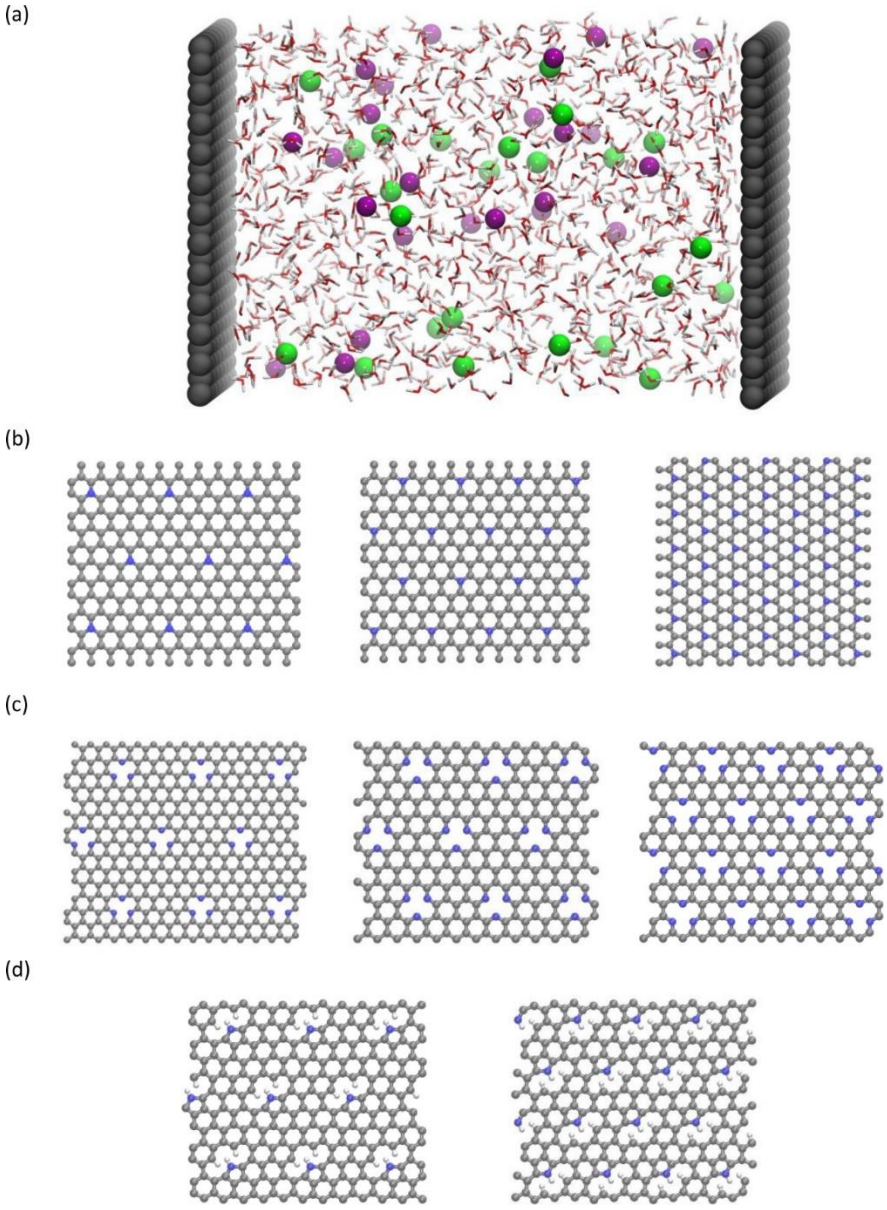


Fig. 4-1. (a) Snapshot of the MD simulation system; (b) graphitic N-doped graphene sheets with doping percentage of 3.1%, 5.5% and 12.5% from left to right; (c) pyridinic N-doped graphene with doping percentage of 6.1%, 9.7% and 17.6% from left to right; (d) pyrrolic N-doped graphene with doping percentage of 3.2% and 5.9% from left to right. The concentration percentage is defined by the atom ratio from the number of atoms in the system (C and N). For instance, the N concentration is N atoms/(N atoms +C atoms). Grey, blue, purple, green, red and white balls denote the carbon, nitrogen, Na^+, Cl^-, oxygen and hydrogen atoms respectively.

4.3 Results and discussion

We first examine the quantum capacitance, then the EDL capacitance, and finally the total capacitance of N-doped graphene electrodes.

4.3.1 Quantum capacitance of different N-doping configurations at low concentration

We calculated the quantum capacitance of the N-doped graphene with different doping mole concentration. The three most common configurations are chosen: graphitic, pyridinic and pyrrolic,[26, 42-44] as shown in Fig. 4-1b, 4-1c and 4-1d, respectively. The quantum capacitance and Density of States (DOS) of these three N-doping configurations are plotted in Fig. 4-2 and Fig. 4-3, respectively. One can see that graphitic and pyridinic N-doping configuration can greatly increase quantum capacitance, but pyrrolic N shows a "V"-shaped curve similar to pristine graphene.

The quantum capacitance shown in Fig. 4-2 can be explained by the n-doping and p-doping mechanism in graphene sheet.[45] In the pyrrolic N-doping configuration, N atom can donate an extra electron in the P_z orbital due to the formation of N-H bond but the associated C vacancy results in the loss of one electron in the delocalized $\boldsymbol{\pi}$ bond. Thus, the total number of electron does not change compared to pristine graphene. This explains why the pyrrolic N-doping configuration shows a "V"-shaped quantum capacitance similar to pristine graphene; the DOS plots of pristine graphene and pyrrolic-N-doped graphene are also similar (Fig. 4-3). Graphitic N-doping can be regarded as an electron donator, which contributes one more electron to the delocalized $\boldsymbol{\pi}$ bond than C atom. Thus, the "Dirac Point" moves toward higher energy position and the DOS near the Fermi level

increases (Fig. 4-3), so the quantum capacitance increases. In pyridinic N-doping, the number of electron on the P_z orbital of nitrogen does not change, but pyridinic N-doping causes a C vacancy and the system loses one electron compared to pristine graphene. Thus, the system is like a p-doping semiconductor, which shifts the "Dirac Point" down; the DOS near the Fermi level increases greatly (Fig. 4-3) and the quantum capacitance increases consequently.

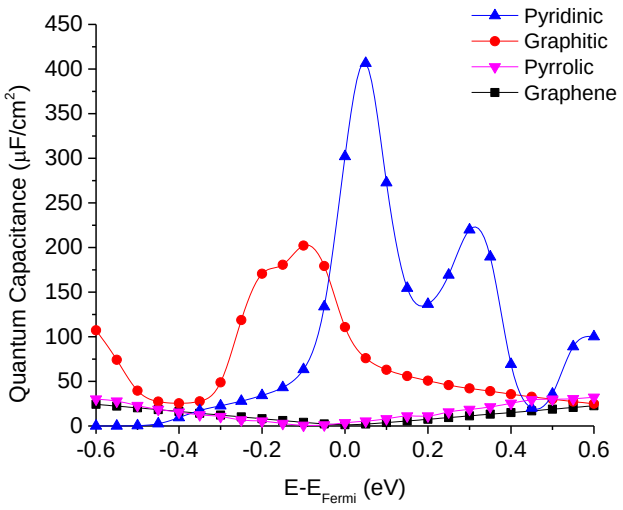


Fig. 4-2. Quantum capacitances of graphitic, pyridinic, and pyrrolic N-doped graphenes, with mole fraction of nitrogen at 3.1%, 9.7%, and 5.5%, respectively, in comparison with that of pristine graphene.

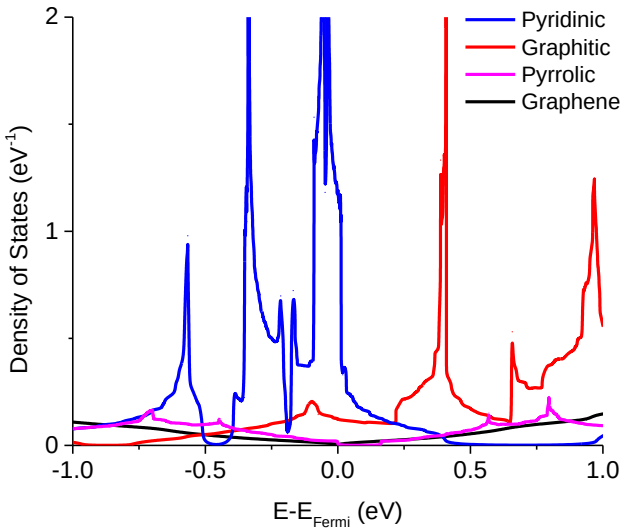


Fig. 4-3. Total Density of States (DOS) of graphitic, pyridinic, and pyrrolic N-doped graphenes, with mole fraction of nitrogen at 3.1%, 9.7%, and 5.5%, respectively, in comparison with that of pristine graphene.

4.3.2 Quantum capacitance of graphitic N-doped graphene at different doping levels

We computed the quantum capacitance of graphitic N-doping configuration with different doping concentrations and the results are plotted in Fig. 4-4. One can see that quantum capacitance exhibits considerable fluctuation, which is different from a smooth curve from a previous report.[46] This may be due to our much denser k-point sampling in the Brillouin zone. We found that high doping concentration can increase quantum capacitance and change the peak position, due to the corresponding change in the total DOS with concentration. As mentioned above, graphitic N-doping can be treated as the n-doping type semiconductor, which will cause the "Dirac Point" move to the position below

Fermi level. Thus, as the concentration goes down, quantum capacitance decreases and the "Dirac Point" tends to move back to the Fermi level.

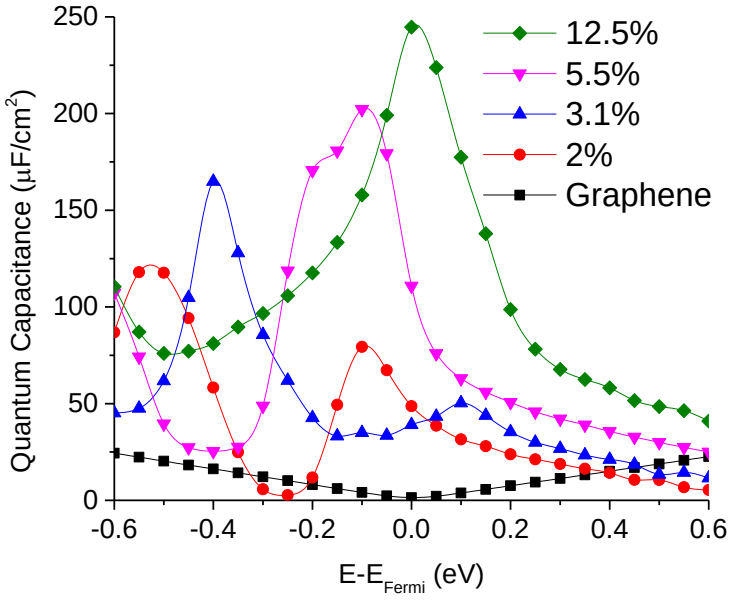


Fig 4-4. Quantum capacitance of graphitic N-doped single layer graphene with different doping concentrations in comparison with that of pristine graphene.

4.3.3 Quantum capacitance of pyridinic N-doped graphene at different doping levels

The quantum capacitance of pyridinic N-doped graphene with different doping concentrations is plotted in Fig. 4-5. In pyridinic N-doping configuration, the quantum capacitance enhancement is much stronger than graphitic N-doping under a comparable doping concentration. The quantum capacitance maximum can reach 400 μF/cm^2 in pyridinic N-doping configuration with the 9.7% doping concentration, but the quantum capacitance maximum is only ~250 μF/cm^2 with 12.5% graphitic N-doping. However, the

quantum capacitance fluctuation in pyridinic configuration is much stronger. Unlike graphitic N-doping, the quantum capacitance of pyridinic N-doping configuration will be very close to zero when the potential is below more negative than -0.4 eV. This character in pyridinic configuration does not depend on the doping concentration and will severely limit the total capacitance when the applied voltage is significantly negative. This extremely low quantum capacitance can be explained by the existence of a small gap at the "Dirac Point" caused by the p-type doping mechanism. One can see this gap in the DOS plot (Figure 4-3) at 0.5 ~1.0 eV, corresponding to a negative electrode potential of about -0.5 to -1.0 V.

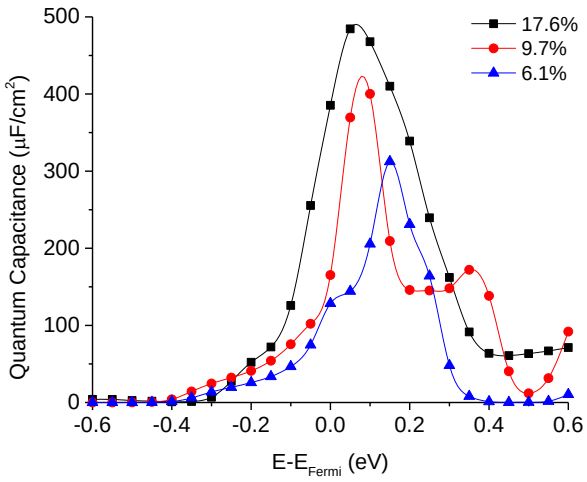


Fig 4-5. Quantum capacitance of pyridinic N-doped graphene with different doping concentrations.

4.3.4 Quantum capacitance of pyrrolic N-doped graphene.

The quantum capacitance of pyrrolic N-doping graphene with different doping concentration is plotted in Fig. 4-6. Unlike the graphitic and pyridinic N-doping configurations, pyrrolic N-doping configuration exhibits a "V"-shaped quantum

capacitance similar to that of pristine graphene when the doping concentration is low. As discussed previously,[45] pyrrolic N-doping configuration has the same amount of electrons as pristine graphene and can be regarded as neither n-type nor p-type doped graphene due to the formation of N-H bond and vacancy. For a graphene or quasi-graphene type of 2D materials, the total DOS always shows a "V" shape and the "Dirac Point" will be near the Fermi level. At low doping concentration, the correlation of pyrrolic N-doped graphene and vacancy between each unit cell can be treated as a small perturbation. Thus, the total DOS and quantum capacitance are very close to those of pristine graphene. However, things are different when doping concentration is quite large. In this situation (doping concentration is 5.9%), quantum capacitance approaches zero near the Fermi level due to a gap in the total DOS as shown in Fig. 4-7.

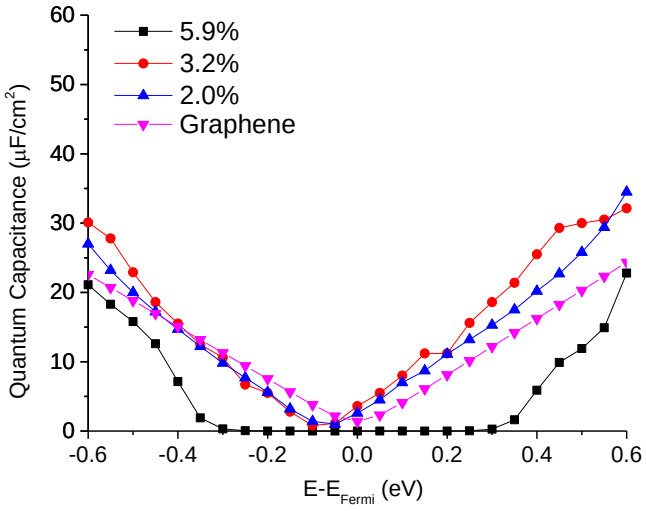


Fig 4-6. Quantum capacitance of pyrrolic N-doped graphene with different doping concentrations in comparison with that of pristine graphene.

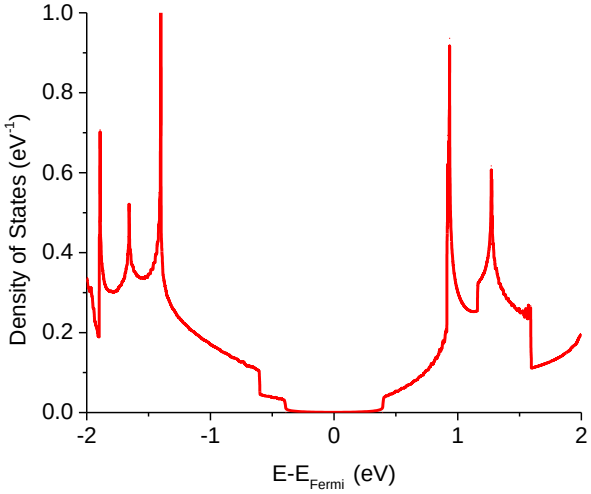


Fig 4-7. Total electronic density of states of pyrrolic N-doped graphene with the doping concentration of 5.9%.

4.3.5 EDL capacitance of N-doped graphene in 1M NaCl aqueous electrolyte

Generally speaking, the EDL capacitance of carbon electrodes is ~20 μF/cm^2 in aqueous electrolyte[8] and ~8 μF/cm^2 in ionic liquid.[47-49] The voltage window is about PZC ±0.6 V in an aqueous electrolyte and about PZC ±1.5 V in an ionic liquid. Since the quantum capacitance that we explored lie mainly and is more reliable in PZC ±0.6 V, we focus on the capacitance of doped graphene electrodes in an aqueous electrolyte.

The differential capacitance of N-doped graphene calculated by MD simulation in 1M NaCl aqueous electrolyte is plotted in Fig. 4-8. One can see that comparing with pristine graphene, the EDL capacitance is almost the same for the pyrrolic configuration and perturbed to a small degree in the case of graphitic and pyridinic configurations. At high levels of doping, the differential capacitance is likely affected by the partial charge of dopant, causing the change on EDL capacitance curves as shown in Fig. 4-8b and 4-8c. In

most experimental studies, the total nitrogen content is lower than 10%;[42] in this case, Fig. 4-8 shows that the EDL capacitance does not change much in comparison with that of pristine graphene. This conclusion was also found previously for N-doped graphene in an ionic liquid electrolyte.[46]

From the EDL capacitance in Fig. 4-8, we can conclude that the capacitance enhancement caused by N-doping effect is not due to EDL capacitance. From Eq. 4-1, we know that total capacitance can be estimated from knowledge of both the quantum capacitance and EDL capacitance. Consequently, quantum capacitance may be the key factor in explaining the capacitance enhancement of N-doping effect. Specifically, the inequality $C_{total} < \min(C_Q, C_{EDL})$ suggests that in those N-doped systems in which $C_Q < C_{EDL}$, the quantum capacitance will be the predominant determinant of the total capacitance. For systems in which $C_Q > C_{EDL}$, the EDL capacitance will be the predominant determinant of total capacitance.

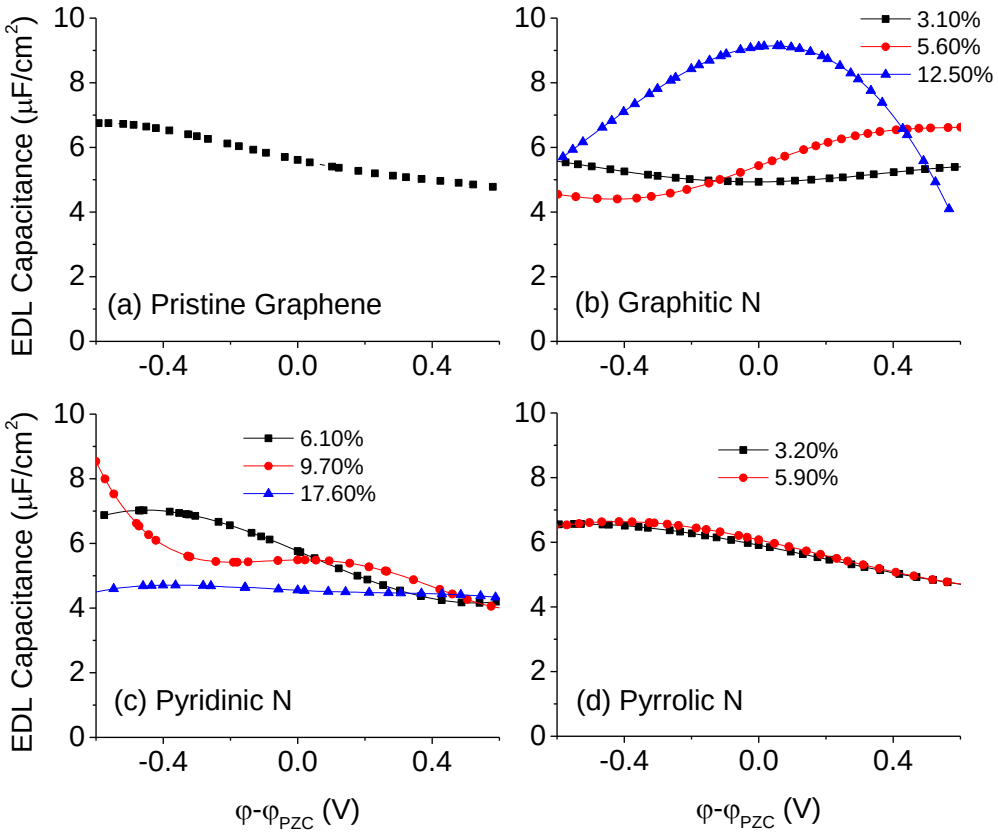


Fig 4-8. Electric double-layer (EDL) capacitance of (a) pristine graphene, (b) graphitic, (c) pyridinic and (d) pyrrolic Nitrogen-doped single layer graphene with different doping concentrations. The EDL capacitance is obtained from classical MD simulation for 1M NaCl aqueous electrolyte.

4.3.6 Total integral and differential capacitance of N-doped graphene in 1M NaCl electrolyte

Now that we have computed both quantum and EDL capacitances separately, we can combine them to obtain total capacitance. To compare with experiment more clearly, we used the charging curve based on C_Q and C_{EDL} to calculate the integral capacitance from

-0.6 V to 0.6 V (Table 4-1). One can see that compared to pristine single-layer graphene, the integral capacitance increases about 63% in graphitic and 82% in pyridinic N-doping, but only by 4% in pyrrolic N-doped graphene. The capacitance enhancement in our prediction is in good experiment with Fu et al.'s experimental work[22] that showed capacitance enhancement about 50% for graphitic- and pyridinic-dominated configurations. Choi et al. applied nitrogen plasma to treat the graphene sample that may have caused more defects, and they found higher increases (over two times).[18]

We can obtain further insights from the total differential capacitance plotted in Fig. 4-9. Graphitic and pyridinic N-doped graphene both have high and similar integral capacitance, but very different differential capacitance. Graphitic N-doped graphene exhibits a more stable and flat differential capacitance in the voltage window. Pyridinic N-doped graphene exhibits a larger differential capacitance than graphitic N-doped graphene at negative surface potential, but the differential capacitance goes down as the electrode potential go up. In addition, the calculated total differential capacitance curves of graphitic and pyridinic are very close to the EDL capacitance obtained from MD simulation. This is because for both graphitic and pyridinic nitrogens, quantum capacitances are much larger than EDL capacitances and the total charging dictated by the EDL charging. Unlike graphitic and pyridinic N-doped graphenes, pyrrolic N-doped graphene shows a "V"-shaped differential capacitance similar to that of pristine graphene and in good agreement with the experiment.[16]

Table 4-1. Integral capacitance of different types of N-doped graphene. The voltage window is from -0.6 V to 0.6 V.

N-type	Integral Capacitance (μF/cm^2)
Pristine Graphene	2.93
Graphitic	4.79
Pyridinic	5.34
Pyrrolic	3.05

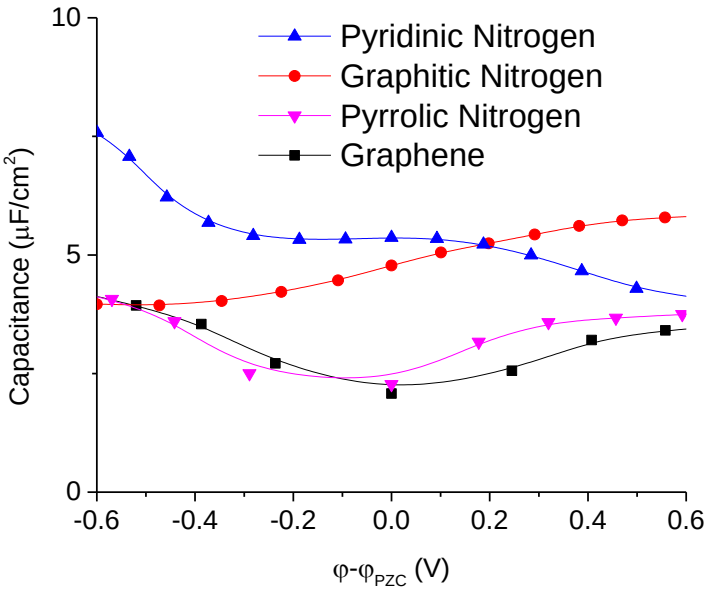


Fig 4-9. Total differential capacitance of different types of N-doped graphene for 1M NaCl aqueous electrolyte

4.3.7 Relevance to real N-doped carbon electrodes

In real carbon or nitrogen-doped carbon materials, the electrode structure is very complicated. Experimentalists always measure BET surface area and pore size distribution to obtain some porosity information in carbon material. For N-doped graphene, the commonly used way to identify different nitrogen types and their relative concentrations is XPS measurement of N 1s binding energy (B.E.). Our calculation has shown that different types of N-doping configuration have different quantum capacitance and differential capacitance. In real situation, experimentally obtained nitrogen doped graphene is a mixture of different N-doping configurations. Thus, the integrated capacitance should depend on the relative proportion of each configuration, which can be well controlled by synthesis method[42, 43] and characterized by XPS. It has been shown both experimentally and theoretically that pyridinic and pyrrolic nitrogens have stronger thermal stability than graphitic nitrogen in high temperature.[18, 22, 23, 50] Combining the thermal stability and our capacitance study, one can arrive at important implications for capacitance enhancement in N-doped graphene systems. The most important implication is that one should increase the concentrations of pyridinic and graphitic nitrogens and decrease that of pyrollic type to increase capacitance. Since graphitic nitrogen is much less stable than the other two types, one should focus on the pyridinic type if high-temperature treatment is needed in synthesis.

Our calculated quantum capacitance (Fig. 4-6) and differential capacitance (Fig. 4-9) of pyrrolic N-doped graphene both show a "V"-shaped capacitance vs. voltage curve, which is very similar to pristine graphene. This calculation shows very good agreement with Ruoff et al.'s experimental measurement in aqueous electrolyte;[16] their XPS analysis

showed that most nitrogen atoms are in the pyrrolic configuration. The large capacitance enhancement observed by Choi[18] and Liu[17, 19] is probably caused by graphitic and pyridinic N-doping configuration.

4.4 Summary and Conclusions

We have calculated the quantum, electric double-layer (EDL), and total capacitances of N-doped graphenes of different N types and concentrations to investigate their effects on capacitance. The EDL capacitance was calculated by classical MD simulation and quantum capacitance by Kohn-Sham DFT. Graphitic and pyridinic configurations greatly increase quantum capacitance, proportional to the doping concentration. Pyrrolic configuration shows a "V"-shaped quantum capacitance similar to that of pristine graphene, hence no enhancement. Classical MD simulations of the doped graphene electrodes in 1M NaCl aqueous electrotype showed that N-doping has little effect on EDL capacitance for the doping concentrations examined. Total capacitance, from combining quantum capacitance and EDL capacitance, exhibits good agreement with experimental results. When the pyrrolic configuration is dominant, measured differential capacitance shows a "V"-shaped curve similar to pristine graphene. When the graphitic or pyridinic configuration is dominant, large capacitance enhancement is observed. In conclusion, graphitic and pyridinic nitrogens can greatly increase total capacitance by increasing quantum capacitance and the pyrrolic configuration will limit the total capacitance increase. Given the much higher stability of pyridinic and pyrollic nitrogens than graphitic nitrogen, one should dope more pyridinic nitrogen and avoid the pyrrolic type.

References

(1) Zhang, L. L.; Zhao, X. S. Carbon-based materials as supercapacitor electrodes. *Chem. Soc. Rev.* **2009**, 38, 2520-2531

(2) Wang, Y.; Shi, Z. Q.; Huang, Y.; Ma, Y. F.; Wang, C. Y.; Chen, M. M.; Chen, Y. S. Supercapacitor Devices Based on Graphene Materials. *J. Phys. Chem. C* **2009**, 113, 13103-13107

(3) Chmiola, J.; Yushin, G.; Gogotsi, Y.; Portet, C.; Simon, P.; Taberna, P. L. Anomalous increase in carbon capacitance at pore sizes less than 1 nanometer. *Science* **2006**, 313, 1760-1763

(4) Fuertes, A. B.; Pico, F.; Rojo, J. M. Influence of pore structure on electric double-layer capacitance of template mesoporous carbons. *J. Power Sources* **2004**, 133, 329-336

(5) Vix-Guterl, C.; Frackowiak, E.; Jurewicz, K.; Friebe, M.; Parmentier, J.; Beguin, F. Electrochemical energy storage in ordered porous carbon materials. *Carbon* **2005**, 43, 1293-1302

(6) Stoller, M. D.; Park, S. J.; Zhu, Y. W.; An, J. H.; Ruoff, R. S. Graphene-Based Ultracapacitors. *Nano Lett.* **2008**, 8, 3498-3502

(7) Wang, D. W.; Li, F.; Wu, Z. S.; Ren, W. C.; Cheng, H. M. Electrochemical interfacial capacitance in multilayer graphene sheets: Dependence on number of stacking layers. *Electrochem. Commun.* **2009**, 11, 1729-1732

(8) Stoller, M. D.; Magnuson, C. W.; Zhu, Y. W.; Murali, S.; Suk, J. W.; Piner, R.; Ruoff, R. S. Interfacial capacitance of single layer graphene. *Energ Environ. Sci.* **2011**, 4, 4685-4689

(9) Alzari, V.; Sanna, V.; Biccai, S.; Caruso, T.; Politano, A.; Scaramuzza, N.; Sechi, M.; Nuvoli, D.; Sanna, R.; Mariani, A. Tailoring the physical properties of nanocomposite films by the insertion of graphene and other nanoparticles. *Compos Part B-Eng* **2014**, 60, 29-35

(10) Kott, T. M.; Hu, B. H.; Brown, S. H.; Kane, B. E. Valley-Degenerate Two-Dimensional Electrons in the Lowest Landau Level. *Phys. Rev. B* **2014**, 89, 041107

(11) Brooksby, P.; Farquhar, A.; Dykstra, H.; Waterland, M.; Downard, A. Quantum capacitance of aryldiazonium modified large area few-layer graphene electrodes. *J. Phys. Chem. C* **2015**, 119, 25778–25785

(12) Shan, X. N.; Chen, S.; Wang, H.; Chen, Z. X.; Guan, Y.; Wang, Y. X.; Wang, S. P.; Chen, H. Y.; Tao, N. J. Mapping Local Quantum Capacitance and Charged Impurities in Graphene via Plasmonic Impedance Imaging. *Adv Mater* **2015**, 27, 6213-6219

(13) Paek, E.; Pak, A. J.; Hwang, G. S. On the Influence of Polarization Effects in Predicting the Interfacial Structure and Capacitance of Graphene-like Electrodes in Ionic Liquids. *J. Chem. Phys.* **2015**, 142, 024701

(14) Paek, E.; Pak, A. J.; Hwang, G. S. A computational study of the interfacial structure and capacitance of graphene in [BMIM][PF_6] ionic liquid. *J. Electrochem. Soc.* **2013**, 160, A1-A10

(15) Vatamanu, J.; Ni, X.; Liu, F.; Bedrov, D. Tailoring graphene-based electrodes from semiconducting to metallic to increase the energy density in supercapacitors. *Nanotechnology* **2015**, 26, 464001

(16) Zhang, L. L.; Zhao, X.; Ji, H. X.; Stoller, M. D.; Lai, L. F.; Murali, S.; Mcdonnell, S.; Cleveger, B.; Wallace, R. M.; Ruoff, R. S. Nitrogen doping of graphene and its effect on quantum Capacitance, and a new insight on the enhanced capacitance of N-doped carbon. *Energ Environ. Sci.* **2012**, 5, 9618-9625

(17) Zhang, C. H.; Fu, L.; Liu, N.; Liu, M. H.; Wang, Y. Y.; Liu, Z. F. Synthesis of Nitrogen-Doped Graphene Using Embedded Carbon and Nitrogen Sources. *Adv. Mater.* **2011**, 23, 1020-1024

(18) Jeong, H. M.; Lee, J. W.; Shin, W. H.; Choi, Y. J.; Shin, H. J.; Kang, J. K.; Choi, J. W. Nitrogen-doped graphene for high-performance ultracapacitors and the importance of nitrogen-doped sites at basal planes. *Nano Lett.* **2011**, 11, 2472-2477

(19) Cao, H. L.; Zhou, X. F.; Qin, Z. H.; Liu, Z. P. Low-temperature preparation of nitrogen-doped graphene for supercapacitors. *Carbon* **2013**, 56, 218-223

(20) Wang, K.; Li, L. W.; Zhang, T. Z.; Liu, Z. F. Nitrogen-Doped Graphene for Supercapacitor with Long-term Electrochemical Stability. *Energy* **2014**, 70, 612-617

(21) Wen, Z. H.; Wang, X. C.; Mao, S.; Bo, Z.; Kim, H.; Cui, S. M.; Lu, G. H.; Feng, X. L.; Chen, J. H. Crumpled Nitrogen-Doped Graphene Nanosheets with Ultrahigh Pore Volume for High-Performance Supercapacitor. *Adv. Mater.* **2012**, 24, 5610-5616

(22) Jiang, B. J.; Tian, C. G.; Wang, L.; Sun, L.; Chen, C.; Nong, X. Z.; Qiao, Y. J.; Fu, H. G. Highly concentrated, stable nitrogen-doped graphene for supercapacitors: Simultaneous doping and reduction. *Appl. Surf. Sci.* **2012**, 258, 3438-3443

(23) Sun, L.; Wang, L.; Tian, C. G.; Tan, T. X.; Xie, Y.; Shi, K. Y.; Li, M. T.; Fu, H. G. Nitrogen-doped graphene with high nitrogen level via a one-step hydrothermal reaction of graphene oxide with urea for superior capacitive energy storage. *RSC Adv.* **2012**, 2, 4498-4506

(24) Zou, Y. Q.; Kinloch, I. A.; Dryfe, R. A. W. Nitrogen-Doped and Crumpled Graphene Sheets with Improved Supercapacitance. *J. Mater. Chem. A* **2014**, 2, 19495-19499

(25) Gammon, W. J.; Kraft, O.; Reilly, A. C.; Holloway, B. C. Experimental comparison of N(1s) X-ray photoelectron spectroscopy binding energies of hard and elastic amorphous carbon nitride films with reference organic compounds. *Carbon* **2003**, 41, 1917-1923

(26) Zhao, L. Y.; He, R.; Rim, K. T.; Schiros, T.; Kim, K. S.; Zhou, H.; Gutierrez, C.; Chockalingam, S. P.; Arguello, C. J.; Palova, L., et al. Visualizing Individual Nitrogen Dopants in Monolayer Graphene. *Science* **2011**, 333, 999-1003

(27) Petrosyan, S. A.; Rigos, A. A.; Arias, T. A. Joint Density-Functional Theory: Ab initio Study of Cr_2O_3 Surface Chemistry in Solution. *J. Phys. Chem. B* **2005**, 109, 15436-15444

(28) Letchworth-Weaver, K.; Arias, T. A. Joint density functional theory of the electrode-electrolyte interface: application to fixed electrode potentials, interfacial capacitances, and potentials of zero charge. *Phys. Rev. B* **2012**, 86, 075140

(29) Perdew, J. P.; Burke, K.; Ernzerhof, M. Generalized Gradient Approximation Made Simple. *Phys. Rev. Lett.* **1996**, 77, 3865-3868

(30) Garrity, K. F.; Bennett, J. W.; Rabe, K. M.; Vanderbilt, D. Pseudopotentials for High-throughput DFT Calculations. *Comput. Mater. Sci.* **2014**, 81, 446-452

(31) Berendsen, H. J. C.; Grigera, J. R.; Straatsma, T. P. The Missing Term in Effective Pair Potentials. *J. Phys. Chem.* **1987**, 91, 6269-6271

(32) Smith, D. E.; Dang, L. X. Interionic Potentials of Mean Force for Srcl2 in Polarizable Water - a Computer-Simulation Study. *Chem. Phys. Lett.* **1994**, 230, 209-214

(33) Sun, H.; Mumby, S. J.; Maple, J. R.; Hagler, A. T. An Ab-Initio Cff93 All-Atom Force-Field for Polycarbonates. *J. Am. Chem. Soc.* **1994**, 116, 2978-2987

(34) Sun, H. Ab-Initio Characterizations of Molecular-Structures, Conformation Energies, and Hydrogen-Bonding Properties for Polyurethane Hard Segments. *Macromolecules* **1993**, 26, 5924-5936

(35) Hess, B.; Kutzner, C.; van der Spoel, D.; Lindahl, E. GROMACS 4: Algorithms for highly efficient, load-balanced, and scalable molecular simulation. *J. Chem. Theory. Comput.* **2008**, 4, 435-447

(36) Yeh, I. C.; Berkowitz, M. L. Ewald summation for systems with slab geometry. *J. Chem. Phys* **1999**, 111, 3155-3162

(37) Darden, T.; York, D.; Pedersen, L. Particle Mesh Ewald - an N.Log(N) Method for Ewald Sums in Large Systems. *J. Chem. Phys.* **1993**, 98, 10089-10092

(38) Chialvo, A. A.; Vlcek, L.; Cummings, P. T. Surface Corrugation Effects on the Water-Graphene Interfacial and Confinement Behavior. *J Phys Chem C* **2013**, 117, 23875-23886

(39) Chialvo, A. A.; Vlcek, L.; Cummings, P. T. Surface Strain Effects on the Water-Graphene Interfacial and Confinement Behavior. *J Phys Chem C* **2014**, 118, 19701-19711

(40) Feng, G. A.; Qiao, R.; Huang, J. S.; Sumpter, B. G.; Meunier, V. Atomistic Insight on the Charging Energetics in Subnanometer Pore Supercapacitors. *J. Phys. Chem. C* **2010**, 114, 18012-18016

(41) Zhan, C.; Neal, J.; Wu, J. Z.; Jiang, D. E. Quantum Effects on the Capacitance of Graphene-Based Electrodes. *J. Phys. Chem. C* **2015**, 119, 22297–22303

(42) Wang, H. B.; Maiyalagan, T.; Wang, X. Review on Recent Progress in Nitrogen-Doped Graphene: Synthesis, Characterization, and Its Potential Applications. *ACS Catal.* **2012**, 2, 781-794

(43) Lu, Y. H.; Huang, Y.; Zhang, M. J.; Chen, Y. S. Nitrogen-Doped Graphene Materials for Supercapacitor Applications. *J. Nanosci. Nanotechnol.* **2014**, 14, 1134-1144

(44) Lv, R.; Li, Q.; Botello-Mendez, A. R.; Hayashi, T.; Wang, B.; Berkdemir, A.; Hao, Q. Z.; Elias, A. L.; Cruz-Silva, R.; Gutierrez, H. R., et al. Nitrogen-doped graphene: beyond single substitution and enhanced molecular sensing. *Sci. Rep.* **2012**, 2, 586

(45) Wang, B.; Tsetseris, L.; Pantelides, S. T. Introduction of nitrogen with controllable configuration into graphene via vacancies and edges. *J. Mater. Chem. A* **2013**, 1, 14927-14934

(46) Paek, E.; Pak, A. J.; Kweon, K. E.; Hwang, G. S. On the origin of the enhanced supercapacitor performance of nitrogen-doped graphene. *J. Phys. Chem. C* **2013**, 117, 5610-5616

(47) Vatamanu, J.; Cao, L. L.; Borodin, O.; Bedrov, D.; Smith, G. D. On the Influence of Surface Topography on the Electric Double Layer Structure and Differential Capacitance of Graphite/Ionic Liquid Interfaces. *J. Phys. Chem. Lett.* **2011**, 2, 2267-2272

(48) Vatamanu, J.; Borodin, O.; Smith, G. D. Molecular Simulations of the Electric Double Layer Structure, Differential Capacitance, and Charging Kinetics for N-Methyl-N-propylpyrrolidinium Bis(fluorosulfonyl)imide at Graphite Electrodes. *J. Phys. Chem. B* **2011**, 115, 3073-3084

(49) Vatamanu, J.; Borodin, O.; Smith, G. D. Molecular Insights into the Potential and Temperature Dependences of the Differential Capacitance of a Room-Temperature Ionic Liquid at Graphite Electrodes. *J. Am. Chem. Soc.* **2010**, 132, 14825-14833

(50) Tian, Z. Q.; Dai, S.; Jiang, D. E. Stability and Core-Level Signature of Nitrogen Dopants in Carbonaceous Materials. *Chem. Mater.* **2015**, 27, 5775-5781

Chapter 5 Contribution of Dielectric Screening to the Total Capacitance of Few-Layer Graphene Electrodes

5.1 Introduction

Electric double-layer capacitors (EDLCs), as a type of supercapacitors, are playing an important role in energy storage because of its high power density and long cycle life.[1] In recent years, graphene and advanced porous carbons have been found to be very promising for EDLCs.[2-11] Unlike traditional electrode materials, graphene has quantum capacitance (C_Q) due to its limited density of states (DOS), which could have a significant influence on its overall capacitive performance.[12-14] Hwang et al. first developed an approach to calculate total capacitance (C_{tot}) by separately modeling quantum capacitance and EDL capacitance (C_{EDL}) on single layer graphene:[15] quantum capacitance is modeled by the electronic DOS of the neutral electrode[14-16] and EDL capacitance is from classical molecular dynamics (CMD) simulation.[17-24] This approach of computing the total capacitance ignores the close interaction between the electronic structure of the electrode and the distribution of the mobile ions in the electrolyte. Especially, screening effect and charge penetration into the electrode surface could be important and contribute to total capacitance, which the separate, non-self-consistent approach cannot account for.

Few-layer graphene (FLG) electrode is a typical system that screening effect could affect the capacitance. However, the physical picture is still not clear in this system though several recent experiments have been done.[25-27] Although it is straightforward to measure the total differential capacitance by electrochemistry, C_{EDL} and C_Q of few layer graphene are not experimentally available from direct measurement. Ruoff et al.[28] measured C_{EDL} on

Pt surface and combined the measured C_{EDL} with calculated C_Q to calculate the C_{tot} of single layer graphene. This calculated C_{tot} for the single-layer graphene shows good agreement with experimental measurement.[28] But in few layer graphene, a fixed C_{EDL} with increasing C_Q with the layer number[29] seems unable to explain the experimental results of how C_{tot} changes with the layer number.[25] Tao measured the C_Q of single layer graphene by subtracting C_{EDL} from C_{tot}, and his measured value is also quite comparable to theoretical prediction.[12] However, the measured C_Q of few layer graphene from Downard et al. is very low and does not match the theoretical C_Q.[15] Consequently, a comprehensive and clear theoretical understanding of the capacitance in few layer graphene is very necessary and the non-self-consistent approach of separately modeling C_{EDL} and C_Q has not been able to fulfill such a purpose. In this paper, we use an approach that describes the electrode and the electrolyte together self-consistently, in order to seek a clear physical picture of the capacitance of FLG electrodes and the role of screening effect.

5.2 Method

5.2.1 Electronic structure calculation of solvated electrodes

Electronic structure of a solvated graphene electrode is solved by Joint Density Functional Theory with an implicit solvation model, using the JDFTx package developed by Arias et al.[30] Periodic boundary condition is applied to describe the interface: Single layer graphene is modeled in a 2.460×2.460 Å^2 rhombus sheet as a unit cell. Few layer graphene is modeled as ABAB stacking pattern with the interlayer distance of 3.400 Å. The vacuum layer thickness is 20 Å along z-direction, which will be filled with an electrolyte described by the linear polarizable continuum model (LPCM).[30] The exchange-

correlation energy for the graphene electrode is described by Generalized Gradient Approximation in the form of Perdew-Burke-Ernzerhof functional (GGA-PBE).[31] Ultrasoft pseudopotential is used to describe the nuclei-electron interaction in carbon, with 40 hartree kinetic energy cutoff for plane-wave basis. 60×60×1 k-point mesh is used in sampling Brillouin zone of graphene electrodes to accurately capture the electronic chemical potential in the periodic system. Figure 5-1 shows the model setup.

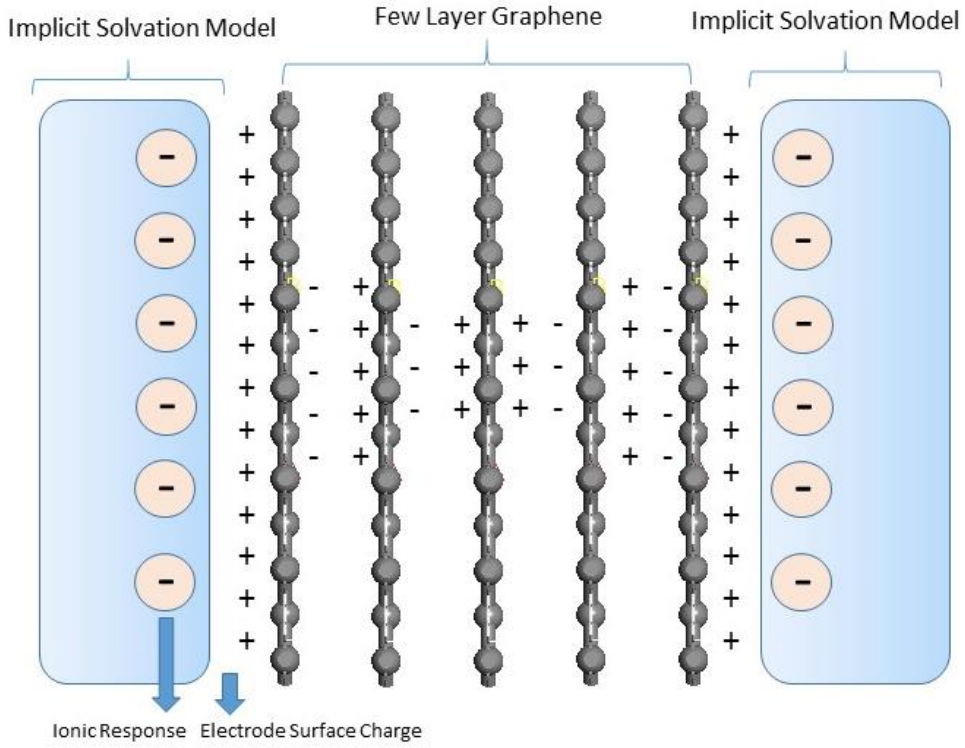


Figure 5-1. Schematic of a charged few layer graphene in contact with an implicit electrolyte on both sides.

5.2.2 Charging simulation and Fermi level shift

In calculations from JDFTx,[30, 32] C_{tot} is defined by the derivative of excess charge with respect to the chemical potential shift ($\Delta\varphi$). Potential of zero charge (PZC) is defined

by the electronic chemical potential of the neutral electrode system (Figure 5-2b). We separate the chemical potential shift ($\Delta\varphi$) into two parts as shown in Figure 5-2. The Fermi level shift (φ_Q) corresponds to band filling or emptying and therefore gives rise to quantum capacitance (C_Q). The band shift (φ_{NQ}), as we will show later, is the overall consequence of electrolyte response (giving rise to EDL capacitance) and electrode screening (giving rise to dielectric capacitance).

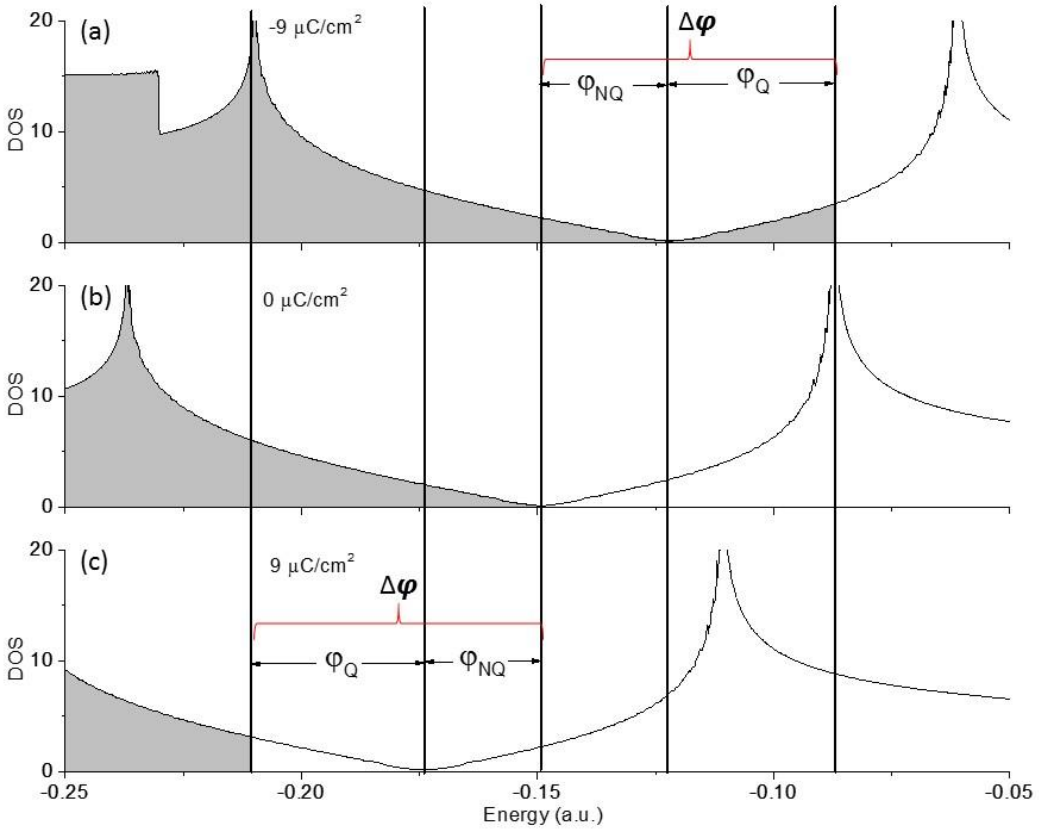


Figure 5-2. The definitions of the total potential drop ($\Delta\varphi$) across the electrode/electrolyte interface and its quantum (φ_Q) and non-quantum (φ_{NQ}) contributions in a JDFTx calculation: $\Delta\varphi$ is the shift in chemical potential under either a negative (a) or positive (c) surface charge density relative to the neutral surface (b); φ_Q is the shift of the Fermi level relative to the Dirac point; φ_{NQ} is the band shift relative to the neutral surface.

5.3 Results and discussion

5.3.1 Differential capacitance and total capacitance of FLG and Pt electrodes

We calculated area-normalized total differential capacitance and total integral capacitance of FLG in 6M implicit electrolyte, as shown in Figure 5-3a and 5-3b. A "U"-shaped differential capacitance in graphene capacitor has been observed both in experimental measurement[25, 28] and theoretical simulation,[14, 15, 32] and can be explained by the low quantum capacitance near PZC. With layer stacking, total differential capacitance and integral capacitance increase, but converge when layer number reaches three. For the single layer graphene, the calculated specific capacitance is about 115 F/g in 6M aqueous electrolyte, comparable to experimental value ~135 F/g in 5.5M KOH.[33] To separate the role of EDL contribution, we compared FLG with Pt(111), an ideal metal electrode for which the total capacitance is dominated by the EDL capacitance and the contributions of quantum capacitance and dielectric response are minimal. One can see that the C_{tot} of Pt (111) is pretty constant at about 13 $\mu F/cm^2$. This number can be considered as a good estimate of the C_{EDL} on the graphene surface as assumed previously by Ruoff et al.[28]

5.3.2 Quantum capacitance of FLG separated from total capacitance

Next we show the contribution of quantum capacitance from our JDFT results. Since we solved the Kohn-Sham eigenvalue for the charged system, the Fermi level and DOS are computed after band relaxation (Figure 5-2). Our calculated C_Q of FLG as a derivative of total charge with respect to Fermi level shift is shown in Figure 5-4. One can see that C_Q increases linearly with layer stacking, very similar to the results obtained in fixed band approximation (FBA).[29, 34] In FBA, the analytical solution of C_Q is derived from

the DOS of neutral electrode and electronic Fermi distribution function, which ignored the influence of excess charge on DOS. Recent work from Wood et al.[35] indicated that FBA could overestimate C_Q because of the influence of excess charge on DOS. However, our calculation of quantum capacitance based on relaxed band shows similar results to FBA. The large quantum capacitance beyond three layers of graphene suggests that their contribution to the total capacitance will be minor beyond three layers. The Pt(111) results in Figure 5-3b indicates that the EDL capacitance should be constant at about 13 $\mu F/cm^2$, but the total integral capacitance of FLG is only about 6 $\mu F/cm^2$ beyond three layers (Figure 5-3b). This suggests a third contribution to the total capacitance beyond the quantum and EDL capacitances. This third contribution is due to the dielectric response of the FLG electrode.

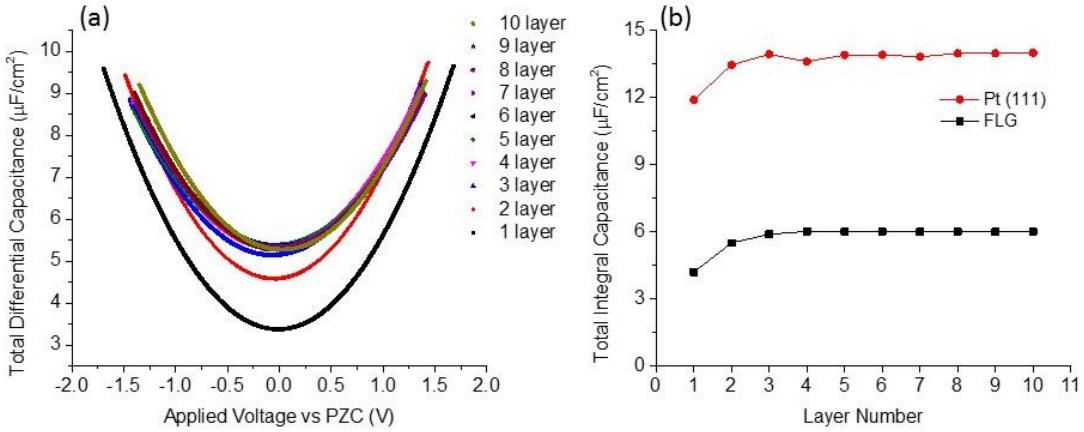


Figure 5-3. (a) Total differential capacitance of few-layer-graphene electrodes (b) Total integral capacitance of few-layer-graphene electrodes and multi-layer Pt (111) (voltage window is from -1V to 1V).

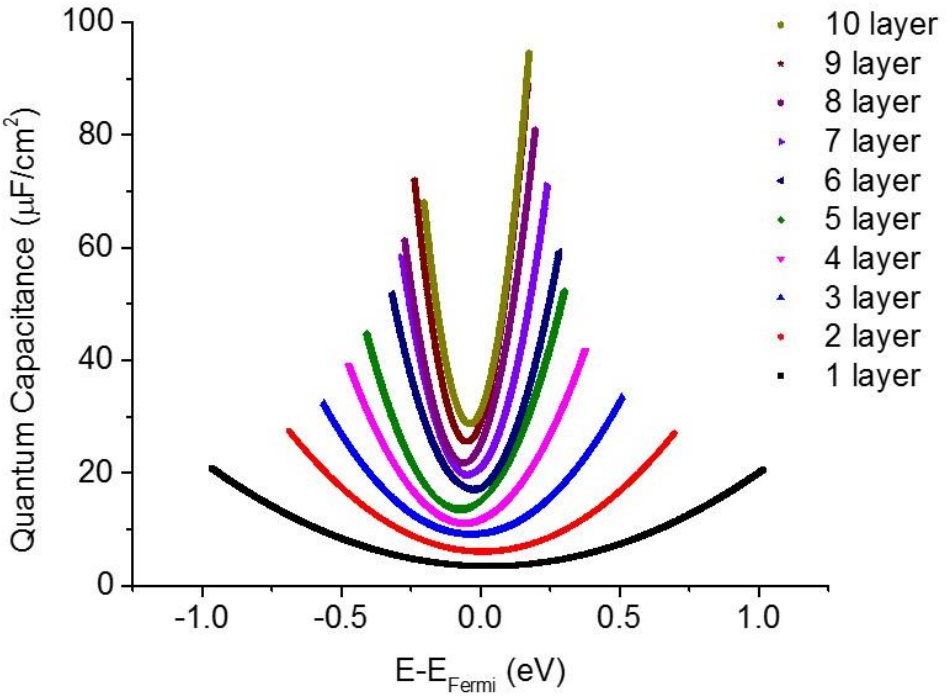


Figure 5-4. Calculated differential quantum capacitance (C_Q) of FLG from the Fermi level shift.

5.3.3 Dielectric screening effect in FLG

The screening of the electric field in FLG under a gate electrode has been examined by tight-binding models previously.[36, 37] Uesugi et al. experimentally studied the differential capacitance of FLG in ionic liquid electrolytes and theoretically analyzed the change of the capacitance with the graphene layers using classical electrostatics based on computed charge distribution of inside the FLG. The dielectric contribution was implicitly included in the so-called geometric capacitance (C_g) together with the double layer contribution in their analysis.[26] Hence the dielectric contribution has not been quantified. The JDFT approach here would allow us to separate and quantify the dielectric contribution via a self-consistent electronic structure calculation for a solvated electrode.

To examine in detail the dielectric response of the electrode, we plotted the change in the average electrostatic potential (computed self-consistently from the Hartree potential of the electronic system), $\Delta\psi(z)$, across the FLG electrode into the electrolyte layer at a fixed electrode charge density in Figure 5-5a. $\Delta\psi(z)$ corresponds to the band shift or φ_{NQ} in Figure 5-2. One can clearly see from Figure 5-5a that $\Delta\psi(z)$ increases as the position moves deeper into the electrode. The slope of $\Delta\psi(z)$ reflects the response electric field inside the FLG and how far the external electric field penetrates into the FLG electrodes; the distributions of the excess charge in the electrodes are plotted in Figure S5-1 in the Supporting Information (SI). When layer number is small, $\Delta\psi(z)$ continues going up as layer stacking since few graphene layer cannot completely screen the external electric field. When the layer number is eight (four layer on each side), FLG can completely screen external field so that $\Delta\psi(z)$ stop increasing in the center. Thus, the 4^{th} and 5^{th} graphene layers have the same potential drop. To show a comparison with the metal electrode, we also computed $\Delta\psi(z)$ in Pt (111). As shown in Figure 5-5b, two layer Pt shows a perfect screening to external field so that $\Delta\psi(z)$ does not increase with Pt layer stacking, which can explain why Pt has an almost constant capacitance. Moreover, $\Delta\psi(z)$ shows identical shape at the surface layer in FLG electrodes in Figure 5-5a, which means the contribution of EDL is roughly constant (the flat line in Figure 5-5a); the EDL region reflected by the fluid charge response is plotted in Figure S5-2 in SI. The corresponding EDL potential drop is about 0.7 V, leading to a C_{EDL} about 12.9 $\mu F/cm^2$. This EDL capacitance is comparable to that of Pt(111), which has a potential drop of 0.65 V and a corresponding EDL capacitance of 13.8 $\mu F/cm^2$. More important, Figure 5-5a shows that the dielectric

response inside the FLG electrodes also contributes to the total capacitance. Below we analyze this contribution in detail.

5.3.4 Contribution of dielectric screening and "three contribution" model

With the same charge density Q, total capacitance of any system is defined by Q/φ_{tot}, where φ_{tot} is the total potential drop or electronic chemical potential shift and can be regarded as the sum of quantum effect (φ_Q) and non-quantum effect (φ_{NQ}) as shown in Figure 5-2. φ_Q is defined by Fermi level shift, which corresponds to C_Q. φ_{NQ} is the overall consequence of electrolyte response (φ_{EDL}) and dielectric screening (φ_{Dielec}) of the electrode, both of which can be evaluated from the electrostatic potential (Figure 5-5a). Thus, total capacitance can be written as:

$$C_{tot} = \frac{Q}{\varphi_Q + \varphi_{Dielec} + \varphi_{EDL}} \quad 5\text{-}1$$

So:

$$\frac{1}{C_{tot}} = \frac{1}{C_Q} + \frac{1}{C_{Dielec}} + \frac{1}{C_{EDL}} \quad 5\text{-}2$$

To evaluate the exact influence of dielectric screening effect on the capacitance, we analyzed the potential drop and capacitance contribution in Figure 5-6a and 5-6b at a fixed surface charge density of 9 μC/cm^2. We found that with the layer number increasing, the quantum contribution (φ_Q) to the total potential drop decreases and the dielectric contribution (φ_{Dielec}) increases, while the EDL contribution remains about constant. The decreasing φ_Q and increasing φ_{Dielec} make the total potential drop (φ_{tot}) only change a little with layer stacking, which explains why total capacitance does not change much when n > 3. Figure 5-6b shows that the total capacitance in FLG electrode has three contributions:

C_Q, C_{EDL} and C_{Dielec}; dielectric capacitance (C_{Dielec}) becomes comparable to C_{EDL} beyond three layers, leading to a much smaller C_{tot}.

The present JDFT calculation employed an implicit solvation model. With an explicit solvation model, C_{EDL} would be more accurately predicted, but we expect that C_{Dielec} and C_Q would not be affected much by the solvation model since they are dominated by the electronic structure of the FLG electrode. Indeed, Hwang et al.[38] have shown through DFT-MD that C_Q is basically electrolyte-independent. In addition, we greatly varied the solvation parameter in our implicit model and found that the dielectric screening behavior inside the electrode is not influenced by the surface potential (Figure S5-3 in SI).

In few layer graphene, C_Q will increase linearly with the layer stacking, but C_{Dielec} will decrease, which could explain the converging behavior of total capacitance when layer number is above three. To increase total capacitance through electrode modification, on the one hand we can increase C_Q by doping effect[16, 39 40]and surface functionalization, on the other hand we should weaken the dielectric screening in electrode by increasing conductivity or decreasing material thickness. Our calculation also provides a deeper understanding on experimental work by Ruoff et al.[25]: the decreasing non-quantum capacitance with graphene layer stacking is due to dielectric screening effect in few layer graphene and not related to the Helmholtz layer structure as suggested.

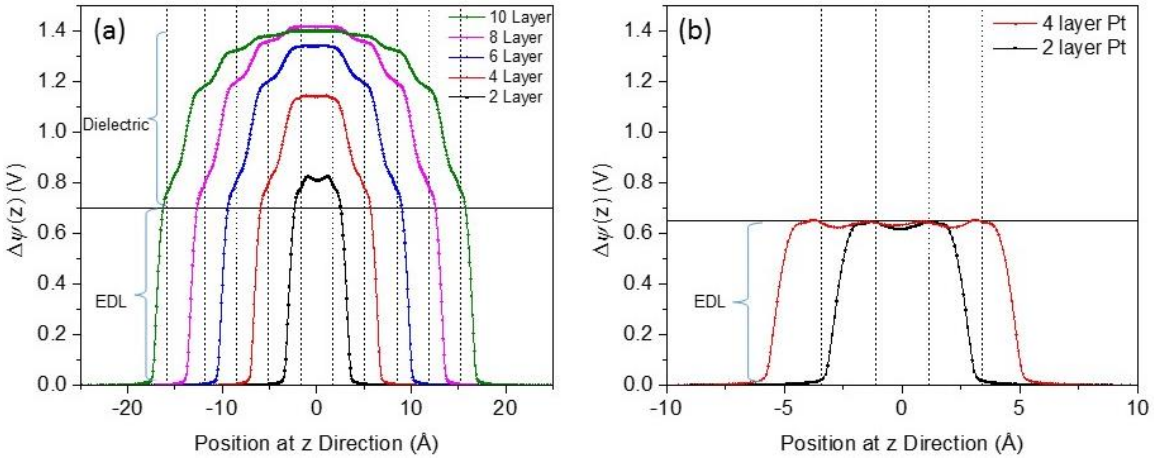


Figure 5-5. Planar average electrostatic potential drop, $\Delta\psi(z)$, in (a) few-layer-graphene (FLG) electrodes and (b) Pt (111). FLG and Pt have the same planar charge density. The dashed line indicates the position of each graphene and Pt layer.

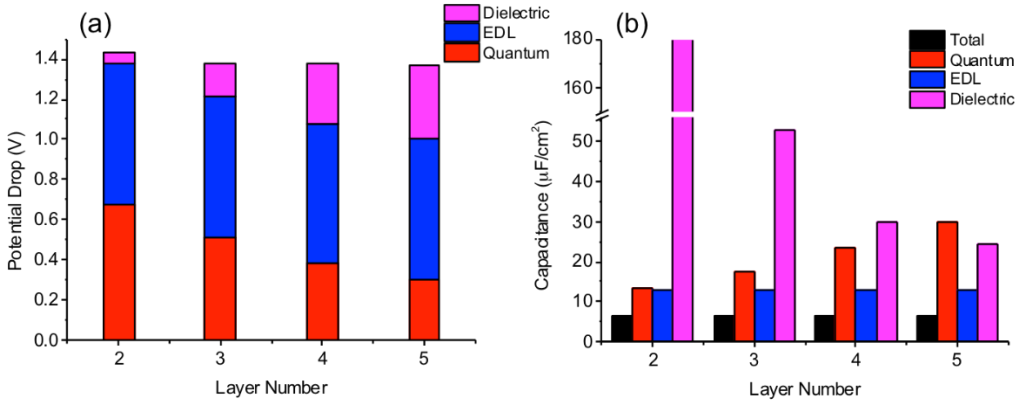


Figure 5-6. (a) Breakdown of the potential drop into quantum, EDL and dielectric screening contributions with the layer number under the same surface charge density of 9 μC/cm^2. (b) The corresponding capacitance contributions.

5.4 Summary and conclusion

In sum, we have applied the Joint Density Functional Theory to examine the capacitance of few layer graphene electrodes in contact with an implicit electrolyte. We found that the total capacitance converges to about 6 μF/cm^2 beyond about three layers of graphene. Quantum capacitance, as evaluated by the Fermi level shift, increases linearly

with the layer number and shows consistency with calculation from fixed-band-approximation.[29] EDL capacitance was found to be constant at about 13 μF/cm^2 with the layer number from the comparison with a perfect metal surface, Pt(111). The much lower total capacitance in comparison with the EDL capacitance for the few-layer-graphene electrode with three or more layers was found to be due to the dielectric screening effect of the electrode being a semiconductor. This dielectric screening converges at about four layers into the electrode. Thus, the change of the total capacitance with layer stacking is the overall consequence of increasing quantum capacitance, constant EDL capacitance, and decreasing dielectric capacitance. Our work provides a deeper understanding on the capacitance in few-layer-graphene electrodes and shows that the dielectric screening of a semiconducting electrode material is also a very important part of the total capacitance for an electric double layer capacitor.

References

(1) Zhang, L. L.; Zhao, X. S. Carbon-based materials as supercapacitor electrodes. *Chem. Soc. Rev.* **2009**, 38, 2520-2531

(2) Zhai, Y. P.; Dou, Y. Q.; Zhao, D. Y.; Fulvio, P. F.; Mayes, R. T.; Dai, S. Carbon materials for chemical capacitive energy storage. *Adv. Mater.* **2011**, 23, 4828-4850

(3) Wang, Y.; Shi, Z. Q.; Huang, Y.; Ma, Y. F.; Wang, C. Y.; Chen, M. M.; Chen, Y. S. Supercapacitor devices based on graphene materials. *J. Phys. Chem. C* **2009**, 113, 13103-13107

(4) Simon, P.; Gogotsi, Y. Materials for electrochemical capacitors. *Nat. Mater.* **2008**, 7, 845-854

(5) Chmiola, J.; Largeot, C.; Taberna, P. L.; Simon, P.; Gogotsi, Y. Monolithic carbide-derived carbon films for micro-supercapacitors. *Science* **2010**, 328, 480-483

(6) Dyatkin, B.; Gogotsi, Y. Effects of Structural Disorder and Surface Chemistry on Electric Conductivity and Capacitance of Porous Carbon Electrodes. *Faraday Discuss.* **2014**, 172, 139-162

(7) Black, J. M.; Feng, G.; Fulvio, P. F.; Hillesheim, P. C.; Dai, S.; Gogotsi, Y.; Cummings, P. T.; Kalinin, S. V.; Balke, N. Strain-Based In Situ Study of Anion and Cation Insertion into Porous Carbon Electrodes with Different Pore Sizes. *Adv. Energy Mater.* **2014**, 4, 1300683

(8) Richey, F. W.; Dyatkin, B.; Gogotsi, Y.; Elabd, Y. A. Ion Dynamics in Porous Carbon Electrodes in Supercapacitors Using in Situ Infrared Spectroelectrochemistry. *J. Am. Chem. Soc.* **2013**, 135, 12818-12826

(9) Hou, C. H.; Liang, C. D.; Yiacoumi, S.; Dai, S.; Tsouris, C. Electrosorption capacitance of nanostructured carbon-based materials. *J. Colloid Interface Sci.* **2006**, 302, 54-61

(10) Zhang, P. F.; Qiao, Z. A.; Zhang, Z. Y.; Wan, S.; Dai, S. Mesoporous graphene-like carbon sheet: high-power supercapacitor and outstanding catalyst support. *J. Mater. Chem. A* **2014**, 2, 12262-12269

(11) Saha, D.; Li, Y. C.; Bi, Z. H.; Chen, J. H.; Keum, J. K.; Hensley, D. K.; Grappe, H. A.; Meyer, H. M.; Dai, S.; Paranthaman, M. P., et al. Studies on supercapacitor electrode material from activated lignin-derived mesoporous carbon. *Langmuir* **2014**, 30, 900-910

(12) Xia, J. L.; Chen, F.; Li, J. H.; Tao, N. J. Measurement of the quantum capacitance of graphene. *Nat. Nanotechnol.* **2009**, 4, 505-509

(13) Wang, L.; Chen, X.; Zhu, W.; Wang, Y.; Zhu, C.; Wu, Z.; Han, Y.; Zhang, M.; Li, W.; He, Y., et al. Detection of resonant impurities in graphene by quantum capacitance measurement. *Phys. Rev. B* **2014**, 89, 075410

(14) Pak, A. J.; Paekw, E.; Hwang, G. S. Relative contributions of quantum and double layer capacitance to the supercapacitor performance of carbon nanotubes in an ionic liquid. *Phys. Chem. Chem. Phys.* **2013**, 15, 19741-19747

(15) Paek, E.; Pak, A. J.; Hwang, G. S. A computational study of the interfacial structure and capacitance of graphene in [BMIM][PF_6] ionic liquid. *J. Electrochem. Soc.* **2013**, 160, A1-A10

(16) Paek, E.; Pak, A. J.; Kweon, K. E.; Hwang, G. S. On the origin of the enhanced supercapacitor performance of nitrogen-doped graphene. *J. Phys. Chem. C* **2013**, 117, 5610-5616

(17) Xing, L. D.; Vatamanu, J.; Borodin, O.; Bedrov, D. On the Atomistic Nature of Capacitance Enhancement Generated by Ionic Liquid Electrolyte Confined in Subnanometer Pores. *J. Phys. Chem. Lett.* **2013**, 4, 132-140

(18) Vatamanu, J.; Cao, L. L.; Borodin, O.; Bedrov, D.; Smith, G. D. On the Influence of Surface Topography on the Electric Double Layer Structure and Differential Capacitance of Graphite/Ionic Liquid Interfaces. *J. Phys. Chem. Lett.* **2011**, 2, 2267-2272

(19) Vatamanu, J.; Borodin, O.; Smith, G. D. Molecular Simulations of the Electric Double Layer Structure, Differential Capacitance, and Charging Kinetics for N-Methyl-N-propylpyrrolidinium Bis(fluorosulfonyl)imide at Graphite Electrodes. *J. Phys. Chem. B* **2011**, 115, 3073-3084

(20) Vatamanu, J.; Borodin, O.; Smith, G. D. Molecular Insights into the Potential and Temperature Dependences of the Differential Capacitance of a Room-Temperature Ionic Liquid at Graphite Electrodes. *J. Am. Chem. Soc.* **2010**, 132, 14825-14833

(21) Feng, G.; Zhang, J. S.; Qiao, R. Microstructure and Capacitance of the Electrical Double Layers at the Interface of Ionic Liquids and Planar Electrodes. *J. Phys. Chem. C* **2009**, 113, 4549-4559

(22) Feng, G.; Jiang, D. E.; Cummings, P. T. Curvature Effect on the Capacitance of Electric Double Layers at Ionic Liquid/Onion-Like Carbon Interfaces. *J. Chem. Theory Comput.* **2012**, 8, 1058-1063

(23) Feng, G.; Cummings, P. T. Supercapacitor Capacitance Exhibits Oscillatory Behavior as a Function of Nanopore Size. *J. Phys. Chem. Lett.* **2011**, 2, 2859-2864

(24) Feng, G.; Huang, J. S.; Sumpter, B. G.; Meunier, V.; Qiao, R. Structure and Dynamics of Electrical Double Layers in Organic Electrolytes. *Phys. Chem. Chem. Phys.* **2010**, 12, 5468-5479

(25) Ji, H.; Zhao, X.; Qiao, Z.; Jung, J.; Zhu, Y.; Lu, Y.; Zhang, L. L.; MacDonald, A. H.; Ruoff, R. S. Capacitance of carbon-based electrical double-layer capacitors. *Nat. Commun.* **2014**, 5, 3317

(26) Uesugi, E.; Goto, H.; Eguchi, R.; Fujiwara, A.; Kubozono, Y. Electric double-layer capacitance between an ionic liquid and few-layer graphene. *Sci. Rep.* **2013**, 3, 1595

(27) Brooksby, P.; Farquhar, A.; Dykstra, H.; Waterland, M.; Downard, A. Quantum capacitance of aryldiazonium modified large area few-layer graphene electrodes. *J. Phys. Chem. C* **2015**, 119, 25778–25785

(28) Stoller, M. D.; Magnuson, C. W.; Zhu, Y. W.; Murali, S.; Suk, J. W.; Piner, R.; Ruoff, R. S. Interfacial capacitance of single layer graphene. *Energ Environ. Sci.* **2011**, 4, 4685-4689

(29) Zhan, C.; Neal, J.; Wu, J. Z.; Jiang, D. E. Quantum Effects on the Capacitance of Graphene-Based Electrodes. *J. Phys. Chem. C* **2015**, 119, 22297–22303

(30) Letchworth-Weaver, K.; Arias, T. A. Joint density functional theory of the electrode-electrolyte interface: application to fixed electrode potentials, interfacial capacitances, and potentials of zero charge. *Phys. Rev. B* **2012**, 86, 075140

(31) Perdew, J. P.; Burke, K.; Ernzerhof, M. Generalized Gradient Approximation Made Simple. *Phys. Rev. Lett.* **1996**, 77, 3865-3868

(32) Sun, S.; Qi, Y.; Zhang, T. Y. Dissecting Graphene Capacitance in Electrochemical Cell. *Electrochim. Acta* **2015**, 163, 296-302

(33) Stoller, M. D.; Park, S. J.; Zhu, Y. W.; An, J. H.; Ruoff, R. S. Graphene-based ultracapacitors. *Nano Lett.* **2008**, 8, 3498-3502

(34) Vatamanu, J.; Ni, X. J.; Liu, F.; Bedrov, D. Tailoring graphene-based electrodes from semiconducting to metallic to increase the energy density in supercapacitors. *Nanotechnology* **2015**, 26, 464001

(35) Radin, M. D.; Ogitsu, T.; Biener, J.; Otani, M.; Wood, B. C. Capacitive Charge Storage at an Electrified Interface Investigated via Direct First-Principles Simulations. *Phys. Rev. B* **2015**, 91, 125415

(36) Koshino, M. Interlayer Screening Effect in Graphene Multilayers with ABA and ABC Stacking. *Phys. Rev. B* **2010**, 81, 125304

(37) Guinea, F. Charge Distribution and Screening in Layered Graphene Systems. *Phys. Rev. B* **2007**, 75, 235433

(38) Paek, E.; Pak, A. J.; Hwang, G. S. On the influence of polarization effects in predicting the interfacial structure and capacitance of graphene-like electrodes in ionic liquids. *J. Chem. Phys.* **2015**, 142, 024701

(39) Zhang, L. L.; Zhao, X.; Ji, H. X.; Stoller, M. D.; Lai, L. F.; Murali, S.; Mcdonnell, S.; Cleveger, B.; Wallace, R. M.; Ruoff, R. S. Nitrogen doping of graphene and its effect on quantum Capacitance, and a new insight on the enhanced capacitance of N-doped carbon. *Energ Environ. Sci.* **2012**, 5, 9618-9625

(40) Zhan, C.; Zhang, Y.; Cummings, P.; Jiang, D. E. Enhancing graphene capacitance by nitrogen: effects of doping configuration and concentration. *Phys. Chem. Chem. Phys.* **2016**, 18, 4668-4674

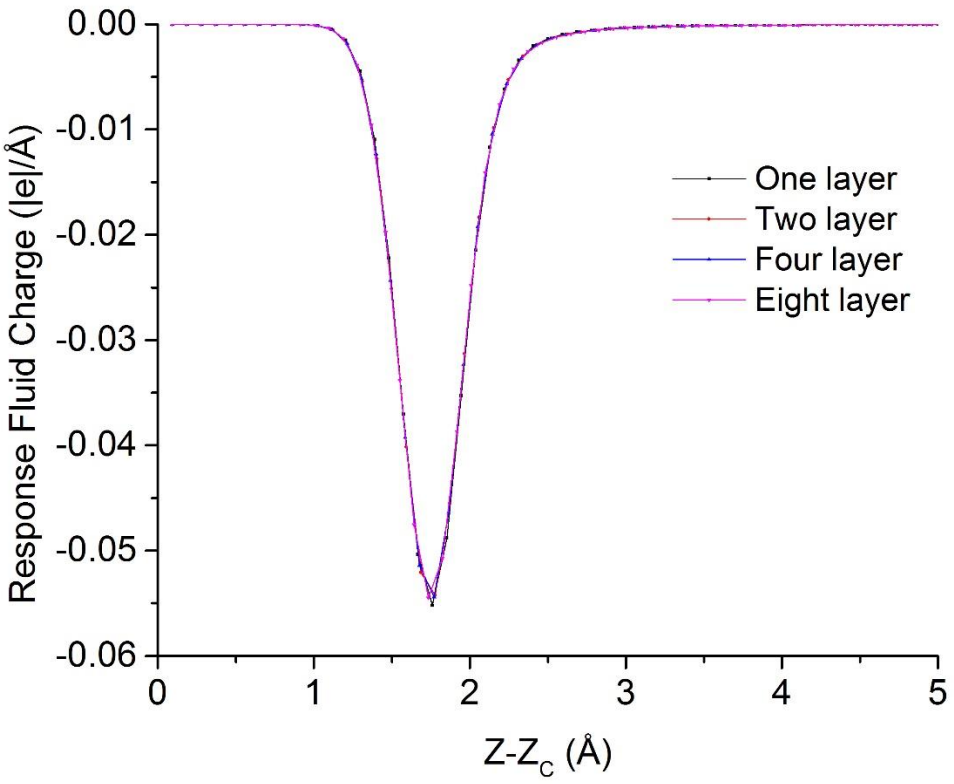


Figure S5-1. Fluid charge response. The total charge on electrode is 0.06 e and the few layer graphene is in contact with electrolyte on both sides. Fluid response charge equals to the integral of fluid response charge: $Q_{electrode} = -Q_{fluid}$.

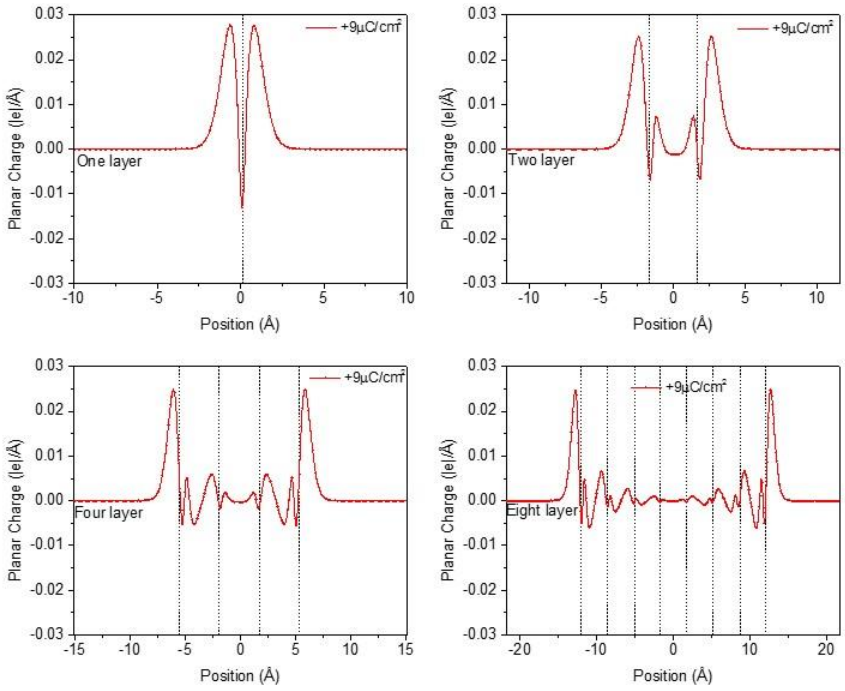


Figure S5-2. Excess charge distribution in FLG. Layer number is one, two, four and eight in (a)-(d).

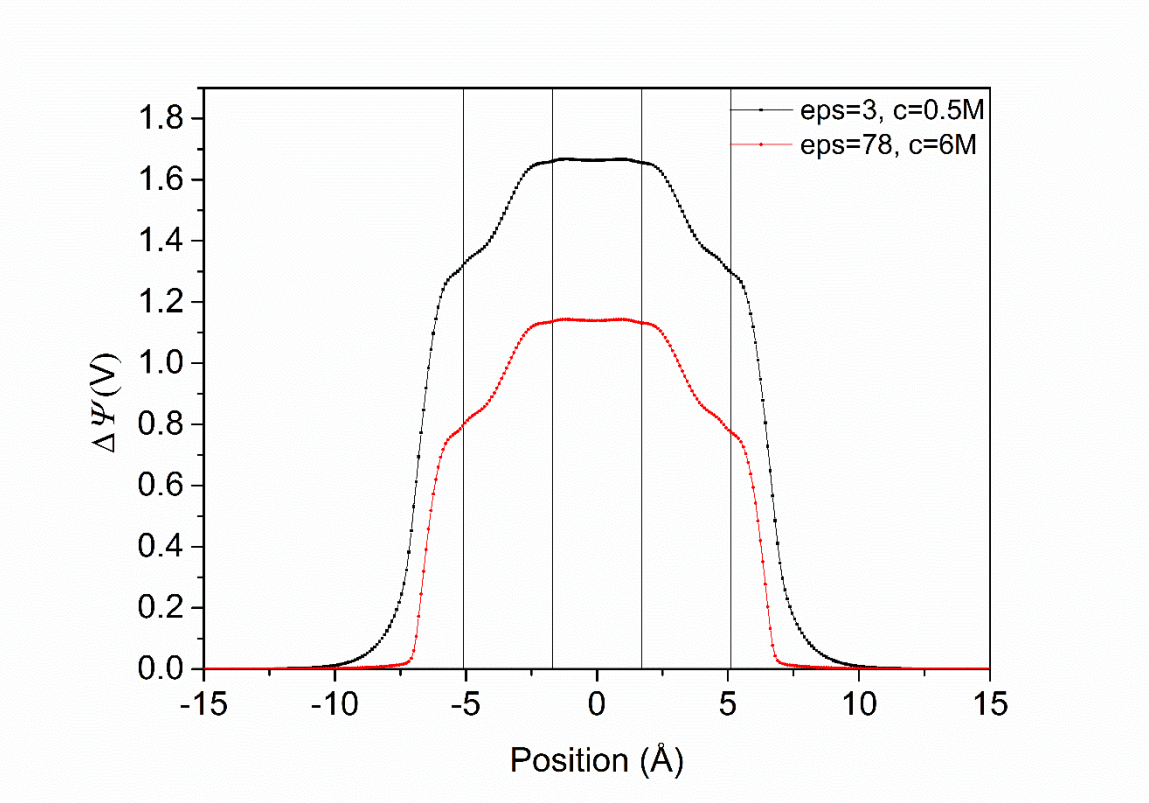


Figure S5-3. The electrostatic potential drop in different solvation parameter ($\Delta\psi\ (z)$) of 4 layer graphene with the surface charge density of 9 $\boldsymbol{\mu}$C/cm^2. "eps" represents the bulk dielectric of solvent and "c" is the concentration of ions in electrolyte, which will influence the dielectric function and Debye screening length in Linear PCM.

Chapter 6 Computational insight into the capacitive performance of graphene edge planes

6.1 Introduction

Capacitors are widely used electronic devices that store and release electric energy quickly. There are two types of capacitors: a dielectric capacitor achieves its energy storage through a dielectric medium [1-3] (such as an oxide layer); an electrochemical capacitor (also called "supercapacitor") stores electric energy based on surface redox reaction ("pseudocapacitor") or electric double layer ("electric double-layer capacitor" or EDLC). Compared with dielectric capacitors, supercapacitors have much higher energy density; compared with batteries, they have much higher power densities and long cycle lives [4-7]. Carbon materials, including activated carbons, graphene, and advanced porous carbons, are used as electrode materials for EDLCs because of their low cost, high conductivity, good chemical stability, and low density [8-15]. However, the capacitance of graphene is limited by its low electronic density of states (DOS) at the Fermi level [16-19]. This quantum capacitance can be separately computed through electronic density functional theory (DFT), while the EDL capacitance can be obtained through classical methods (molecular dynamics, classical DFT, or Monte Carlo) [18, 20-24].

To increase the quantum capacitance (C_Q) and hence the total capacitance, one effective way is to increase the electronic density of states at the Fermi level for the electrode material via nitrogen functionalization and doping of the graphene electrode [25, 26] or using the lighter and more metallic borophene [27]. Several simulations have focused on how to improve C_Q of graphene-based electrode [28-33]. For few-layer-graphene

electrodes, our recent work showed that dielectric screening also contributes to the total capacitance [34]. Most of the theoretical studies on graphene systems have focused on the graphene basal plane [13, 18, 28, 31, 33, 35, 36], while little has been done on the capacitive performance of graphene edge planes. Recent experiments have indicated that the graphene edge plane could have higher capacitance than graphene basal plane [37-41]. Theoretical understanding on the capacitance of graphene edge plane is still limited [42], and the dielectric contribution has not been taken into account to provide a complete physical picture of the capacitance behavior.

In this work, we apply the self-consistent joint density functional theory to simulate the graphene edge plane in contact with the electrolyte via an implicit solvation model. We will separate the contributions from quantum, EDL, and dielectric capacitances. To include explicit ion solvation, we will also apply classical molecular dynamics to investigate the contribution of the EDL capacitance of graphene edges.

6.2 Methods

6.2.1 Joint density functional theory

Electronic structure of the solvated electrode in implicit electrolyte is solved by joint density functional theory, using the JDFTx package with the charge-asymmetric nonlocally-determined local-electric (CANDLE) solvation model solvation [43, 44]. The interface model is described by periodic boundary conditions: pristine graphite crystal is modeled in a 2.460×2.460 Å^2 rhombus lattice in ABAB stacking pattern with the interlayer distance of 3.40 Å. We used the (110) and (100) surfaces of graphite to model the armchair edge and zigzag edge, respectively. The sp^2 carbon atom at the edge site is

terminated by H atom with the C-H bond length of 1.140 Å. The vacuum layer thickness is 20 Å and will be filled by implicit solvation model (6M monovalent aqueous electrolyte). The model is shown in Fig. 6-1. The exchange-correlation energy for the electronic system is described by Generalized-Gradient-Approximation with Perdew-Burke-Ernzerhof functional (GGA-PBE) [45]. The ultrasoft pseudopotential is used to describe the nuclei-electron interaction for carbon and hydrogen atoms [46]. To accurately capture the electronic chemical potential shift, the kinetic energy cutoff of plane wave basis set is 30 hartree and the k-point mesh for Brillouin zone sampling is 24×36×1 for armchair edge and 36×24×1 for zigzag edge.

The total differential capacitance $C_{D,tot}$ is defined by: $C_{D,tot} = e_0 dQ/d\mu_e$, where Q is area-normalized excess charge density of electrode and $\boldsymbol{\mu}$e is the electronic chemical potential of the solvated electrode [34]. The integral capacitance C_{tot} is defined by: $C_{tot} = e_0 \Delta Q/\Delta\mu_e$. The shift in the electronic chemical potential ($\Delta\mu_e$) includes three contributions:

$$C_{tot} = \frac{\Delta Q}{\Delta\mu_e/e_0} = \frac{\Delta Q}{\varphi_Q+\varphi_{NQ}} = \frac{\Delta Q}{\varphi_Q+\varphi_{EDL}+\varphi_{Dielec}} \quad 6\text{-}1$$

$$C_{tot}^{-1} = C_Q^{-1} + C_{NQ}^{-1} = C_Q^{-1} + C_{EDL}^{-1} + C_{Dielec}^{-1} \quad 6\text{-}2$$

where C_Q and C_{NQ} correspond to quantum capacitance and non-quantum capacitance, respectively. e_0 in equation 5-1 is the unit charge. C_{NQ} originates from the electrostatic energy change of the electrode/electrolyte system due to the external electric field of EDL, which can be obtained from the band shift in the JDFT calculation [34]. C_{NQ} is the total consequence of C_{EDL} and C_{Dielec}, which correspond to the EDL response of the electrolyte and the dielectric screening of the electrode, respectively. The EDL and dielectric

screening contribution can be separated by plotting the electrostatic potential for an ideal planar electrode surface, such as Pt and graphene. However, these two contributions are not separable in the graphene edge plane electrode due to the difficulty in defining the electrolyte/electrode interface for such a non-ideal and corrugated surface. Thus, we will use classical molecular dynamics to better understand the surface morphology effect on the EDL capacitance. Besides, based on the definition of capacitance in equation 6-1, the capacitance can be obtained from two ways: (1) fixing the electrode to obtain $\boldsymbol{\mu}$e shift, (2) fixing the $\boldsymbol{\mu}$e to obtain the electron number change. These two ways are both doable in JDFTx code and they gives identical result. In this project, we used the first way since it is more convenient for the potential drop contribution analysis.

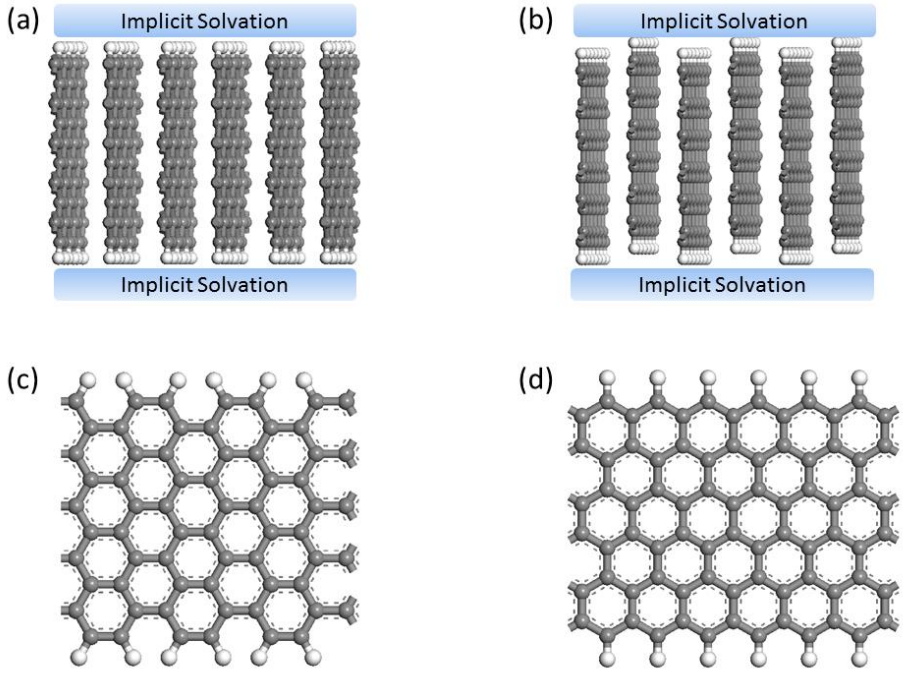


Fig. 6-1. The model used in the joint density functional theory calculation: (a) and (b) are the side view of graphite (110)-armchair and (100)-zigzag surfaces, respectively. (c) and (d) are the front view of single layer armchair edge and zigzag edge, respectively.

6.2.2 Classical molecular dynamics (CMD) simulations

We applied CMD in the NVT ensemble using the GROMACS [47] package to simulate the EDL capacitance of different graphene edge planes. As illustrated in Fig. S5-1 in the supplementary data, each simulated system consists of a slab of 6 M NaCl aqueous solution enclosed between two electrodes, which were set at least 5.0 nm away to guarantee a bulk-like behavior of the electrolyte in the channel center. All the electrode atoms were fixed during the simulation. The force field parameters for the electrode and the electrolyte are adopted from our previous work [26]. When simulating the charged electrode, additional partial charges were added to surface H atoms only. The slab-PME method [48] was used to compute the electrostatic interaction, and the dimension vertical to the electrode surface was set to be 5 times the separation distance of the electrodes, to ensure that the accuracy of the electrostatic calculation is comparable to that of the two-dimensional Ewald method [49]. Each simulation was initiated at 800 K for 2 ns, followed by 8 ns of annealing to 298 K and then equilibrated at 298 K for 10 ns. Another production run of 10 ns was performed for data analysis. The temperature was controlled by using a Berendsen thermostat [50]. The time step of 1 fs was applied. Each simulation was repeated three times with different initial configurations to reduce statistical errors. Here, one should note that the reason we use fix-charge method on surface H atom is that DFT calculation (Figure S6-6) showed that the excess charge mainly focus on the H atom at interface. Generally speaking, at this point, the constant potential MD should be a better way to capture the EDL capacitance more accurately.[51] However, although some charge penetration is observed in Figure S6-6, but is doesn't have large influence on the EDL capacitance when electrode surface morphology

is similar. This point has been indicated in our previous work through JDFT study by comparing the few layer graphene and Pt electrode.[34] Thus, in this work, using constant charge MD is enough to capture the influence of surface morphology on the EDL capacitance and estimate the EDL contribution in total capacitance.

6.3 Results and discussion

6.3.1 Electronic chemical potential (μ_e) shift and potential at the point of zero charge (ψ_{PZC}) for the graphene edge plane

To determine the charge vs potential curve for the graphene edge-plane electrodes, we need to determine their ψ_{PZC}. We calculated the electronic chemical potential (μ_e) of the graphene edge solvated in the implicit electrolyte with various electrode thicknesses. The calibrated Standard Hydrogen Electrode (SHE) in the CANDLE solvation model in JDFTx is -4.66 eV [44]. The calculated μ_e of the graphene basal plane at zero charge is -4.0 eV, so its theoretical ψ_{PZC} is -0.6 V vs SHE. The experimental ψ_{PZC} of graphene is located at -0.2 V to 0.1 V vs SHE [52]. Table 6-1 shows the calculated μ_e of neutral graphene edges (both armchair and zigzag type) of different thickness (see Fig. S6-2 and S6-3 for the range of thickness). Consistent with a previous theoretical study on the work function of graphene nanoribbon that the graphene edge has lower work function than pristine graphene [53], we found that μ_e of neutral graphene edges are higher than that of the graphene basal plane. The theoretical ψ_{PZC} of a graphene zigzag edge is -1.6 V vs SHE, while that of the graphene armchair edge is -1.7 V vs SHE, so the graphene edge planes are more suitable to be the anode material for positive charge. In addition, Table 6-1 shows that the thickness of edge plane has minor influence on ψ_{PZC}, a trend also found in few-layer graphene systems [13].

Table 6-1 Electronic chemical potential (μ_e) of armchair and zigzag graphene edges of different thickness at zero surface charge and the corresponding potential (ψ_{PZC}) at the point of zero charge vs standard hydrogen electrode (SHE). (see Fig. S5-2 and S5-3 for the so-named edge structures).

Edge Structure	μ_e (eV)	ψ_{PZC} vs SHE (V)
Armchair-1	-2.93	-1.73
Armchair-2	-2.84	-1.81
Armchair-3	-2.95	-1.71
Armchair-4	-2.93	-1.72
Armchair-5	-2.87	-1.78
Zigzag-1	-3.06	-1.59
Zigzag-2	-3.09	-1.57
Zigzag-3	-3.09	-1.56
Zigzag-4	-3.09	-1.57
Zigzag-5	-3.09	-1.57

6.3.2 Charge-potential curve of graphene edges in contact with an implicit solvation model

The calculated electrode charge vs electrode potential (derived from μe shift at a fixed electrode charge Q) curve is plotted in Fig. 6-2a and 6-2b for the armchair and zigzag edges, respectively; the differential capacitance is plotted in Fig. 6-2c and 6-2d, obtained by applying numerical differentiation on the fitted charge-potential curves. In Fig. 6-2a and 6-2c, one can see that the capacitance of the armchair edge shows strong dependence on the potential near PZC and then becomes flat at high voltage. This is due to the semiconducting nature of the armchair edges: the Fermi level is located in the middle of the band gap (the electronic density of states, DOS, is shown in Fig. S6-4), which causes a greater μ_e shift when the edge plane is charged from its neutral state. At higher voltage (>

1V), the differential capacitance of the armchair edge loses its strong voltage dependence due to a quite flat DOS below the band gap, as shown in Fig. S6-4. Armchair-3 edge has higher capacitance at PZC than other edges (Fig. 6-2c) due to its narrower gap and special electronic structure (see Fig. S6-4). Unlike armchair edges, zigzag edges have higher capacitance which is less voltage dependent (Fig. 6-2d). This can be explained by the special edge state of the zigzag edges (see Fig. S6-5), which yields a large DOS at the Fermi level and makes the quantum capacitance contribution ($1/C_Q$) trivial.

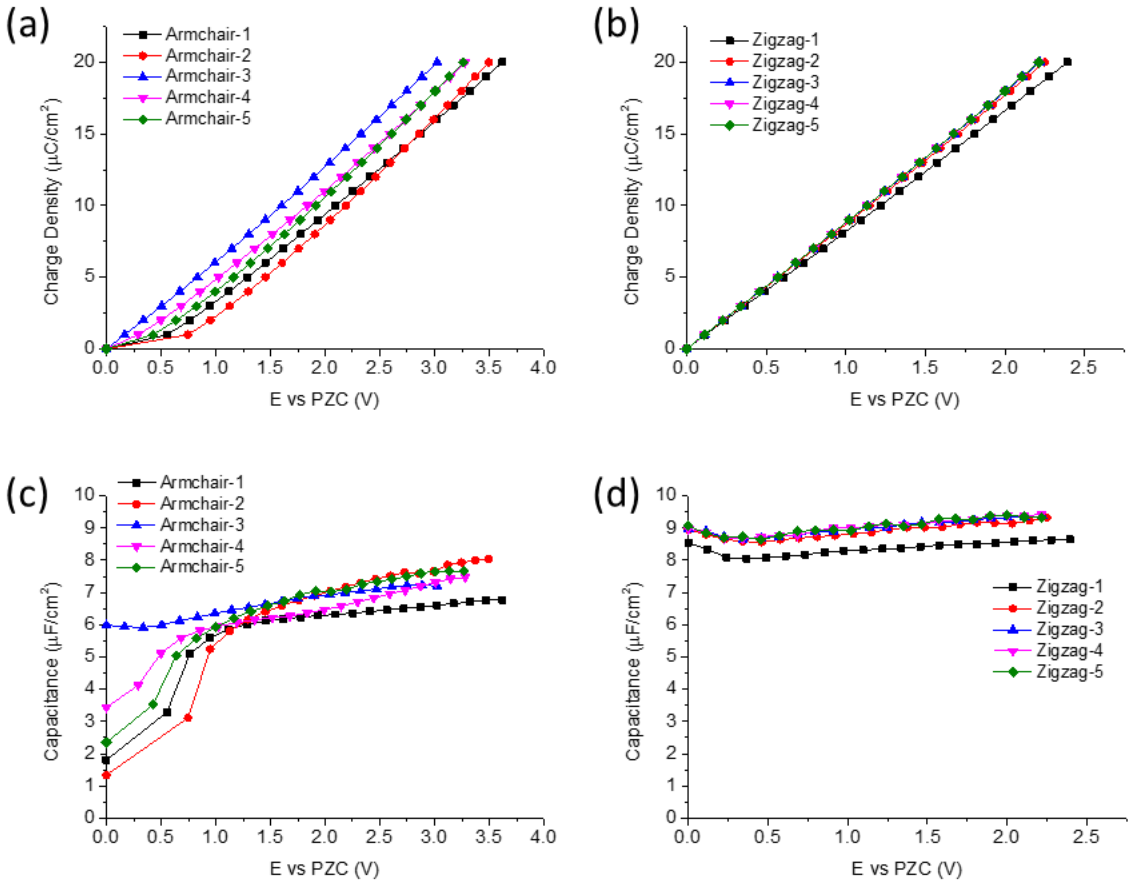


Fig. 6-2. Charge vs potential (a, b) and differential capacitance (c, d) vs potential curves for the armchair edge (a, c) and the zigzag edge (b, d) of different electrode thickness. Armchair 1 through 5 thicknesses: 4.43, 5.66, 6.89, 8.12, 9.35Å; zigzag 1 through 5 thicknesses: 5.12, 7.25, 9.38, 11.51, 13.64 Å. Corresponding structures are in Fig. S2 and S3.

6.3.3 Electrostatic potential drop inside the electrode

To understand the charging inside the graphene edge plane, we plotted the planar-average total electrostatic drop, $\Delta\boldsymbol{\psi}(r)$, of a positively charged edge plane in Fig. 6-3. As shown in Fig. 6-3a, $\Delta\boldsymbol{\psi}(r)$ of the armchair edge keeps increasing in the electrode region, meaning that the electrode cannot completely screen the external electric field from the Helmholtz layer at the electrode/electrolyte interface. This phenomenon is the same as the screening effect in the few-layer graphene electrode as shown in Fig. 6-3c. The $\Delta\boldsymbol{\psi}(r)$ curve in Fig. 6-3a still tends to increase in the center position of the electrode, so we expect that increasing the edge plane thickness will make the $\Delta\boldsymbol{\psi}(r)$ continue to increase and it will plateau when the edge plane reaches a critical thickness. Thus, the armchair edge is not a promising candidate for the EDLC electrode material. Compared with armchair edges, zigzag edges show different $\Delta\boldsymbol{\psi}(r)$ in the electrode region: as shown in Fig. 6-3b, $\Delta\boldsymbol{\psi}(r)$ increases steeply at the edge region and then becomes flat inside the electrode. The external electric field only penetrates into a small distance in the zigzag edge and then it is completely screened. Thus, the zigzag edge has a higher capacitance than the armchair edge and the basal plane.

6.3.4 Potential drop and capacitance contribution for graphene edge

We next analyze the contributions to C_{tot}. Unlike the case of few-layer graphene where we can clearly distinguish three contributions (quantum, dielectric, and EDL), we cannot separate the EDL and dielectric screening parts in the potential drop for the edge planes because the electrode-electrolyte interface (dashed lines in Fig. 6-3a,b) is hard to define. Thus, in this work they are grouped together as a non-quantum contribution, which

together with the quantum capacitance yields C_{tot} (Eq. 6-2). Fig. 6-3d shows that the armchair edge has a similar potential contribution to a 10-layer graphene and both contain significant contributions from quantum capacitance. The calculated areal capacitance of each electrode is listed in Table 6-2. The predicted total capacitance of the armchair edge is 6.12 μF/cm^2, which is lower than the capacitance of the 10-layer graphene (6.52 μF/cm^2). Compared with the armchair edge and the 10-layer graphene, the zigzag edge shows very different results: it has a lower electrostatic potential drop inside the electrode region (in Fig. 6-3b). In addition, the quantum contribution to the potential drop is also negligible due to the high C_Q of zigzag edge (Table 6-2) and its large DOS at the Fermi level (Fig. S6-5). The calculated capacitance of zigzag edge is 9.04 μF/cm^2, significantly higher than those of the armchair edge and the few-layer graphene.

Recent experiment showed that the edge-enriched graphene showed about 50% capacitance enhancement over that of the graphene basal plane [39], while theoretical understanding on this capacitance increase focuses on the C_Q issue [42]. Our work here shows that the capacitance enhancement depends on the edge type.

Table 6-2 Quantum (C_Q) and non-quantum (C_{NQ}) contributions to capacitance for the graphene edge planes in comparison with the basal plane of a 10-layer graphene, according to Eq. 5-2.

Electrode	C_{tot} (μF/cm^2)	C_Q (μF/cm^2)	C_{NQ} (μF/cm^2)
Armchair-5	6.12	22.83	8.37
Zigzag-5	9.04	1142	9.11
10-layer graphene	6.52	56.18	7.38

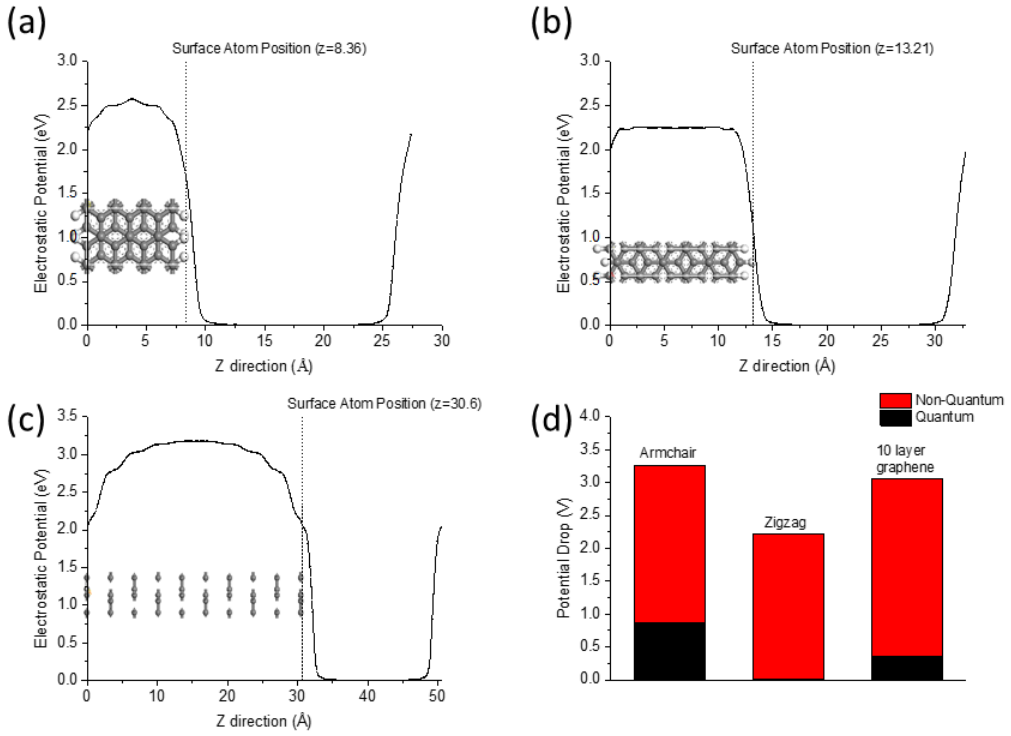


Fig. 6-3. Planar-average electrostatic potential drop in the electrode, $\Delta\boldsymbol{\psi}(r)$, along the electrode surface normal at a fixed surface charge density of 20 $\boldsymbol{\mu}C/cm^2$ for: (a) armchair edge, (b) zigzag edge, and (c) 10-layer graphene; (d) is the corresponding total potential drop including both quantum (Fermi level shift) and non-quantum (band shift) contributions. The corresponding planar average charge distribution is plotted in Fig. S6. The dashed lines in (a), (b) and (c) indicate the position of surface atom that could be roughly treated as the electrode/electrolyte interface.

6.3.5 Classical molecular dynamics (CMD) study on the armchair and zigzag edge

In our JDFT study of the edge planes above**,** we cannot separate the EDL and dielectric contributions in C_{NQ}. To examine the EDL structure and capacitance of the edge planes, we used CMD to study the armchair and zigzag edges in contact with a 6M NaCl aqueous solution. To find out how the surface morphology would influence the EDL capacitance, we charged the surface in two different ways: (i) the surface carbon atoms

were assigned with the partial charges from force fields (labeled as FF); (ii) the partial charges on the surface carbon atoms were manually set to zero (labeled as non-FF). In both cases, additional electrode charges were homogenously added to the surface H atoms when charging the electrodes because the JDFT study above showed that the excess charge mainly resides on the surface atoms (Fig. S6-6). The non-FF case can directly show how the surface charge inhomogeneity affects EDL capacitance, while the FF case gives the combined consequence of surface morphology and partial charges inside the electrode.

The differential EDL capacitance from CMD is plotted in Fig. 6-4. Because the graphene edge plane is non-flat, we need to consider the effect of solvent accessible surface area (SASA; Table 6-3). We plotted both SASA-normalized (Fig. 6-4a) and un-normalized (Fig. 6-4b) EDL capacitances. One can see that the edge plane always has the higher EDL capacitance than the basal plane, but the difference is smaller for the SASA-normalized one; so the SASA is one of the reasons for the higher EDL capacitance of the edge plane than the basal plane. Fig. 6-4a shows that near the PZC, the EDL capacitances of edge planes are about 20 to 25 μF/cm^2, and decrease as the potential goes up. When there is less surface charge inhomogeneity (non-FF), the differential capacitance is smaller at low potentials. Overall, the higher EDL capacitance of the zigzag edge is in line with our JDFT results for both the total capacitance and the non-quantum contribution that contains the EDL part (Table 6-2).

The ion distribution and EDL structure at various potentials are plotted in Fig. 6-5. With the same potential drop, the responses of counter-ions are shown in Fig. 6-5c and 6-5d. One can see that the edge planes have higher counter-ion (Cl^-) concentrations near the

electrode surface than the basal plane, which means that the edge planes could form a thinner Helmholtz layer and hence higher EDL capacitance. Thus, there are two factors causing the EDL capacitance increase at the edge. First, the surface morphology of graphene edges favors adsorption of Cl^-. The counter-ion in the FF cases also has higher peaks than in the non-FF cases, indicating that surface charge inhomogeneity also makes the EDL capacitance higher. Second, the corrugation on the edge planes leads to higher SASA which at the same bias potential can induce a stronger counter ion response, thereby yielding higher EDL capacitance.

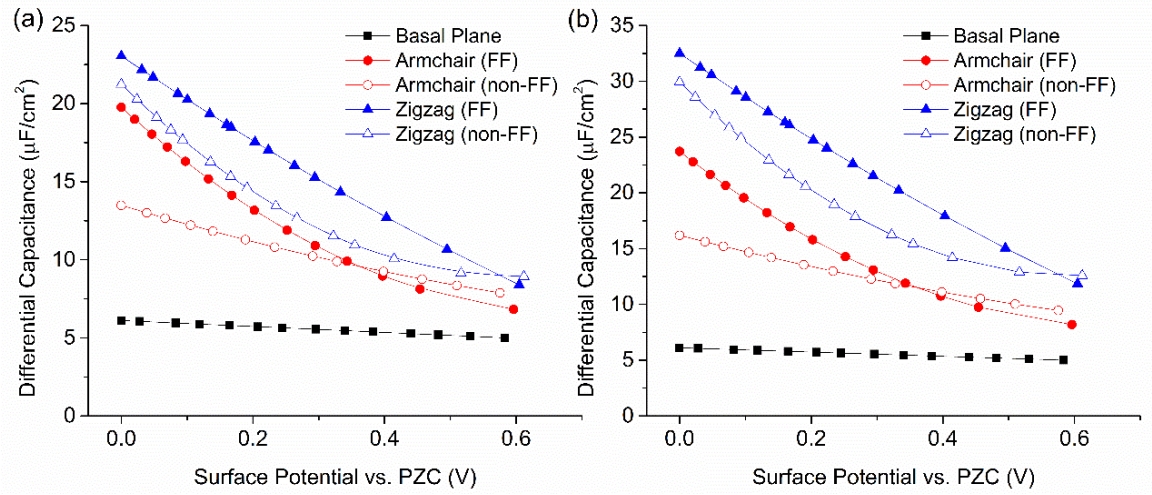


Fig. 6-4. Differential capacitance of graphene basal and edge planes from classical molecular dynamics simulations: (a) solvent accessible surface area (SASA)-normalized; (b) un-normalized, surface area determined by the lateral cell size. FF means the partial charges of carbon atoms are from the force field, while non-FF means that the partial charge on carbon atoms is manually set to be zero. Charging is realized by changing the charges on the surface H atoms.

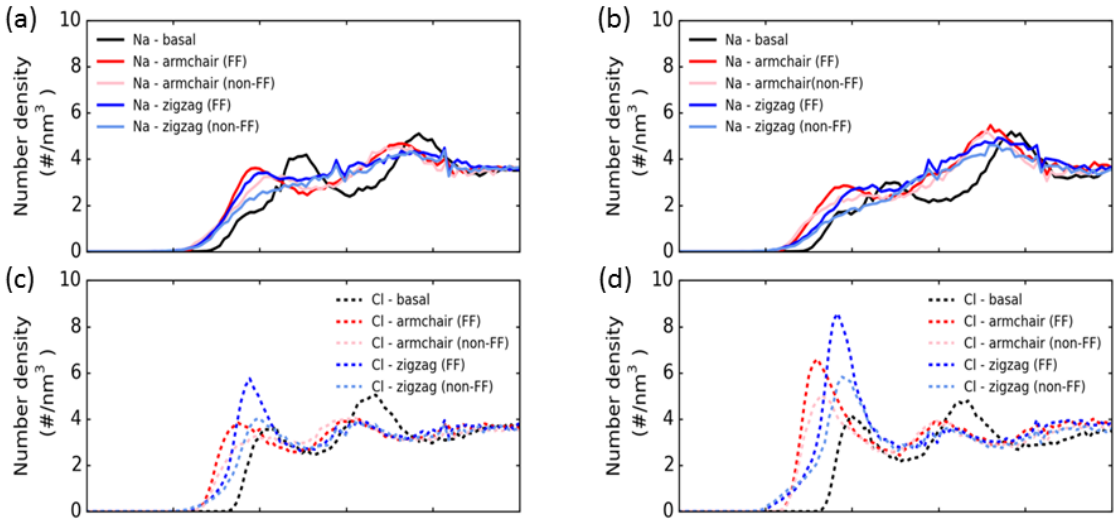


Fig. 6-5. Na^+ (a, b) and Cl^- (c, d) distributions in the electrolyte at PZC (left panel) and 0.3 V vs PZC (right panel) from classical MD simulations for various electrodes; FF means the partial charges of carbon atoms are from the force field, while non-FF means that the partial charge on carbon atoms is manually set to be zero. Charging is realized by changing the charges on the surface H atoms.

6.3.6 Combining JDFT and CMD results

The JDFT results offer the total capacitance together with the quantum and non-quantum contributions, while the CMD simulations provide the EDL capacitance. To estimate the third contribution due to the dielectric screening, we plotted the potential drops by combining both JDFT and CMD results in Fig. 6-6. The dielectric contribution is separated from the non-quantum potential drop (obtained from JDFT) by subtracting the EDL contribution (obtained from CMD). The calculated dielectric capacitance is 19.28 μF/cm^2 for the armchair edge and 13.33 μF/cm^2 for the zigzag edge, in agreement with the different electronic structures between the armchair and zigzag edges (Fig. S6-4 and S6-5). Here again we note that due to the less-defined electrode/electrolyte boundary for the edge planes, the separation of the dielectric and EDL contributions for them can be subject to large uncertainty.

The areal capacitance of pristine graphene is about 6 μF/cm^2, which has been reported by many experimental studies [13, 18, 54]. Liu et al. reported the experimentally measured areal capacitance of edge-enriched graphene nano-ribbon at about 10 μF/cm^2 at low scan rates [39], which shows good consistency with our results in Table 5-2 for zigzag edges. Moreover, recently published experimental work by Cen et al. also found that the edge plane has higher capacitance than the basal plane [41]. Recently published work by Yang et al [55] studied the EDL capacitance of graphene edge site via MD simulation and found that the EDL capacitance enhancement from edge effect is caused by its larger interlayer spacing and higher screening efficiency in electrolyte, which is basically consistent to our MD work, but we provide a more comprehensive understanding on the edge effect from electronic DFT perspective. Besides, the role of edge effect can be very different and more complicated in realistic porous carbon: Merlet et al [56] studied the electrolyte confinement in real porous carbon model and found that edge site (carbon electrode with concave curvature) tends to retain lower local charge than other configurations at constant potential ensemble in porous carbon and it could have significant influence on the nano-confinement of electrolyte, which revealed the importance of nano-confinement effect.

Atomic level imaging [57] and DFT calculations [58, 59] have indicated that the zigzag edge is more favorable than the armchair edge on metal surfaces. The experimental synthesis of the pure zigzag graphene edge has been achieved by Fasel et al [60]. We think that the experimentally observed capacitance enhancement in graphene nano-ribbons may be attributed more to the zigzag edge than to the armchair edge [39].

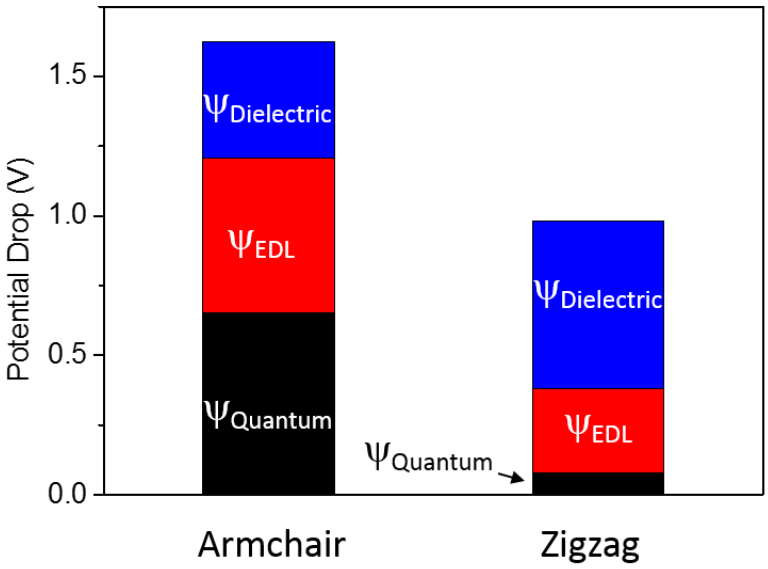


Fig. 6-6. Comparison of the potential drop contributions between armchair and zigzag edges by combining JDFT and CMD data. The surface charge density is 8 μC/cm^2 in both cases. The dielectric contribution is calculated by subtracting the CMD-obtained EDL potential drop from the non-quantum contribution obtained by JDFT.

Table 6-3 Solvent accessible surface area (SASA) relative to that of the basal plane

Electrode	Solvent Accessible Surface Area (SASA)
Basal Plane	1
Armchair Edge	1.2
Zigzag Edge	1.41

6.4 Summary and conclusions

We have studied the capacitance of graphene edge planes in contact with an electrolyte. Joint density functional theory with an implicit solvation model showed that the zigzag edge has higher capacitance than the armchair edge and the basal plane due to the edge state (giving extremely large quantum capacitance) and the combined effect of dielectric screening and EDL response. Classical molecular dynamics (CMD) with an

explicit electrolyte revealed the EDL capacitance in the order of zigzag edge > armchair edge > basal plane. The edge planes have higher solvent-accessible surface area and surface charge inhomogeneity that favors the adsorption of counter-ions, leading to higher capacitance. Our theoretical work therefore provides a complete picture of the various factors contributing to the charge capacitive performance of graphene edges and suggests that the zigzag graphene edge should be created for enhanced capacitance.

References

(1) Stengel, M.; Spaldin, N. A. Origin of the dielectric dead layer in nanoscale capacitors. *Nature* **2006**, 443, 679-682

(2) Ozcelik, V. O.; Ciraci, S. High-performance planar nanoscale dielectric capacitors. *Phys. Rev. B* **2015**, 91, 195445

(3) Ozcelik, V. O.; Ciraci, S. Nanoscale dielectric capacitors composed of graphene and boron nitride layers: a first-principles study of high capacitance at nanoscale. *J. Phys. Chem. C* **2013**, 117, 15327-15334

(4) Zhang, L. L.; Zhao, X. S. Carbon-based materials as supercapacitor electrodes. *Chem. Soc. Rev.* **2009**, 38, 2520-2531

(5) Simon, P.; Gogotsi, Y.; Dunn, B. Where do batteries end and supercapacitors begin? *Science* **2014**, 343, 1210-1211

(6) Rolison, D. R.; Long, J. W.; Lytle, J. C.; Fischer, A. E.; Rhodes, C. P.; McEvoy, T. M.; Bourga, M. E.; Lubers, A. M. Multifunctional 3D nanoarchitectures for energy storage and conversion. *Chem. Soc. Rev.* **2009**, 38, 226-252

(7) Simon, P.; Gogotsi, Y. Materials for electrochemical capacitors. *Nat. Mater.* **2008**, 7, 845-854

(8) Zhang, P. F.; Qiao, Z. A.; Zhang, Z. Y.; Wan, S.; Dai, S. Mesoporous graphene-like carbon sheet: high-power supercapacitor and outstanding catalyst support. *J. Mater. Chem. A* **2014**, 2, 12262-12269

(9) Zhai, Y. P.; Dou, Y. Q.; Zhao, D. Y.; Fulvio, P. F.; Mayes, R. T.; Dai, S. Carbon materials for chemical capacitive energy storage. *Adv. Mater.* **2011**, 23, 4828-4850

(10) Wang, Y.; Shi, Z. Q.; Huang, Y.; Ma, Y. F.; Wang, C. Y.; Chen, M. M.; Chen, Y. S. Supercapacitor devices based on graphene materials. *J. Phys. Chem. C* **2009**, 113, 13103-13107

(11) Stoller, M. D.; Park, S. J.; Zhu, Y. W.; An, J. H.; Ruoff, R. S. Graphene-based ultracapacitors. *Nano Lett.* **2008**, 8, 3498-3502

(12) Saha, D.; Li, Y. C.; Bi, Z. H.; Chen, J. H.; Keum, J. K.; Hensley, D. K.; Grappe, H. A.; Meyer, H. M.; Dai, S.; Paranthaman, M. P., et al. Studies on supercapacitor electrode material from activated lignin-derived mesoporous carbon. *Langmuir* **2014**, 30, 900-910

(13) Ji, H.; Zhao, X.; Qiao, Z.; Jung, J.; Zhu, Y.; Lu, Y.; Zhang, L. L.; MacDonald, A. H.; Ruoff, R. S. Capacitance of carbon-based electrical double-layer capacitors. *Nat. Commun.* **2014**, 5, 3317

(14) Hou, C. H.; Liang, C. D.; Yiacoumi, S.; Dai, S.; Tsouris, C. Electrosorption capacitance of nanostructured carbon-based materials. *J. Colloid Interface Sci.* **2006**, 302, 54-61

(15) Chmiola, J.; Largeot, C.; Taberna, P. L.; Simon, P.; Gogotsi, Y. Monolithic carbide-derived carbon films for micro-supercapacitors. *Science* **2010**, 328, 480-483

(16) Xia, J. L.; Chen, F.; Li, J. H.; Tao, N. J. Measurement of the quantum capacitance of graphene. *Nat. Nanotechnol.* **2009**, 4, 505-509

(17) Wang, L.; Chen, X.; Zhu, W.; Wang, Y.; Zhu, C.; Wu, Z.; Han, Y.; Zhang, M.; Li, W.; He, Y., et al. Detection of resonant impurities in graphene by quantum capacitance measurement. *Phys. Rev. B* **2014**, 89, 075410

(18) Stoller, M. D.; Magnuson, C. W.; Zhu, Y. W.; Murali, S.; Suk, J. W.; Piner, R.; Ruoff, R. S. Interfacial capacitance of single layer graphene. *Energ Environ. Sci.* **2011**, 4, 4685-4689

(19) Brooksby, P.; Farquhar, A.; Dykstra, H.; Waterland, M.; Downard, A. Quantum capacitance of aryldiazonium modified large area few-layer graphene electrodes. *J. Phys. Chem. C* **2015**, 119, 25778–25785

(20) Paek, E.; Pak, A. J.; Hwang, G. S. On the influence of polarization effects in predicting the interfacial structure and capacitance of graphene-like electrodes in ionic liquids. *J. Chem. Phys.* **2015**, 142, 024701

(21) Paek, E.; Pak, A. J.; Hwang, G. S. A computational study of the interfacial structure and capacitance of graphene in [BMIM][PF_6] ionic liquid. *J. Electrochem. Soc.* **2013**, 160, A1-A10

(22) Punnathanam, S. N. A Gibbs-ensemble based technique for Monte Carlo simulation of electric double layer capacitors (EDLC) at constant voltage. *J. Chem. Phys.* **2014**, 140,

(23) Kiyohara, K.; Asaka, K. Monte carlo simulation of porous electrodes in the constant voltage ensemble. *J. Phys. Chem. C* **2007**, 111, 15903-15909

(24) Kiyohara, K.; Asaka, K. Monte carlo simulation of electrolytes in the constant voltage ensemble. *J. Chem. Phys.* **2007**, 126,

(25) Zhang, L. L.; Zhao, X.; Ji, H. X.; Stoller, M. D.; Lai, L. F.; Murali, S.; Mcdonnell, S.; Cleveger, B.; Wallace, R. M.; Ruoff, R. S. Nitrogen doping of graphene and its effect on quantum Capacitance, and a new insight on the enhanced capacitance of N-doped carbon. *Energ Environ. Sci.* **2012**, 5, 9618-9625

(26) Zhan, C.; Zhang, Y.; Cummings, P.; Jiang, D. E. Enhancing graphene capacitance by nitrogen: effects of doping configuration and concentration. *Phys. Chem. Chem. Phys.* **2016**, 18, 4668-4674

(27) Zhan, C.; Zhang, P.; Dai, S.; Jiang, D. E. Boron supercapacitors. *ACS Energy Lett.* **2016**, 1, 1241-1246

(28) Vatamanu, J.; Ni, X. J.; Liu, F.; Bedrov, D. Tailoring graphene-based electrodes from semiconducting to metallic to increase the energy density in supercapacitors. *Nanotechnology* **2015**, 26, 464001

(29) Pak, A. J.; Paekw, E.; Hwang, G. S. Relative contributions of quantum and double layer capacitance to the supercapacitor performance of carbon nanotubes in an ionic liquid. *Phys. Chem. Chem. Phys.* **2013**, 15, 19741-19747

(30) Paek, E.; Pak, A. J.; Kweon, K. E.; Hwang, G. S. On the origin of the enhanced supercapacitor performance of nitrogen-doped graphene. *J. Phys. Chem. C* **2013**, 117, 5610-5616

(31) Yang, G. M.; Zhang, H. Z.; Fan, X. F.; Zheng, W. T. Density functional theory calculations for the quantum Capacitance performance of graphene-based electrode material. *J. Phys. Chem. C* **2015**, 119, 6464-6470

(32) Paek, E.; Pak, A. J.; Hwang, G. S. Curvature effects on the interfacial capacitance of carbon nanotubes in an ionic liquid. *J. Phys. Chem. C* **2013**, 117, 23539-23546

(33) Mousavi-Khoshdel, M.; Targholi, E.; Momeni, M. J. First-principles calculation of quantum capacitance of codoped graphenes as supercapacitor electrodes. *J. Phys. Chem. C* **2015**, 119, 26290-26295

(34) Zhan, C.; Jiang, D. E. Contribution of dielectric screening to the total capacitance of few-layer graphene electrodes. *J. Phys. Chem. Lett* **2016**, 7, 789

(35) Wood, B. C.; Ogitsu, T.; Otani, M.; Biener, J. First-principles-inspired design strategies for graphene-based supercapacitor electrodes. *J. Phys. Chem. C* **2014**, 118, 4-15

(36) Dyatkin, B.; Zhang, Y.; Mamontov, E.; Kolesnikov, A. I.; Cheng, Y. Q.; Meyer, H. M.; Cummings, P. T.; Gogotsi, Y. Influence of surface oxidation on ion dynamics and capacitance in porous and nonporous carbon electrodes. *J. Phys. Chem. C* **2016**, 120, 8730-8741

(37) Yuan, W. J.; Zhou, Y.; Li, Y. R.; Li, C.; Peng, H. L.; Zhang, J.; Liu, Z. F.; Dai, L. M.; Shi, G. Q. The edge- and basal-plane-specific electrochemistry of a single-layer graphene sheet. *Sci. Rep.* **2013**, 3, 2248

(38) Pope, M. A.; Aksay, I. A. Four-fold increase in the intrinsic capacitance of graphene through functionalization and lattice disorder. *J. Phys. Chem. C* **2015**, 119, 20369-20378

(39) Zheng, C.; Zhou, X. F.; Cao, H. L.; Wang, G. H.; Liu, Z. P. Edge-enriched porous graphene nanoribbons for high energy density supercapacitors. *J. Mater. Chem. A* **2014**, 2, 7484-7490

(40) Banerjee, S.; Shim, J.; Rivera, J.; Jin, X. Z.; Estrada, D.; Solovyeva, V.; You, X.; Pak, J.; Pop, E.; Aluru, N., et al. Electrochemistry at the edge of a single graphene layer in a nanopore. *Acs Nano* **2013**, 7, 834-843

(41) Yang, H. C.; Yang, J. Y.; Bo, Z.; Zhang, S.; Yan, J. H.; Cen, K. F. Edge effects in vertically-oriented graphene based electric double-layer capacitors. *J. Power Sources* **2016**, 324, 309-316

(42) Pak, A. J.; Paek, E.; Hwang, G. S. Impact of graphene edges on enhancing the performance of electrochemical double layer capacitors. *J. Phys. Chem. C* **2014**, 118, 21770-21777

(43) Letchworth-Weaver, K.; Arias, T. A. Joint density functional theory of the electrode-electrolyte interface: application to fixed electrode potentials, interfacial capacitances, and potentials of zero charge. *Phys. Rev. B* **2012**, 86, 075140

(44) Sundararaman, R.; Goddard, W. A. The Charge-Asymmetric Nonlocally Determined Local-Electric (CANDLE) Solvation Model. *J. Chem. Phys.* **2015**, 142, 064107

(45) Perdew, J. P.; Burke, K.; Ernzerhof, M. Generalized Gradient Approximation Made Simple. *Phys. Rev. Lett.* **1996**, 77, 3865-3868

(46) Garrity, K. F.; Bennett, J. W.; Rabe, K. M.; Vanderbilt, D. Pseudopotentials for High-throughput DFT Calculations. *Comput. Mater. Sci.* **2014**, 81, 446-452

(47) James, M. M., T.; Schulz, R.; Smith, J. C.; Hess, B.; Lindahl, E. GROMACS: High performance molecular simulations through multi-level parallelism from laptops to supercomputers. *SoftwareX* **2015**, 2, 19-25

(48) Yeh, I. C.; Berkowitz, M. L. Ewald summation for systems with slab geometry. *J. Chem. Phys.* **1999**, 111, 3155-3162

(49) Darden, T.; York, D.; Pedersen, L. Particle mesh ewald - an N.Log(N) method for ewald sums in large systems. *J. Chem. Phys.* **1993**, 98, 10089-10092

(50) Berendsen, H. J. C.; Postma, J. P. M.; Vangunsteren, W. F.; Dinola, A.; Haak, J. R. Molecular-dynamics with coupling to an external bath. *J. Chem. Phys.* **1984**, 81, 3684-3690

(51) Merlet, C.; Pean, C.; Rotenberg, B.; Madden, P. A.; Simon, P.; Salanne, M. Simulating supercapacitors: can we model electrodes as constant charge surfaces? *J Phys. Chem. Lett.* **2013**, 4, 264-268

(52) Poon, J.; Batchelor-McAuley, C.; Tschulik, K.; Compton, R. G. Single graphene nanoplatelets: capacitance, potential of zero charge and diffusion coefficient. *Chem. Sci.* **2015**, 6, 2869-2876

(53) Kvashnin, D. G.; Sorokin, P. B.; Bruning, J. W.; Chernozatonskii, L. A. The impact of edges and dopants on the work function of graphene nanostructures: the way to high electronic emission from pure carbon medium. *Appl. Phys. Lett.* **2013**, 102, 183112

(54) Uesugi, E.; Goto, H.; Eguchi, R.; Fujiwara, A.; Kubozono, Y. Electric double-layer capacitance between an ionic liquid and few-layer graphene. *Sci. Rep.* **2013**, 3, 1595

(55) Yang, H.; Zhang, X.; Yang, J.; Bo, Z.; Hu, M.; Yan, J.; Cen, K. F. Molecular origin of electric double-layer capacitance at multilayer graphene edges. *J. Phys. Chem. Lett.* **2017**, 8, 153–160

(56) Merlet, C.; Pean, C.; Rotenberg, B.; Madden, P. A.; Daffos, B.; Taberna, P. L.; Simon, P.; Salanne, M. Highly confined ions store charge more efficiently in supercapacitors. *Nat. Commun.* **2013**, 4, 2701

(57) Tian, J. F.; Cao, H. L.; Wu, W.; Yu, Q. K.; Chen, Y. P. Direct imaging of graphene edges: atomic structure and electronic scattering. *Nano Lett.* **2011**, 11, 3663-3668

(58) Shu, H. B.; Chen, X. S.; Tao, X. M.; Ding, F. Edge structural stability and kinetics of graphene chemical vapor deposition growth. *Acs Nano* **2012**, 6, 3243-3250

(59) Wei, D. S.; Wang, F. Relative stability of armchair, zigzag and reczag graphene edges on the Ru(0001) surface. *Surf. Sci.* **2012**, 606, 485-489

(60) Ruffieux, P.; Wang, S. Y.; Yang, B.; Sanchez-Sanchez, C.; Liu, J.; Dienel, T.; Talirz, L.; Shinde, P.; Pignedoli, C. A.; Passerone, D., et al. On-surface synthesis of graphene nanoribbons with zigzag edge topology. *Nature* **2016**, 531, 489–492

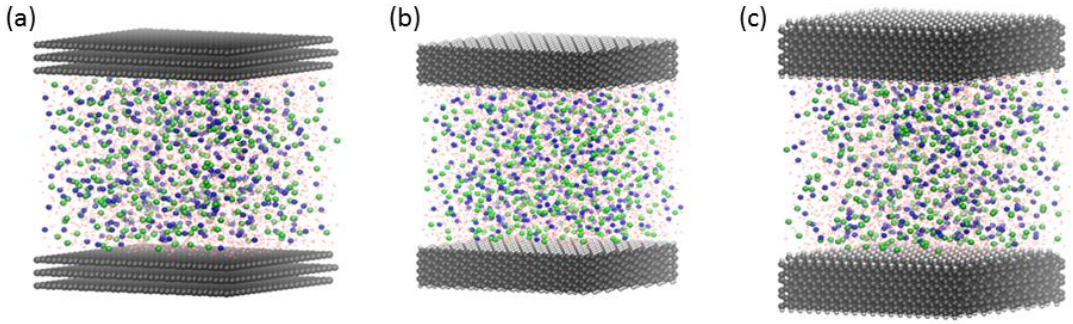


Fig. S6-1. Snapshots of classical molecular dynamics simulations of 6 M NaCl aqueous solution enclosed between two graphite electrodes: (a) basal plane; (b) armchair edge; (c) zigzag edge.

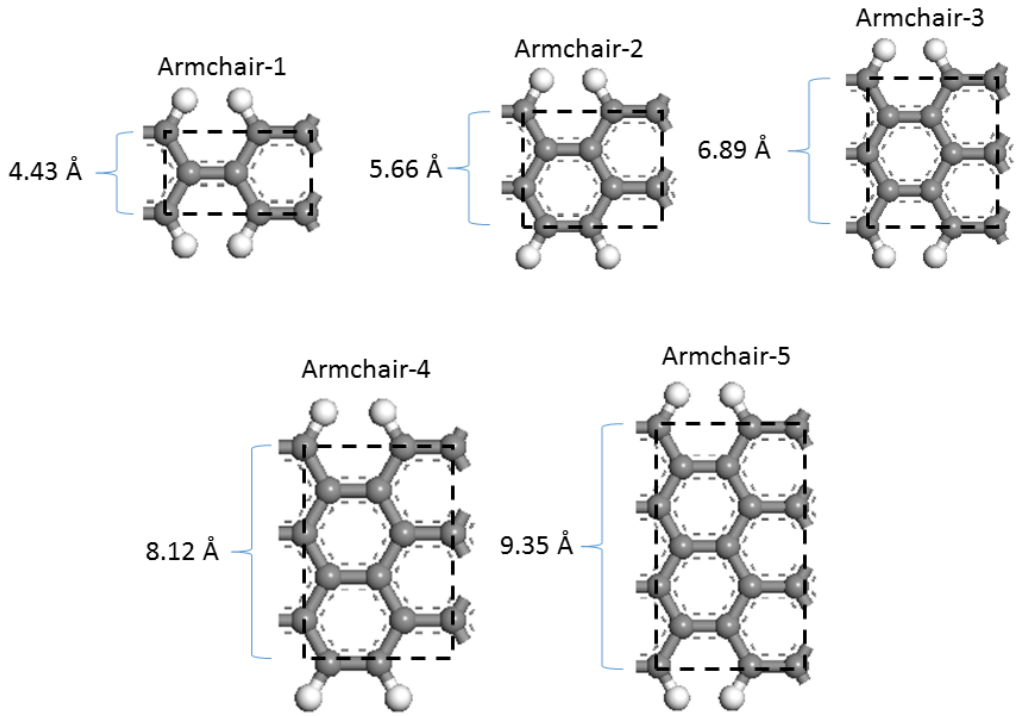


Fig. S6-2. Structures of armchair edges (1 to 5) with different thickness.

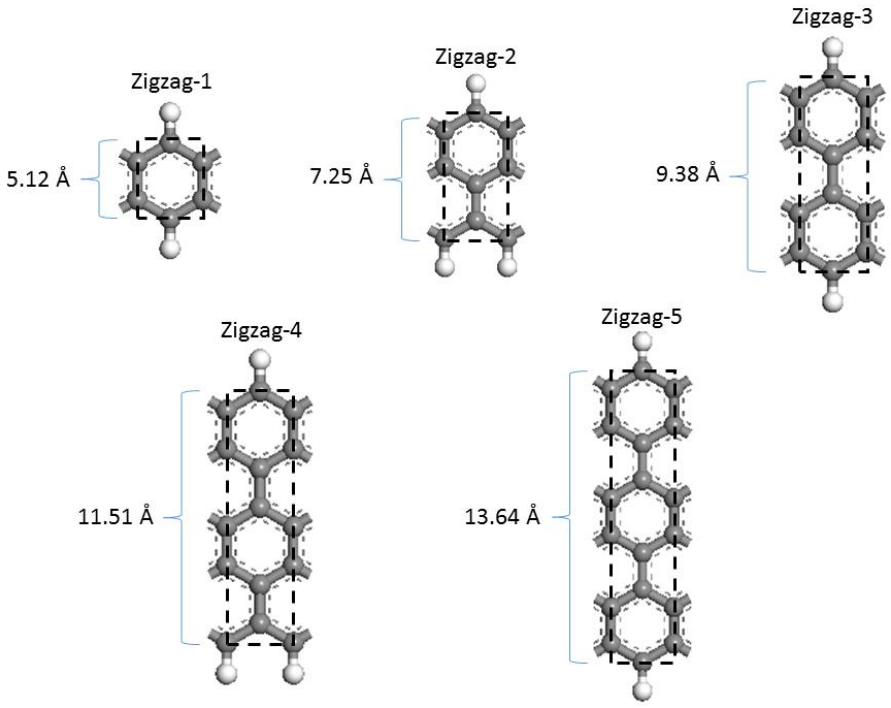


Fig. S6-3. Structures of zigzag edges (1 to 5) with different thickness.

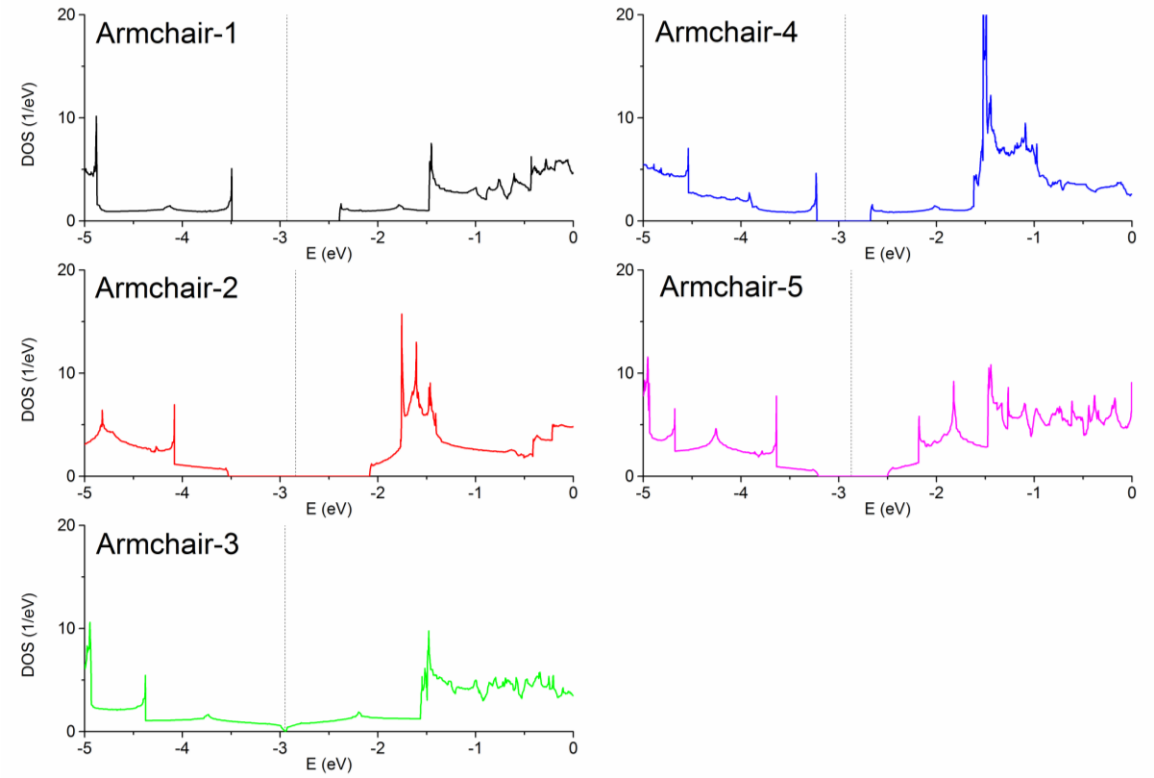


Fig. S6-4. Total Density of States (TDOS) of armchair graphene edges. Dashed lines indicate the Fermi levels.

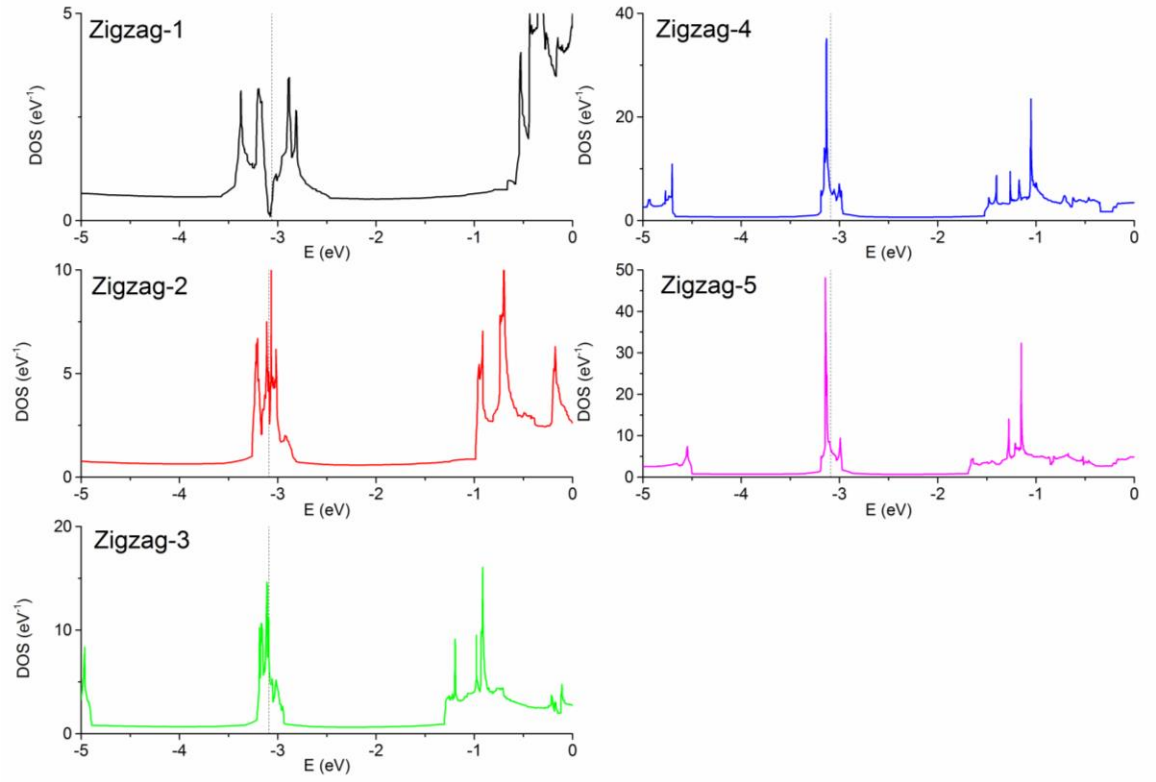


Fig. S6-5. Total Density of States (TDOS) of zigzag graphene edges. Dashed lines indicate the Fermi levels.

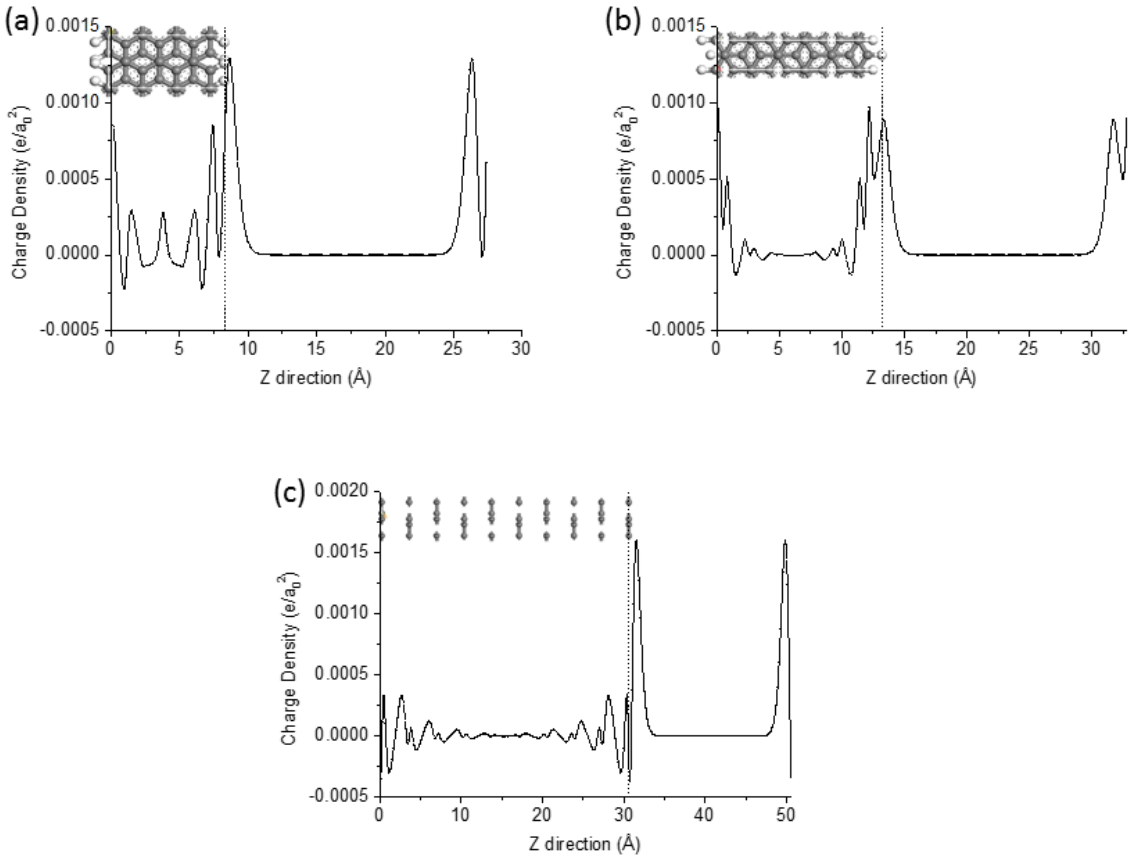


Fig. S6-6. Excess charge distribution of positively charged electrodes: (a) armchair edge; (b) zigzag edge; (c) 10-layer graphene. The surface charge density is fixed to be 20 μC/cm^2.

Chapter 7 Boron Supercapacitors

7.1 Introduction

Supercapacitors have much higher power density than batteries and much greater capacities than conventional dielectric or electrolytic capacitors. They store electric energy electrochemically[1-5] and can be divided into two main types: electric double layer capacitors (EDLCs) and pseudocapacitors. EDLCs stores electrical energy by the formation of electric double layers at the electrode/electrolyte interface, while pseudocapacitors store energy via reversible redox reactions at the electrode surface.[6-8] Due to the simple mechanism of electrostatic charge separation and absence of chemical reactions, EDLCs have much longer cycle life than pseudocapacitors.

Activated carbon is the most widely used electrode material for EDLCs because of its low cost, good conductivity, and chemical stability.[9-13] Many other types of porous carbons have also been explored for EDLCs, including carbide-derived carbons[14, 15] and other nanostructured carbons.[16] The specific capacitance of these carbon materials ranges from 100 to 200 F/g.[1] Due to its high specific surface area (~ 2600 m^2/g) and conductivity,[17-20] the specific capacitance of graphene has been measured recently: it is about 130 F/g in aqueous electrolyte and 90 F/g in ionic liquid.[8] Graphene EDLCs also exhibit very long cycle life.[21] However, unlike a traditional metal electrode, the total capacitance of graphene is limited by its quantum capacitance (C_Q), due to its low density of states (DOS) near the Fermi level.[22-25] To address this issue, one promising way is to dope the graphene with heteroatoms such as nitrogen to increase the DOS at the Fermi

level (in other words, making it more metallic). This strategy has been explored both experimentally and theoretically in many previous studies.[26-34]

A new idea to move beyond graphene EDLCs in terms of specific capacitance is to use a lighter and more metallic material. This idea leads us to boron. There is a recent surge of interest in exploring novel 2D structures of boron.[35, 36] Theoretical studies suggested many possible types of structures of boron, including $\boldsymbol{\alpha}/\boldsymbol{\beta}/\boldsymbol{\gamma}/\mathbf{g}$ types and the less stable triangular and hexagonal sheets.[37-41] The density and configuration of the holes in the 2D hexagonal lattice are important indicators of the relative stability of different types of the 2D boron sheet.[37, 41] Recently, Wu et al. successfully synthesized a stable 2D boron sheet on the Ag(111) surface and visualized the structure by scanning tunneling microscope (STM).[42] The experimentally obtained structures are named $\boldsymbol{\beta}12$ and $\boldsymbol{\chi}3$ whose hole density ($\boldsymbol{\eta}$) is higher than 1/8.[42] The $\boldsymbol{\beta}12$ structure has been theoretically predicted before,[43] while $\boldsymbol{\chi}3$ is a new configuration. Since the 2D boron sheets can have higher specific surface area than graphene and some of them were predicted to be metallic,[43] we believe that 2D boron could be a promising electrode material for supercapacitors. To test this idea, we choose six typical 2D boron configurations and simulate their performance for capacitive energy storage. We show that they are highly promising for EDLC applications.

7.2 Model and Method

The six chosen configurations based on previous experimental and theoretical studies are shown in Figure 7-1. They differ in hole density ($\boldsymbol{\eta}$ values) and the arrangement of the holes. The 2D boron sheets are modeled with the B-B bond length of 1.70 Å, very close to many previous theoretical simulation results.[37, 38] To simulate their charge

capacitive behavior, we applied joint density functional theory (JDFT) developed by Arias et al.,[44, 45] which solves the electrode/electrolyte system self-consistently and is implemented in the code JDFTx v.0.99. Periodic boundary condition was applied to describe the interface; the two sides of the 2D boron electrode were solvated by a 10-Å electrolyte described by a polarizable continuum model (PCM) called the charge-asymmetric nonlocally-determined local-electric (CANDLE) solvation model which explicitly takes into account the solvent charge asymmetry.[45] This solvation model improves upon the linear[44] and nonlinear PCM[46] implementations in JDFT. Here we use the CANDLE model to simulate a 6M aqueous solution. The exchange-correlation energy of the electronic system was calculated by generalized gradient approximation in the form of Perdew-Burke-Ernzerhof functional (GGA-PBE).[47] Ultrasoft pseudopotential was used to describe the nuclei-electron interaction in boron, with 30 Hartree cutoff energy for the plane wave basis.[48] A 24×24×1 k-point mesh was used to sample the Brillouin zone to accurately capture the electron-density optimization at fixed potential calculations in JDFT. To simulate the capacitance, we first fixed the electronic chemical potential on the electrode (ψ) and then computed the surface charge density on the electrode (Q) from the self-consistent JDFT calculation.[49] The differential capacitance of the boron electrode is defined by the derivative of Q vs. ψ: $C_D = dQ/d\psi$, while the integral capacitance is defined as: $C_I = Q/(\psi - \psi_{PZC})$, where ψ_{PZC} is the potential at the point of zero charge. More details of the methodology and the calculations are provided in Supporting Information.

7.3 Results and Discussion

7.3.1 Cohesive energy, electronic structure and PZC of boron sheets

We first examine the stability and electronic structure of the six typical 2D boron or borophene structures in Figure 7-1. We calculated their cohesive energy (E_b) according to: $E_b = E_{atom} - E_{sheet}$, where E_{atom} is the energy of a single boron atom in the ^{2}P state and E_{sheet} is the energy per atom of a 2D boron sheet. So more positive E_b, more stable the structure. From Table 7-1, one can see that the calculated E_b of the six boron sheets varies from 5.84 to 5.90 eV/atom, consistent with previous DFT results.[37] B3, B4, B5, and B6 have about the same stability (within 0.02 eV/atom) and are about 0.05 eV more stable than B1 and B2 because their lower $\boldsymbol{\eta}$ values are closer to the optimal $(1/9 \text{ and } 2/15)$ as predicted by Ismail-Beigi and Yakobson.[37, 41] Electronic density of states (DOS) in Figure 7-2 shows that all the six boron sheets are metallic, indicating that they will be good electrode materials for supercapacitors.

Potential at the point of zero charge (ψ_{PZC}) is an important quantity of an electrode that one can use to evaluate the electrochemical window of charging for an electrode/electrolyte interface. The calculated ψ_{PZC} values of the six 2D boron sheets from JDFT referenced to the standard hydrogen electrode (SHE) are listed in Table 7-1. One can see that the predicted PZC values of B3 to B6 are quite close to that of graphene, implying that the voltage windows of commonly used electrolytes such as KOH for graphene electrodes will also be suitable for charging the 2D boron electrodes. Although the ψ_{PZC} values of B1 and B2 are higher, the difference (~ 0.6 V) is much less than the voltage windows of common electrolytes (~ 1.2 V for aqueous and ~ 2.5 V for organic electrolytes).

Table 7-1. Hole density ($\boldsymbol{\eta}$), calculated cohesive energy (E_b), and potential at the point of zero charge (PZC) of the six boron sheets

Model[a]	$\boldsymbol{\eta}$	E_b (eV/atom)	ψ_{PZC} vs. SHE (V)
B1 ($\boldsymbol{\beta}$12)	1/6	5.85	0.06
B2 ($\boldsymbol{\chi}$3)	1/5	5.84	-0.04
B3 (new $\boldsymbol{\alpha}$)	1/9	5.90	-0.69
B4 (new $\boldsymbol{\beta}$)	1/7	5.88	-0.39
B5 ($\boldsymbol{\alpha}$1)	1/8	5.90	-0.55
B6 ($\boldsymbol{\beta}$1)	1/8	5.88	-0.46
Graphene	-	-	-0.58

[a]The notations in the parentheses are from the literature: $\boldsymbol{\beta}$12 and $\boldsymbol{\chi}$3 from ref. [42]; new $\boldsymbol{\alpha}$ and new $\boldsymbol{\beta}$ from ref. [37]; $\boldsymbol{\alpha}$1 and $\boldsymbol{\beta}$1 from ref.[43].

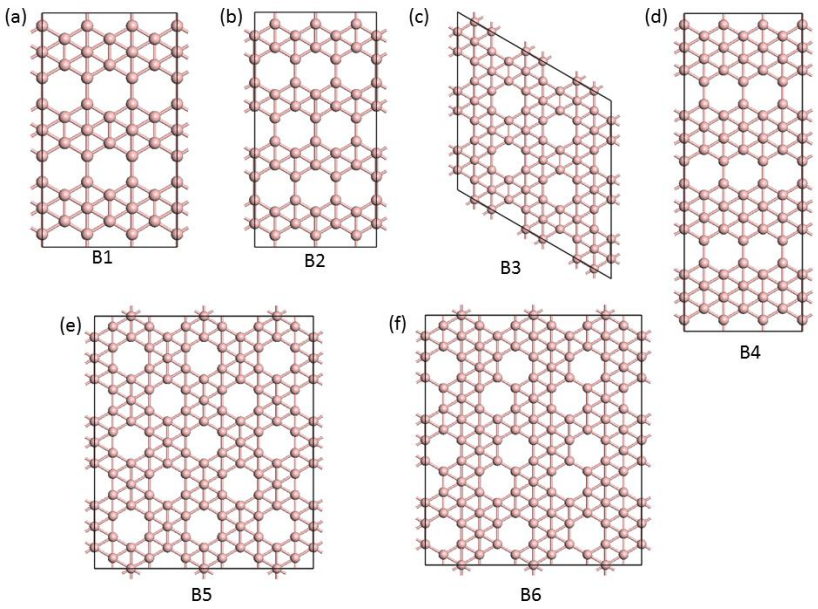


Figure 7-1. Structure models of the six 2D boron sheets examined in this work: (a) B1, 3×3 supercell; (b) B2, 3×2 supercell; (c) B3, 3×3 supercell; (d) B4, 3×2 supercell; (e) B5, 3×3 supercell; (f) B6, 3×3 supercell.

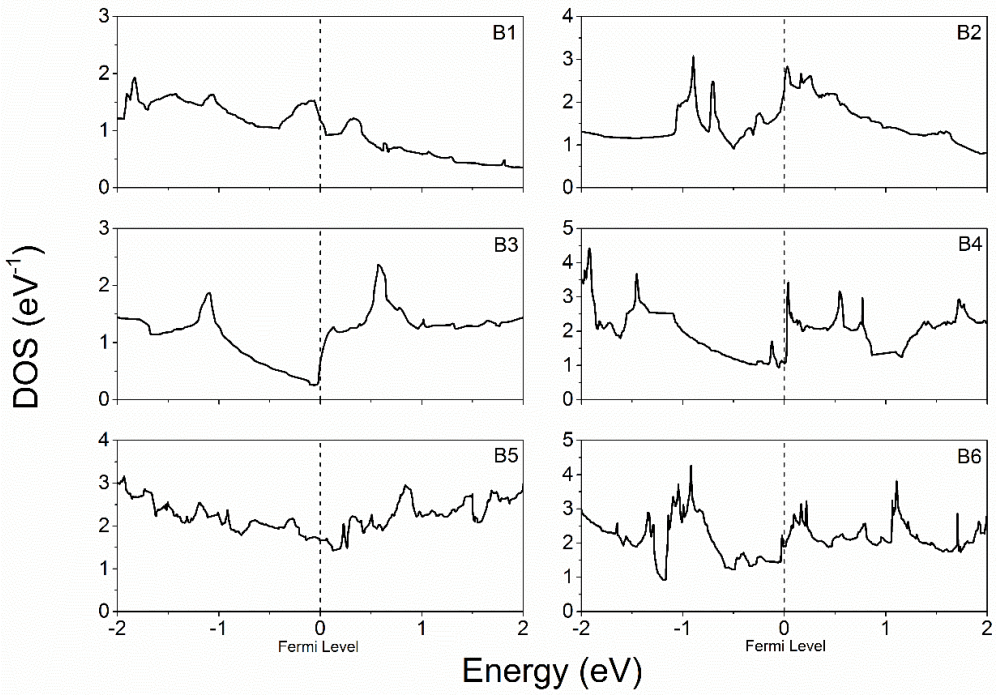


Figure 7-2. Total electronic density of states (DOS) of the six boron sheets as labeled in Figure 7-1.

7.3.2 Charging behavior and capacitive performance of 2D boron sheets

We next examined how the 2D boron sheets respond to negative and positive charging up to 1 V relative to the ψ_{PZC}. Figure 7-3 shows a typical charging state of the electrode/electrolyte interface in the JDFT calculation, where the electrode is at 1 V vs. PZC. One can see that the positive charge on the electrode centers at above 1 Å away the plane of the boron nuclei, while the electrolyte ions (or the Helmholtz layer) peaks at 2 Å away from the boron plane. By integrating the planar charge on the electrode, we can obtain the surface charge density, Q. Figure 7-4 shows how the surface charge density (Q) changes with the applied potential (ψ). One can see that all of the 2D boron sheets examined can store more charge than graphene at the same applied potential.

By differentiating the numerically fitted Q vs. ψ curves, we obtained the area-normalized differential capacitance in Figure 7-5. One can see that the differential capacitance of graphene is about 3 to 5 μF/cm^2, much lower than those of the 2D boron sheets. The differential capacitances of B1 and B2 boron sheets are highest, ranging from 20-30 μF/cm^2 at the -1 V to 13-15 μF/cm^2 at the 1 V and never lower than 12 μF/cm^2. The charging asymmetry or the higher capacitance at the negative voltages is related to the asymmetric response of the boron sheets' electronic structure to the applied potential across the electrode/electrolyte interface. The asymmetric electrolyte response in aqueous electrolyte has been experimentally observed at metal electrode surface.[50] The asymmetry can arise from either the EDL capacitance (for example, the solvation model) or the quantum capacitance. We compared the CANDLE model with the linear PCM model (Figure S7-1) and found that indeed the CANDLE model gives more charge response at the negative side, while the linear PCM model gives more symmetric charging. This difference confirms the effect of explicitly treating solvent charge asymmetry in the CANDLE model. In addition, we separately computed quantum capacitance of B1-B6 through the fixed-band-approximation (Figure S7-2),[22] and found that they all show non-symmetric behavior. Hence, quantum capacitance also contributes to the asymmetric charging as seen in Figure 7-5.

Specific or gravimetric capacitance is an important measure to compare the performances of different electrode materials for EDLCs. We calculated the integral specific capacitance of the six 2D boron sheets for the voltage window from -0.6 V to 0.6 V around ψ_{PZC} in Figure 7-6, corresponding to charging in an aqueous electrolyte. For

comparison, the calculated specific capacitance of graphene is 92.6 F/g in the same voltage window. 2D boron sheets show much higher capacitances, partly due to their light weight. The B1 and B2 structures possess very large specific capacitance close to 400 F/g, nearly four times of that of graphene. The other four structures (B3 to B6) have specific capacitance around 300 F/g. Thus, our results show that 2D boron sheets are a very promising electrode material for EDLCs.

Comparison between our predicted capacitance and the experimental measurements for graphene can offer an estimate of the accuracy for our predicted capacitances for the 2D boron sheets. In 2008, Rouff et al. measured the capacitance of reduced graphene oxide in the KOH electrolyte and obtained a capacitance 100 F/g based on cyclic voltammogram and 135 F/g based galvanostatic discharge.[8] In 2014, Ruoff et al. measured the areal capacitance of a CVD graphene sheet with one side in contact with 6M KOH, and obtained an average value of about 6 μF/cm^2, which corresponds to a gravimetric capacitance of 158 F/g based on the specific surface area of graphene at 2630 m^2/g.[17] So our theoretical capacitance of 93 F/g for graphene underestimates the experimental values. Our predicted capacitances for the 2D boron sheets may be underestimated as well.

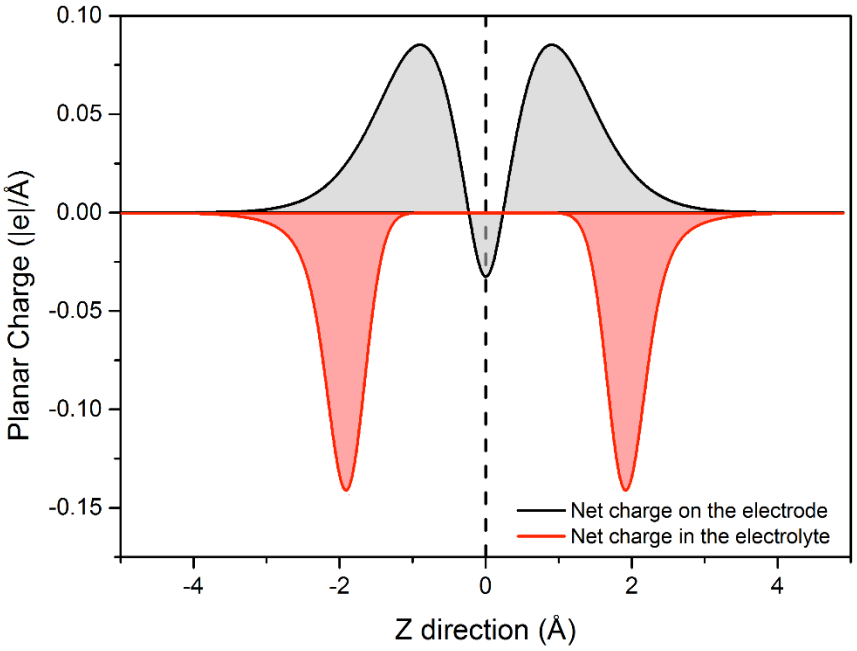


Figure 7-3. The net charge distribution of the electrode/electrolyte system along the z direction, where the position of the B1 sheet is at z=0 Å; the electrode bias potential is 1 V vs. PZC

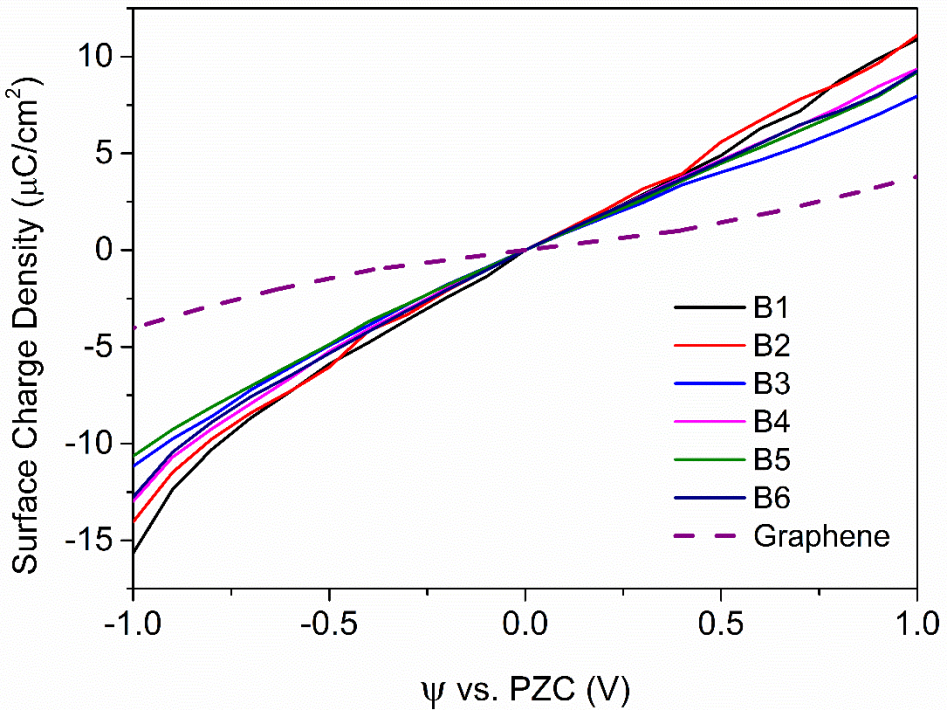


Figure 7-4. Surface charge density (Q) vs. applied potential (ψ) curves of the six 2D boron sheets, in comparison with that of graphene.

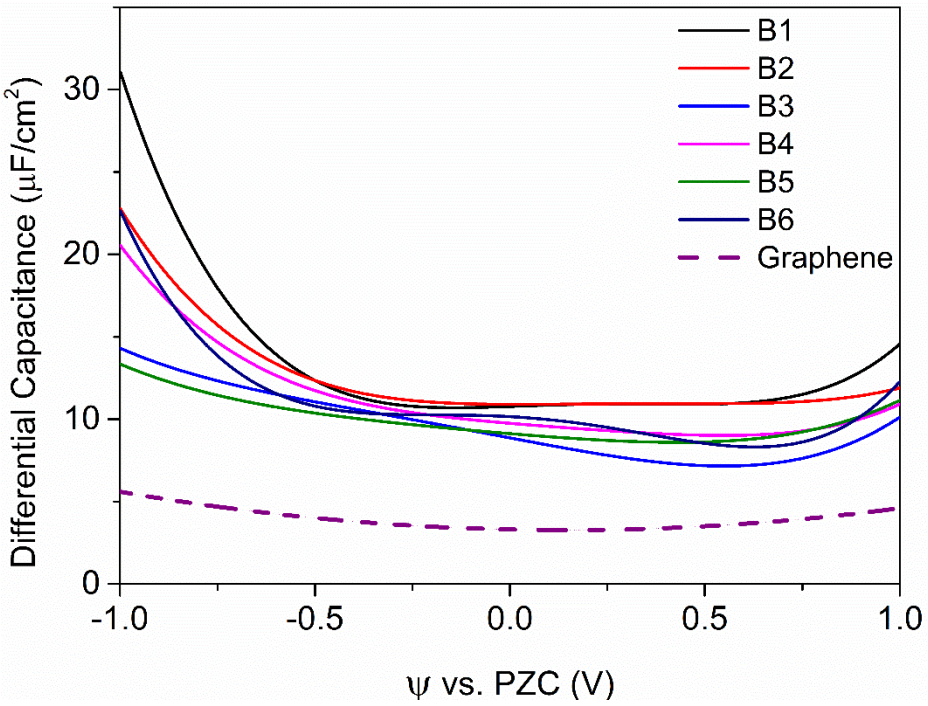


Figure 7-5. Differential capacitance of 2D boron sheets (obtained from differentiation on the numerically fitted Q- ψ curves in Figure 6-4).

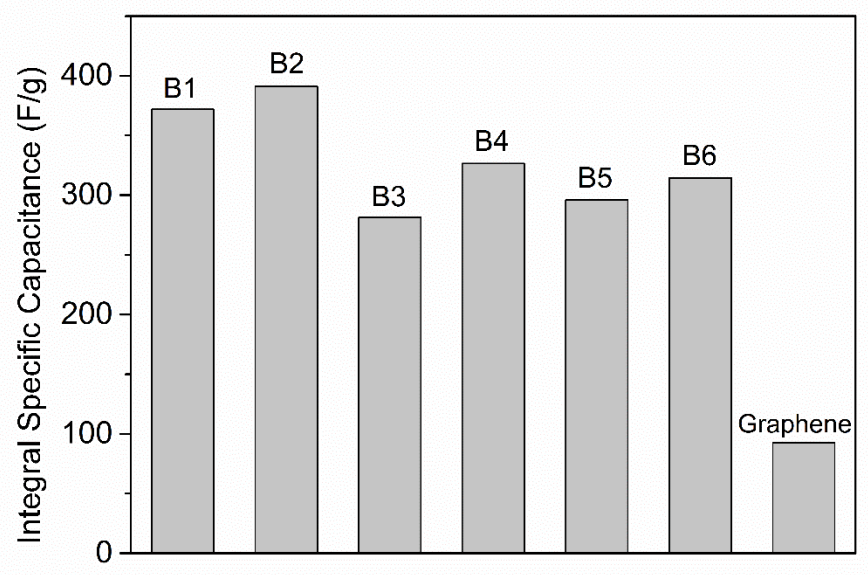


Figure 7-6. Calculated Integral specific capacitance of 2D boron sheets in the voltage window of -0.6 V to 0.6 V around ψ_{PZC}.

7.3.3 Potentiality and challenges of 2D boron supercapacitor

Given our prediction of the high capacitance of 2D boron EDLCs, we suggest that an electrochemical measurement be done on them. Recent progress in growing 2D boron on a metal substrate[42] leads us to believe that experimental setups similar to capacitance measurement of graphene[25] can translated to 2D boron sheets, for example, impedance measurement to obtain the differential capacitance under a specified bias potential.[51] Although the synthesis of free-standing 2D boron has not been realized yet, several potential alternatives are suggested here: i) Preparing 2D boron by selectively etching the metal substrate; ii) Designing porous boron with thin boron wall while some sacrificial templates may be needed for porosity control; iii) CVD growth of 2D boron-graphene hybrids with high boron loading. Since the technologies for graphene processing are rich, it may be possible to prepare the hybrid for EDLC study. Due to its electron deficiency, the 2D boron sheet could be instable in an aqueous electrolyte, especially during electrochemical charging. This problem can be mitigated by using a non-aqueous electrolyte such as organic electrolytes or ionic liquids which have higher electrochemical windows and less chemical reactivity toward boron. Although we modeled the capacitive performance of 2D boron sheets in an implicit aqueous electrolyte, our conclusion can be equally applied to non-aqueous electrolytes.

7.4 Summary and conclusion

In summary, we studied the capacitive performance of 2D boron sheets and found that they exhibit extremely high specific capacitance, about three to four times of that of graphene, due to their metallicity and light weight. Hence we suggest boron as a very

promising EDLC electrode. The huge potential of 2D boron sheets in supercapacitor applications as computationally demonstrated here invites experiments to examine their electrochemical behavior, and the recent success in growing single-layer boron sheets laid foundation for such efforts.

References:

(1) Zhang, L. L.; Zhao, X. S. Carbon-based materials as supercapacitor electrodes. *Chem. Soc. Rev.* **2009**, 38, 2520-2531

(2) Wang, J.; Polleux, J.; Lim, J.; Dunn, B. Pseudocapacitive Contributions to Electrochemical Energy Storage in TiO2 (Anatase) Nanoparticles. *J. Phys. Chem. C* **2007**, 111, 14925-14931

(3) Sassin, M. B.; Chervin, C. N.; Rolison, D. R.; Long, J. W. Redox Deposition of Nanoscale Metal Oxides on Carbon for Next-Generation Electrochemical Capacitors. *Acc. Chem. Res.* **2013**, 46, 1062-1074

(4) Sarangapani, S.; Tilak, B. V.; Chen, C. P. Materials for Electrochemical Capacitors - Theoretical and Experimental constraints. *J. Electrochem. Soc.* **1996**, 143, 3791-3799

(5) Makino, S.; Ban, T.; Sugimoto, W. Towards Implantable Bio-Supercapacitors: Pseudocapacitance of Ruthenium Oxide Nanoparticles and Nanosheets in Acids, Buffered Solutions, and Bioelectrolytes. *J. Electrochem. Soc.* **2015**, 162, A5001-A5006

(6) Zhai, Y. P.; Dou, Y. Q.; Zhao, D. Y.; Fulvio, P. F.; Mayes, R. T.; Dai, S. Carbon materials for chemical capacitive energy storage. *Adv. Mater.* **2011**, 23, 4828-4850

(7) Wang, Y.; Shi, Z. Q.; Huang, Y.; Ma, Y. F.; Wang, C. Y.; Chen, M. M.; Chen, Y. S. Supercapacitor devices based on graphene materials. *J. Phys. Chem. C* **2009**, 113, 13103-13107

(8) Stoller, M. D.; Park, S. J.; Zhu, Y. W.; An, J. H.; Ruoff, R. S. Graphene-based ultracapacitors. *Nano Lett.* **2008**, 8, 3498-3502

(9) Yang, X. W.; Cheng, C.; Wang, Y. F.; Qiu, L.; Li, D. Liquid-Mediated Dense Integration of Graphene Materials for Compact Capacitive Energy Storage. *Science* **2013**, 341, 534-537

(10) Wang, Y. F.; Yang, X. W.; Qiu, L.; Li, D. Revisiting the Capacitance of Polyaniline by Using Graphene Hydrogel Films as a Substrate: the Importance of Nano-architecturing. *Energ Environ. Sci.* **2013**, 6, 477-481

(11) Hahm, M. G.; Reddy, A. L. M.; Cole, D. P.; Rivera, M.; Vento, J. A.; Nam, J.; Jung, H. Y.; Kim, Y. L.; Narayanan, N. T.; Hashim, D. P., et al. Carbon Nanotube-Nanocup Hybrid Structures for High Power Supercapacitor Applications. *Nano Lett.* **2012**, 12, 5616-5621

(12) Futaba, D. N.; Hata, K.; Yamada, T.; Hiraoka, T.; Hayamizu, Y.; Kakudate, Y.; Tanaike, O.; Hatori, H.; Yumura, M.; Iijima, S. Shape-Engineerable and Highly Densely Packed Single-Walled Carbon Nanotubes and Their Application as Super-capacitor Electrodes. *Nat. Mater.* **2006**, 5, 987-994

(13) Huang, P.; Lethien, C.; Pinaud, S.; Brousse, K.; Laloo, R.; Turq, V.; Respaud, M.; Demortiere, A.; Daffos, B.; Taberna, P. L., et al. On-Chip and Freestanding Elastic Carbon Films for Micro-Supercapacitors. *Science* **2016**, 351, 691-695

(14) Chmiola, J.; Largeot, C.; Taberna, P. L.; Simon, P.; Gogotsi, Y. Monolithic Carbide-Derived Carbon Films for Micro-Supercapacitors. *Science* **2010**, 328, 480-483

(15) Gogotsi, Y.; Nikitin, A.; Ye, H. H.; Zhou, W.; Fischer, J. E.; Yi, B.; Foley, H. C.; Barsoum, M. W. Nanoporous Carbide-Derived Carbon with Tunable Pore Size. *Nat. Mater.* **2003**, 2, 591-594

(16) Candelaria, S. L.; Shao, Y. Y.; Zhou, W.; Li, X. L.; Xiao, J.; Zhang, J. G.; Wang, Y.; Liu, J.; Li, J. H.; Cao, G. Z. Nanostructured Carbon for Energy Storage and Conversion. *Nano Energy* **2012**, 1, 195-220

(17) Ji, H.; Zhao, X.; Qiao, Z.; Jung, J.; Zhu, Y.; Lu, Y.; Zhang, L. L.; MacDonald, A. H.; Ruoff, R. S. Capacitance of carbon-based electrical double-layer capacitors. *Nat. Commun.* **2014**, 5, 3317

(18) Uesugi, E.; Goto, H.; Eguchi, R.; Fujiwara, A.; Kubozono, Y. Electric double-layer capacitance between an ionic liquid and few-layer graphene. *Sci. Rep.* **2013**, 3, 1595

(19) Stoller, M. D.; Magnuson, C. W.; Zhu, Y. W.; Murali, S.; Suk, J. W.; Piner, R.; Ruoff, R. S. Interfacial capacitance of single layer graphene. *Energ Environ. Sci.* **2011**, 4, 4685-4689

(20) Liu, C. G.; Yu, Z. N.; Neff, D.; Zhamu, A.; Jang, B. Z. Graphene-Based Supercapacitor with an Ultrahigh Energy Density. *Nano Lett.* **2010**, 10, 4863-4868

(21) Cheng, Y. W.; Lu, S. T.; Zhang, H. B.; Varanasi, C. V.; Liu, J. Synergistic Effects from Graphene and Carbon Nanotubes Enable Flexible and Robust Electrodes for High-Performance Supercapacitors. *Nano Lett.* **2012**, 12, 4206-4211

(22) Zhan, C.; Neal, J.; Wu, J. Z.; Jiang, D. E. Quantum Effects on the Capacitance of Graphene-Based Electrodes. *J. Phys. Chem. C* **2015**, 119, 22297–22303

(23) Brooksby, P.; Farquhar, A.; Dykstra, H.; Waterland, M.; Downard, A. Quantum capacitance of aryldiazonium modified large area few-layer graphene electrodes. *J. Phys. Chem. C* **2015**, 119, 25778–25785

(24) Paek, E.; Pak, A. J.; Hwang, G. S. A computational study of the interfacial structure and capacitance of graphene in [BMIM][PF_6] ionic liquid. *J. Electrochem. Soc.* **2013**, 160, A1-A10

(25) Xia, J. L.; Chen, F.; Li, J. H.; Tao, N. J. Measurement of the quantum capacitance of graphene. *Nat. Nanotechnol.* **2009**, 4, 505-509

(26) Vatamanu, J.; Ni, X. J.; Liu, F.; Bedrov, D. Tailoring graphene-based electrodes from semiconducting to metallic to increase the energy density in supercapacitors. *Nanotechnology* **2015**, 26, 464001

(27) Wood, B. C.; Ogitsu, T.; Otani, M.; Biener, J. First-principles-inspired design strategies for graphene-based supercapacitor electrodes. *J. Phys. Chem. C* **2014**, 118, 4-15

(28) Paek, E.; Pak, A. J.; Kweon, K. E.; Hwang, G. S. On the origin of the enhanced supercapacitor performance of nitrogen-doped graphene. *J. Phys. Chem. C* **2013**, 117, 5610-5616

(29) Zhang, L. L.; Zhao, X.; Ji, H. X.; Stoller, M. D.; Lai, L. F.; Murali, S.; Mcdonnell, S.; Cleveger, B.; Wallace, R. M.; Ruoff, R. S. Nitrogen doping of graphene and its effect on quantum Capacitance, and a new insight on the enhanced capacitance of N-doped carbon. *Energ Environ. Sci.* **2012**, 5, 9618-9625

(30) Zou, Y. Q.; Kinloch, I. A.; Dryfe, R. A. W. Nitrogen-Doped and Crumpled Graphene Sheets with Improved Supercapacitance. *J. Mater. Chem. A* **2014**, 2, 19495-19499

(31) Wang, K.; Li, L. W.; Zhang, T. Z.; Liu, Z. F. Nitrogen-Doped Graphene for Supercapacitor with Long-term Electrochemical Stability. *Energy* **2014**, 70, 612-617

(32) Wen, Z. H.; Wang, X. C.; Mao, S.; Bo, Z.; Kim, H.; Cui, S. M.; Lu, G. H.; Feng, X. L.; Chen, J. H. Crumpled Nitrogen-Doped Graphene Nanosheets with Ultrahigh Pore Volume for High-Performance Supercapacitor. *Adv. Mater.* **2012**, 24, 5610-5616

(33) Zhao, L. Y.; He, R.; Rim, K. T.; Schiros, T.; Kim, K. S.; Zhou, H.; Gutierrez, C.; Chockalingam, S. P.; Arguello, C. J.; Palova, L., et al. Visualizing Individual Nitrogen Dopants in Monolayer Graphene. *Science* **2011**, 333, 999-1003

(34) Zhang, C. H.; Fu, L.; Liu, N.; Liu, M. H.; Wang, Y. Y.; Liu, Z. F. Synthesis of Nitrogen-Doped Graphene Using Embedded Carbon and Nitrogen Sources. *Adv. Mater.* **2011**, 23, 1020-1024

(35) Boustani, I. New Quasi-Planar Surfaces of Bare Boron. *Surf. Sci* **1997**, 370, 355-363

(36) Tai, G. A.; Hu, T. S.; Zhou, Y. G.; Wang, X. F.; Kong, J. Z.; Zeng, T.; You, Y. C.; Wang, Q. Synthesis of Atomically Thin Boron Films on Copper Foils. *Angew Chem Int Edit* **2015**, 54, 15473-15477

(37) Tang, H.; Ismail-Beigi, S. Novel Precursors for Boron Nanotubes: The Competition of Two-Center and Three-Center Bonding in Boron Sheets. *Phys. Rev. Lett.* **2007**, 99, 115501

(38) Tang, H.; Ismail-Beigi, S. First-Principles Study of Boron Sheets and Nanotubes. *Phys. Rev. B* **2010**, 82, 115412

(39) Miller, J. New Sheet Structures may be the Basis for Boron Nanotubes. *Phys. Today* **2007**, 60, 20-21

(40) Ozdogan, C.; Mukhopadhyay, S.; Hayami, W.; Guvenc, Z. B.; Pandey, R.; Boustani, I. The Unusually Stable B-100 Fullerene, Structural Transitions in Boron Nanostructures, and a Comparative Study of alpha- and gamma-Boron and Sheets. *J. Phys. Chem. C* **2010**, 114, 4362-4375

(41) Penev, E. S.; Bhowmick, S.; Sadrzadeh, A.; Yakobson, B. I. Polymorphism of Two-Dimensional Boron. *Nano Lett.* **2012**, 12, 2441-2445

(42) Feng, B. J.; Zhang, J.; Zhong, Q.; Li, W. B.; Li, S.; Li, H.; Cheng, P.; Meng, S.; Chen, L.; Wu, K. H. Experimental Realization of Two-Dimensional Boron Sheets. *Nat. Chem.* **2016**, 8, 564-569

(43) Wu, X. J.; Dai, J.; Zhao, Y.; Zhuo, Z. W.; Yang, J. L.; Zeng, X. C. Two-Dimensional Boron Monolayer Sheets. *Acs Nano* **2012**, 6, 7443-7453

(44) Letchworth-Weaver, K.; Arias, T. A. Joint density functional theory of the electrode-electrolyte interface: application to fixed electrode potentials, interfacial capacitances, and potentials of zero charge. *Phys. Rev. B* **2012**, 86, 075140

(45) Sundararaman, R.; Goddard, W. A. The Charge-Asymmetric Nonlocally Determined Local-Electric (CANDLE) Solvation Model. *J. Chem. Phys.* **2015**, 142, 064107

(46) Gunceler, D.; Letchworth-Weaver, K.; Sundararaman, R.; Schwarz, K. A.; Arias, T. A. The Importance of Nonlinear Fluid Response in Joint Density-Functional Theory Studies of Battery Systems. *Modell. Simul. Mater. Sci. Eng.* **2013**, 21, 074005

(47) Perdew, J. P.; Burke, K.; Ernzerhof, M. Generalized Gradient Approximation Made Simple. *Phys. Rev. Lett.* **1996**, 77, 3865-3868

(48) Garrity, K. F.; Bennett, J. W.; Rabe, K. M.; Vanderbilt, D. Pseudopotentials for High-throughput DFT Calculations. *Comput. Mater. Sci.* **2014**, 81, 446-452

(49) Zhan, C.; Jiang, D. E. Contribution of dielectric screening to the total capacitance of few-layer graphene electrodes. *J. Phys. Chem. Lett* **2016**, 7, 789

(50) Rosen, M.; Flinn, D. R.; Schuldin.S Double Layer Capacitance on Platinum in 1m H2s04 from Reversible Hydrogen Potential to Oxygen Formation Region. *J. Electrochem. Soc.* **1969**, 116, 1112

(51) Segalini, J.; Daffos, B.; Taberna, P. L.; Gogotsi, Y.; Simon, P. Qualitative Electrochemical Impedance Spectroscopy Study of Ion Transport into Sub-nanometer Carbon Pores in Electrochemical Double Layer Capacitor Electrodes. *Electrochim. Acta* **2010**, 55, 7489-7494

Supporting Information

Joint Density Functional Theory (JDFT) is a DFT-based electronic structure calculation method embedded with solvation model. The treatment of solvation has several levels: Classical Density Functional Theory (Classical DFT) for explicit solvation model and Polarizable Continuum Model (PCM) for implicit solvation. In this work, we used CANDLE solvation[1], which is one type of implicit solvation model (PCM) in JDFTx code. JDFT do the self-consistent solid/liquid calculation by iteratively updating electrostatic potential from Kohn-Sham equation in solute and Poisson-Boltzmann equation in solvent.[2] The exact calculation process and technical details are in Ref.1 and Ref.2. From the electronic chemical potential (Fermi level) and electron number of the solute, we can obtain the capacitance of the electrode. There are two ways to calculate the capacitance: 1. Fix the charge of electrode and calculate the electronic chemical potential. 2. Fix the electronic chemical potential and optimize the electron number. The method we used is the latter one. The exact process of how to compute the capacitance can be found in the JDFTx webpage: http://jdftx.org/

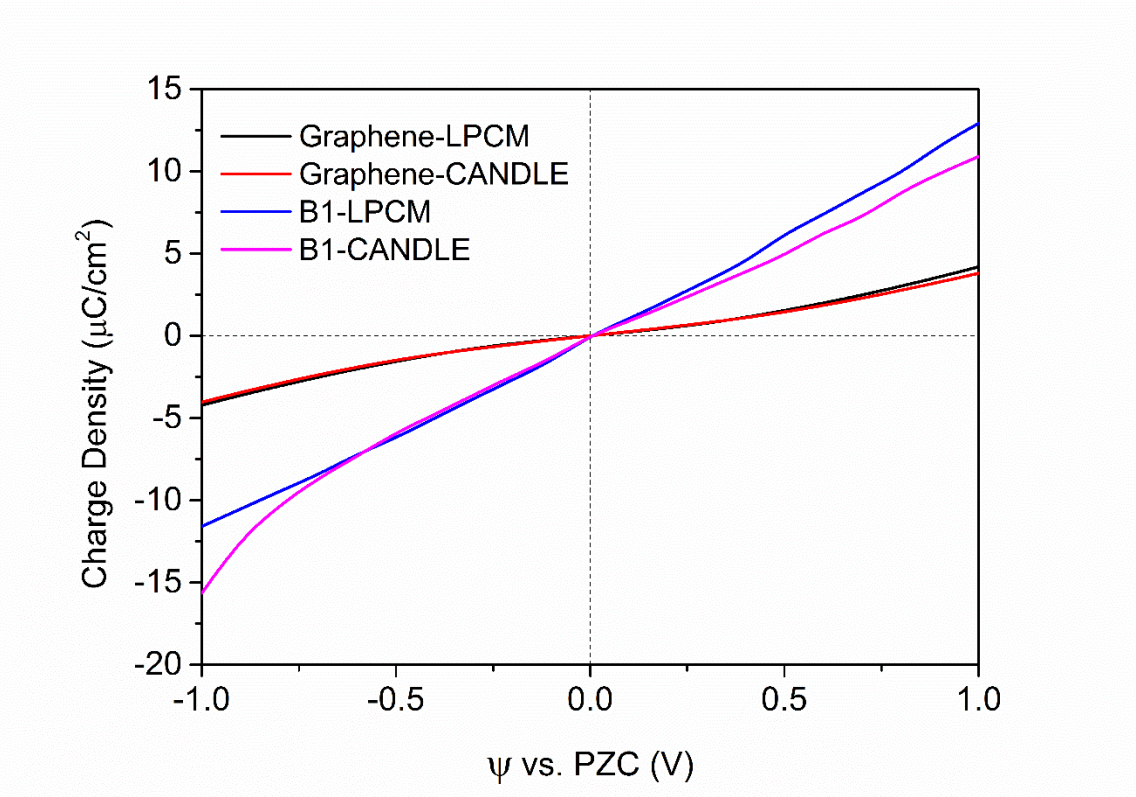


Figure S7-1. Solvation model test on the charging simulation of graphene and boron sheet (B1). Linear Polarizable Continuum Model (LPCM) describe the solvent through empirical cavity function, while the CANDLE solvation improved the cavity function of PCM by adding asymmetric correction

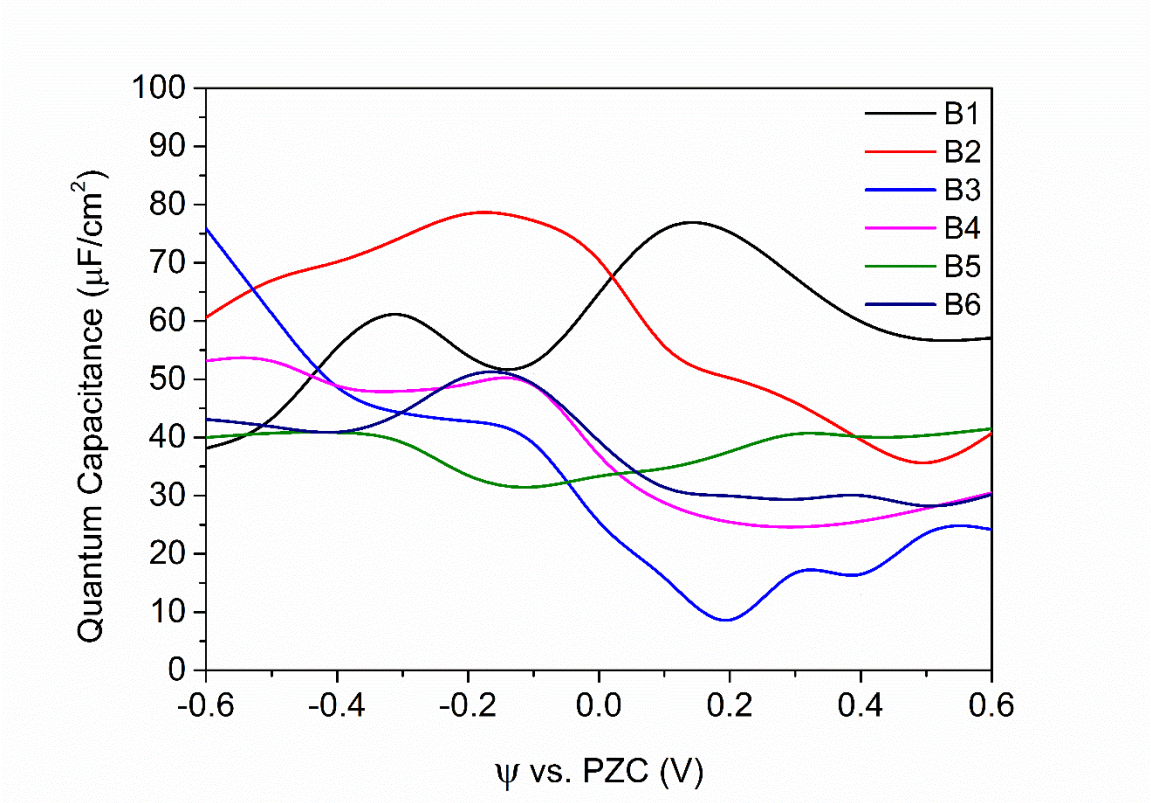


Figure S7-2. Quantum capacitance of B1-B6 calculated through Fixed-Band-Approximation. PZC is set on the Fermi level of the neutral electrodes.

References:

1. Sundararaman, R.; Goddard, W. A. The Charge-Asymmetric Nonlocally Determined Local-Electric (CANDLE) Solvation Model. *J. Chem. Phys.* **2015**, *142*, 064107.

2. Letchworth-Weaver, K.; Arias, T. A. Joint Density Functional Theory of the Electrode-Electrolyte Interface: Application to Fixed Electrode Potentials, Interfacial Capacitances, and Potentials of Zero Charge. *Phys. Rev. B* **2012**, *86*, 075140.

Chapter 8. Understanding the pseudocapacitance of RuO_2 from joint density functional theory

8.1 Introduction

Capacitors are an important electronic device that can store and release electrical energy very quickly. Traditional capacitors consist of a dielectric layer sandwiched by two electrodes. By making the dielectric layer very thin, nanocapacitors have been explored both computationally and experimentally.[1-4] Due to their much larger capacity than traditional dielectric capacitors, supercapacitors store energy electrochemically and are playing important roles in electric energy storage.[5, 6] Two main types of supercapacitors are used: an electric double-layer capacitor (EDLC) stores energy in the electric double layer (EDL) and a pseudocapacitor stores energy via a surface redox process. Comparing with EDLCs, pseudocapacitor has higher energy density due to the advantage of redox reaction in charge storage.[7-9] Transition metal oxide is a typical electrode material to achieve pseudocapacitive energy storage due to its multivalence oxidation states.[10-19] In particular, ruthenium oxide has been studied for many years as a promising pseudocapacitor material.[20-26]

Trasatti proposed that the charge storage mechanism of ruthenium oxide capacitor can be interpreted by the redox reaction:[21]

$$RuO_x(OH)_y + zH^+ + ze^- \leftrightarrows RuO_{x-z}(OH)_{y+z} \qquad 8\text{-}1$$

The oxidation state of Ru can be +4, +3 and +2 during the charge storage process, which could give a maximum theoretical capacitance over 1400 F/g.[9] Experimental study on the RuO_2 pseudocapacitor showed that the measured capacitance from cyclic voltammetry

(CV) is sensitive to the scan rate: a sharp redox peak showed up at low scan rate in the voltage of 0.1 to 0.4 V vs. reverse hydrogen electrode, while at high scan rate the CV curve is rectangle.[27, 28]

Specific capacitance of ruthenium oxide can also be greatly influenced by the particle size and the amount of structure water.[28] There have been many hypotheses for explaining the capacitive behavior of ruthenium oxide,[29, 30] but first principles studies have been limited. Although classical simulations and theory have been successfully applied to model EDLCs,[31-41] a first principles method such as electronic density functional theory (DFT) is needed to include the electronic structure and surface chemistry of the electrode into consideration when modeling RuO_2 pseudocapacitance. Although the DFT approach has been successfully applied to model the solid-state dielectric nanocapacitors,[1-4] previous DFT calculations on the RuO_2 electrode examined proton adsorption and intercalation, but could not quantify the pseudocapacitance of RuO_2.[42, 43] Directly calculating the Gibbs free energy of redox reaction could not accurately predict the electrode voltage of the reaction since it ignored the electrode-electrolyte interaction and the influence of overpotential.[44]

To be able to accurately quantify the pseudocapacitance of RuO_2 from first principles, one needs to take into account both the EDL and redox mechanisms at the same time. To this end, herein we employ the joint density functional theory (JDFT) that allows us to examine the electrode/electrolyte interface self-consistently by treating the electrode at the electronic-structure level and the electrolyte classically. This approach enables us to calculate the electronic chemical potential shift with the surface redox reaction and to compute the differential capacitance versus the electrode voltage, thereby providing a

capacitive curve from first principles that can be directly compared with the measured pseudocapacitive behavior. In Sec. 8-2, we explain in detail the JDFT approach for the pseudocapacitive charge storage. Our main results are discussed in Sec. 8-3, and we conclude in Sec. 8-4.

8.2 Methods

Electronic chemical potential and total energy were calculated by Joint Density Functional Theory (JDFT) in the JDFTx package with the implementation of linear polarizable continuum model (linear PCM),[45] which has been used in several theoretical electrochemical studies before.[45-47] Periodic boundary condition (supercell) was used to describe the solid/liquid interface: here we chose the most stable and active surface of rutile type RuO_2, the (110) surface[48, 49], modeled in an orthogonal crystal with a=6.24 Å, b=12.74 Å and c=25.14 Å (2×2×1 supercell). More structural details about RuO_2 crystal are in Supporting Information. The space along the c direction between two periodic slabs was filled with the implicit solvation model, as shown in Figure 8-1a. The Generalized Gradient Approximation in the form of Perdew−Burke−Ernzerhof (GGA-PBE) functional was chosen to describe the exchange-correlation energy.[50] Ultrasoft pseudopotential was used to describe the nuclei-electron interaction.[51] The cutoff energy of plane wave basis set was 20 hartree in structure optimization and 30 hartree in electronic structure calculation. The k-points mesh for Brillouin zone sampling was 4×2×1 in structure optimization and 8×4×1 in electronic chemical potential calculation.

In our simulation, the total capacitance is defined by the total charge over the electronic chemical potential shift: $Q_{tot}/\Delta\boldsymbol{\mu}$.[52, 53] The total charge (Q_{tot}) includes both

Faradaic (Q_{ps}) and non-Faradaic (Q_{EDL}) parts as shown in Figure 8-1b, corresponding to pseudocapacitance (C_{ps}) and EDL capacitance (C_{EDL}), respectively. Thus, it is important for us to determine how to assign Q_{ps} and Q_{EDL} for a given Q_{tot}. To solve this problem, we propose a redox-EDL competition mechanism: at very low scan rate, the electrochemical behavior is at thermodynamic equilibrium and the capacitive behavior is dominated by thermodynamic energy preference. When the electrode is charged by a certain amount such as 1 e^-, we can compare the EDL energy (U_{EDL}) and hydrogen adsorption energy (E_H) to predict the capacitive behavior.

U_{EDL} is defined by the energy drop of electrode to form the EDL to neutralize the surface charge of 1 e^-:

$$U_{EDL} = -\int_{V1}^{V2} C_{EDL} V \, dV \tag{8-2}$$

where V_1 and V_2 correspond to the electronic chemical potential shift with the excess charge of 1 e^-. E_H, the hydrogen adsorption energy for a single H atom, is defined by

$$E_H = U_{sub+H} - U_{sub} - \frac{1}{2} U_{H2} + \Delta ZPE \tag{8-3}$$

where U_{sub+H} and U_{sub} are the total energy of H adsorbed substrate and bare substrate, respectively. ΔZPE is the difference in zero point energy of hydrogen on the substrate and that of H_2 molecule. We use the ΔZPE of 0.165 eV/H from previous DFT work.[42] For consecutive hydrogen adsorption, then we define E_H (n), the hydrogen adsorption energy when n H atoms have been absorbed on the substrate:

$$E_H(n) = U_{sub+(n+1)H} - U_{sub+nH} - \frac{1}{2} U_{H2} + \Delta ZPE \tag{8-4}$$

By comparing the U_{EDL} and $E_H(n)$, we can estimate which way of charge storage is more preferable to neutralize the charged surface as we progressively charge up the electrode, as indicated in Figure 8-2.

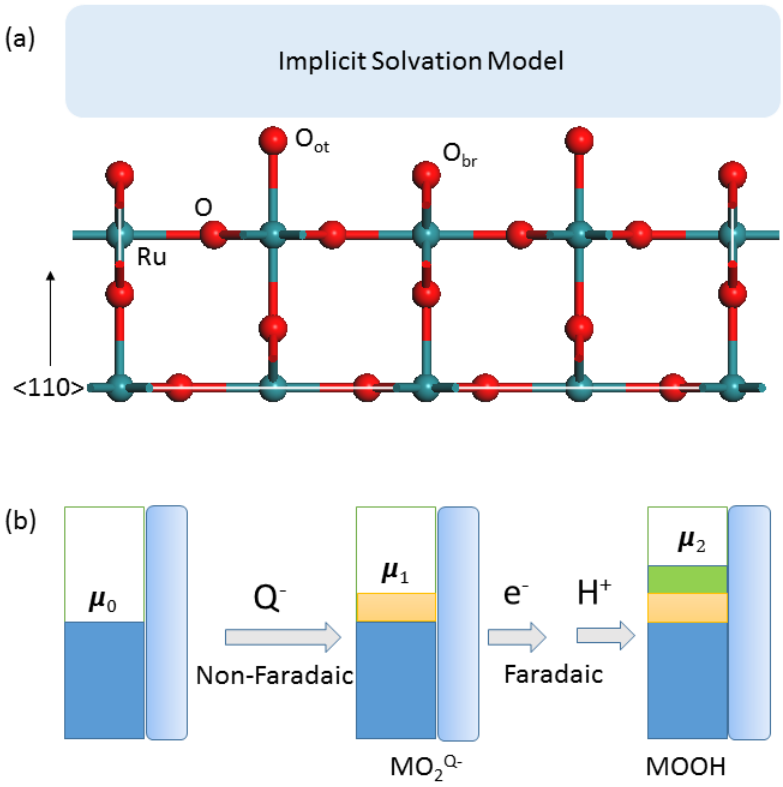


Figure 8-1. (a) Side view of RuO_2 (110). (b) Scheme of modeling the capacitance in transition metal oxide, MO_2.

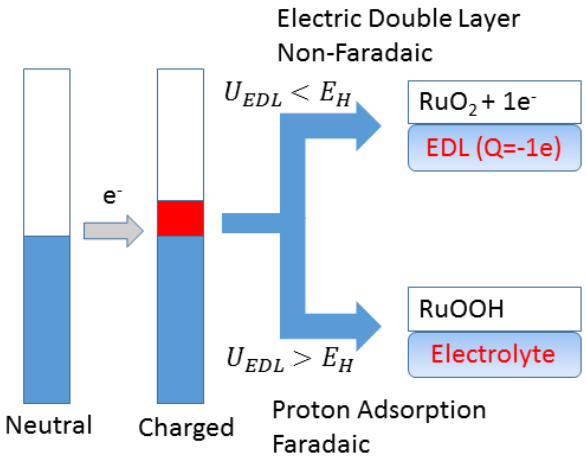


Figure 8-2. A brief scheme to show how to determine the capacitive behavior by comparing the U_{EDL} and E_H.

8.3 Results and Discussion

First, we determine the potential of zero charge (PZC) and distinguish the different charge storage behavior of the anode and the cathode. Then, we focus on the capacitive behavior of the cathode. Since the EDL capacitance is always in existence as long as there is a charged surface, we will examine the intrinsic EDL capacitance of the RuO_2(110) surface, and then compare the competition between EDL charge storage and redox charge storage on the cathode. Finally, based on the redox-EDL competition analysis, we will plot a capacitance-potential curve and provide a surface structure-based interpretation on the pseudocapacitive charge storage behavior of RuO_2(110).

8.3.1 Potential of zero charge on RuO_2(110).

We need to find out the potential of zero charge on RuO_2(110) in our system to assign potential region of positive and negative electrode charging behavior. For a pure RuO_2(110) surface in contact with a 1M implicit electrolyte, the calculated electronic

chemical potential is -4.70 eV. This calculated electronic chemical potential comes from the total consequence of work function and implicit solvation model, while the zero potential is defined far inside the electrolyte. From the JDFT benchmark calculation, the standard hydrogen electrode (SHE) is at -4.52 eV with the GGA-PBE functional.[45] Thus, our calculated potential of zero charge (PZC) is 0.18 V vs SHE. In addition, the calculated PZC is substrate thickness-independent. Experimental PZC of RuO_2(110) is 0.15 V vs SHE in 10^{-3} M Na_2SO_4,[54] consistent with our DFT calculation. Here we should note that our PZC calculation is based on the electronic work function of the material with the consideration of solvation effect. The JDFTx code performs well when calculating the PZC by using linear PCM if there is no surface reaction that affects the PZC.[45] In the acidic electrolyte such as H_2SO_4, the PZC of transition metal oxide should be more positive so that it can resist proton adsorption to keep the surface neutral. When the electrode potential is higher than PZC, the electrode is positively charged and the capacitance is determined by the EDL because there is no available redox reaction of SO_4^{2-} anion. Below the PZC, the electrode is negatively charged and the capacitance contribution is determined by the competition between the proton adsorption reaction and EDL. Thus, it is necessary to analyze the redox-EDL competition to determine the capacitive behavior of cathode.

8.3.2 Influence of surface hydrogen adsorption on EDL capacitance.

Since the EDL and redox reaction could simultaneously exist when electrode is negatively charged, it is important to know how H adsorption influences the EDL capacitance. We calculated the EDL capacitance (C_{EDL}) of RuO_2(110) surface with different hydrogen coverage at various surface charge density range (Figure 8-3). One can

see that the EDL capacitance of a pure RuO_2(110) is about 19 μF/cm^2, comparable to experimental measurement for aqueous electrolyte.[55] With the surface H adsorption, C_{EDL} changed about ±2 μF/cm^2 within the first three H adsorption. The calculated electronic density of states in Figure 8-4 also showed that H-adsorbed RuO_2(110) is metallic. Thus, the electronic chemical potential shift is dominated by the electrolyte response (EDL capacitance). When the forth H is adsorbed on the surface, C_{EDL} shows a large change and becomes very sensitive to charge. Since at the forth H adsorption, the electrode potential is close to that of hydrogen evolution on RuO_2, we mainly focus on the first three H adsorption.

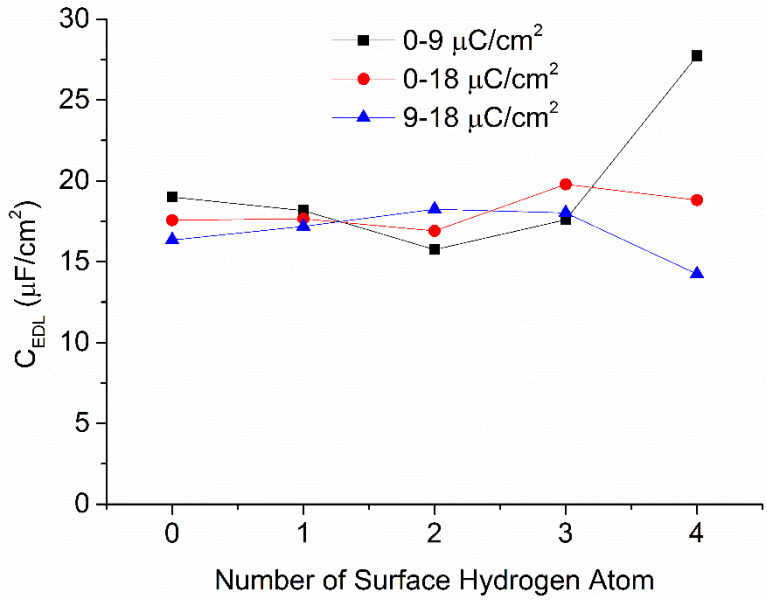


Figure 8-3. The electric double layer capacitance (C_{EDL}) at different surface H adsorption and different surface charge density range on RuO_2(110), based on a lateral unit cell of 79.5 Å^2 (6.24 Å x 12.74 Å); see Figure 8-7 for the lateral cell.

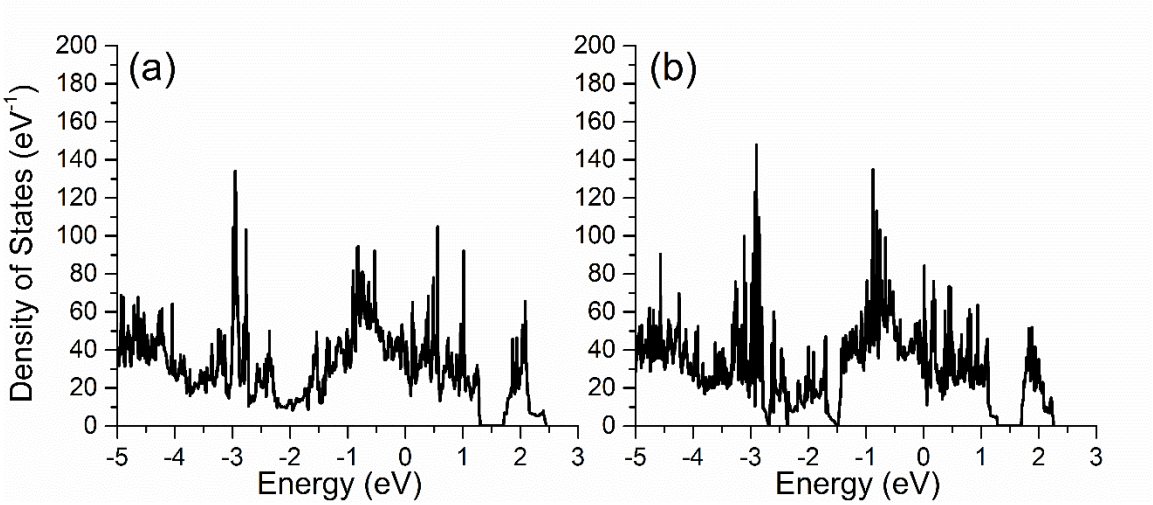


Figure 8-4. Total electronic density of states (DOS) of H-adsorbed RuO_2 with different H coverage: (a) 0; (b) 3 H atoms. See Figure 7 for the lateral cell. Fermi level is at energy zero.

8.3.3 Comparison of EDL energy and H adsorption energy.

Based on the relatively constant C_{EDL} of 80 F/g for the first three H adsorption, we can calculate the EDL formation energy (U_{EDL}) by Eq. 8-2 and compare U_{EDL} with the H adsorption energy (E_H) to predict the capacitive behavior. With the surface charge of $1e^-$, the charged electrode will be neutralized either by electric double layer (EDL) or H adsorption, so we plot the H adsorption energy with the EDL energy in Figure 8-5. One can see that H adsorption should be more preferable than the EDL formation since the H adsorption energy is more negative than U_{EDL}. Consequently, we conclude that the pseudocapacitive behavior of RuO_2(110) is dominated by the surface redox reaction for the first few proton adsorption steps when the electrode is negatively charged:

$$RuO_2 + xH^+ + xe^- \rightarrow RuO_{2-x}(OH)_x \qquad 8\text{-}5$$

8.3.4 Capacitive behavior on RuO_2(110).

Now that we have found out the PZC and the preferred capacitive mechanism below PZC, the overall capacitive behavior should be: below PZC, redox reaction based on H adsorption; above PZC, EDL charge storage. The calculated charge-voltage (Q-V) and capacitance-voltage (C-V) curves are plotted in Figure 8-6. The calculated PZC is 0.18 V vs SHE in the Figure 8-6a. In the redox reaction, each proton could provide the charge density of 10.07 μC/cm^2.

We calculated the electronic chemical potential shift after the redox reaction and the capacitance by C=Q/$\Delta\mu$. The pseudocapacitive region in the experimental CV curve is 0.1 – 0.4 V vs SHE, corresponding to the -0.1 – 0.2 V in our simulated CV curve in Figure 6b, since we cannot take into account the influence of pH on the PZC calculation due to the limitation of implicit solvation model. The first two H adsorption could give the potential drop about 0.3 V, which exactly matched the pseudocapacitive region in the experimental CV.[28] Consequently, we propose that the experimentally measured pseudocapacitance of RuO_2 at 0.1 – 0.4 V vs SHE is contributed by the first two proton adsorption reaction in our simulation and the turning point in CV is due to the charge storage mechanism change from electric double layer to redox reaction at the PZC. The calculated areal capacitance is about 50-80 μF/cm^2. It is expected that the capacitance will have a large increase when the electrode potential is more negative (still higher than the hydrogen evolution reaction potential), corresponding to the third H adsorption on the surface. The calculated capacitance for the third H adsorption (the slope of 2H and 3H in Figure 8-6a) is over 260 μF/cm^2. This very high capacitance is due to the surface phase

transition and could be a reason to explain the extremely high capacitance in hydrous RuO_2 nanoparticle, which will be discussed below. For the forth H adsorption on the surface, the calculated capacitance (the slope of 3H and 4H in Figure 8-6a) decreases to 66 μF/cm^2; here we note that the potential is negative enough (-0.4 vs. SHE) that hydrogen evolution reaction may occur.[56]

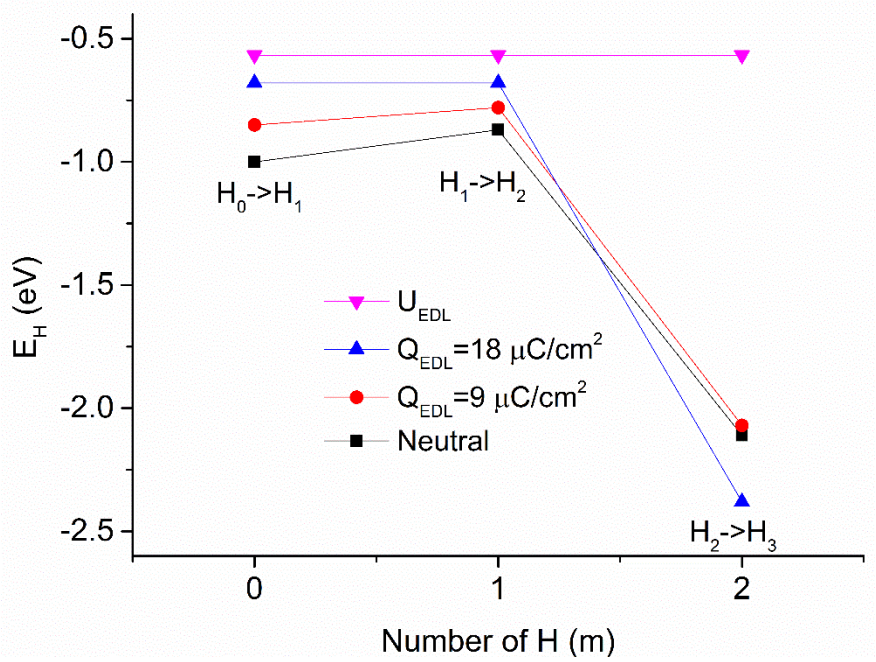


Figure 8-5. Comparison of the EDL formation energy (U_{EDL}; top line) and H adsorption energies at three different EDL charges (bottom three lines) for the three H-adsorption steps on RuO_2(110). See Figure 8-7 for the lateral cell.

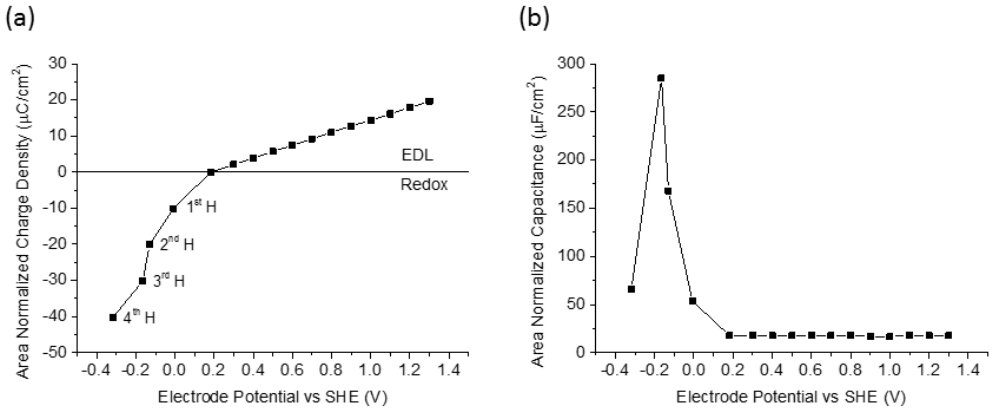


Figure 8-6. (a) Charge vs. voltage curve of RuO_2(110) in 1M LPCM electrolyte. (b) Capacitance vs. voltage curve corresponding to (a). Hydrogen adsorption sequence is labeled in both curves. Specific capacitance curve is provided in Figure S8-3 calculated by the equation a(BET)=6/(D$\boldsymbol{\rho}$)[60], where D is average particle diameter (10 nm in Ref 28) and $\boldsymbol{\rho}$ is bulk density of RuO_2.(6.97 g/cm^3) In (b), the differential capacitance of each point is calculated by doing numerical differentiation with respect to the previous point.

8.3.5 Adsorption structure of hydrogen on RuO_2(110) and its influence on pseudocapacitance.

Now we analyze the adsorption structures of H on RuO_2 (110) for the redox mechanism below PZC. For the first H adsorption step (Figure 8-7a), the adsorption energy is about -1.0 eV both on O_{ot} (on top) and O_{br} (bridge) indicating that these two types of surface oxygen atoms show similar reactivity. The structure optimization after the second H adsorption also gave a perpendicular OH bond to surface (Figure 8-7b) and H adsorption energy of -0.87 eV. The perpendicular OH bond on RuO_2(110) has been experimentally observed in basic condition.[57] The first and second hydrogen adsorption yielded a capacitance of 53.3 $\boldsymbol{\mu}$F/cm^2 (slope of 0H and 1H in Figure 8-6a) and 81.9 $\boldsymbol{\mu}$F/cm^2 (slope of 1H and 2H in Figure 8-6a), respectively. When the third proton is adsorbed on the surface (Figure 8-7c), it pushed the perpendicular OH bond on O_{ot} to bended OH bond and

caused the surface phase transition. Thus, the third H adsorption energy is below -2.0 eV, which is much lower than the first two and closer to the previous DFT work.[42] The corresponding capacitance caused by the third H adsorption is 266 μF/cm^2 (slope of 2H and 3H), an unexpectedly high value. When we put the forth H atom on the surface, the forth OH bond is perpendicular to the surface after structure optimization (Figure 8-7d), and the corresponding capacitance is 66 μF/cm^2 (slope of 3H and 4H). Consequently, we conclude that the capacitance provided by H adsorption reaction is structure-dependent: the perpendicular OH bond formation gives the capacitance about 60 μF/cm^2 and the capacitance from bended OH bond formation is over 200 μF/cm^2. This conclusion could be a possible interpretation of the experimentally observed size-dependent pseudocapacitance of RuO_2 nanoparticle and high capacitance of hydrous RuO_2.[27, 28] When breaking down the crystal to small nanoparticles, it could have more O_{ot} atoms that can form the bended OH bond, which can have higher capacitance than ideal surface. Hydrous RuO_2 has had some H atoms and OH bond on the surface, thus it could directly form bended OH bond instead of perpendicular OH bond at low H coverage.

Recently, Watanabe et al. investigated the interfacial structure of RuO_2(110) and water in different electrochemical conditions from first principles,[58] and found that the orientation of OH bond and the surface coverage ratio of proton are strongly dependent on the pH and electrode potential. Our simulation was limited by the implicit solvation model. The implicit solvation model describes the electrolyte by the modified Poisson-Boltzmann equation, so the ion is considered to be a point charge in the Debye screening theory and the solvent is a continuum dielectric medium with an electron density-dependent local

dielectric constant. In this electrode/electrolyte system, the JDFT method considers only the electrostatic interaction between the electrode and the electrolyte, so the ion/solvent interaction and hydration are not included, but the H^+ ion is explicitly included via formation of the surface OH groups. In addition, the JDFT approach is intended to study the equilibrium properties, so the transport behavior such as diffusion cannot be examined. Despite these limitations, the JDFT approach with the implicit solvation model allows us to capture the most important physics and chemistry behind the capacitive behavior of RuO2. Since surface electrochemistry is a really complex problem, factors such as the ion/solvent interaction, diffusion, hydration, et al. will all impact the capacitance, and we hope that more advanced methods such as the ESM[59] can address these factors by including both the explicit solvation model and the ion dynamics.

With an explicit solvation model, we expect that the bending angle of Ru-O-H would be influenced by the hydrogen bonding with water molecules in the electrolyte. Nevertheless, the present work provides a reasonable interpretation of the pseudocapacitive peak in the experimental CV curve of RuO_2:[28] the steep increase of capacitance (or current) at 0.4 V in low scan rates is caused by the charge storage mechanism changing from EDL to H adsorption reaction.

The present work focused on the (110) surface of RuO_2. The experimentally synthesized RuO_2 film has (110), (101), (100), and (1010) facets. Although these surfaces have close surface energies from DFT calculation, the surface energy of (110) is the lowest facet.[48] That is why we chose this surface. It would be interesting to examine the pseudocapacitance on other surfaces as well. We expect that the specific values of

capacitance would change for those different surfaces, but the general idea of coverage dependence and OH formation would still apply.

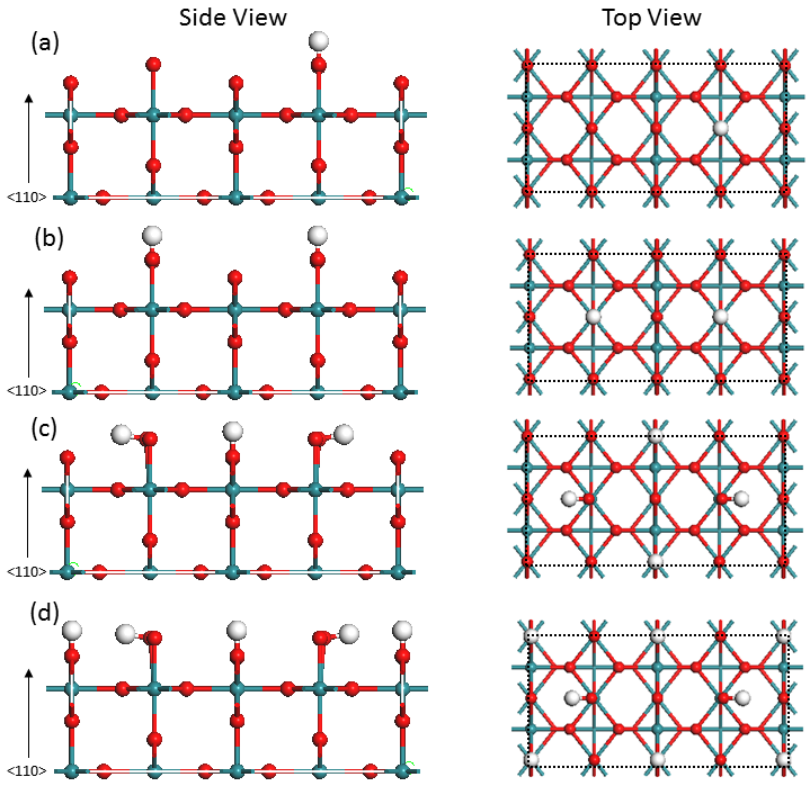


Figure 8-7. Side and top views of H adsorption on the RuO_2 (110) surface: (a) 1 H; (b) 2 H; (c) 3H; (d) 4 H atoms in a lateral unit cell (dotted lines) of 79.5 $Å^2$ (6.24 Å x 12.74 Å). Color code: Ru, cyan; O, red; H, white.

8.4 Summary and conclusions

Based on the Joint Density Functional Theory with an implicit solvation model, we calculated the pseudocapacitive behavior of the RuO_2(110) surface. Our calculated pseudocapacitance and corresponding voltage region show a qualitative agreement with the experimental CV curve, thereby providing a reasonable interpretation on the capacitive behavior of RuO_2. When electrode potential is above PZC, measured capacitance is dominated by the electric double layer capacitance. Below the PZC, the capacitance is

contributed by H adsorption reaction with low surface H coverage and perpendicular OH bond, which giving the capacitance of ~60 μF/cm^2. As the electrode potential goes to more negative, surface phase transition happens due to the increasing H coverage and the bended OH bond formation produces a very high capacitance over 200 μF/cm^2. These different capacitances of perpendicular and bended OH bond could explain why the small RuO_2 nanoparticle and hydrous RuO_2 have much higher capacitance than the RuO_2 film. Hence, our theoretical investigation provides an understanding of the pseudocapacitive charge storage behavior of the RuO_2 surface.

References:

(1) Shi, G.; Hanlumyuang, Y.; Liu, Z.; Gong, Y. J.; Gao, W. L.; Li, B.; Kono, J.; Lou, J.; Vajtai, R.; Sharma, P., et al. Boron Nitride-Graphene Nanocapacitor and the Origins of Anomalous Size-Dependent Increase of Capacitance. *Nano Lett.* **2014**, 14, 1739-1744

(2) Ozcelik, V. O.; Ciraci, S. Nanoscale dielectric capacitors composed of graphene and boron nitride layers: a first-principles study of high capacitance at nanoscale. *J. Phys. Chem. C* **2013**, 117, 15327-15334

(3) Ozcelik, V. O.; Ciraci, S. High-performance planar nanoscale dielectric capacitors. *Phys. Rev. B* **2015**, 91, 195445

(4) Stengel, M.; Spaldin, N. A. Origin of the dielectric dead layer in nanoscale capacitors. *Nature* **2006**, 443, 679-682

(5) Gogotsi, Y.; Simon, P. True Performance Metrics in Electrochemical Energy Storage. *Science* **2011**, 334, 917-918

(6) Simon, P.; Gogotsi, Y.; Dunn, B. Where do batteries end and supercapacitors begin? *Science* **2014**, 343, 1210-1211

(7) Stoller, M. D.; Park, S. J.; Zhu, Y. W.; An, J. H.; Ruoff, R. S. Graphene-based ultracapacitors. *Nano Lett.* **2008**, 8, 3498-3502

(8) Zhang, L. L.; Zhao, X. S. Carbon-based materials as supercapacitor electrodes. *Chem. Soc. Rev.* **2009**, 38, 2520-2531

(9) Augustyn, V.; Simon, P.; Dunn, B. Pseudocapacitive Oxide Materials for High-rate Electrochemical Energy Storage. *Energ Environ. Sci.* **2014**, 7, 1597-1614

(10) Long, J. W.; Swider, K. E.; Merzbacher, C. I.; Rolison, D. R. Voltammetric Characterization of Ruthenium Oxide-based Aerogels and other RuO2 Solids: The Nature of Capacitance in Nanostructured Materials. *Langmuir* **1999**, 15, 780-785

(11) Wang, J.; Polleux, J.; Lim, J.; Dunn, B. Pseudocapacitive Contributions to Electrochemical Energy Storage in TiO2 (Anatase) Nanoparticles. *J. Phys. Chem. C* **2007**, 111, 14925-14931

(12) Fischer, A. E.; Pettigrew, K. A.; Rolison, D. R.; Stroud, R. M.; Long, J. W. Incorporation of Homogeneous, Nanoscale MnO2 within Ultraporous Carbon Structures via Self-limiting Electroless Deposition: Implications for Electrochemical Capacitors. *Nano Lett.* **2007**, 7, 281-286

(13) Brezesinski, T.; Wang, J.; Polleux, J.; Dunn, B.; Tolbert, S. H. Templated Nanocrystal-Based Porous TiO2 Films for Next-Generation Electrochemical Capacitors. *J. Am. Chem. Soc.* **2009**, 131, 1802-1809

(14) Rolison, D. R.; Long, J. W.; Lytle, J. C.; Fischer, A. E.; Rhodes, C. P.; McEvoy, T. M.; Bourga, M. E.; Lubers, A. M. Multifunctional 3D nanoarchitectures for energy storage and conversion. *Chem. Soc. Rev.* **2009**, 38, 226-252

(15) Brezesinski, T.; Wang, J.; Tolbert, S. H.; Dunn, B. Ordered Mesoporous Alpha-MoO3 with Iso-oriented Nanocrystalline Walls for Thin-film Pseudocapacitors. *Nat. Mater.* **2010**, 9, 146-151

(16) Mirmohseni, A.; Dorraji, M. S. S.; Hosseini, M. G. Influence of Metal Oxide Nanoparticles on Pseudocapacitive Behavior of Wet-spun Polyaniline-multiwall Carbon Nanotube Fibers. *Electrochim. Acta* **2012**, 70, 182-192

(17) Sassin, M. B.; Chervin, C. N.; Rolison, D. R.; Long, J. W. Redox Deposition of Nanoscale Metal Oxides on Carbon for Next-Generation Electrochemical Capacitors. *Acc. Chem. Res.* **2013**, 46, 1062-1074

(18) Jiang, Y. Q.; Wang, P. B.; Zang, X. N.; Yang, Y.; Kozinda, A.; Lin, L. W. Uniformly Embedded Metal Oxide Nanoparticles in Vertically Aligned Carbon Nanotube Forests as Pseudocapacitor Electrodes for Enhanced Energy Storage. *Nano Lett.* **2013**, 13, 3524-3530

(19) Ren, Z. H.; Li, J. P.; Ren, Y. Q.; Wang, S. G.; Qiu, Y. J.; Yu, J. Large-scale Synthesis of Hybrid Metal Oxides through Metal Redox Mechanism for High-performance Pseudocapacitors. *Sci. Rep.* **2016**, 6, 20021

(20) Conway, B. E. Transition from Supercapacitor to Battery Behavior in Electrochemical Energy-Storage. *J. Electrochem. Soc.* **1991**, 138, 1539-1548

(21) Trasatti, S. Physical Electrochemistry of Ceramic Oxides. *Electrochim. Acta* **1991**, 36, 225-241

(22) Sarangapani, S.; Tilak, B. V.; Chen, C. P. Materials for Electrochemical Capacitors - Theoretical and Experimental constraints. *J. Electrochem. Soc.* **1996**, 143, 3791-3799

(23) Conway, B. E.; Birss, V.; Wojtowicz, J. The Role and Utilization of Pseudocapacitance for Energy Storage by Supercapacitors. *J. Power Sources* **1997**, 66, 1-14

(24) Burke, A. Ultracapacitors: Why, How, and Where is the Technology. *J. Power Sources* **2000**, 91, 37-50

(25) Lin, K. M.; Chang, K. H.; Hu, C. C.; Li, Y. Y. Mesoporous RuO2 for the Next Generation Supercapacitors with an Ultrahigh Power Density. *Electrochim. Acta* **2009**, 54, 4574-4581

(26) Makino, S.; Ban, T.; Sugimoto, W. Towards Implantable Bio-Supercapacitors: Pseudocapacitance of Ruthenium Oxide Nanoparticles and Nanosheets in Acids, Buffered Solutions, and Bioelectrolytes. *J. Electrochem. Soc.* **2015**, 162, A5001-A5006

(27) Sugimoto, W.; Kizaki, T.; Yokoshima, K.; Murakami, Y.; Takasu, Y. Evaluation of the Pseudocapacitance in RuO_2 with a RuO_2/GC thin Film Electrode. *Electrochim. Acta* **2004**, 49, 313-320

(28) Sugimoto, W.; Yokoshima, K.; Murakami, Y.; Takasu, Y. Charge Storage Mechanism of Nanostructured Anhydrous and Hydrous Ruthenium-based Oxides. *Electrochim. Acta* **2006**, 52, 1742-1748

(29) Sugimoto, W.; Iwata, H.; Yokoshima, K.; Murakami, Y.; Takasu, Y. Proton and Electron Conductivity in Hydrous Ruthenium Oxides Evaluated by Electrochemical Impedance Spectroscopy: The Origin of Large Capacitance. *J. Phys. Chem. B* **2005**, 109, 7330-7338

(30) Juodkazis, K.; Juodkazyte, J.; Sukiene, V.; Griguceviciene, A.; Selskis, A. On the Charge Storage Mechanism at RuO_2/0.5 M H_2SO_4 Interface. *J. Solid State Electrochem.* **2008**, 12, 1399-1404

(31) Feng, G.; Huang, J. S.; Sumpter, B. G.; Meunier, V.; Qiao, R. Structure and Dynamics of Electrical Double Layers in Organic Electrolytes. *Phys. Chem. Chem. Phys.* **2010**, 12, 5468-5479

(32) Vatamanu, J.; Borodin, O.; Smith, G. D. Molecular Insights into the Potential and Temperature Dependences of the Differential Capacitance of a Room-Temperature Ionic Liquid at Graphite Electrodes. *J. Am. Chem. Soc.* **2010**, 132, 14825-14833

(33) Vatamanu, J.; Borodin, O.; Smith, G. D. Molecular Simulations of the Electric Double Layer Structure, Differential Capacitance, and Charging Kinetics for N-Methyl-N-propylpyrrolidinium Bis(fluorosulfonyl)imide at Graphite Electrodes. *J. Phys. Chem. B* **2011**, 115, 3073-3084

(34) Bazant, M. Z.; Storey, B. D.; Kornyshev, A. A. Double Layer in Ionic Liquids: Overscreening versus Crowding. *Phys. Rev. Lett.* **2011**, 106, 046102

(35) Jiang, D. E.; Jin, Z. H.; Wu, J. Z. Oscillation of Capacitance inside Nanopores. *Nano Lett.* **2011**, 11, 5373-5377

(36) Feng, G.; Cummings, P. T. Supercapacitor Capacitance Exhibits Oscillatory Behavior as a Function of Nanopore Size. *J. Phys. Chem. Lett.* **2011**, 2, 2859-2864

(37) Wu, P.; Huang, J. S.; Meunier, V.; Sumpter, B. G.; Qiao, R. Complex Capacitance Scaling in Ionic Liquids-Filled Nanopores. *Acs Nano* **2011**, 5, 9044-9051

(38) Jiang, D. E.; Jin, Z. H.; Henderson, D.; Wu, J. Z. Solvent Effect on the Pore-Size Dependence of an Organic Electrolyte Supercapacitor. *J. Phys. Chem. Lett.* **2012**, 3, 1727-1731

(39) Jiang, D. E.; Wu, J. Z. Microscopic Insights into the Electrochemical Behavior of Nonaqueous Electrolytes in Electric Double-Layer Capacitors. *J. Phys. Chem. Lett.* **2013**, 4, 1260-1267

(40) Fedorov, M. V.; Kornyshev, A. A. Ionic Liquids at Electrified Interfaces. *Chem. Rev.* **2014**, 114, 2978-3036

(41) Uysal, A.; Zhou, H.; Feng, G.; Lee, S. S.; Li, S.; Cummings, P. T.; Fulvio, P. F.; Dai, S.; McDonough, J. K.; Gogotsi, Y., et al. Interfacial ionic 'liquids': connecting static and dynamic structures. *J. Phys.: Condens. Matter* **2015**, 27, 032101

(42) Liu, Y. D.; Zhou, F.; Ozolins, V. Ab Initio Study of the Charge-Storage Mechanisms in RuO_2-Based Electrochemical Ultracapacitors. *J. Phys. Chem. C* **2012**, 116, 1450-1457

(43) Ozolins, V.; Zhou, F.; Asta, M. Ruthenia-Based Electrochemical Supercapacitors: Insights from First-Principles Calculations. *Acc. Chem. Res.* **2013**, 46, 1084-1093

(44) Zheng, Y.; Jiao, Y.; Zhu, Y. H.; Li, L. H.; Han, Y.; Chen, Y.; Du, A. J.; Jaroniec, M.; Qiao, S. Z. Hydrogen Evolution by a Metal-free Electrocatalyst. *Nat. Commun.* **2014**, 5, 3783

(45) Letchworth-Weaver, K.; Arias, T. A. Joint density functional theory of the electrode-electrolyte interface: application to fixed electrode potentials, interfacial capacitances, and potentials of zero charge. *Phys. Rev. B* **2012**, 86, 075140

(46) Sun, S.; Qi, Y.; Zhang, T. Y. Dissecting Graphene Capacitance in Electrochemical Cell. *Electrochim. Acta* **2015**, 163, 296-302

(47) Zhan, C.; Jiang, D. E. Contribution of dielectric screening to the total capacitance of few-layer graphene electrodes. *J. Phys. Chem. Lett* **2016**, 7, 789

(48) Over, H.; Knapp, M.; Lundgren, E.; Seitsonen, A. P.; Schmid, M.; Varga, P. Visualization of atomic processes on ruthenium dioxide using scanning tunneling microscopy. *Chemphyschem* **2004**, 5, 167-174

(49) Over, H.; Kim, Y. D.; Seitsonen, A. P.; Wendt, S.; Lundgren, E.; Schmid, M.; Varga, P.; Morgante, A.; Ertl, G. Atomic-scale structure and catalytic reactivity of the RuO2(110) surface. *Science* **2000**, 287, 1474-1476

(50) Perdew, J. P.; Burke, K.; Ernzerhof, M. Generalized Gradient Approximation Made Simple. *Phys. Rev. Lett.* **1996**, 77, 3865-3868

(51) Garrity, K. F.; Bennett, J. W.; Rabe, K. M.; Vanderbilt, D. Pseudopotentials for High-throughput DFT Calculations. *Comput. Mater. Sci.* **2014**, 81, 446-452

(52) Radin, M. D.; Ogitsu, T.; Biener, J.; Otani, M.; Wood, B. C. Capacitive Charge Storage at an Electrified Interface Investigated via Direct First-Principles Simulations. *Phys. Rev. B* **2015**, 91, 125415

(53) Ji, X.; Xu, K.; Chen, C.; Zhang, B.; Ruan, Y. J.; Liu, J.; Miao, L.; Jiang, J. J. Probing the Electrochemical Capacitance of MXene Nanosheets for High-performance Pseudocapacitors. *Phys. Chem. Chem. Phys.* **2016**, 18, 4460-4467

(54) Tomkiewicz, M.; Huang, Y. S.; Pollak, F. H. The Potential of Zero Charge of Oriented Single-Crystal Ruo2 in Aqueous-Electrolytes. *J. Electrochem. Soc.* **1983**, 130, 1514-1518

(55) Pajkossy, T.; Kolb, D. M. Double Layer Capacitance of Pt(111) Single Crystal Electrodes. *Electrochim. Acta* **2001**, 46, 3063-3071

(56) Lister, T. E.; Tolmachev, Y. V.; Chu, Y.; Cullen, W. G.; You, H.; Yonco, R.; Nagy, Z. Cathodic Activation of RuO2 Single Crystal Surfaces for Hydrogenevolution Reaction. *J. Electroanal. Chem.* **2003**, 554, 71-76

(57) Chu, Y. S.; Lister, T. E.; Cullen, W. G.; You, H.; Nagy, Z. Commensurate Water Monolayer at the RuO2(110)/water Interface. *Phys. Rev. Lett.* **2001**, 86, 3364-3367

(58) Watanabe, E.; Rossmeisl, J.; Björketun, M.; Ushiyama, H.; Yamashita, K. Atomic-Scale Analysis of the RuO_2/Water Interface under Electrochemical Conditions. *J. Phys. Chem. C* **2016**, 120, 8096-8103

(59) Otani, M.; Sugino, O. First-principles calculations of charged surfaces and interfaces: A plane-wave nonrepeated slab approach. *Phys. Rev. B* **2006**, 73, 115407

(60) Kim, H.; Popov, B. N. Characterization of hydrous ruthenium oxide/carbon nanocomposite supercapacitors prepared by a colloidal method. *J. Power Sources* **2002**, 104, 52-61

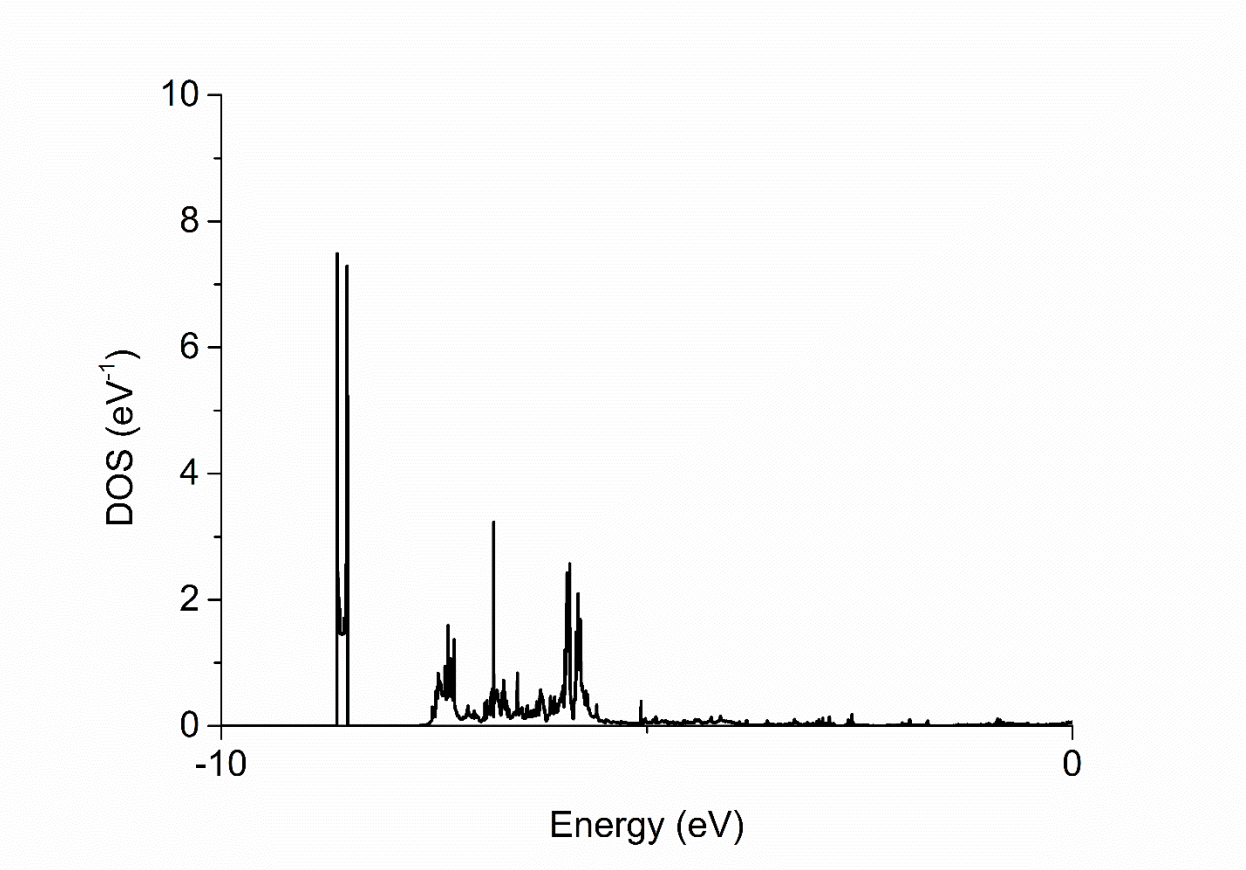


Figure S8-1. The projected DOS of H atom in RuO_2-3H. Fermi level has been move to 0 eV

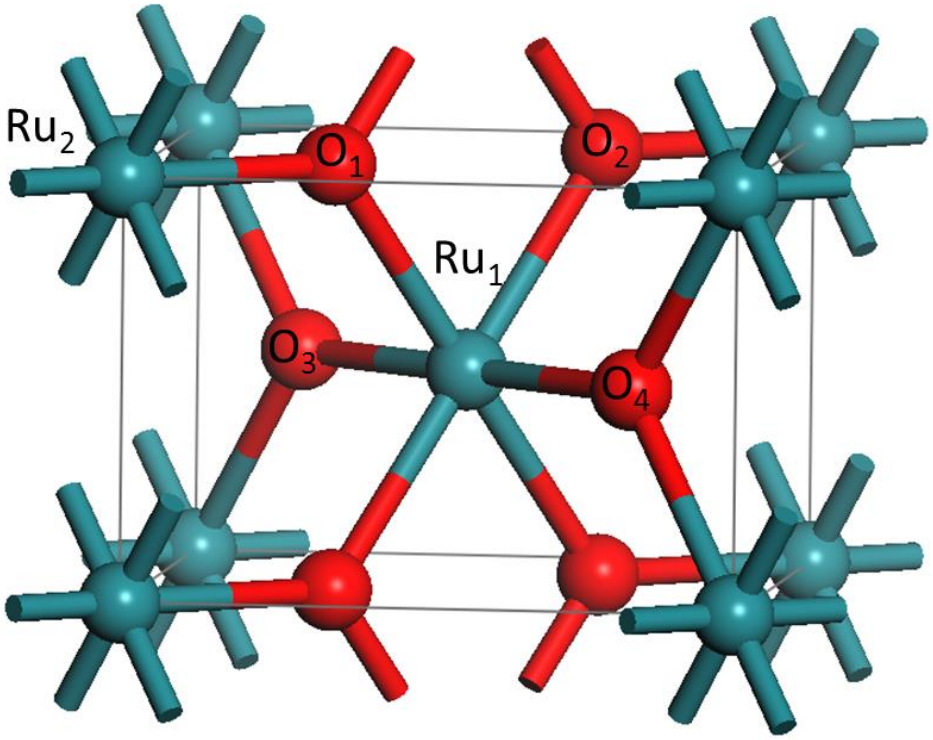


Figure S8-2. The crystal structure of rutile RuO_2 used in our simulation. Lattice Parameter: a= 4.504, b= 4.504, c= 3.120

Table S8-1. Bond length (Å) and bond angle (degree) information

Bond and angle type	Bond length and angle
d (Ru1-O1)	1.988
d (Ru1-O3)	1.953
d (Ru2-O1)	1.953
d (Ru2-O3)	1.988
a (O1-Ru1-O2)	76.594
a (O1-Ru1-O3)	90.000
a (Ru1-O1-Ru2)	128.297
a (Ru1-O3-Ru2)	128.297

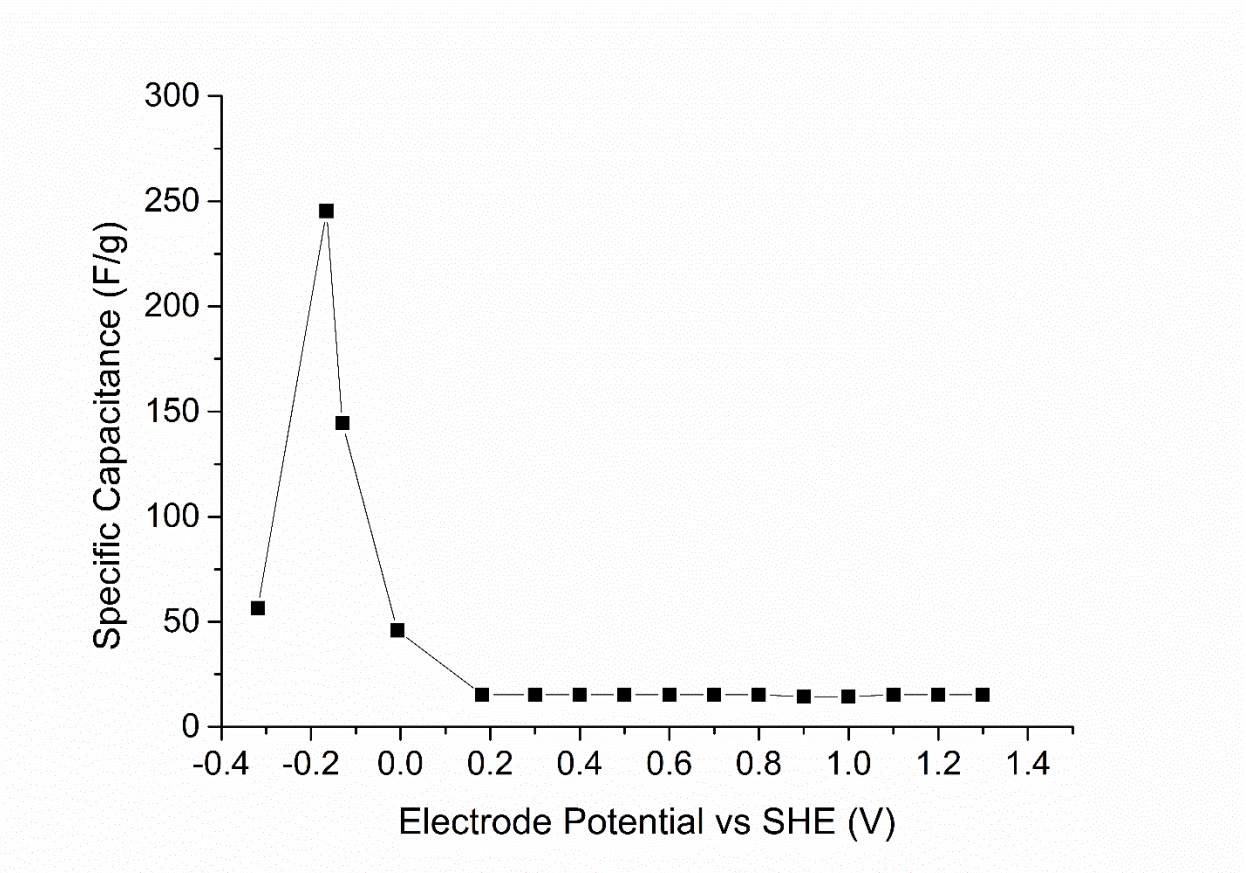


Figure S8-3. Specific capacitance of RuO2 (110) surface calculated from the equation aBET=6/(D$\boldsymbol{\rho}$), where D is average particle diameter (10 nm in experimental measurement) and $\boldsymbol{\rho}$ is RuO2 bulk density. (6.97 g/cm^3)

Chapter 9 Understanding the MXene Pseudocapacitance

9.1 Introduction

MXenes are novel two-dimensional inorganic compounds based on transition metal carbides, nitrides, and carbonitrides. They have been found to be very promising materials for electrochemical energy storage and electrocatalysis applications.[1-4] For example, MXenes showed great promise in lithium-ion batteries.[5, 6] Density functional theory (DFT) calculations have proved that MXenes offer low lithium diffusion barriers and high lithium storage capacity.[7] In addition, molybdenum-carbide MXenes have exhibited good performance in hydrogen evolution reaction.[8]

In the field of capacitive energy storage, MXenes have been tested as a novel electrode material. Their behavior as a supercapacitor depends on the choice of the electrolyte. When ionic liquids or neutral aqueous solutions are used as the electrolyte, MXenes exhibit either the double layer capacitance or an ion-intercalation capacitance.[2, 9-12] However, in acidic electrolytes such as H_2SO_4, MXenes exhibit pseudocapacitance due to surface redox chemistry.[13-15] Although many characterization techniques have been used to understand the pseudocapacitance of MXenes in acidic electrolytes,[14] the atomic and electronic level mechanism on the surface redox process is still unclear due to the complexity of MXene's surface structure and terminal groups.[16-18] Many questions remain unanswered. For instance, how does the surface configuration (O/OH ratio) change with the applied voltage? What is the relation between double layer charging and surface redox behavior as the voltage changes? Which behaviors limit the capacitance in practice?

Atomistic insight into the capacitive storage mechanism in MXenes from computational modeling would be highly desirable but hampered by the difficulty in simulating the double layer charging and the surface redox behavior simultaneously. Recent simulation of MXene pseudocapacitors assumed an ideal Faradaic process and ignored the electric double layer (EDL) response.[19] Similar methods have been applied to RuO_2 electrodes to investigate its pseudocapacitive behavior in aqueous electrolytes.[20-23] More importantly, in recent years, many computational studies on interfacial electrochemistry have indicated that it is important to use constant electrochemical potential methods in DFT calculations to capture the influence of Fermi level on the electrode during the reaction process.[24-26]

To obtain a complete picture of the pseudocapacitive behavior of MXenes in acidic electrolytes, here we propose a theoretical model to effectively and reliably capture the energetic competition between the surface redox chemistry and the double layer charging at the electronic structure level by using the constant-potential free energy analysis combined with joint Density Functional Theory (joint DFT),[27, 28] which could capture the electronic structure and property of a solvated electrode. Joint DFT provides a formally exact variational theory for the free energy of an electronic DFT system combined with classical DFT or a polarizable continuum model, which could further reliably predict the solvation behavior and potential at the point of zero charge (PZC) of electrode.[29-31]

9.2 Method and Model

9.2.1 Electronic structure calculation of solvated system via implicit solvation model

We chose $Ti_3C_2O_2$ as a prototypical MXene electrode whose pseudocapacitance has been measured in aqueous electrolyte[13, 14] and modeled a 3×3 supercell to examine enough hydrogen coverage (Figure 9-1). To examine how the electrode potential influences the surface redox behavior, we used the joint DFT method with an implicit solvation model, as implemented in the simulation package JDFTx, to obtain the electronic structure and the potential at the point of zero charge (PZC) of each H coverage for further computation of charge-dependent free energy function.[29, 30] All the MXene configurations explored are provided in the Supporting Information Figure S1. The implicit electrolyte is described by the charge-asymmetric nonlocally determined local-electric (CANDLE) model to capture the solvation effect and the electrolyte response to the surface net charge.[32] For the electrode, the electron exchange-correlation is described by Generalized-Gradient-Approximation with Perdew-Burke-Enzerhof functional (GGA-PBE)[33] and the ion-electron interaction is described ultrasoft pseudopotentials.[34] For the plane-wave basis set, a kinetic energy cutoff of 20 Hartree was used in structure optimization and 30 Hartree in the single-point calculation at the optimized geometry. The k-mesh for Brillouin zone sampling is 8×8×1 for structure optimization and 12×12×1 for the single-point calculation of the optimized geometry, to reach a convergence criterion of 10^{-6} Hartree in energy.

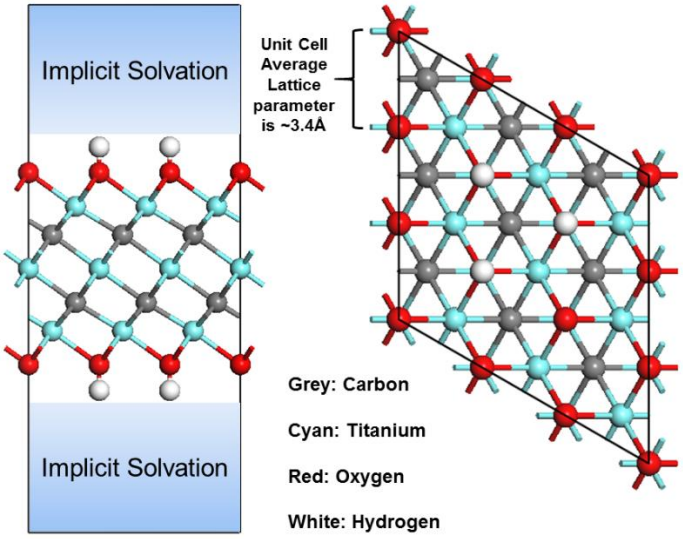


Figure 9-1. Partially protonated $Ti_3C_2O_2$ as a prototypical MXene electrode in an acidic electrolyte: side view (left) and top view (right). Hydrogen atoms are symmetrically added on both sides.

9.2.2 Voltage-dependent Gibbs Free Energy in Redox Reaction

Considering a non-ideal Faradaic process (where electron transfer and proton transfer are not equal in number) of $Ti_3C_2O_2$ in H_2SO_4 for two-side symmetric charging, the redox reaction can be written as:

$$Ti_3C_2O_2^q + 2H^+(aq) \rightarrow Ti_3C_2O_{2-2x}(OH)_{2x}^{q'} + 2(1-x)H^+(aq) \qquad 9\text{-}1$$

where x is the surface H coverage (ranging from 0 to 1) and q is the net charge on electrode. At a fixed electrode potential, the partially protonated $Ti_3C_2O_2$ surface can hold a net charge when the electrode potential differs from the PZC. Thus, the applied voltage controls both q and x during the redox process. For any intermediate state with the coverage x and electrode potential φ, the free energy (normalized to a single unit cell interface) can be written as:

$$G(x,\varphi) = E(x) + xE_{ZPE} + Q\big(V(x,\varphi)\big)\varphi + E_{EDL}\big(V(x,\varphi)\big) + (1-x)\mu_{H^+} \qquad 9\text{-}2$$

E(x) is the total electronic energy of a solvated electrode with the H coverage of x in zero surface charge, while E_{ZPE} is the zero-point energy (ZPE) difference between x=0 and x=1 states, which is 0.55 eV per H atom from our DFT calculation. The third term, $Q\varphi$, is the electrical work to move the charge Q (net charge on the electrode) from zero potential (in the bulk electrolyte) to the electrode with the potential φ. E_{EDL} is the energy of induced electric double layer by the electrode charge Q. The last term is the chemical potential of a solvated proton in the electrolyte. In the third and fourth terms, V(x, φ) is the relative potential with respect to PZC at coverage x and electrode potential φ, given by:

$$V(x,\varphi) = \varphi - \varphi_{PZC}(x) \tag{9-3}$$

Once V(x, φ) is known, the charge Q and E_{EDL} can be obtained by:

$$Q(x,\varphi) = \int_{V=0}^{V=\varphi-\varphi_{PZC}(x)} C_{EDL}\,dV \tag{9-4}$$

$$E_{EDL}(x,\varphi) = \int_{V=0}^{V=\varphi-\varphi_{PZC}(x)} Q(x,\varphi)\,dV \tag{9-5}$$

The final term μ_{H^+} (proton's chemical potential) in Eq. 8-2 can be explicitly written as:

$$\mu_{H^+} = \frac{1}{2}G[H_2] + e\Phi_{SHE} - 0.059 \times pH \tag{9-6}$$

where

$$G[H_2] = E[H_2] + ZPE[H_2] + \frac{7}{2}k_BT - TS_{H_2} \tag{9-7}$$

All physical quantities in Eq.9-7 can be obtained by DFT calculation and standard thermodynamic database. In Eq.9-6, Φ_{SHE} is the computational standard hydrogen electrode that has been determined to be 4.66 V from PZC calibration of the CANDLE solvation in JDFTx.[32] For the C_{EDL} in Eq.9-4, we use constant C_{EDL} approximation based on the Debye–Hückel model to include the influence of double-layer charging. C_{EDL} is

estimated to be 32 μF/cm^2 for 1M H_2SO_4. In Eq.9-2 and Eq.9-3, since our DFT calculation of E(x) and PZC with various configuration and coverage exhibited a strong linear relation with x, E(x) and $\varphi_{PZC}(x)$ can be described by a linear equation of x (see Figure S9-2 and detail in SI). Thus, with an explicit expression of E(x) and $\varphi_{PZC}(x)$, we can use Eq.9-2 to calculate the relative free energy of various H coverage x at any given electrode potential φ, and then obtain the ensemble-average x and Q. Since there are degenerate H adsorption configurations at each coverage (Figure S9-1), we have developed a simple statistical method to obtain the average x and Q at any given electrode potential φ (see Figures S9-3 and S9-4 and detail in SI). The charging behavior can be obtained by calculating the average x and Q at different electrode potentials.

The difference between our model and realistic MXene material should be noted here: our DFT model is based on a single layer MXene, while experimentally synthesized MXene materials have a layer-by-layer stacked structure. The interlayer space varied significantly from 10Å to 40 Å, depending on synthesis method. The ion intercalation capacitance in MXene, physically speaking, can be regarded as a special "double layer" charging behavior in a constrained electrode region. When interlayer space is narrow, the hydronium ion intercalation cannot be described by Debye–Hückel model and constant C_{EDL}, and might further influence the energetic competition of redox and double layer charging. Thus, our model is more applicable to "MXene clay", which has lager interlayer space and its ion intercalation behaves as general double layer charging.

We use $Ti_3C_2O_2$ as a prototypical MXene electrode to obtain a comprehensive understanding of its surface redox behavior in H_2SO_4 electrolyte. We address the following

key questions: (i) How does the electrode potential simultaneously govern the surface redox behavior and the double layer charging? (ii) How do the redox and EDL behavior contribute to the overall capacitive performance? (iii) How does the electronic structure change with the electrode potential in the pseudocapacitive process?

9.3 Results and Discussion

9.3.1 Influence of H coverage on the point of zero charge (PZC) of MXene.

$Ti_3C_2O_2$ and $Ti_3C_2(OH)_2$ represent two extreme cases of hydrogen coverage, 0 and 1, respectively. Our optimized lattice parameters are 3.038 Å and 3.087 Å for $Ti_3C_2O_2$ and $Ti_3C_2(OH)_2$, respectively, which are very consistent with previous DFT calculation.[35] We use $Ti_3C_2T_x$ to denote the intermediate states between $Ti_3C_2O_2$ and $Ti_3C_2(OH)_2$, where T represents a mixture of O and OH groups. When the surface is partially covered by H, we observed a small monotonic lattice expansion with the H coverage (Figure S9-5), while at the same coverage, the lattice parameter is insensitive to the configuration of adsorbed H atoms on the surface. To determine the contribution of the EDL capacitance (in Eq.9-3, Eq.9-4 and Eq.9-5), we had to find out PZC for each H coverage and configuration. As shown in Figure S9-2, we found that the PZC of $Ti_3C_2T_x$ linearly decreases with the H coverage. With this dependence, we can then proceed to obtain the free energy as a function of the applied potential and hydrogen coverage.

9.3.2 Gibbs free energy, ensemble-averaged H coverage, and surface charge.

As shown in Eq. 9-1, the surface redox chemistry is dictated by the proton adsorption on the MXene surface and the accompanying electron transfer to the electrode at a fixed electrode potential. To determine the extent of the surface redox chemistry, we

calculated the Gibbs free energy, $G(x,\varphi)$, according to Eq. 9-2 for each H coverage, x, at various fixed electrode potential, φ, from -1.0 V to 1.0 V vs SHE in 1.0M H_2SO_4. From Figure 9-2, one can see that when the applied voltage is -1 V, $G(x,\varphi)$ exhibits a parabolic shape with an ensemble-average coverage x_{avg}=0.68. When the electrode potential increases, the $G(x,\varphi)$ curves shift up and x_{avg} shifts to a smaller value.

From the $G(x,\varphi)$ data for each configuration, we obtained the most probable H coverage at any given electrode potential (Figure S9-4), which is in fact quite close to x_{avg} in Figure 9-2. Figure 9-3a shows how the most probable H coverage changes with the electrode potential. When the potential is -1.0 V vs. SHE, the average H coverage is about 0.68, meaning that the surface O groups are not completely protonated at -1.0 V. With the electrode potential increase, we observed a smooth decrease of surface H coverage. Fig. 9-3b plots the surface net charge (responsible for the EDL capacitance), the redox or Faradic charge storage (which is the opposite of surface H adsorption number per Eq. 9-1), and the electron transfer number (total charge storage) as a function of the applied potential. One can see that the electrode is slightly positively charged in the voltage window and surface charge decreases with the applied voltage. Thus, although the total capacitive behavior is dominated by the redox charging (proton-coupled electron transfer), the EDL part works slightly against the redox charge storage due to their opposite sign. In other words, part of the positive charge from proton transfer becomes the net surface charge responsible for the EDL capacitance, so the magnitude of the electron transfer (from the electron reservoir or the power source to the electrode) to compensate the positive-charge transfer (from the electrolyte to the electrode surface) decreases as a result.

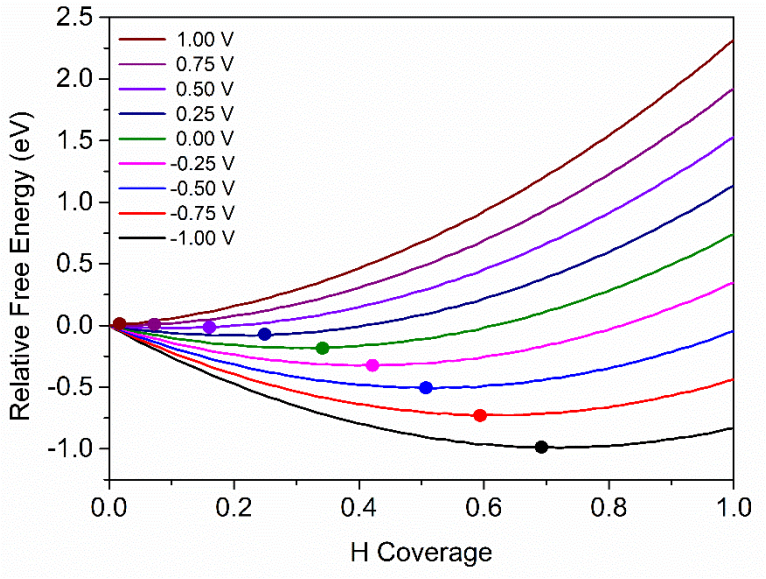


Figure 9-2. Gibbs free energy of $Ti_3C_2T_x$ (T=O, OH) in 1M H_2SO_4 electrolyte as a function of H coverage *x* for at different electrode potentials, φ, relative to SHE. The ensemble-average coverage x_{avg} is marked by circle. The marked x values from -1.00V to 1.00 V are: 0.68, 0.60, 0.51, 0.43, 0.34, 0.24, 0.14, 0.07, 0.04.

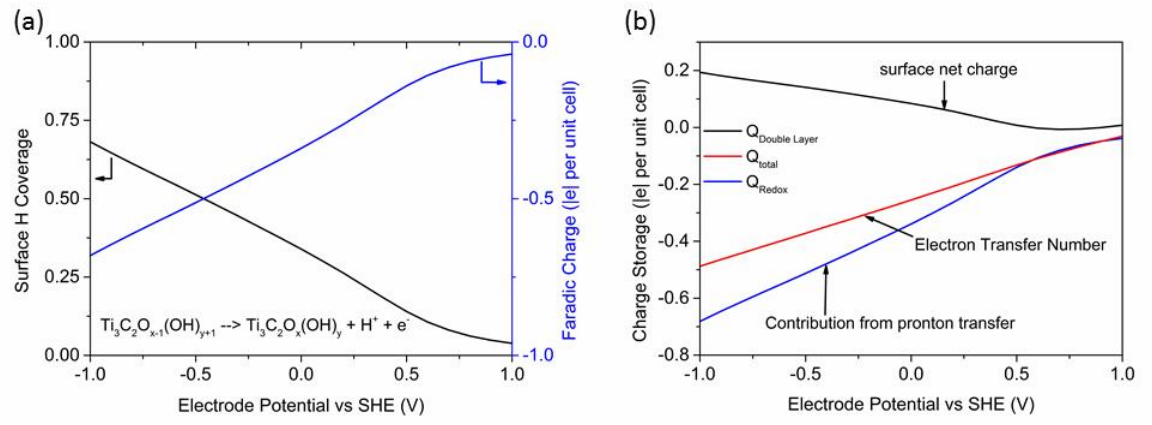


Figure 9-3. (a) Average H coverage (black) and Faradic charge (blue) of $Ti_3C_2T_x$ in 1M H_2SO_4 at different electrode potentials. (b) Faradic charge (blue, to balance proton transfer), EDL charge (black, due to surface net charge), and total charge (red, net electron transfer number) stored at different electrode potentials.

9.3.3 Comparison with the experimental capacitances.

We used the total charge (i.e., electron-transfer number in Figure 9-3b) to obtain the specific differential capacitance, C_{diff}. Figure 9-4 shows that for the redox-dominated region where the electrode potential is below 0.5 V vs SHE, C_{diff} is ~230 F/g. This is the same voltage window as the experimental measurements. Lukatskaya et al.[14] first measured the capacitive performance of $Ti_3C_2T_x$ in 1M H_2SO_4 electrolyte and reported the capacitance of 205 F/g in -0.35 ~ 0.35 V vs Ag/AgCl (corresponding to -0.12 ~ 0.58 V vs SHE in our simulation; window Expt-1 in Figure 9-4). This is in good agreement with our calculated capacitance of 235.6 F/g in the same voltage window. Hu et al.[13] reported the capacitance of 400 F/g in -0.45 ~ -0.05 V vs Ag/AgCl (window Expt-2 in Figure 9-4). For areal capacitance, the estimated specific surface area of $Ti_3C_2T_x$ from our model is ~478.8 m^2/g, which gives the areal capacitance of 48.2 $\boldsymbol{\mu}F/cm^2$.

More recently, Lukatskaya et al. reported a capacitance up to 450 F/g for a 90-nm-thick $Ti_3C_2T_x$ electrode in 3M H_2SO_4 for an extended voltage window (−1.1 to −0.1 V vs Hg/Hg_2SO_4). These capacitance values are higher than our predicted capacitance of ~230 F/g. Many factors can contribute to this discrepancy. From the experimental side, sample preparation, electrode thickness, electrolyte concentration, voltage window, etc., could all influence capacitive performance of a MXene electrode.[15] Furthermore, a recent NMR study has reported that the $Ti_3C_2T_x$ synthesized by LiF-HCl etching contains about 13% of –F group on surface.[18] There are two possible impacts from –F group: first, the oxidation state of Ti will be lower than un-fluoridized $Ti_3C_2T_x$ because F's formal charge (-1) is lower than O's formal charge (-2); second, since -F group is not redox-active, highly

fluoridized $Ti_3C_2T_x$ have lower capacitance in H_2SO_4, as indicated by experimental study.[36] From the modeling side, the implicit solvation model and the assumption of a constant EDL capacitance could also lead to uncertainty in the predicted values. Despite these factors, we think that our model does provide a semiquantitative description of the pseudocapactive charging behavior of MXene in H_2SO_4. This model should be able to predict the general trend of capacitance variation among different MXene materials, provided that the same solvation model is used.

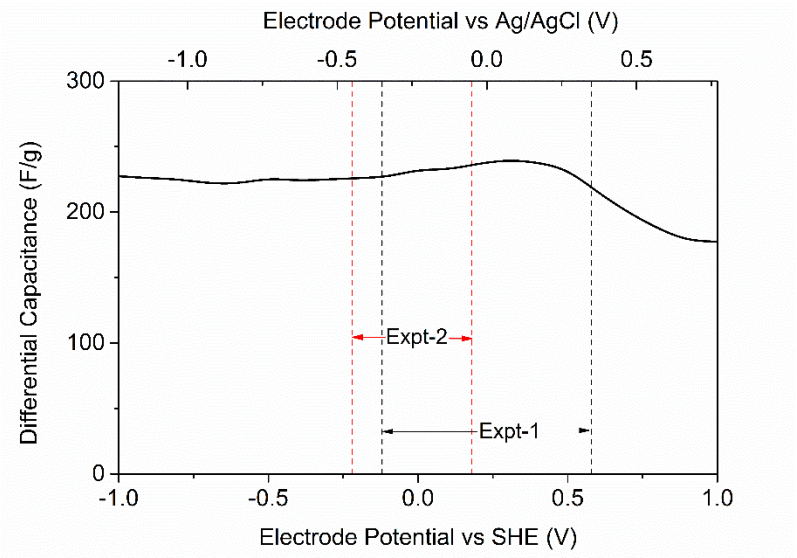


Figure 9-4. Differential capacitance of $Ti_3C_2T_x$ in 1M H_2SO_4. The voltage windows from two experiments are also shown: Expt-1 from ref. [14] and Expt-2 from ref. [13].

9.3.4 Electronic structure and charge distribution.

To pinpoint the atomic center responsible for the redox charging, we used fixed-charge DFT calculations with an implicit solvation model and plotted the total density of states (DOS) and local DOS of the $Ti_3C_2T_x$ electrode with the H coverages of 0.11 and 0.22 in Figure 9-5, corresponding to the voltage of 0.59 V and 0.3 V vs SHE in Figure 9-4,

respectively. One can see that the total DOS is mainly contributed by Ti near the Fermi level, so the electron transfer process mainly happens on the Ti atom. Figure 8-3a has shown that at a fixed electrode potential, a non-zero surface net charge always co-exists with the redox reaction. To determine how the excess charge is distributed on the electrode, we plotted the change in the planar electron density between the charged and the neutral $Ti_3C_2T_x$ electrodes at different H coverages. As can be seen in Figure 9-6, the excess charge on the electrode is mainly distributed on the surface oxygen layer that directly interacts with the electrolyte to form the electric double layer.

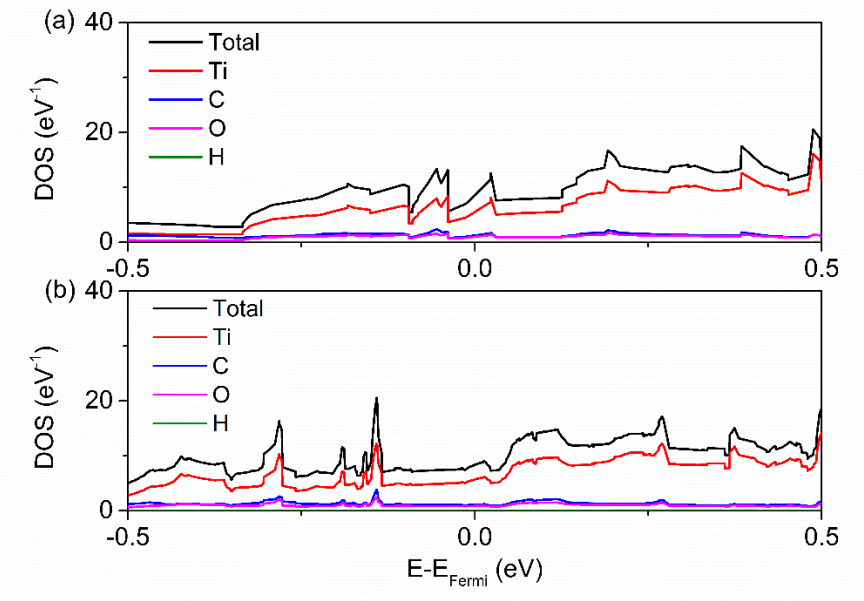


Figure 9-5. Total electronic density of states (DOS) and local DOS of the $Ti_3C_2T_x$ electrode: (a) H coverage is 1/9, (b) H coverage is 2/9.

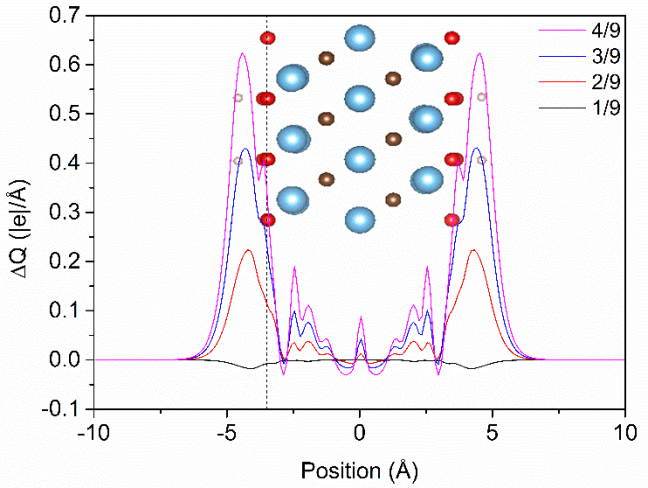


Figure 9-6. Planar charge density change (ΔQ) of the $Ti_3C_2T_x$ electrode after charging from a neutral surface with different H coverages. The dashed lines mark the position of the oxygen atoms.

9.3.5 Analysis of oxidation state of Ti.

To get a deeper understanding on this complicated electrochemical behavior, we estimated the oxidation state change by the proportional relation between valence and atomic Bader charge[37-40] on Ti atom at various H coverage and electrode potential (Figure S9-6 in SI). We found that when electrode potential changed from -0.29 to 0.59 V vs SHE, the oxidation state of Ti changed from +2.45 to +2.54. Experimental study by K-edge XANES (X-ray absorption near edge structure) has shown that the oxidation state change of Ti is from +2.33 to +2.43 in the voltage window of -0.12 ~ 0.58 V vs SHE,[14] which is very comparable to our simulation result. The small difference on Ti's valence can be attributed to the existence of –F groups on surface, which could lower the Ti oxidation state.

9.4 Summary and Conclusion

In summary, we have developed a theoretical model to describe the pseudocapacitive behavior of $Ti_3C_2T_x$ (T=O, OH) in the H_2SO_4 electrolyte by considering both the electronic double-layer (EDL) capacitance and the surface redox behavior. We used the electronic density functional theory with an implicit solvation model to determine the point of zero charge (PZC) for $Ti_3C_2T_x$ with different hydrogen coverages. From PZC, we deduced the voltage-dependent free energy of the electrode/electrolyte system that includes both the EDL and the redox contributions. In the experimentally relevant voltage window of 0.5 V down to -1.0 V vs SHE, we found 0.6 |e| proton transfer from the electrolyte to the electrode and 0.4 e^- electron transfer to the electrode from the applied voltage, which led to 0.2 |e| net surface charge, per unit formula. In other words, the capacitive mechanism is dominated by the redox process but the EDL charge works against the redox process. Analysis of the electronic structure and oxidation state of charged $Ti_3C_2T_x$ showed that the electron transfer mainly takes place on Ti at 0.1 |e| per Ti, which cause the change on Ti valence from +2.45 to +2.54, in good agreement with experiment. Since our simulation is mainly based on electronic structure calculation via DFT, it is feasible to build a relation between intrinsic electronic property (PZC shift during redox and hydrogenation energy) of different MXenes and their pseudocapacitance, which can be further used in high-throughput computational screening of novel MXene supercapacitors. The transferability of our model could help experimentalist to explore novel electrode material in MXene family more efficiently in the future. Our work provides

a general scheme to understand and predict the pseudocapacitive behavior of MXene materials.

References:

(1) Xie, Y.; Naguib, M.; Mochalin, V. N.; Barsoum, M. W.; Gogotsi, Y.; Yu, X. Q.; Nam, K. W.; Yang, X. Q.; Kolesnikov, A. I.; Kent, P. R. C. Role of Surface Structure on Li-Ion Energy Storage Capacity of Two-Dimensional Transition-Metal Carbides. *J. Am. Chem. Soc.* **2014**, 136, 6385-6394

(2) Lukatskaya, M. R.; Mashtalir, O.; Ren, C. E.; Dall'Agnese, Y.; Rozier, P.; Taberna, P. L.; Naguib, M.; Simon, P.; Barsoum, M. W.; Gogotsi, Y. Cation Intercalation and High Volumetric Capacitance of Two-Dimensional Titanium Carbide. *Science* **2013**, 341, 1502-1505

(3) Eames, C.; Islam, M. S. Ion Intercalation into Two-Dimensional Transition-Metal Carbides: Global Screening for New High-Capacity Battery Materials. *J. Am. Chem. Soc.* **2014**, 136, 16270-16276

(4) Zhang, X.; Zhang, Z.; Zhou, Z. MXene-based Materials for Electrochemical Energy Storage. *J. Energy Chem.* **2018**, 27, 73-85

(5) Naguib, M.; Come, J.; Dyatkin, B.; Presser, V.; Taberna, P. L.; Simon, P.; Barsoum, M. W.; Gogotsi, Y. MXene: a Promising Transition Metal Carbide Anode for Lithium-ion Batteries. *Electrochem. Commun.* **2012**, 16, 61-64

(6) Liang, X.; Garsuch, A.; Nazar, L. F. Sulfur Cathodes Based on Conductive MXene Nanosheets for High-Performance Lithium-Sulfur Batteries. *Angew. Chem. Int. Edit.* **2015**, 54, 3907-3911

(7) Tang, Q.; Zhou, Z.; Shen, P. W. Are MXenes Promising Anode Materials for Li Ion Batteries? Computational Studies on Electronic Properties and Li Storage Capability of Ti_3C_2 and $Ti_3C_2X_2$ (X = F, OH) Monolayer. *J. Am. Chem. Soc.* **2012**, 134, 16909-16916

(8) Seh, Z. W.; Fredrickson, K. D.; Anasori, B.; Kibsgaard, J.; Strickler, A. L.; Lukatskaya, M. R.; Gogotsi, Y.; Jaramillo, T. F.; Vojvodic, A. Two-Dimensional Molybdenum Carbide (MXene) as an Efficient Electrocatalyst for Hydrogen Evolution. *ACS Energy Lett.* **2016**, 1, 589-594

(9) Lin, Z. F.; Rozier, P.; Duployer, B.; Taberna, P. L.; Anasori, B.; Gogotsi, Y.; Simon, P. Electrochemical and In-situ X-ray Diffraction Studies of $Ti_3C_2T_x$ MXene in Ionic Liquid Electrolyte. *Electrochem. Commun.* **2016**, 72, 50-53

(10) Rakhi, R. B.; Ahmed, B.; Hedhili, M. N.; Anjum, D. H.; Alshareef, H. N. Effect of Postetch Annealing Gas Composition on the Structural and Electrochemical Properties of Ti_2CT_x MXene Electrodes for Supercapacitor Applications. *Chem. Mater.* **2015**, 27, 5314-5323

(11) Ling, Z.; Ren, C. E.; Zhao, M. Q.; Yang, J.; Giammarco, J. M.; Qiu, J. S.; Barsoum, M. W.; Gogotsi, Y. Flexible and Conductive MXene Films and Nanocomposites with High Capacitance. *Proc. Natl. Acad. Sci. U. S. A.* **2014**, 111, 16676-16681

(12) Levi, M. D.; Lukatskaya, M. R.; Sigalov, S.; Beidaghi, M.; Shpigel, N.; Daikhin, L.; Aurbach, D.; Barsoum, M. W.; Gogotsi, Y. Solving The Capacitive Paradox of 2D MXene using Electrochemical Quartz-Crystal Admittance and In Situ Electronic Conductance Measurements. *Adv. Energy. Mater.* **2015**, 5, 1400815

(13) Hu, M. M.; Li, Z. J.; Hu, T.; Zhu, S. H.; Zhang, C.; Wang, X. H. High-Capacitance Mechanism for $Ti_3C_2T_X$ MXene by in Situ Electrochemical Raman Spectroscopy Investigation. *Acs Nano* **2016**, 10, 11344-11350

(14) Lukatskaya, M. R.; Bak, S. M.; Yu, X. Q.; Yang, X. Q.; Barsoum, M. W.; Gogotsi, Y. Probing the Mechanism of High Capacitance in 2D Titanium Carbide Using In Situ X-Ray Absorption Spectroscopy. *Adv. Energy Mater.* **2015**, 5, 1500589

(15) Lukatskaya, M. R.; Kota, S.; Lin, Z.; Zhao, M.; Shpigel, N.; Levi, M. D.; Halim, J.; Taberna, P. L.; Barsoum, M. W.; Simon, P., et al. Ultra-high-rate Pseudocapacitive Energy Storage in Two-Dimensional Transition Metal Carbides. *Nat. Energy* **2017**, 2, 17105

(16) Sang, X. H.; Xie, Y.; Lin, M. W.; Alhabeb, M.; Van Aken, K. L.; Gogotsi, Y.; Kent, P. R. C.; Xiao, K.; Unocic, R. R. Atomic Defects in Monolayer Titanium Carbide ($Ti_3C_2T_x$) MXene. *Acs Nano* **2016**, 10, 9193-9200

(17) Come, J.; Xie, Y.; Naguib, M.; Jesse, S.; Kalinin, S. V.; Gogotsi, Y.; Kent, P. R. C.; Balke, N. Nanoscale Elastic Changes in 2D $Ti_3C_2T_x$ (MXene) Pseudocapacitive Electrodes. *Adv. Energy. Mater.* **2016**, 6, 1502290

(18) Hope, M. A.; Forse, A. C.; Griffith, K. J.; Lukatskaya, M. R.; Ghidiu, M.; Gogotsi, Y.; Grey, C. P. NMR Reveals the Surface Functionalisation of Ti_3C_2 MXene. *Phys. Chem. Chem. Phys.* **2016**, 18, 5099-5102

(19) Ji, X.; Xu, K.; Chen, C.; Zhang, B.; Ruan, Y. J.; Liu, J.; Miao, L.; Jiang, J. J. Probing the Electrochemical Capacitance of MXene Nanosheets for High-Performance Pseudocapacitors. *Phys. Chem. Chem. Phys.* **2016**, 18, 4460-4467

(20) Watanabe, E.; Rossmeisl, J.; Björketun, M.; Ushiyama, H.; Yamashita, K. Atomic-Scale Analysis of the RuO_2/Water Interface under Electrochemical Conditions. *J. Phys. Chem. C* **2016**, 120, 8096-8103

(21) Liu, Y. D.; Zhou, F.; Ozolins, V. Ab Initio Study of the Charge-Storage Mechanisms in RuO_2-Based Electrochemical Ultracapacitors. *J. Phys. Chem. C* **2012**, 116, 1450-1457

(22) Watanabe, E.; Ushiyama, H.; Yamashita, K.; Morikawa, Y.; Asakura, D.; Okubo, M.; Yamada, A. Charge Storage Mechanism of RuO_2/water Interfaces. *J. Phys. Chem. C* **2017**, 121, 18975-18981

(23) Zhan, C.; Jiang, D. E. Understanding the Pseudocapacitance of RuO_2 from Joint Density Functional Theory. *J. Phys.: Condens. Matter* **2016**, 28, 464004

(24) Steinmann, S. N.; Michel, C.; Schwiedernoch, R.; Sautet, P. Impacts of Electrode Potentials and Solvents on the Electroreduction of CO_2: a Comparison of Theoretical Approaches. *Phys. Chem. Chem. Phys.* **2015**, 17, 13949-13963

(25) Xiao, H.; Cheng, T.; Goddard, W. A. Atomistic Mechanisms Underlying Selectivities in C_1 and C_2 Products from Electrochemical Reduction of CO on Cu(111). *J. Am. Chem. Soc.* **2017**, 139, 130-136

(26) Schwarz, K.; Xu, B. J.; Yan, Y. S.; Sundararaman, R. Partial Oxidation of Step-bound Water Leads to Anomalous pH Effects on Metal Electrode Step-Edges. *Phys. Chem. Chem. Phys.* **2016**, 18, 16216-16223

(27) Petrosyan, S. A.; Rigos, A. A.; Arias, T. A. Joint Density-Functional Theory: Ab initio study of Cr_2O_3 Surface Chemistry in Solution. *J. Phys. Chem. B* **2005**, 109, 15436-15444

(28) Petrosyan, S. A.; Briere, J. F.; Roundy, D.; Arias, T. A. Joint Density-Functional Theory for Electronic Structure of Solvated Systems. *Phys. Rev. B* **2007**, 75, 205105

(29) Sundararaman, R.; Goddard, W. A.; Arias, T. A. Grand Canonical Electronic Density-Functional Theory: Algorithms and Applications to Electrochemistry. *J. Chem. Phys.* **2017**, 146, 114104

(30) Letchworth-Weaver, K.; Arias, T. A. Joint Density Functional Theory of the Electrode-electrolyte Interface: Application to Fixed Electrode Potentials, Interfacial Capacitances, and Potentials of Zero Charge. *Phys. Rev. B* **2012**, 86, 075140

(31) Gunceler, D.; Letchworth-Weaver, K.; Sundararaman, R.; Schwarz, K. A.; Arias, T. A. The Importance of Nonlinear Fluid Response in Joint Density-Functional Theory Studies of Battery Systems. *Modell. Simul. Mater. Sci. Eng.* **2013**, 21, 074005

(32) Sundararaman, R.; Goddard, W. A. The Charge-Asymmetric Nonlocally Determined Local-Electric (CANDLE) Solvation Model. *J. Chem. Phys.* **2015**, 142, 064107

(33) Perdew, J. P.; Burke, K.; Ernzerhof, M. Generalized Gradient Approximation Made Simple. *Phys. Rev. Lett.* **1996**, 77, 3865-3868

(34) Garrity, K. F.; Bennett, J. W.; Rabe, K. M.; Vanderbilt, D. Pseudopotentials for High-throughput DFT Calculations. *Comput. Mater. Sci.* **2014**, 81, 446-452

(35) Bai, Y. L.; Zhou, K.; Srikanth, N.; Pang, J. H. L.; He, X. D.; Wang, R. G. Dependence of Elastic and Optical Properties on Surface Terminated Groups in Two-dimensional MXene Monolayers: A First-principles Study. *RSC Adv.* **2016**, 6, 35731-35739

(36) Ghidiu, M.; Lukatskaya, M. R.; Zhao, M. Q.; Gogotsi, Y.; Barsoum, M. W. Conductive Two-Dimensional Titanium Carbide 'Clay' with High Volumetric Capacitance. *Nature* **2014**, 516, 78

(37) Xu, M. W.; Xiao, P. H.; Stauffer, S.; Song, J.; Henkelman, G.; Goodenough, J. B. Theoretical and Experimental Study of Vanadium-Based Fluorophosphate Cathodes for Rechargeable Batteries. *Chem. Mater.* **2014**, 26, 3089-3097

(38) Sadoc, A. G. J., *Charge Disproportionation in Transition Metal Oxides : [D]. Groningen : University of Groningen, **2008**.*

(39) Tang, W.; Sanville, E.; Henkelman, G. A Grid-based Bader Analysis Algorithm without Lattice Bias. *J. Phys.: Condens. Matter* **2009**, 21, 084204

(40) Yu, M.; Trinkle, D. R. Accurate and Efficient Algorithm for Bader Charge Integration. *J. Chem. Phys.* **2011**, 134, 064111

Supporting Information

MXene configurations at different hydrogen coverages

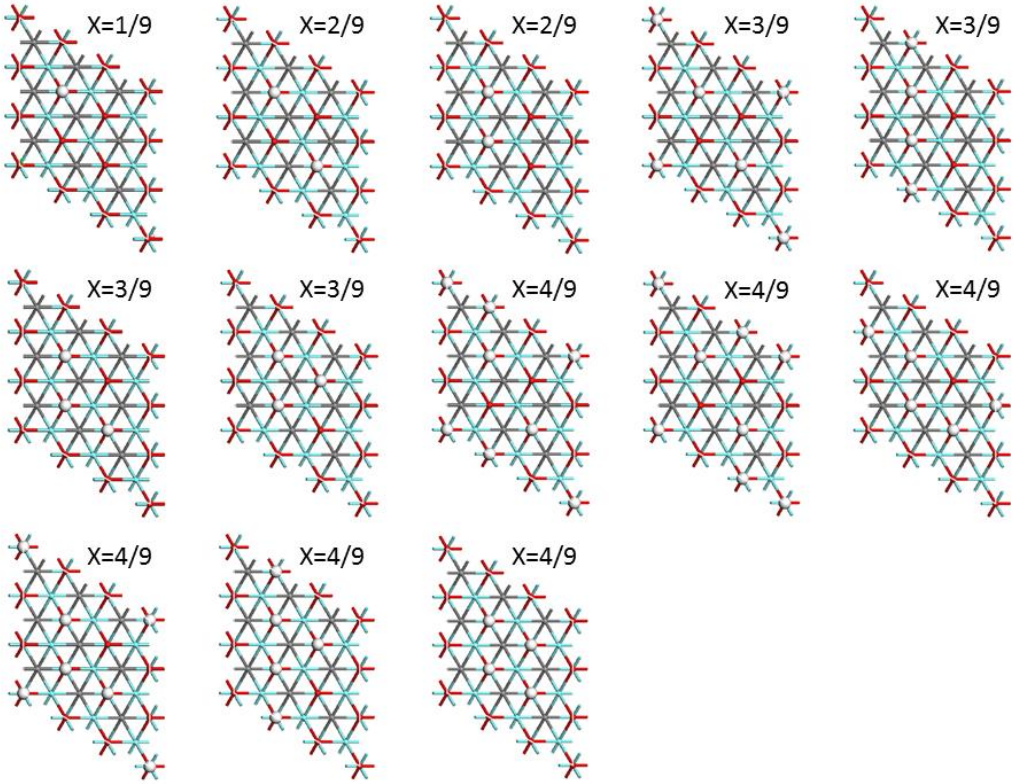


Figure S9-1. The structures of $Ti_3C_2T_x$ (T=O, OH) for H coverage from 1/9 to 4/9. The structures for higher coverages such as 5/9, 6/9, 7/9, 8/9 can be obtained similarly. In total, we examined 28 configurations for H coverage from 0/9 to 9/9.

The relationship of energy of the neutral system, E(x), and the electrode potential at the point of zero charge, $\boldsymbol{\varphi}_{PZC}(x)$, with hydrogen coverage, x.

Our DFT calculations with an implicit solvation of various $Ti_3C_2T_x$ configurations have shown that both E(x) and $\boldsymbol{\varphi}_{PZC}(x)$ exhibit a linear relation with x. The data were therefore fitted to a simple linear equation (Figure S2) to correlate E(x) in eV and $\boldsymbol{\varphi}_{PZC}(x)$ in V to x: $E(x) = -15.704x - 0.13742$ and $\varphi_{PZC}(x) = -4.919x + 5.800$.

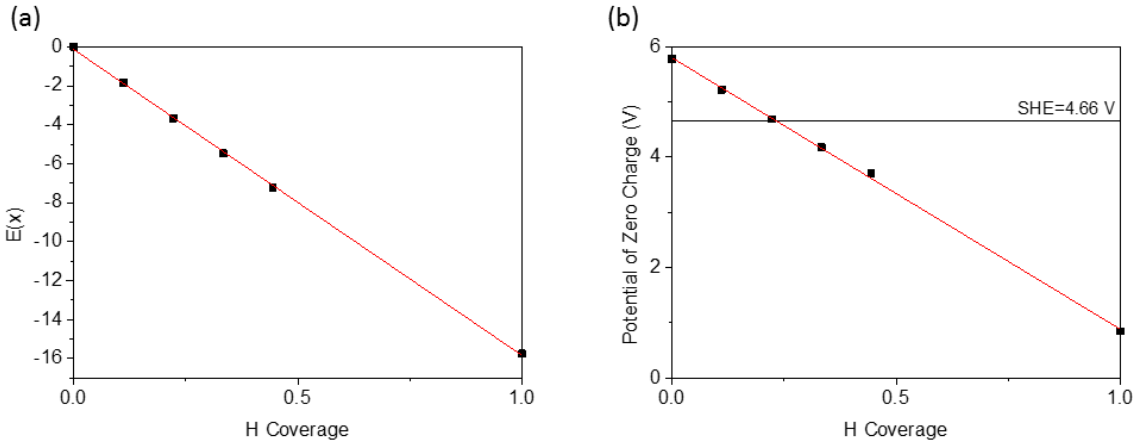


Figure S9-2. The linear relationship of (a) energy of the neutral system, E(*x*), and (b) the electrode potential at the point of zero charge, $\boldsymbol{\varphi}_{PZC}(x)$, with hydrogen coverage, *x*.

Average for degenerate H adsorption structures on $Ti_3C_2T_x$ (T=O, OH)

At a fixed H coverage, the configurational degeneracy is captured by a Gaussian function *g(x)* that fitted from manually obtained configurations in our model. The corresponding configuration numbers for the H coverage of 0/9, 1/9, 2/9, 3/9, 4/9, 5/9, 6/9, 7/9, 8/9, 9/9 are 1, 1, 2, 4, 6, 6, 4, 2, 1, 1, respectively. They were fitted to a Gaussian function as shown in Figure S9-3, to generate a continuous function, g(*x*). The motivation of selecting Gaussian function here are: 1. Gaussian function is widely used in statistics and easy to fit; 2. The combination of different H configuration (at same coverage) in a large supercell model can be briefly described by Binomial distribution, which eventually approaches normal distribution (Gaussian function) at large scale. Then, the partition function *Z* of the system at a specified electrode potential $\boldsymbol{\varphi}$ can be expressed as:

$$Z(\varphi) = \int_{x=0}^{x=1} g(x)\exp(-\beta G(x,\varphi))\,dx \qquad \text{S9-1}$$

where $\beta = 1/k_B T$. Based on the partition function Z, we can obtain the average H coverage and surface net charge at electrode potential $\boldsymbol{\varphi}$:

$$x_{avg}(\varphi) = \frac{\int_{x=0}^{x=1} x g(x) \exp(-\beta G(x,\varphi)) dx}{Z(\varphi)} \quad \text{S9-2}$$

$$Q_{avg}(\varphi) = \frac{\int_{x=0}^{x=1} Q(x,\varphi) g(x) \exp(-\beta G(x,\varphi)) dx}{Z(\varphi)} \quad \text{S9-3}$$

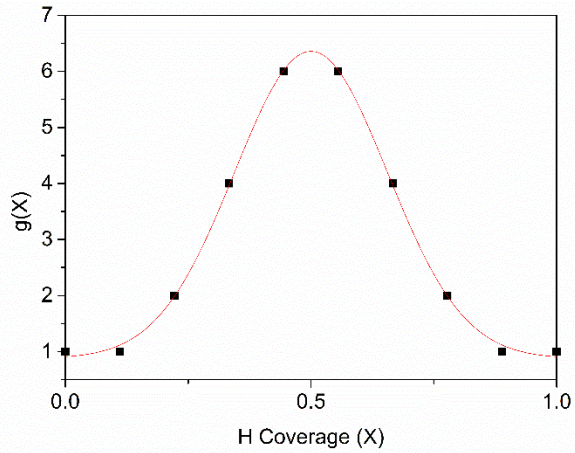


Figure S9-3. Gaussian function g(x) fitting to describe the configurational degeneracy.

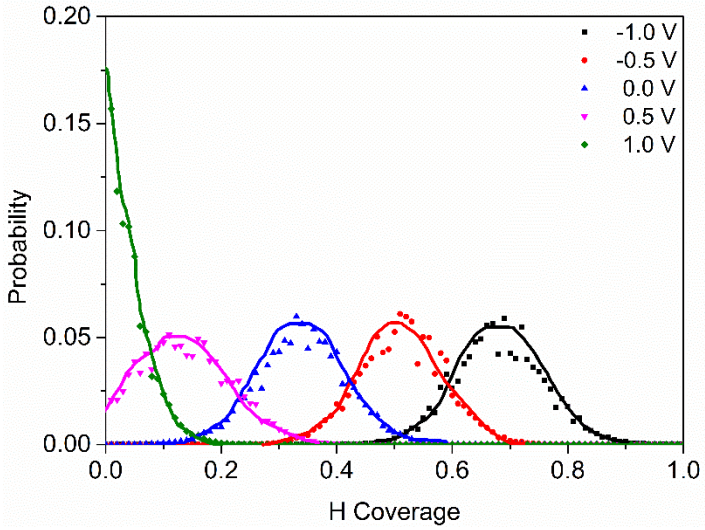


Figure S9-4. H coverage distribution at different electrode potentials applied to $Ti_3C_2T_x$.

Optimized lattice parameter as a function of H coverage on $Ti_3C_2T_x$ (T=O, OH)

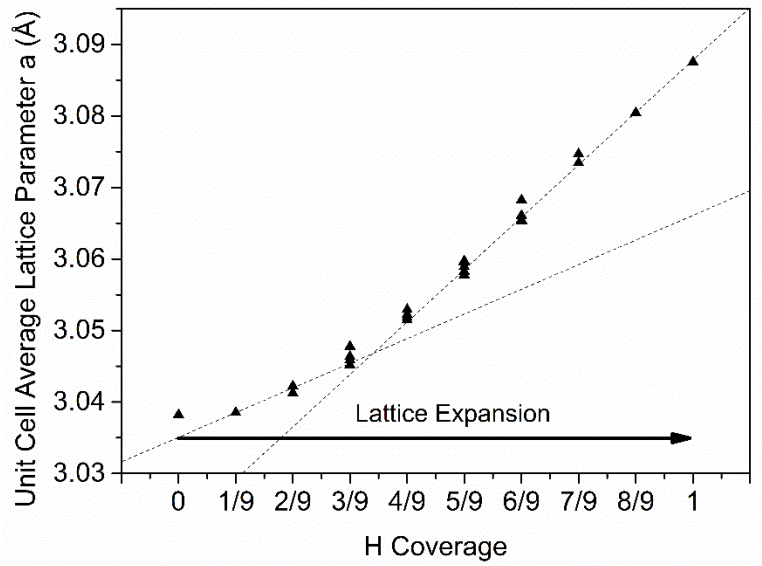


Figure S9-5. DFT-optimized lattice parameter as a function of H coverage on $Ti_3C_2T_x$ (T=O, OH).

Oxidation state of Ti in $Ti_3C_2T_x$ at various H coverages

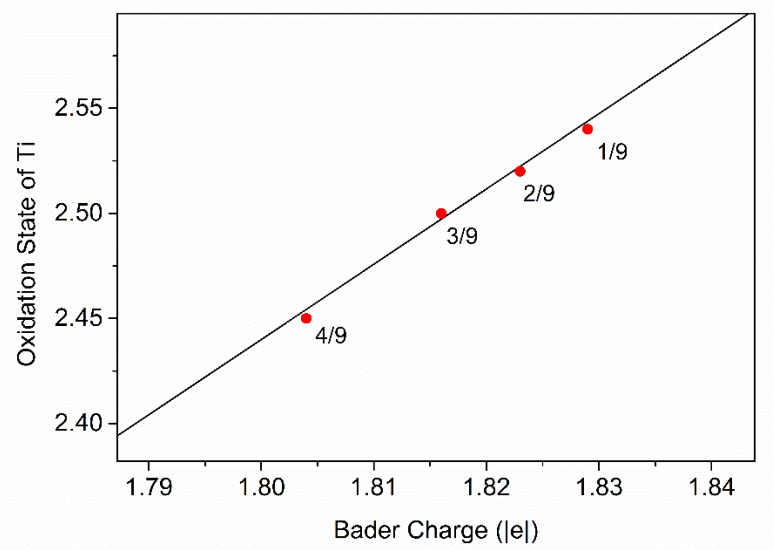


Figure S9-6. Estimated oxidation state of Ti in $Ti_3C_2T_x$ at various H coverages (1/9, 2/9, 3/9 and 4/9), from a linear scaling of the oxidation state vs Bader charge for Ti in TiO and TiO_2.

Chapter 10 Summary and future work on capacitive energy storage and solid/liquid interfacial model:

10.1 Summary

In this dissertation project, we applied first-principle simulation to study the capacitive mechanism of EDLCs and pseudocapacitors. First, studied the influence of quantum capacitance in graphene based electrodes by combining C_Q and C_{EDL} from DFT and classical simulation respectively. By including the C_Q in C_{tot}, we found that C_Q dominate the C_{tot} when applied voltage is low in single layer graphene electrode. With the layer stacking of graphene, C_Q increase with layer number and becomes less dominative. To enhance the capacitive performance of graphene, nitrogen doping is a commonly used way. We studied the N-doped graphene with three typical nitrogen configuration: graphitic, pyridinic and pyrrolic. From C_Q study, we found that graphitic and pyridinic N can increase C_{tot} by increasing C_Q, while pyrrolic N cannot. This conclusion is consistent with many experimental works. Beyond the "two contribution" model (C_Q+C_{EDL}), we applied JDFT to study the interfacial polarization in graphene EDLC and revealed the "third contribution" named "dielectric screening" effect. A complete physical picture of graphene EDLC is proposed and it include three parts: DOS charging (C_Q), electrolyte response (C_{EDL}) and dielectric screening inside electrode (C_{Dielec}). The contribution of C_{Dielec} is highly dependent on the layer number in FLG: the C_{Dielec} becomes dominative when $n > 3$. Moreover, the dielectric screening behavior was found to be electrolyte-independent. With the advantage of JDFT, we further studied the capacitive charging behavior of graphene edge sites, which cannot be solved by conventional methods due to the complicated surface

morphology and interfacial polarization. We investigated the armchair and zigzag edge, and found that the dielectric screening plays an important role in the capacitance of edge sites and couples with electrolyte response (EDL part). Comparing with graphene basal plane, the zigzag edge exhibit higher capacitance due to its large C_Q, C_{Dielec} and C_{EDL}, while armchair edge doesn't. Although both armchair and zigzag edge has higher C_{EDL}, the capacitance of armchair edge is limited by C_Q and C_{Dielec}, which revealed the importance of including the dielectric screening in EDLCs simulation. Based on our understanding on the capacitive mechanism of EDLCs, we designed 2D boron supercapacitors and found 2D boron sheets have very promising capacitive behavior (calculated capacitance higher than 400 F/g), comparing with conventional graphene EDLCs.

Different from EDLCs, pseudocapacitor has more complicated capacitive mechanism due to the solvation effect on redox reaction at interfacial region. To understand the pseudocapacitive mechanism, we studied two systems: RuO_2(110) and $Ti_3C_2T_x$ (T=O, OH). In our RuO_2 work, we obtained the charging curve by computing the hydrogen adsorption on RuO_2(110) surface in contact with implicit solvation model. The calculated differential capacitance curve exhibit good agreement with experimental CV measurement in terms of redox peak position and capacitance. In our $Ti_3C_2T_x$ work, we proposed a DFT-based model and it revealed the coexistence of redox and EDL behavior during charging/discharging process. The electronic structure calculation showed that the charge transfer is mainly contributed by the Ti's d orbital, and the calculated Ti's valence change is comparable to experimental XAS results. Our work provide new insight into understanding the capacitive energy storage at solid/liquid interface.

10.2 Challenges and future work

The capacitive behavior stems from the electrolyte response to the electrode surface charging: charged electrode causes the electrolyte response through ionic screening and polar solvent response; then the rearranged electrolyte structure polarizes the electrode and affects the charge distribution. Constant charge CMD with all-atom force field can accurately predict the electrolyte response, but the electrode charge distribution is not optimized. Constant potential MD and MC were proposed in recent years, but could not capture the electrode polarization. Electronic DFT coupled with a solvation model, such as JDFT and ESM, can capture the polarization of electrode from ionic screening in the electrolyte at the electronic-structure level, but the electrolyte response is limited by the implicit solvation model in the case of JDFT. Moreover, the computational cost can be prohibitive for the solvation-embedded DFT code due to the expensive computation for solid/liquid coupling, especially in ESM.

Another difficulty in EDLC modeling is the influence of surface chemistry. When the surface functional group could react with the ions or solvent, only considering the electrostatic interaction is not enough to capture the capacitive behavior. So how to cover the surface chemistry in EDLC modeling is also a challenging and unsolved issue, since it blurs the line between EDLC and pseudocapacitor. Modeling pseudocapacitor is still in its infancy. KS-DFT study can provide insights into the micro-dynamics of lithium diffusion and transport in the oxide. For the pseudocapacitor governed by the surface redox reaction, currently there is no good model to describe it due to the complexity of the interfacial physical chemistry. Although we have proposed an appropriate model for MXene system,

but it is still highly simplified and current not transferable to other pseudocapacitive electrodes. A typical case is the transition metal oxides in an acid electrolyte: the surface structure, surface reaction pathway, reaction kinetics, over-potential, solvent effect and electrolyte pH are all able to greatly influence the pseudocapacitive behavior.

In recent years, combining two or more types of conventional electrode materials to make hybrid electrodes also became a promising way to improve the capacitive performance of supercapacitor. One typical case is the pseudocapacitive polypyrrole/MXene hybrid electrode reported by Boota et al.[1] Another typical example of a hybrid electrode is based on 2,5-dimethoxy-1,4-benzoquinone on reduced graphene-oxide sheets.[2] For these hybrid systems, theoretical simulation can be extremely difficult due to the complex capacitive mechanism, which could include surface redox, ion intercalation, ion diffusion and EDL formation at the same time. Thus, a step-by-step and multi-scale approach is necessary.

References

(1) Boota, M.; Anasori, B.; Voigt, C.; Zhao, M. Q.; Barsoum, M. W.; Gogotsi, Y. Pseudocapacitive Electrodes Produced by Oxidant-Free Polymerization of Pyrrole between the Layers of 2D Titanium Carbide (MXene). *Adv. Mater.* **2016**, 28, 1517-1522

(2) Boota, M.; Chen, C.; Becuwe, M.; Miao, L.; Gogotsi, Y. Pseudocapacitance and excellent cyclability of 2,5-dimethoxy-1,4-benzoquinone on graphene. *Energ Environ Sci* **2016**, 9, 2586-2594